Wet spinning fibres from imogolite and carbon nanotubes

Joseph F. Moore

Department of Materials

Imperial College London

A thesis submitted for the degree of

Doctor of Philosophy

April 2022

Declaration

I declare that this thesis has been composed solely by myself and that all work presented within is my own, except for where specific reference is made. This work has not been submitted previously for the reward of a degree at this or any other university.

Joseph F. Moore

2022

The copyright of this thesis rests with the author and is made available under a Creative Commons Attribution-Non Commercial 4.0 International Licence (CC BY-NC). Under this licence, you may copy and redistribute the material in any medium or format. You may also create and distribute modified versions of the work. This is on the condition that: you credit the author and do not use it, or any derivative works, for a commercial purpose. When reusing or sharing this work, ensure you make the licence terms clear to others by naming the licence and linking to the licence text. Where a work has been adapted, you should indicate that the work has been changed and describe those changes. Please seek permission from the copyright holder for uses of this work that are not included in this licence or permitted under UK Copyright Law.'

Abstract

As 1D materials with high intrinsic strength and stiffness, nanotubes are promising building blocks for the next generation of fibres in structural composites. This thesis explores wet spinning techniques for assembling macroscale fibres from nanotubes. Carbon nanotubes (CNTs) are an obvious target material to compete with commercial carbon fibres, based on their excellent intrinsic mechanical properties and low density, alongside high electrical conductivity for multifunctional applications. However, studying CNT materials is challenging due to their intrinsically high optical absorbance and low X-ray scattering cross-section, as well as the dispersity of typical feedstocks in both size and helicity. Imogolite nanotubes (INTs) are an inorganic analogue that offers an opportunity to observe the assembly of nanotubes into fibres using both polarised optical microscopy (POM) and X-ray scattering (XRS). In contrast to CNTs, INTs are optically transparent and can be synthesised at low temperature to provide feedstocks that are uniform in structure and diameter.

In this work, the first known pure INT fibres have been produced and used to understand the nanotube wet spinning process. *In situ* POM demonstrated that in cylindrical spinnerets the spinning dope undergoes plug flow with inhomogeneous alignment due to the shear thinning nature of the solutions. The use of a tapered spinneret enables good alignment of the spinning dope, due to the induced extensional flow. Using this information, CNT fibres were spun from reduced CNT solutions and the wet spinning process was refined using a combination of *in situ* observation and statistical experimental design. The dissolution of negatively-charged CNTs (nanotubides) was examined both from a theoretical perspective and experimentally to identify the key conditions required to obtain homogeneous spinning dopes. The optimal dissolution depended upon both degree of charging and effective stirring. The optimised CNT dope was then wet spun using a variety of coagulating systems to identify the accessible process window and optimum parameters for spinning from these reactive charged solutions.

Further improvement of the CNT fibre properties is predicted to arise through the use of higher aspect ratio CNT feedstocks. However, challenges still remain in the liquid phase processing of longer CNTs. In order to create CNT fibres competitive with commercial CFs, future research should focus on how to process these longer feedstocks following the guidance in this thesis.

Table of contents

Declaration 2

Abstract 3

Table of contents 4

Acknowledgements 8

List of figures 9

List of tables 15

List of symbols 16

List of abbreviations 17

1 Introduction 18

1.1 Motivations 18

1.2 Aims, objectives and structure 19

2 Literature review 21

2.1 Technical fibres 21

2.1.1 Glass fibres 24

2.1.2 Carbon fibres 25

2.1.3 Polymer fibres 29

2.2 Nanotubular materials 32

2.2.1 Carbon nanotubes 32

2.2.2 Imogolite nanotubes 35

2.3 Nanotube fibres 36

2.3.1 Wet spinning CNT fibres 37

2.3.2 Dry spinning CNT fibres 41

2.3.3 Structure-property relationships in CNT fibres 43

3 Materials and methods 48

3.1 Materials 48

3.1.1 Imogolite nanotubes 48

3.1.2 Carbon nanotubes 48

3.2 Experimental methods 49

3.2.1 CNT dissolution 49

3.2.2 Wet spinning nanotube fibres 50
3.2.3 Cross-linking INT fibres 54
3.2.4 Polymer infusion into INT fibres 56
3.2.5 Molecular dynamics simulations 57
3.3 Characterisation techniques 58
3.3.1 (Polarised) optical microscopy 58
3.3.2 Electron microscopy 62
3.3.3 X-ray scattering 64
3.3.4 Raman spectroscopy 69
3.3.5 Single filament tensile testing 71
3.3.6 Capillary rheometry 73
3.3.7 Thermogravimetric analysis 74
3.3.8 Electrical conductivity 75
4 Exploring the spinning and properties of imogolite nanotube fibres 76
4.1 Synthesis of aluminogermanate INTs 77
4.2 Spinning INT fibres 78
4.2.1 Initial coagulation and washing trials 78
4.2.2 Spinnability of INT fibres 80
4.3 INT fibre mechanical properties 81
4.3.1 Impact of INT length on mechanical properties 81
4.3.2 Impact of humidity on mechanical properties 83
4.3.3 Impact of alignment on mechanical properties 85
4.4 Summary 88
5 *In situ* investigation of INT fibre spinning 89
5.1 Rheology and flow alignment of INT solutions 89
5.1.1 INT rheology 89
5.1.2 Flow alignment in cylindrical channels 92
5.1.3 Flow alignment in tapered channels 93
5.1.4 Impact of draw on INT alignment during spinning 95
5.2 Properties of INT fibres with varied draw ratio and constant washing time 96
5.3 Washing strategies for microstructural control of INT fibres 98
5.3.1 Impact of washing on densification and alignment in INT fibres 98

5.3.2 Mechanical properties of washed INT fibres 103
5.4 Summary 108
6 Cross-linking INT fibres 109
6.1 Ionic cross-linking of INT fibres 109
6.2 Covalent cross-linking of INT fibres 114
6.2.1 Dehydration reactions 114
6.2.2 Silanisation reactions 117
6.3 Polymer infusion into INT fibres 119
6.4 Summary 122
7 Dissolution of reduced CNT polyelectrolytes 123
7.1 Introduction 123
7.2 Theoretical framework for CNT polyelectrolyte solutions 123
7.2.1 Van der Waals energy 123
7.2.2 Electrostatic energy 124
7.2.3 Charging conditions for spontaneous dissolution 126
7.2.4 Counter-ion condensation 127
7.3 Molecular dynamics simulations of CNT solutions 128
7.4 Experimental determination of optimal CNT dissolution conditions 131
7.4.1 CNT feedstock characterisation 132
7.4.2 Stirring and mechanical agitation 134
7.4.3 Charging ratio and CNT mass loading 135
7.4.4 Filtration of CNT solutions 140
7.5 Summary 141
8 Wet spinning CNT fibres 143
8.1 Rheology of CNT solutions 143
8.2 Preparation of CNT spinning dopes 146
8.3 Identifying the CNT spinning processing window 148
8.3.1 Coagulant 148
8.3.2 Dope concentration 151
8.3.3 Extrusion velocity 152
8.3.4 Draw ratio 155
8.3.5 CNT feedstock 156

8.4 Effect of process parameters on CNT fibre tensile properties 157
8.4.1 Coagulant 157
8.4.2 Draw ratio 159
8.4.3 CNT feedstock 160
8.4.4 Dope concentration and extrusion velocity 162
8.5 Batch-to-batch variation in CNT fibre properties 165
8.6 Optimising CNT fibre spinning 168
8.7 Spinning higher aspect ratio CNTs 177
8.7.1 Dissolving higher aspect ratio CNTs 177
8.7.2 Tensile properties of higher aspect ratio CNT fibres 179
8.8 Summary 180
9 Conclusions and further work 182
Appendix 187
A1 Technical fibres properties 187
A2 Appendix figures 188
A3 Stepper motor wiring schematic 192
A4 Spinning rig code 193
A5 ImageJ macro for determining fibre diameter 196
A6 Calculating the INT orientational distribution function 197
References 200

Acknowledgements

This thesis would not have been possible without the help of the people and organisations which have supported me over the course of this project. Firstly, I would like to thank DSTL for funding this project through their UK-France PhD scheme. I have greatly appreciated the opportunities to collaborate internationally, improve my language skills and be exposed to the wider context of this work and a host of other PhD projects.

I would particularly like to thank my primary supervisor, Milo Shaffer, for his guidance, support and enlightening scientific discussions. His valuable suggestions have been instrumental in many hypothesis brainstorming sessions and have helped shaped the work throughout this thesis. I would also like to thank my co-supervisor at Université Paris-Saclay, Pascale Launois, and collaborator, Erwan Paineau. Their contributions of knowledge, experience and materials have enabled the work on imogolite nanotubes and their experimental support has been crucial in the X-ray analysis of fibres.

I would like to also thank my undergraduate project students, Jian Bi and Jiawei Zhang, whose experimental contributions have been critical to a chapter within this thesis, and also the wider support team at Imperial College London from stores to the Advanced Hackspace and the Chemistry technicians who have enabled much of this work.

Of course my thanks also go to my research colleagues including the post-docs (Dave A., Chris, Evgeny, Noelia, Adri, Chenchen, Ja Kyung, Arti) who have taught me so much and the PhD students (Dave S., Tommaso, Gabe, Hugo, Yuhan, Alex, Peach, Kalpana, Sandy, Sam, Charlie, Shirley, Maariyah, Syazana, Yunfei and newly Monaly, Luca and Hassan) whose collective support has been invaluable.

My final thanks are for my family who have supported me throughout. Particular thanks go to my in-laws who I have gratefully lived with at various points, my sister who formed my COVID bubble and my parents who are always there for me. Last (but certainly not least!), thanks to my wife, Emily, for her love, encouragement and support. I am excited for our next adventures.

List of figures

Figure 2.1 Ashby plots for commercial technical fibres. 22

Figure 2.2 Schematic of glass fibre production line. 24

Figure 2.3 Schematic of PAN-derived carbon fibre with a turbostratic, partially graphitised structure. 28

Figure 2.4 Molecular structure of liquid crystalline polymers, PBO and PPTA. 29

Figure 2.5 Schematic of dry-jet wet spinning process for rigid rod polymer fibres. 31

Figure 2.6 Schematic of shish kebab morphology of polyethylene crystals and microstructural changes during hot drawing. 32

Figure 2.7 Schematic of armchair, zigzag and chiral CNTs, wrapping vectors and density of states of metallic and semi-conducting CNTs. 33

Figure 2.8 Atomic structures of various INTs. 35

Figure 2.9 TEM images of double-walled Ge-INTs and OCSiAl Tuball CNTs. 36

Figure 2.10 Log-log plots of tensile strength and specific strength against bulk density for CNT fibres across the literature. 45

Figure 2.11 Specific strength as a function of bulk density for CNT fibres across the literature and from individual studies. 45

Figure 2.12 SEM of direct-spun CNT fibre and TEM of a bundle of aligned and densely packed CNTs. 47

Figure 3.1 Photograph of wet spinning equipment for producing CNT and INT fibres. 51

Figure 3.2 Photograph of collection spools used for in-line washed INT fibres and CNT fibres. 51

Figure 3.3 Photographs of CNT fibres on collection spool immediately after collection and after drying for 5 minutes. 54

Figure 3.4 Micrographs of tapered glass spinneret used to spin CNT fibres. 54

Figure 3.5 Photograph of metal support frame used to immerse INT fibres in polymer solution. 56

Figure 3.6 Michel-Lévy chart with markers for λ plates. 61

Figure 3.7 Secondary electron SEM images of coating materials for electron microscopy of non-conductive samples. 64

Figure 3.8 Illustration of Bragg's Law for a crystalline material. 65

Figure 3.9 Illustration of the definition of scattering vector Q. 66

Figure 3.10 Comparison of experimental and simulated diffraction patterns for oriented imogolite nanotubes. 67

Figure 3.11 Wide angle and small angle X-ray scattering patterns for CNT fibres alongside azimuthal scans of the equatorial diffraction peaks. 68

Figure 3.12 Illustration of the excitation and relaxation steps of the scattering processes in non-resonant Raman spectroscopy. 69

Figure 3.13 Representative Raman spectrum for single-walled CNTs and D/G intensity ratio as a function of inter-defect spacing. 70

Figure 3.14 Typical stress-strain curve for CNT fibres with indicated definitions of elastic modulus, tensile strength and strain at failure. 72

Figure 3.15 Photographs of CNT fibre mounted on cardstock frame and gripped in tensile tester. 72

Figure 3.16 Photograph of capillary rheometry equipment. 74

Figure 4.1 Length number distributions of synthesised INT feedstocks alongside representative TEM images. 77

Figure 4.2 Photograph, SEM images and polarised optical micrograhs of INT fibres. 80

Figure 4.3 Tensile strength and stress-strain curves for fibres made from INT-5d, INT-12d, INT-20d, INT-30d and INT-40d feedstocks. 83

Figure 4.4 Dynamic vapour sorption isotherm of INT fibre at 25°C. 83

Figure 4.5 Stress-strain curves for INT fibre tested at various controlled humidity alongside optical micrographs of fracture surfaces. 84

Figure 4.6 Fibre mechanical properties as a function of Hermans order parameter. 86

Figure 4.7 Photographic analogies of stress transfer models in rod and fibre assemblies. 87

Figure 5.1 Polarised optical micrographs of INT solutions with mass loading of 1 to 11 mg_{INT} mL^{-1}. 90

Figure 5.2 Flow curves of INT solutions determined by capillary rheometry. 91

Figure 5.3 Viscosity and predicted velocity profile of 11 mg mL^{-1} solution of INTs in water. 92

Figure 5.4 Polarised optical micrographs of INT solution flowing through a cylindrical capillary. 93

Figure 5.5 Schematic of optical arrangement for *in situ* observation of INT alignment and polarised optical micrographs of INT solutions flowing through tapered glass nozzles. 94

Figure 5.6 *In situ* polarised optical micrographs of INT fibre spinning with and without draw. 96

Figure 5.7 Structural and mechanical parameters of INT fibres prepared with varying draw ratios and constant washing time. 97

Figure 5.8 *In situ* polarised optical micrographs of INT fibres drying in ambient conditions with and without prior washing. 98

Figure 5.9 Polarised optical micrographs of INT gel fibre during immersion in DI water. 99

Figure 5.10 Polarised optical micrographs of dry INT fibres after washing for varying time periods. 100

Figure 5.11 Hermans orientation parameter for INT fibres as a function of washing time and normalised $CaCl_2$ diffusion distance. 103

Figure 5.12 Stress strain curves and mechanical and structural parameters of INT fibres spun from tapered spinnerets with varying washing bath lengths and draw ratios. 106

Figure 5.13 Stress strain curves and mechanical and structural parameters of INT fibres spun from cylindrical spinnerets with varying washing bath lengths and draw ratios. 106

Figure 6.1 *In situ* POM of spinning INT fibres in a sodium succinate coagulation bath. 111

Figure 6.2 Structural and mechanical properties of gel cross-linked and water washed INT fibres. 113

Figure 6.3 TGA traces of INT fibres with constant heating rate and with heating and cooling cycles. 116

Figure 6.4 Stress-strain curves for as-spun and heat treated INT fibres. 116

Figure 6.5 SEM micrographs of as-spun, ethanol soaked and TEOS treated INT fibres. 118

Figure 6.6 Stress-strain curves for as-spun, ethanol soaked and TEOS treated INT fibres. 119

Figure 6.7 SEM images of polymer-infused and as-spun INT fibres. 121

Figure 6.8 Stress-strain curves of as-spun and polymer infused INT fibres. 121

Figure 7.1 Illustration of assumed charge density on a CNT. 125

Figure 7.2 Calculated interaction energies for pairs of CNTs with varying degrees of charging. 126

Figure 7.3 Calculated energy barrier for separation of pairs of charged CNTs. 127

Figure 7.4 Snapshots of molecular dynamics simulation box during equilibration. 129

Figure 7.5 Snapshots of simulation box during steered molecular dynamics for NaC_8 CNTs. 130

Figure 7.6 Force profiles for separating a pair of CNTs calculated using steered molecular dynamics. 131

Figure 7.7 TGA traces for Tuball and eDIPS EC1.5 CNTs. 133

Figure 7.8 Raman spectra and I_D/I_G ratios for Tuball and eDIPS EC1.5 CNTs. 133

Figure 7.9 Transmission optical microscopy images of CNT solutions prepared with varying stirring conditions and solution volumes. 135

Figure 7.10 Transmission optical micrographs of CNT solutions in DMAc at varying charging ratios and mass loadings. 137

Figure 7.11 Agglomerate content of CNT solutions as a function of CNT mass loading and charging ratio. 137

Figure 7.12 Optical micrographs of CNT solutions at charging ratios between NaC_6 and NaC_{20} and mass loadings from 5 mg mL^{-1} to 1 mg mL^{-1}. 139

Figure 7.13 Agglomerate content of reduced CNT solutions from Tuball 01RW03 CNTs (batch 788) as a function of CNT mass loading and charging ratio. 140

Figure 7.14 Transmission optical microscopy images of CNT solutions before and after filtration. 140

Figure 8.1 Flow curves for CNT and INT solutions with power law indices and predicted velocity profiles. 145

Figure 8.2 Transmission optical micrographs of CNT spinning dopes. 147

Figure 8.3 Transmission polarised optical micrographs of CNT spinning dopes. 147

Figure 8.4 Microscope images of CNT solutions extruded into polar aprotic solvents. 150

Figure 8.5 Microscope images of CNT solutions extruded into ethanol, DMAc and binary mixtures. 150

Figure 8.6 Microscope images of CNT solutions extruded into acetone showing necking and filament fracture. 151

Figure 8.7 Microscope images comparing extrusion of CNT solutions with dope concentrations of 5 and 2.5 mg mL^{-1}. 151

Figure 8.8 Microscope images and processing window of CNT extrusion as a function of injection velocity and coagulant. 153

Figure 8.9 Processing window for extrusion of CNT spinning dope into binary mixtures of ethanol and DMAc as a function of extrusion velocity. 154

Figure 8.10 Critical draw ratios for draw resonance instabilities. 156

Figure 8.11 Microscope images of 5 mg mL^{-1} eDIPS CNT solutions extruded into a 50% ethanol/DMAc coagulation bath at varying extrusion velocity. 156

Figure 8.12 Mechanical and structural properties for Tuball CNT fibres spun with a variety of process conditions into acetone and ethanol/DMAc coagulation baths. 158

Figure 8.13 Mechanical properties of fibres spun at various draw ratios, with otherwise identical conditions. 159

Figure 8.14 Mechanical and structural properties of CNT fibres spun from 5 mg mL^{-1} Tuball and eDIPS spinning dopes. 161

Figure 8.15 Mechanical and structural properties of Tuball CNT fibres coagulated in (red) acetone and (green) ethanol coagulation baths with spinning dope mass loadings of 2.5 and 5 mg_{CNT} mL^{-1}. 163

Figure 8.16 Mechanical and structural properties of eDIPS CNT fibres coagulated in acetone with spinning dope mass loadings of 1 and 5 mg_{CNT} mL^{-1}. 164

Figure 8.17 Batch-to-batch variation in CNT fibre properties prepared from 1 mg mL^{-1} eDIPS CNT dopes coagulated in acetone with DR 1.2. 167

Figure 8.18 Surface plots and contour maps of specific strength of CNT fibres as a function of coagulation time and extrusion velocity for acetone, 25% ethanol/THF and 75% ethanol/THF coagulation baths. 171

Figure 8.19 Surface plots and contour maps of specific modulus of CNT fibres as a function of coagulation time and extrusion velocity for acetone, 25% ethanol/THF and 75% ethanol/THF coagulation baths. 172

Figure 8.20 SEM images of fibres spun in acetone with an extrusion velocity of 21 mm s^{-1} and coagulation time of 1.6 and 12 s. 173

Figure 8.21 SEM images of fibres spun in 25% ethanol/THF with an extrusion velocity of 21 mm s^{-1} and coagulation time of 1.6 and 14 s. 174

Figure 8.22 SEM images of fibres spun in 75% ethanol/THF with an extrusion velocity of 21 mm s^{-1} and coagulation time of 1.6 and 12 s. 175

Figure 8.23 Scatter plots of specific modulus against specific conductivity and modulus against conductivity for fibres in this work and the literature. 176

Figure 8.24 Photograph of as-received Tuball, eDIPS EC1.5 and eDIPS EC-DX CNTs. 177

Figure 8.25 Transmission optical micrographs of EC-DX NaC_8 CNT solutions. 178

Figure 8.26 Transmission (polarised) optical micrographs of EC-DX CNT solutions before and after bath sonication. 179

Figure 8.27 Mechanical properties and representative specific stress-strain curves for EC1.5 and EC-DX CNT fibres. 180

Figure A1 Infrared spectra of INT feedstocks as a function of growth time. 188

Figure A2 Illustration of modified Wilhelmy method to estimate fibre gel strengths. 189

Figure A3 Stress strain curves of fibers from INT-20d with no prior conditioning or with initial conditioning at 85% RH. 189

Figure A4 SEM image of INT fibre with corresponding elemental composition as calculated by energy dispersive spectroscopy. 190

Figure A5 Small angle X-ray scattering diffractogram for INT solutions at mass loadings of 5 and 11 mg mL^{-1}. 191

Figure A6 Stitched optical micrographs of tapered glass spinnerets used to assess impact of extrusion velocity on CNT extrusion stability. 191

Figure A7 Definitions of angles used in determining INT order parameter and example XRS pattern and azimuthal scan. 197

Figure A8 Simulated azimuthal scans of intensity from hypothetical direct space orientation distribution functions. 198

Figure A9 Comparison of azimuthal scans of intensity on XRS patterns with the corresponding deduced orientation distribution function of INTs relative to the fibre axis. 199

List of tables

Table 1	Properties of various commercial technical fibres.	23
Table 2	Summary of effects of coagulation bath solvent content and temperature on wet spun PAN fibre morphology.	27
Table 3	Properties of wet spun and manually washed INT fibres.	82
Table 4	Estimated elongational strain rate for complete flow alignment of INT solutions at varying flow rates.	95
Table 5	Properties of wet spun and in-line washed INT fibres produced with tapered spinneret.	107
Table 6	Stability of INT fibres prepared with various coagulants after washing in water.	110
Table 7	Mechanical properties of as-spun and thermally treated INT fibres.	116
Table 8	EDS elemental analysis of as-spun, ethanol soaked and 1 M TEOS treated INT fibres.	118
Table 9	Mechanical properties of as-spun, ethanol soaked and TEOS treated INT fibres.	119
Table 10	Van der Waals interaction parameters for a pair of 1.2 and 2.4 nm diameter CNTs.	126
Table 11	Technical specifications of Tuball 01RW03 and eDIPS EC1.5 CNTs.	134

List of symbols

$A_{f,0}$	Initial fibre cross-sectional area
A_{nozz}	Spinneret nozzle area
c_{dope}	Spinning dope mass loading
c_n	Number concentration of rods
d	Interplanar spacing
d_{CNT}	CNT diameter
d_f	Fibre diameter
d_{gf}	Gel fibre diameter
d_r	Diameter of a rigid rod
D	Diffusion coefficient
D_r	Rotational diffusion coefficient
DR	Draw ratio
e	Elementary charge
E	Electric field
E_L	Laser excitation energy
$f(\beta)$	Orientational distribution function
F	Force
g	CNT wall separation
g_0	Equilibrium CNT wall separation
I_{calc}	X-ray intensity as calculated from an orientational distribution function
$I_{D/G}$	Raman intensity ratio of D and G peaks
I_{exp}	Lorentzian fit to azimuthal scan of X-ray intensity
k_B	Boltzmann constant
K	Flow consistency index (of a power law fluid)
L_{bath}	Length of washing bath
L_c	Length of a capillary
L_r	Length of a rigid rod
L_0	Initial length (of a fibre)
ΔL	Extension (of a fibre)
n	Integer
n_c	Charging ratio, number of carbons per elementary charge
n_i	Dimensionless flow behaviour index (of a power law fluid)
n_1, n_2	Refractive index in 1, 2 directions
ΔP	Pressure drop (in capillary flow)
Q	Volumetric flow rate
r	Radial position
$\tilde{R}$	Reduced distance parameter (g/g_0)
R_c	Capillary radius
R_{sep}	Nanotube separation
S	Hermans order parameter
t	Time period (of diffusion)
t_{sample}	Sample thickness
T	Temperature
U	Mean velocity
U_{LJ}	Lennard-Jones potential
v_z	Axial velocity
w_d	(Direct space) HWHM of orientation distribution function
w_r	(Reciprocal space) HWHM maximum of a Lorentzian function
x	Linear position/separation
δz	Infinitesimal length segment

α	Taper semi-angle
β	Polar angle between nanotube and fibre axes
$\dot{\gamma}$	Shear strain rate
$\dot{\gamma}_w$	True wall shear strain rate
$\dot{\gamma}_{a,w}$	Apparent wall shear strain rate
Δ_{pd}	Optical path difference
ϵ	Engineering strain
ϵ_f	Failure strain
ϵ_r	Relative permittivity
ϵ_0	Permittivity of free space
$\dot{\epsilon}_z$	Elongational strain rate
η	Shear viscosity
θ	X-ray scattering angle
λ	Wavelength
λ_{cd}	Linear charge density
ξ	Oosawa-Manning condensation parameter
ρ_{INT}	Envelope density of an INT
σ	Engineering stress
σ_f	Failure stress, tensile strength
σ_a	Surface density of atoms
τ_w	Wall shear stress (in capillary flow)
ϕ	Azimuthal angle on X-ray scattering pattern
ϕ_E	Electrical potential energy
ϕ_{vdW}	Van der Waals potential energy
ω_{RBM}	Raman shift of CNT radial breathing mode

List of abbreviations

APS	γ-aminopropyltriethoxysilane
CF	Carbon fibre
CNT	Carbon nanotube
CVD	Chemical vapour deposition
DI	De-ionised
DMAc	N,N-dimethylacetamide
DMF	N,N-dimethylformamide
DMSO	Dimethyl sulfoxide
DR	Draw ratio
DW-CNT	Double-walled CNT
EDS	Energy dispersive spectroscopy
FC-CVD	Floating catalyst CVD
FW-CNT	Few-walled CNT
GCL	Gel cross-linked
HWHM	Half-width-at-half-maximum
ID	Internal diameter
INT	Imogolite nanotube
MW	Molecular weight
MW-CNT	Multi-walled CNT
NMR	Nuclear magnetic resonance
ODF	Orientational distribution function

OPD	Optical path difference
PBO	Poly(p-phenylene-2,6- benzobisoxazole)
POM	Polarised optical microscopy
PPTA	Poly(p-phenylene terephthalamide)
PTFE	Polytetrafluoroethylene
PVOH	Poly(vinyl alcohol)
RBM	Radial breathing mode
RH	Relative humidity
SAXS	Small angle X-ray scattering
SEM	Scanning electron microscopy
SMD	Steered molecular dynamics
SW-CNT	Single-walled CNT
TEM	Transmission electron microscopy
TEOS	Tetraethyl orthosilicate
TGA	Thermogravimetric analysis
THF	Tetrahydrofuran
UHMWPE	Ultra-high molecular weight polyethylene
WAXS	Wide angle X-ray scattering
WW	Water washed
XRS	X-ray scattering

1 Introduction

1.1 Motivations

Carbon fibre (CF) is a strategic resource due to its excellent specific strength and specific modulus, which makes CF reinforced polymers the material of choice for high performance aerospace applications. However, the production of CF is largely localised to the USA, Japan and China which together represent 60% of global production capacity.[1] Production in other countries is dominated by just one or two plants, leading to a vulnerable production landscape for such a strategic material. Meanwhile, there are some limitations to the wider application of CFs. Carbon fibre reinforced composites have a high environmental cost with an embodied energy of approximately 750 MJ kg^{-1} of composite[2] compared to just 25 MJ kg^{-1} for steel[3] and the susceptibility of CFs to brittle failure at ~2% strain can lead to catastrophic failure after the accumulation of undetected damage. Addressing these two drawbacks of current CFs may enable a new material to supersede existing commercial fibres, creating an opportunity to develop and secure a new supply of composite materials whilst bringing environmental and engineering benefits.

Carbon nanotubes (CNTs) are highly appealing materials from which to develop the next generation of structural fibres. Individual, pristine CNTs have extraordinary intrinsic mechanical properties with tensile strength and modulus of ~50 GPa and ~1 TPa respectively.[4] They also have intriguing electronic properties giving them revolutionary potential in electronics and energy storage.[5] As fully graphitic starting materials which are typically produced from growth processes below 1000 °C, CNT fibres do not require the high temperature carbonisation processes which makes PAN-derived CFs so costly. In addition, a route to the zero-CO_2 production of CNT materials as a by-product of the reformation of natural gas has been proposed.[6] Although the current performance of macroscopic CNT fibres falls well short of the intrinsic properties of the individual nanotubes, fibres have been produced with specific strengths greater than commercial CFs (4.1 vs ~3.5 N tex^{-1}) whilst having failure strains of 3-4%.[7] These highly promising results come along with some development risks; scale-up of the floating-catalyst CVD process which produces the highest specific strength fibres may prove challenging, whilst the superacid-based processing route used to spin or densify CNT fibres leads to residual acid in the fibre which may be detrimental

to the matrix when incorporated into a composite material. As an alternative to superacids, CNTs can be charged with alkali metals and then dissolved in polar aprotic solvents as negatively charged polyelectrolytes ("nanotubides") for liquid phase processing. These CNT solutions can form liquid crystalline phases conducive to fibre spinning and the charged CNTs are highly reactive, raising an opportunity to functionalise or cross-link during the spinning process, which may potentially be used to modulate the fibre properties. The dissolution and functionalisation of negatively charged CNTs has been thoroughly demonstrated,[8, 9] and one publication reports spinning fibres from this system,[10] but the process has not been systematically investigated as a method of producing a next generation competitor to carbon fibres.

The optimisation of CNT spinning processes is greatly hindered by a range of characterisation challenges particular to CNTs, particularly due their varied helicity and diameter and their high optical absorbance. In comparison, other (lesser known) nanotubes can be much more conveniently characterised. Imogolite nanotubes are aluminosilicate/aluminogermanate nanotubes which can be synthesised with consistent diameters and readily characterised with both optical and X-ray techniques.[11] Although spinning pure fibres from imogolite nanotubes has not previously been demonstrated, they are an appealing, experimentally convenient analogue material for CNTs and may also create useful fibres in their own right.

1.2 Aims, objectives and structure

This project aims to explore spinning nanotube fibres *via* a scalable wet spinning process. The key aims of this project are to:

- develop a wet spinning approach for imogolite nanotubes and use this analogue system to investigate the liquid phase processing of nanotubes and assembly into fibres,
- identify the processing window for spinning CNT fibres from negatively charged polyelectrolyte solutions and develop an understanding of the key process and structural parameters which affect the properties of nanomaterial fibres,
- suggest a development pathway for a nanomaterial competitor to carbon fibres.

This thesis contains 9 chapters, which are organised as follows. Chapter 1 provides an overview of the motivations, aims and objectives of the thesis and describes the structure. Chapter 2 provides a background to the fields of technical fibres and nanotubes and reviews the current literature of nanomaterial fibres. Chapter 3 describes the materials and methods used this work including brief explanations of the application of characterisation techniques to nanomaterials. Chapter 4 details the development of a wet spinning process for imogolite nanotubes and investigates the properties of these new fibres. In Chapter 5, the imogolite nanotube spinning process is further refined and *in situ* observations of the spinning process are used to inform the wet spinning of nanomaterial fibres. Chapter 6 investigates the effect of a variety of cross-linking and post-processing techniques on imogolite nanotube fibres. In Chapter 7, the dissolution of negatively charged CNTs is investigated from a theoretical and experimental perspective to identify the key process parameters for creating suitable spinning dopes, whilst in Chapter 8 these spinning dopes are used to produce CNT fibres. The process window is determined and the key parameters for stable spinning are identified. The links between the processing and properties of CNT fibres are then analysed to determine a set of ideal spinning conditions for this material system. The work in this thesis is then summarised in Chapter 9, with a concluding perspective on a development pathway for CNT fibres and suggestions for further investigations. Finally, there is an appendix to the thesis, containing supplementary information including descriptions, diagrams and code for key experimental equipment and analysis processes.

2 Literature review

2.1 Technical fibres

Fibre materials have long been used for their inherent processability. Whilst fibrous materials can be strong and stiff in tension, their fineness enables them to be bent, curved and woven into useful structures. Natural fibres, such as wool and hemp, have been used throughout history but a desire for greater durability alongside commercial competitivity led to the development of Nylon and glass fibres in the 1930s. Initially these fibres were used in textiles (and in the case of glass fibres as insulation materials), however the requirement for lightweight materials for aircraft in World War II led to the development of composites with stiff, strong glass fibres embedded in a matrix of the newly-developed polymer resins.

Whilst there are many factors affecting the properties of composites,[12, 13] this review section will focus on the technical fibres which may be used as reinforcements. Firstly, an overview of the properties of key commercial fibres is given, followed by a more detailed description of the process used to produce each fibre and some of the steps taken to develop them into mature technologies.

The landscape of commercial fibres can be explored on Ashby plots of strength and elastic modulus or specific strength and specific modulus (Figure 2.1). For any component which has a realistic constraint on its size, it is advantageous to use materials with good areal-basis properties. Yet for applications in sectors such as transportation, high specific (or mass-basis) properties are essential to create lightweight structures which can yield fuel savings and other benefits.

Of the commercial technical fibres, carbon fibres have the best areal properties with tensile strength up to 6 GPa and modulus up to 550 GPa. Polymer and glass fibres have similar tensile strengths and elastic moduli (2-4 GPa and 70-140 GPa respectively), except for Zylon® fibres made from poly(p-phenylene-2,6-benzobisoxazole) (PBO) which have exceptionally high strength and modulus (5.8 GPa and 270 GPa respectively). Meanwhile, polymer and carbon fibres have similarly high specific strengths of 2-4 N tex^{-1}. Whilst the Zylon® PBO fibres still have the highest specific strength of the polymer fibres, ultrahigh molecular weight poly(ethylene) (UHMWPE) fibres such as Spectra® and Dyneema® perform well in this

category due to their comparably low density (0.97 g cm^{-3}). Carbon fibres have the highest specific modulus of all the technical fibres at ~300 N tex^{-1}. Glass fibres have poorer specific properties than the other technical fibres due to their higher density (2.5-2.6 g cm^{-3}) and are therefore less desirable when light weighting is essential.

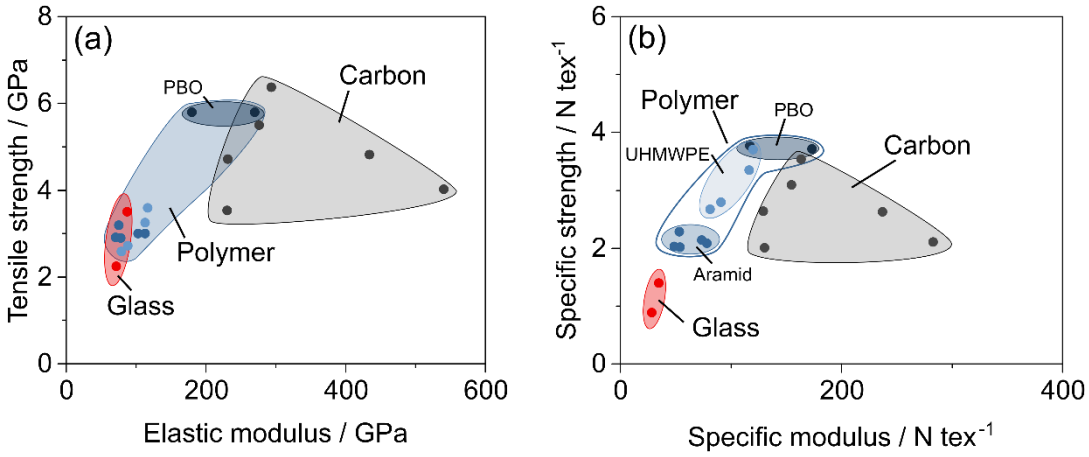


Figure 2.1 Ashby plots for commercial technical fibres. Sourced from manufacturer data sheets (appendix section A1, p.187).

In selecting a technical fibre for a commercial application, there is strong competition between performance and cost (Table 1). Whilst glass fibres have poorer properties than the high performance polymers and carbon fibre, they are significantly cheaper at ~£1-2.5 kg^{-1} compared to £20-25 kg^{-1} for general purpose carbon fibres and ~£20 kg^{-1} for lower grade polyaramid fibres.[14] Some of the highest performance materials are almost prohibitively expensive, particularly PBO fibres which would therefore only be selected for the highest performance applications. Carbon fibres represent a good balance of cost against performance, which explains their selection for aerospace and high-performance automotive applications, as well as their importance as a strategic resource in the global market.

Table 1. Properties of various commercial technical fibres.

		Tensile strength	Elastic modulus	Specific strength	Specific modulus	Density	Failure strain	Cost[14]
		GPa	GPa	N tex^{-1}	N tex^{-1}	g cm^{-3}	%	£ kg^{-1}
Carbon fibre	General purpose [15]	3-5	200-250	1.7-2.2	110-140	1.75-1.9	1.5	20-25
	High strength [16, 17]	5-7	250-300	2.8-3.9	140-170	1.75-1.9	1.8-2.2	40-80
	High modulus [18]	3-5	400-600	1.7-2.2	220-330	1.75-1.9	0.8	40-80
Polymer fibres	Aramid (Kevlar®, Twaron®)	2.5-3	70-120	1.7-2	50-80	1.45	2.5-3.5	20-100
	PBO (Zylon®)	6	180-270	3.9	115-175	1.55	2.5-3.5	100-160
	UHMWPE (Spectra®, Dyneema®)	2.5-3.5	80-115	2.6-3.7	80-120	0.97	2.8-3.6	60-110
Glass fibres [19]	E-glass	1.5-3	70	0.6-1.2	30	2.55	1.8-3.4	1-2.5
	S-glass	3.5	90	1.4	35	2.5	4	15-25

2.1.1 Glass fibres

Glass fibres are primarily comprised of silica plus some additional oxides, such as alumina, boron trioxide, sodium oxide and others, with the variety of compositions designated by letters.[20] These compositions have differing properties but the most widely used in composite materials are E-glass and S-glass fibres due to their high strengths and economies of scale, although when specific chemical resistance is required other compositions may be selected. Glass fibres are typically produced by gravity-fed melt spinning (Figure 2.2). The oxides are weighed, mixed and loaded into a furnace in which they are molten. The pressure of the head of molten glass forces the liquid through a spinneret comprised of several Pt/Rh alloy nozzles known as bushings. The rate of fibre manufacture by mass is controlled by the flow rate of the liquid glass and hence depends upon the dimensions of the bushings, the viscosity of the glass and the head pressure. As such, care must be taken to control the temperature of the glass and machine loading to maintain consistent spinning. After initial extrusion, the fibres are drawn to their final diameter using a winding drum with a typical speed of 2500 m min^{-1}.[19] The fibres are cooled with water and sprayed with a coating (sizing) which is used to improve their handleability and compatibility with composite matrices. Finally, the individual filaments are twisted to form a yarn or strand which is later woven into the desired structure for the composite material.

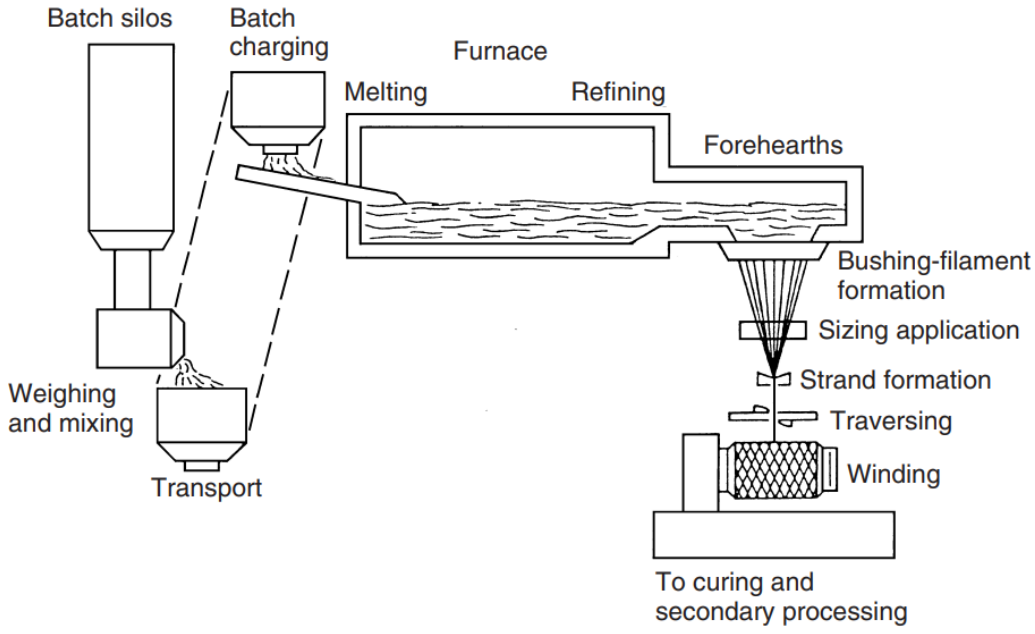


Figure 2.2. Schematic of glass fibre production line. Reprinted from reference [19] with permission from Elsevier.

The tensile strength of pristine single filaments can be as high as ~3-5 GPa,[20] however the strength is highly flaw sensitive and strengths of typical yarns are 20-30% lower (~2-4 GPa) due to the introduction of surface defects during strand forming.[21] As surface flaws have such a large impact on the tensile strengths, careful application of sizing is crucial to obtaining high tensile strengths of glass fibre strands. Robust but lubricious coatings reduce damage during downstream processing and are commonly applied by a roller as a two-component mixture of an organosilane coupling agent and polymer film former.[22] Whilst the tensile strength of glass fibres is strongly dependent upon the fibre surface, the elastic modulus is more strongly affected by the bulk material and depends principally upon the composition of the glass with typical values between 70 and 90 GPa.[19]

Whilst initially used in automotive and aeronautical applications, glass fibres are now widely used in composites where an economical, light-weight, electrically-insulating and thermally-stable material is required. Some key examples are sporting equipment, electrical circuit boards and chemical processing equipment.

2.1.2 Carbon fibres

First commercialised in the early 1960s, carbon fibre reinforced polymer composites have become ubiquitous in high performance applications. The principal method of producing CFs is from a polymer precursor which is then heated and carbonised in an inert environment at temperatures up to 3000 °C. Early CFs were produced using Rayon or viscose precursors, but were superseded by poly(acrylonitrile) (PAN) with its improved yields and lower production costs.[23] In the spinning of PAN-derived CFs, firstly acrylonitrile is polymerised as a random copolymer to a molecular weight of approximately 70-200 kDa where the comonomers are selected to assist the spinning and downstream heat treatment steps.[24] The composition, homogeneity and molecular-weight of the precursor polymer has a significant impact on the spinning and heat treatment process and, therefore, the final fibre structure and properties. Some guiding principles are available in the literature: a bulky acrylic comonomer should be used to improve the drawability of the PAN and an acidic comonomer should be used to aid stabilisation and carbonisation.[24] However, a complete model to link the polymer and fibre properties is not available and significant information on optimised CFs is protected as trade secrets by commercial producers.

After polymerisation, PAN fibres are typically prepared by wet spinning. The polymer is dissolved in a polar aprotic solvent such as dimethyl acetamide (DMAc), dimethyl formamide (DMF) or dimethyl sulfoxide (DMSO) or an aqueous solution of sodium thiocyanate (~50% NaSCN) and then injected into a coagulation bath typically containing a mixture of the solvent and water. For the PAN loadings found in typical spinning dopes (~20 wt%), solid will precipitate at a water content of less than 10% when using aprotic solvents, whilst solutions in aqueous NaSCN precipitate at a bath solvent:water ratio of ~3:4.[25] The rate of coagulation in a typical precipitation bath therefore depends not simply on the coagulation bath concentration, but also on the choice of solvent used to initially dissolve the PAN, further complicating the wet spinning process.

The microstructure and morphology of the PAN precursor fibres depends critically upon the coagulation bath concentration and temperature, as summarised in Table 2, with drastic changes in cross-sectional shape and presence of voids. At higher temperatures, diffusion of solvent and non-solvent occurs more rapidly.[23] In the case of PAN fibres spun from organic aprotic solvents into a mixed organic-water coagulation bath, the in-diffusion of water appears to dominate and therefore at higher temperatures with greater diffusion the proto-fibres are swollen by the coagulant fluid. The water/solvent coagulant fluid then phase separates within the fibre, leading to a fibre with a large circular cross-section but large internal macropores.[26, 27] At lower temperatures less in-diffusion of the coagulant occurs, leading to more dense fibres with fewer pores.[28, 29] The concentration of the coagulation bath (usually given as the percentage of solvent in the solvent-water mixture) impacts the rate of coagulation of the skin of the proto-fibre. A lower solvent content leads to the rapid formation of a rigid skin on the surface of the proto-fibre. Upon drying, densification and shrinkage of the fibre leads to a collapse of the rigid skin into a ‘kidney bean’ shape. The most dense and uniformly circular PAN fibres appear to be produced with a chilled coagulation bath (~20°C) and a high solvent content, with the low temperature preventing excess diffusion of coagulant into the fibre (lowering porosity) and the high solvent content in the coagulation bath preventing the formation of a rigid skin (circular cross-section).[30] However rapid skin coagulation can be useful to ‘lock-in’ the shape of fibres from novel spinnerets such as Y- and X-shapes, and therefore more active coagulants may be chosen.[31]

Table 2. Summary of effects of coagulation bath solvent content and temperature on wet spun PAN fibre morphology.

		Coagulation bath temperature		
		High (≥ 70 °C)	Medium (40-60 °C)	Low (≤ 20 °C)
Coagulation bath solvent content	High (≥ 70%)	Circular shape, porous[32]	Circular shape, some voids[28, 31, 32]	Circular shape, dense[30]
	Medium (~65%)	Elliptical shape, porous[32]	Circular shape[32]	
	Low (≤ 60%)	Circular shape, porous[26-28]	Mostly circular, porous[27, 28, 31, 32]	Kidney shape, dense[26-28, 30, 31]

Once a dense and uniform PAN precursor fibre has been spun, it is then stabilised and carbonised in a series of heat treatment steps. The initial stabilisation occurs at temperatures from 200-300 °C in an air atmosphere. During stabilisation adjacent nitrile groups on the polymer chains cyclise to form rings and the polymer backbone dehydrogenates to form an aromatic structure, whilst oxygen reacts to form hydroxyl, carboxyl and ketone groups on the rings.[24, 33] It is important to maintain tension in the fibre during the stabilisation step to prevent shrinkage of the precursor fibre and aid the formation of an aligned series of hexagonal rings which can be more effectively carbonised.[34] Carbonisation is then conducted in an inert atmosphere at temperatures of around 1300 °C. During carbonisation, the heteroatoms are evolved from the polymer fibre as a variety of species including hydrogen cyanide, ammonia, water and carbon dioxide.[35] After carbonisation, the fibre obtains a turbostratic structure of graphitic planes. Whilst the graphitic planes have a preferred orientation, with their c-axes perpendicular to the fibre axis, there is no registration between the hexagonal lattices on adjacent planes (Figure 2.3). An optional graphitisation step under tension in an inert atmosphere at temperatures up to 3000 °C is used to anneal the turbostratic carbon to a more graphitic structure with a closer inter-layer spacing, larger crystallite size and greater molecular order.[33] The microstructure of the graphitised fibres leads to a higher elastic modulus, but lower tensile strength compared to non-graphitised fibres.[36]

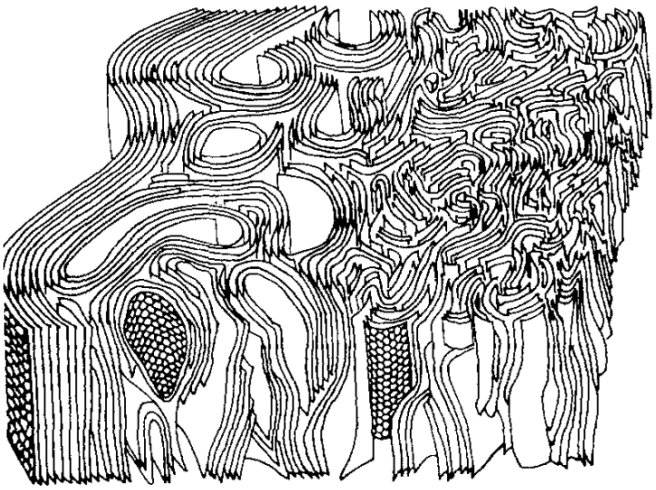


Figure 2.3. Schematic of PAN-derived carbon fibre with a turbostratic, partially graphitised structure. Reprinted from reference [37] with permission from Springer.

An alternative method for producing CFs is to use pitch, a high molecular weight fraction of petroleum feedstocks, as a precursor. In particular, mesophase pitches, which form a liquid crystalline phase when molten, are used to produce high modulus CFs. These high molecular weight pitches are typically melt spun with the assistance of a solvent to form a precursor fibre which is relatively weak and difficult to draw but has excellent ability to reorganise to a graphitic structure in ongoing processing.[38] Achieving stable spinning of pitch precursors is notoriously challenging[39] and many reports are published of researchers adjusting temperature, extrusion rate, winding speed and pitch composition to improve the spinnability.[40-45] Compared to PAN-derived fibres, mesophase pitch-derived CFs carbonise and graphitise more easily[33] and have highly aligned structures with typically a distinctive radial pattern. The resulting fibres are denoted ultrahigh modulus CFs with an elastic modulus often greater than 500 GPa but lower tensile strengths of ~2 GPa.[46]

Whilst having specific strength and modulus which is competitive with all other materials, a critical limitation of carbon fibre (CF) reinforced materials is their high cost and embodied energy, which is dominated by the CFs themselves. Almost 50% of the embodied energy of CFs is attributed to the high temperature stabilisation and carbonisation processes,[47] and so reducing the need for carbonisation is appealing to reduce the environmental cost of producing CFs. Using more easily graphitised, or already graphitic, materials to form fibres will reduce the costs of carbonisation potentially making cheaper and more environmentally friendly carbon fibres.

2.1.3 Polymer fibres

Polymers are high molecular weight molecules comprised of repeating sub-units. The most common polymers are linear polymers where the monomers are linked end-to-end to form a long chain. The ideal form of a linear polymer fibre is one where the polymer chains are fully extended and well oriented along the fibre axis so that tensile load is applied in the direction of the covalent bonds of the polymer chains, whilst inter-molecular interactions transfer stress between the chains and through the fibre. In the context of high-performance technical fibres there are two competing methods for creating a dense structure of highly aligned polymer chains. Highly concentrated solutions of rigid backbone polymers (such as Kevlar®) can be processed in an aligned liquid crystalline phase, or low concentration solutions of flexible chain polymers (such as polyethylene) can be spun with extremely high draw ratios to induce alignment. This section will briefly review these methods in turn to provide background context to the development of these technical fibres.

A variety of different rigid rod polymers have been developed and used to spin fibres, and the breadth of possible structures are illustrated in textbooks on liquid crystalline polymers.[48] In general rigid rod polymers have aromatic backbones with limited rotational freedom and bonding configurations which produce a long, straight fully-extended chain. Poly(p-phenylene terephthalamide) (PPTA) and PBO, two of the most widely used polymers for high performance fibres, have exemplar structures for rigid rod polymers (Figure 2.4). The polymers are initially synthesised by condensation polymerisation from aromatic monomers in acidic solvents which are used to help solvate the polymer chains, catalyse the reaction and aid dehydration.[49] The solubility of the rigid rod polymers is typically low and requires solvents with a strong enthalpic interaction, in particular sulfonic or phosphoric acids which can protonate the polymer backbone.[50]

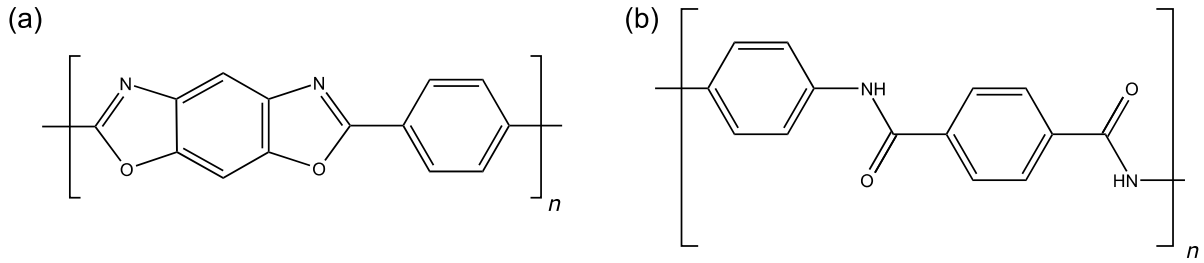


Figure 2.4. Molecular structure of liquid crystalline polymers (a) PBO and (b) PPTA.

The rigid rod polymers can be spun into fibres by either wet spinning or dry-jet wet spinning arrangements. In dry-jet wet spinning, the spin dope is first extruded from the spinneret into a short air gap before entering the coagulation bath. A key benefit of the dry-jet process is that a higher solution temperature can be used (typically 70-90 °C) which enables spinning from higher polymer concentration spin dopes and therefore higher throughput production.[48] Additionally, it provides a region in the spinning line for drawing the fibre before it coagulates, which aligns the polymer chains in an extensional flow field (Figure 2.5).[51] As for wet spinning processes, in the coagulation bath diffusion of non-solvent and solvent in and out of the fibre occurs whilst the fibre densifies, and the fibre is then removed from the coagulation bath for further washing and drying stages followed by optional hot drawing to increase alignment and crystallinity. Significant knowledge of the optimum fibre spinning process is maintained as trade secrets, but various research suggests that the draw ratio in the air gap, coagulation temperature and drying conditions play a role in determining the fibre properties.[51-53] The properties of rigid rod polymers vary quite considerably across the different polymers, with PBO fibres being considerably stiffer and stronger than those made from PPTA. However, there are various drawbacks to some of these fibres. In particular, PBO has poor resistance to UV and visible light and a low axial compressive strength which limits its applications to composites,[54] whilst the performance of para-aramid fibres reduces considerably at temperatures above 190 °C.[55] Development of a new liquid crystalline polymer named M5 was designed to create strong hydrogen bonds between adjacent chains and improve compressive properties.[56] Despite promising initial results, this fibre is yet to be commercialised.

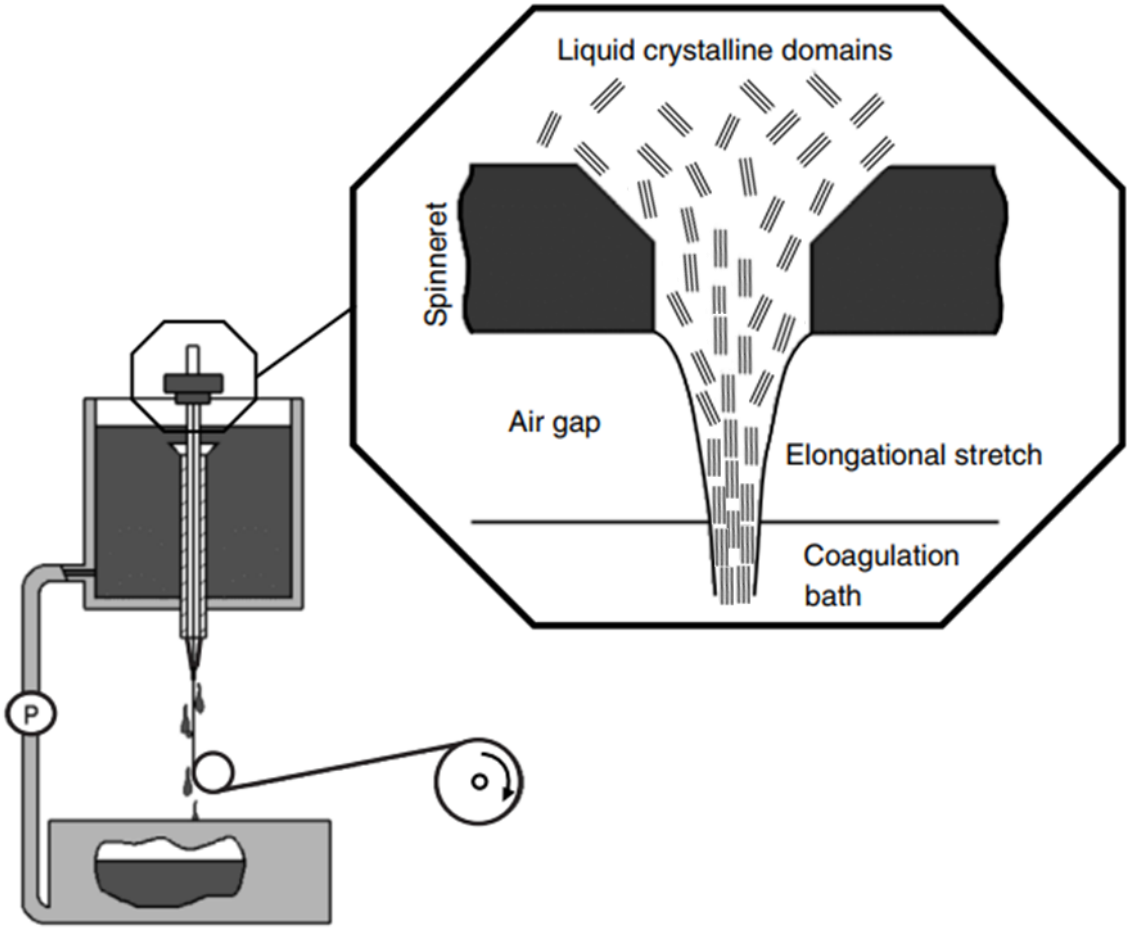


Figure 2.5. Schematic of dry-jet wet spinning process for rigid rod polymer fibres. Reproduced from reference [51] with permission from Elsevier. Note that the diagram has been modified to emphasise the reorientation of the liquid crystalline domains within the taper of the spinneret.

Polyethylene is a highly appealing polymer for producing high specific strength fibres. It has a low density, sterically small side groups (hydrogen atoms) which do not inhibit chain packing and the lowest energy bond conformation is the trans state which means it crystallises in an extended chain form. However, typical crystallisation of polyethylene occurs relatively locally, forming crystalline regions of folded polymer chains with chain entanglements segregating to regions between the crystals. The low modulus non-crystalline regions largely dictate the properties of the resulting fibre.

In order to reduce the number of chain entanglements, enable greater tensile draw and hence increase the crystallinity of the fibres, so-called gel-spinning was developed. Instead of spinning from a melt, the polymer is first dissolved at a low concentration (~2-10 wt%)[57, 58]

at high temperature and spun through a spinneret into a cooling chamber where it forms a gel fibre which is dried and collected on a bobbin.[54] The polymer initially crystallises from the gel into a 'shish kebab' structure which is commonly seen in stirred solutions of polyethylene where lamellae of folded chains nucleate from the side of fibrous regions of aligned, extended chains (Figure 2.6a).[59] The as-spun fibre is then hot drawn to 30-100 times its original length, which is enabled by the low entanglement density. During the hot drawing, the lamellae of the shish kebabs unfold, yielding a highly oriented and crystalline fibrillar structure (Figure 2.6b).[60] The resulting fibres have excellent specific properties with specific strength and modulus of up to 3.7 and 120 N tex^{-1} respectively, but have a low maximum continuous operating temperature of just 70 °C.[61]

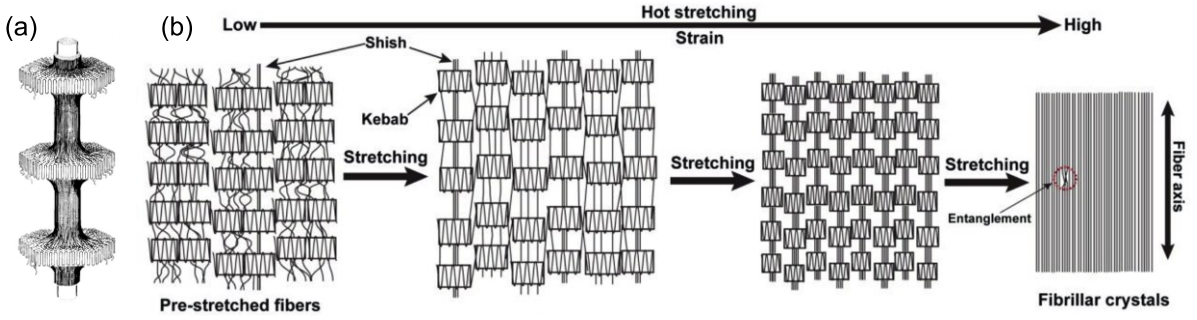


Figure 2.6. (a) Schematic of the shish kebab morphology of polyethylene crystallised from stirred low concentration solutions. Adapted from reference [59] with permission from Springer Nature.
(b) Schematic of microstructural changes to gel-spun polyethylene fibres during hot drawing. Reproduced from reference [60] with permission from Elsevier.

2.2 Nanotubular materials

2.2.1 Carbon nanotubes

Carbon nanotubes (CNTs) are a quasi-one-dimensional allotrope of carbon with the structure of a graphene sheet wrapped into a cylinder. The angle of the wrapping and the length of the tube circumference can be described by a vector on the graphitic plane. Specific high symmetry forms are known as armchair and zig-zag CNTs based on the orientation of the bonds around the tube circumference, whilst other helicities are simply known as chiral (Figure 2.7a). The helicity of CNTs significantly affects their electronic density-of-states resulting in CNTs of both metallic and semi-conducting character (Figure 2.7b). Armchair CNTs are always metallic, whilst zig-zag and chiral CNTs may be either metallic or semi-conducting depending upon their wrapping vector (Figure 2.7c).[62] CNTs are typically synthesised in a

complex mixture of different helicities, diameters and lengths. Additionally, they may be formed as a mixture of single-, double- and multi-walled nanotubes (SW-CNTs, DW-CNTs, MW-CNTs). SW-CNTs have typical diameters of 1-2 nm[63] whilst MW-CNTs can have diameters as large as 200 nm[64] and are comprised of multiple concentric CNTs with a wall spacing of approximately 0.34 nm, similar to the interlayer spacing of graphite.[65]

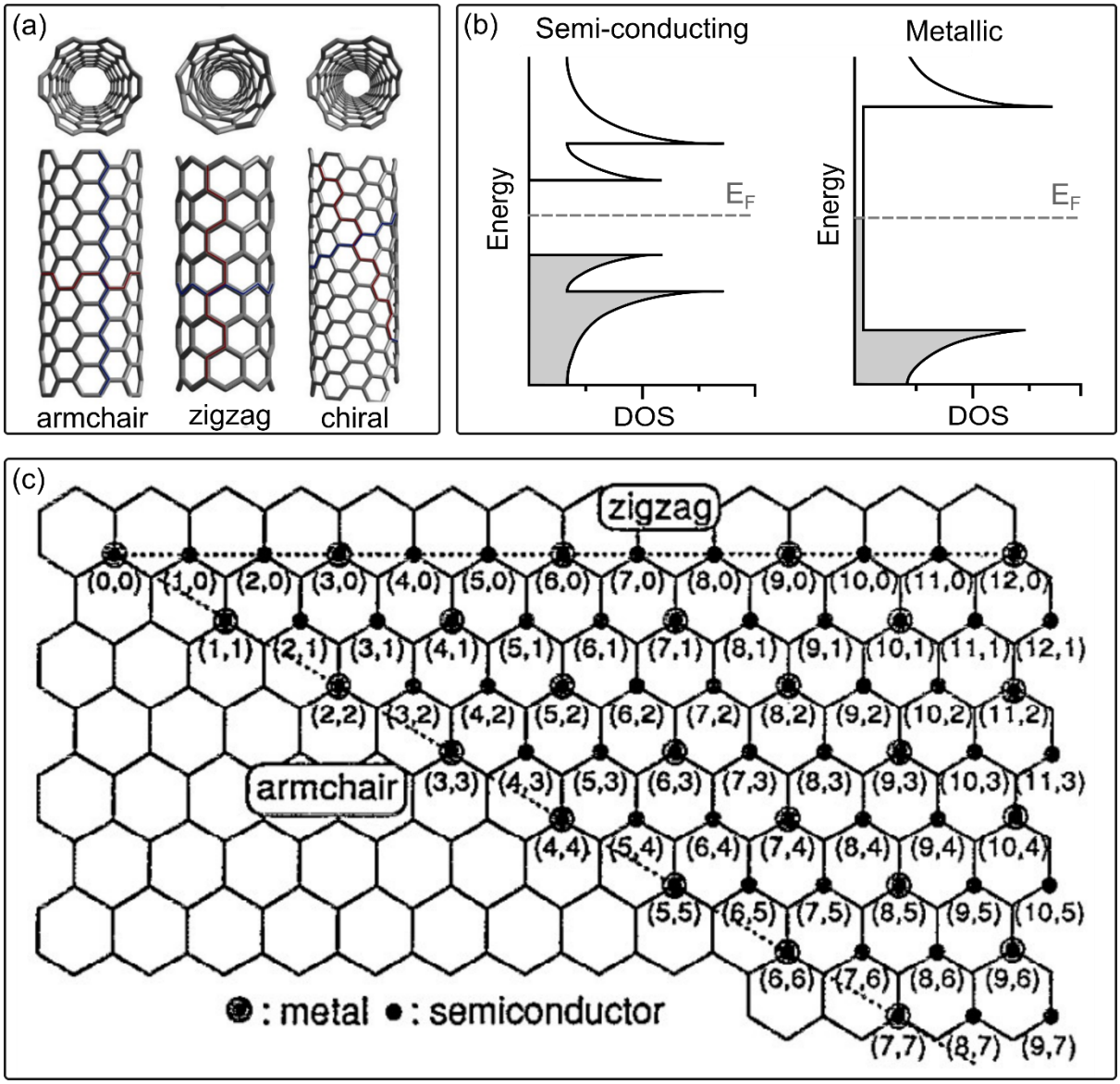


Figure 2.7. (a) Schematic of armchair, zigzag and chiral CNTs. Adapted with permission from reference [66]. (b) Schematic density of states for semi-conducting and metallic CNTs. Reprinted from reference [67] with permission from The Royal Society of Chemistry. (c) Illustration of wrapping vectors of CNTs on a graphene sheet with indication of metallic or semi-conducting helicities. Reprinted from reference [62] with permission from AIP Publishing.

The synthesis of CNTs is conducted in two principal methods; chemical vapour deposition (CVD) and arc-discharge or laser ablation.[68] Whilst arc-discharge and laser ablation can synthesise long CNTs with low number of defects, these synthesis methods are poorly scalable and produce significant carbonaceous impurities[69] and so most commercial CNTs are produced by CVD.[68] In CVD processes, a gaseous carbon source (usually a hydrocarbon or carbon monoxide) is introduced to metal catalyst nanoparticles at moderate temperature (600-1200 °C). The carbon source decomposes on the catalyst surface with the carbon dissolving into the catalyst. Once the solubility limit is reached, the carbon precipitates out on the catalyst surface, steadily growing as a cylindrical tube.[70] The diameter of the CNT is broadly controlled by the size of the catalyst nanoparticle, with smaller nanoparticles tending to produce small diameter single-walled CNTs and larger catalyst nanoparticles producing multi-walled CNTs. Helicity control of CNTs is more challenging but research using carefully designed crystalline catalysts has shown that the synthesis of single-helicity feedstocks may be possible in the future.[71-73] Conventional CVD is typically performed with catalyst particles supported on a solid substrate or on ceramic beads within a fluidised bed. An alternative CVD process involves the *in situ* formation of the catalyst nanoparticles within the synthesis furnace by introducing a gaseous iron source such as ferrocene alongside the carbon source and hydrogen, in a process known as floating catalyst CVD (FC-CVD).

In the context of this project, the length and purity are the most important CNT parameters. Long CNTs with low residual catalyst and amorphous carbon content are desired to achieve good fibre properties. Whilst the CNT length is dictated by the synthesis conditions, various techniques for purifying CNT feedstocks have been demonstrated to reduce the content of metallic and amorphous carbon impurities. Acidic treatments can be used to dissolve exposed metal catalysts. However, after CNT synthesis most of the catalyst particles are covered in a graphitic layer which must first be etched away. A common treatment is, therefore, to use a combination of nitric and sulfuric acid. A disadvantage of this treatment is that the oxidising conditions can damage the CNT framework and functionalise the outer surface with carboxyl groups.[74, 75] Amorphous carbon impurities can be removed *via* controlled heat treatments in air below the CNT combustion temperature[76] whilst functional groups on the CNT walls can be removed by higher temperature thermolysis in an inert atmosphere. The CNTs used in this project (OCSiAl Tuball and Meijo eDIPS) are produced by modified CVD processes, followed

by acid purification treatment to remove catalyst impurities (characterisation in section 7.4.1, p.132) and so to remove any possible surface groups, adsorbed moisture and entrapped gas the as-received CNTs were heated at 500 °C for 10 hours in ultrahigh vacuum before use.

2.2.2 Imogolite nanotubes

Imogolite nanotubes (INTs) are clay minerals formed of aluminosilicate or aluminogermanate sheets wrapped into tubes.[77] The walls of imogolite nanotubes are comprised of an outer gibbsite $Al(OH)_3$ sheet which is decorated on the interior by O_3SiOH or O_3GeOH tetrahedra (Figure 2.8). In contrast to many other nanotubular materials, imogolite nanotubes preferentially form with certain diameters which minimise the strain energy between the inner and outer section of the walls thus leading to feedstocks with consistent structure and diameter.[11, 78, 79] Additional stabilisation of certain helicities also occurs in the case of double-walled INTs due to the formation of hydrogen bonds between the walls.[78]

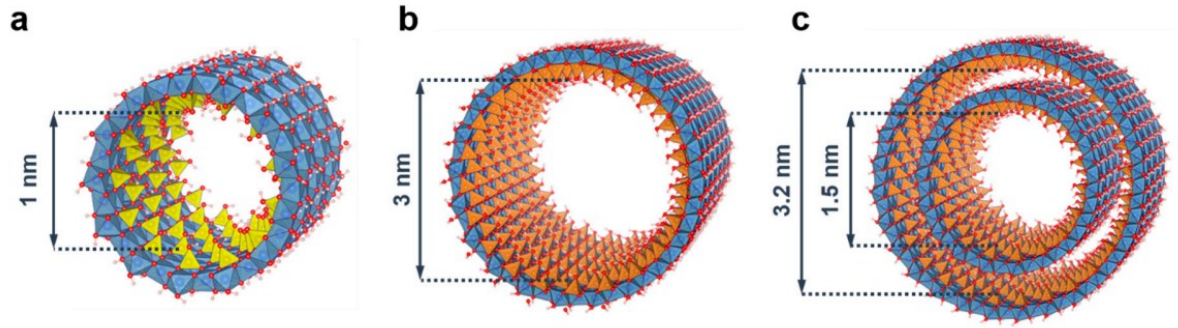


Figure 2.8. Atomic structures of various INTs. (a) Single-walled Si-INT, (b) single-walled Ge-INT, (c) double-walled Ge-INT. (Blue) aluminium, (red) oxygen, (white) hydrogen, (yellow) silicon, (orange) germanium. Reprinted from reference [11] under the CC BY 4.0 license.

INTs can be readily synthesised in a low temperature (<140 °C) aqueous sol-gel process using reactive metal precursors such as $AlCl_3$, $Al(ClO_4)_3$ or $Al(NO_3)_3$ alongside $Ge(OEt)_4$, $Ge(OH)_4$ or $Ge(OCH_3)_4$ or its Si equivalents.[80] The number of walls and diameter of the INTs produced in a synthesis can be controlled by changing the concentration of the initial starting reagents and the degree of Si/Ge substitution.[81-84] In the context of fibre spinning, a significant improvement in INT synthesis was made in 2013, when a synthesis process for INTs with lengths of up to 1 µm was developed.[85] The key step of this synthesis appears to be the steady decomposition of urea which generates hydroxyl ions *in situ* throughout the synthesis. As a high aspect ratio nanotube is expected to be favourable for fibre spinning, the INTs used

in this project were synthesised by collaborator, Erwan Paineau, following the latter method to create long double-walled Ge-INTs.

In contrast to CNTs, INTs are electrically insulating, optically transparent and hydrophilic due to their hydroxylated surface and in this way act as an interesting complementary feedstock for nanotube fibres. INTs materials are expected to be significantly easier to characterise than CNT materials due to their uniform diameter and the higher X-ray scattering cross-sections (particularly in the case of Ge INTs) which greatly increases the intensity of X-ray scattering features. The optical transparency of INTs also enables the use polarised optical techniques (section 3.3.1, p.58) making them useful as an analogue material to explore nanotube assembly. However, the double-walled Ge INTs used in this project are also notably straighter than typical single-walled CNTs with a longer persistence length (Figure 2.9) which may influence the properties and assembly of the corresponding nanotube fibres and so some care is required when comparing the two materials systems.

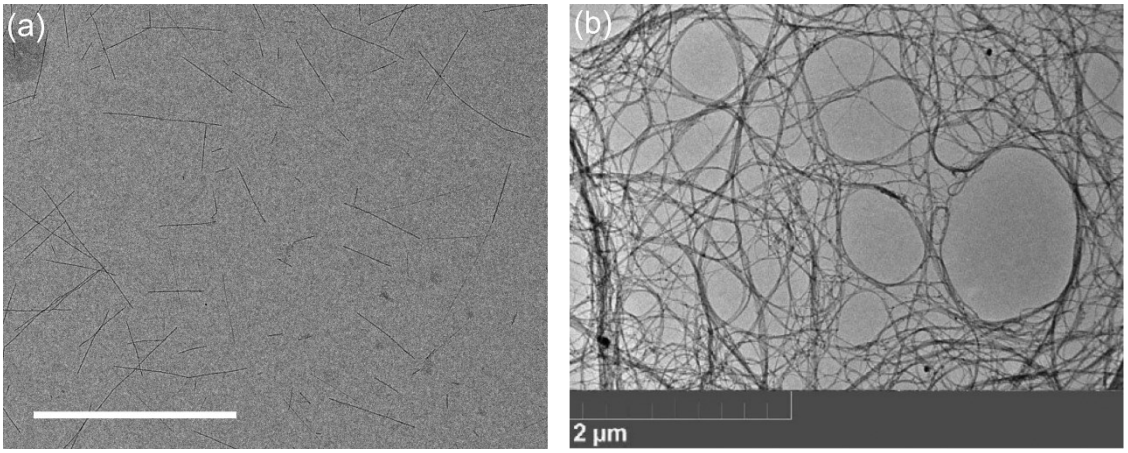


Figure 2.9. TEM images of (a) double-walled Ge-INTs synthesised during this project and (b) OCSiAl Tuball CNTs, reproduced from reference [86] under the CC BY 4.0 license. Scale bars 2 µm.

2.3 Nanotube fibres

Motivated by the excellent intrinsic properties of CNTs, significant research has been conducted in producing CNT fibres. A recent perspective article[87] has compared the R&D progress in CNT fibre spinning to commercial high performance fibres, identifying some parallels in the improvement in performance over time. In contrast to previously developed fibre spinning processes, the scatter in reported performance of CNT fibres has been great, which may be related to the fact that CNT fibre spinning development has largely been

centred in academic research laboratories with comparably less industrial R&D. However, a number of companies are now either collaborating with research groups or spinning-out the development of CNT fibres and non-wovens, such as Teijin Aramid, Nanocomp Technologies, DexMat and Tortech.

Identifying the key parameters affecting CNT properties is challenging due to the large number of fibre spinning parameters and their interactions, alongside the variety of sources and research groups investigating the process. Unpicking the relative influence of various factors on the properties of CNT fibres has been aided by the recent publication of a meta-analysis of the CNT fibre field,[88] but it is still difficult to derive precise conclusions from the literature data. In this section of the literature review, the key published methods of producing CNT fibres will be briefly described and compared and suggestions for how to produce an ideal CNT fibre are made.

2.3.1 Wet spinning CNT fibres

Wet spinning is a principal method for producing CNT fibres, bearing many similarities to the wet spinning of rigid rod polymer fibres. CNTs are dissolved in a suitable solvent and injected into a coagulation bath where a solid fibre condenses and is then collected on a take-up wheel. Similarly to the rigid rod polymers, CNTs are challenging to dissolve, have a high persistence length and solutions form liquid crystals which can be used to orient the CNTs within the fibre.

2.3.1.1 Dissolution

CNTs readily form bundles of tens to hundreds of nanotubes which are strongly bonded by long-range van der Waals forces. These bundles inhibit solution processing and can present as large agglomerates of undissolved material. There are two main approaches to the debundling and subsequent dissolution of CNTs: surfactant stabilisation and CNT charging.

Surfactants can be used to increase the compatibility between CNTs and a solvent, enabling dissolution of individualised species but typically requiring some energy input to initially disaggregate the CNT bundles. The primary surfactants used in the literature include sodium deoxycholate, sodium dodecylbenzenesulfonate and single-stranded DNA.[89] Ultrasonication can be used followed by centrifugation to separate individualised CNTs from larger and

denser bundles. However, the sonication process has been shown to damage the framework of CNTs and shorten their length.[90] The degree of individualisation is often limited and can be improved only by prolonged or more intense sonication, resulting in an energetically costly and difficult to scale process step which also inevitably leads to degradation of the CNTs.

Electrostatic charging processes are of particular interest for CNT dissolution because they can lead to the spontaneous thermodynamic individualisation of CNTs without additional energy input for disaggregation. The addition of charge to CNTs leads to repulsive Coulombic interactions which overcome the strong van der Waals forces holding the nanotubes in a bundle. There are two principal systems used to charge and dissolve CNTs. Superacid mixtures of chlorosulfonic acid and sulfuric acid protonate CNT side-walls leading to a dispersion of positively charged CNTs. This method is reported to dissolve CNTs without the oxidative damage seen with mixtures of sulfuric and nitric acid,[91, 92] and can form nematic liquid crystalline phases with high orientational order.[93-95] Dispersions can be produced at high CNT concentrations, up to 6 wt%,[96] although dispersions at high concentrations have a gel-like appearance. However, there are some significant manufacturing difficulties with using superacids. They are strongly dehydrating, can react with atmospheric moisture and are incompatible with many materials used in plant equipment. Additionally, there is evidence that superacid is retained within macroscopic assemblies even after washing, which may limit applications.

CNTs can also form true solutions as polyelectrolyte anions in organic solvents. The CNTs are reductively charged by transferring an electron from an alkali metal (typically Na or K) onto the nanotube, forming a soluble 'nanotubide salt' of CNT anions and metal cations. This reduction can be conducted in an electride solution of ammonia or in a polar aprotic solvent (THF, DMAc, DMSO) with the aid of a charge transfer agent such as naphthalene. The resulting dispersions are thermodynamically stable and occur with gentle stirring over the course of 1-3 days, depending on CNT length. However, these dispersions are extremely air and moisture sensitive and discharge rapidly if exposed to oxygen or protic reagents.[97] Similarly to superacid dispersions, liquid crystalline phases of nanotubide solutions have been observed.[10, 98, 99] It is proposed that the maximum concentration of dissolved CNTs is limited by a 'salting-out' effect as concentration of the alkali metal counter ions increases, leading to condensation of counter ions on the CNT surface and a screening of the electrostatic forces.[9]

Crown ether can be added to the dispersion to coordinate the metal ions and prevent their condensation onto the nanotube polyelectrolytes. This approach has been reported to achieve concentrations as high as 52 mg mL^{-1} (~4.7 wt%).[10]

The reductive approach to dispersion can also be used to functionalise the CNT side-walls. The highly reactive polyanions can undergo reactions with a variety of reagents, particularly organo-halides and diazonium salts.[9] Reagents with two reactive sites such as diiodobenzene can react at both ends to form covalent cross-links between CNTs and have previously been used to form robust CNTs aerogels.[100, 101] The degree of functionalisation can be tuned by the amount of charge available in the system and the reagent used in the reaction. Notably, iodo-alkanes achieve a higher functionalisation yield than bromo- and chloro-alkanes.[8]

Despite being long, rigid units in solution, the influence of attractive and repulsive forces between CNTs in solutions means that the (athermal) Onsager model of liquid-crystalline phase transitions does not accurately predict CNT solutions. The Onsager model has been developed further by Green *et al.*[102] to include the effects of length-dispersity and a phenomenological square-well potential to describe attractive van der Waals forces in the nematic phase. Care should be taken when interpreting this model, as it is not clear how well justified the square-well potential is. However, the key results show that the nematic cloud point (the rod volume fraction for a fully nematic liquid crystal) is greatly increased by length-dispersity and that increasing the depth of the attractive potential well decreases the isotropic cloud point but increases the nematic cloud point. This trend can be interpreted as the nematic phase becoming more dense but representing a smaller fraction of the fluid in poorer solvents, and suggests that a fully nematic solution is only feasible with good solvents (no potential well) and high volume fraction (greater than 10%). In practice, experimental data typically shows the emergence of a liquid crystalline phase at volume fractions of 0.01-0.3%[93, 94, 98, 103] for polyelectrolyte solutions depending upon the aspect ratio of the CNT feedstocks.

2.3.1.2 Fibre spinning

Once a liquid crystalline solution of well-dissolved CNTs is obtained, fibres can be spun by injection into a suitable coagulant and collection on a take-up wheel. Only one publication is available showing spinning of pure CNT fibres from reduced CNT polyelectrolytes,[10] with modest performance (strength ~120 MPa, modulus ~15 GPa) and so the description here is based primarily on superacid spun fibres.

Initially wet spinning of CNT fibres was conducted from fuming sulfuric acid solutions into water or diluted sulfuric acid coagulants, which produced dense circular fibres whereas using a diethyl ether coagulant bath resulted in a collapsed dog-bone, which may be reminiscent of kidney shaped PAN fibres.[104] In the development of the acid spinning process a transition was made to using chlorosulfonic acid due to its improved solvent characteristics, which then presented a limit on the possible coagulants due to excessive reactivity between the acid and coagulant. Recent work has settled on using chlorosulfonic acid as the solvent and acetone as the coagulant.[96, 105, 106]

It is reported that the ideal solution spinning conditions are dependent upon the CNTs used, with lower dope concentrations required for CNT feedstocks with higher aspect ratios whilst a high spin draw ratio is preferred for most CNT types.[107] Comparing the best processing conditions for each CNT batch, a clear trend has emerged over time that higher CNT aspect ratio leads to better performance.[96] However, higher aspect ratios make the processing from dissolution to mixing and then spinning more challenging due to the higher viscosity and strongly shear thinning character of the solutions. Steady development of this superacid wet spinning process has seen impressive improvements in tensile strength over time from 120 MPa in 2004[104] to 1 GPa in 2013[108] and 4.2 GPa in 2021[106], which is primarily associated with increased length of the nanotube feedstock. However, despite these reported improvements, little information is available on how to predict the best spinning parameters and potential directions for further improving their properties beyond using even longer CNT feedstocks. In general, superacid solution spinning yields dense (1.5-1.9 g cm^{-3})[105, 106] highly packed CNT fibres with high degrees of alignment.[96, 108]

Scale-up of this wet spinning process is expected to be straightforward as it follows a similar line to the wet spinning of rigid rod polymers. Greater production throughput is likely to be

targeted by increasing the mass loading of the spinning dopes and spinning in parallel through multi-filament spinnerets. A key benefit is that the fibre spinning and CNT synthesis processes are decoupled, enabling separate optimisation and scale-up of each process. Challenges in scale-up are possible as increases in both the CNT length and mass loading are desired which may come with a performance penalty to the produced fibre. Nonetheless, the inherent flexibility of the solution spinning approach reduces some of the scale-up risks to CNT fibre spinning making it an attractive prospect for industrial development.

2.3.2 Dry spinning CNT fibres

In dry spinning, CNT fibres are formed from CNT material via drawing and twisting processes similar to those used to form staple fibre yarns such as wool and cotton. Two principal methods of dry spinning have emerged in the literature; direct spinning from a FC-CVD reactor in a continuous CNT synthesis and spinning process, and array spinning from a pre-grown forest of CNTs on a catalyst support.[109]

Direct spinning of CNT fibres relies upon careful set up of the spinning furnace, with initial manual collection of the fibre from the networked cloud using a long cold metal rod followed by collection onto the winding drum. As collected, the fibres have a relatively high degree of CNT alignment but a low density, and so to increase the packing fraction of CNTs and aid processibility, the fibre is sprayed with a mist of acetone to induce densification by capillary wetting.[110] A large number of variables can influence the produced CNT fibres from the furnace temperature (and temperature gradient) to the choice of carbon source, carrier gas, iron source and even the dimensions and materials of the furnace.[111, 112] Sulphur (typically in the form of thiophene) is an important addition to the gas mix to enable direct spinning of CNT fibres and appears to have a number of effects on the gas phase reactions and nucleation processes which occur in the reactor. In particular, it can influence the coarsening of generated iron nanoparticles but also poison their catalytic activity resulting in changes to the diameter, number of walls and rate of CNT synthesis.[113]

Even after solvent densification, as-spun FC-CVD CNT fibres have a relatively low density (0.5-1 g cm^{-3})[111, 114-116] corresponding to a packing fraction of perhaps 25-50% (depending upon the chosen value for fully packed density) and a relatively high degree of CNT alignment.[111, 117, 118] Attempts to improve the (area-basis) tensile strength have centred

around densification techniques using rollers,[118, 119] drawing dies[120, 121] and twisting[122, 123] leading to reported strengths near to or greater than 4 GPa.[118, 124] Alternatively, soaking and wet stretching in chlorosulfonic acid has been demonstrated as an effective way to densify and increase alignment in direct-spun CNT fibres resulting in tensile strengths of 3-5 GPa.[7, 125-127] One publication reports strengths of 9.6 GPa after mechanical densification by rolling[119] however, this result is slightly doubtful due to a lack of reproducibility and may be influenced by a poor measurement of cross-sectional area of the thin film.

As the parameter space of CNT direct spinning is so large, identifying possible directions to further improve fibre properties is challenging. A recent report has shown extremely high specific strengths (3.1 N tex^{-1}) in direct-spun fibres by increasing CNT length through a longer reaction zone and improving orientation by adjusting the winding rate[128] and it is expected that future work may seek to investigate these parameters further. Recent research efforts are also being directed towards modelling the catalyst nucleation and CNT agglomeration processes to better understand the parameters which affect fibre microstructure[129-131] and it is hoped that these investigations will better inform researchers on how to navigate the wide parameter space to improve fibre properties.

A disadvantage of the direct-spinning process is the relatively low throughput of the furnace, with a laboratory scale furnace producing approximately 0.12 g of CNT fibre per hour. Some industrial scale-up has demonstrated throughput increase of a factor of 100, but this rate is still many orders of magnitude short of the ton-level quantities which would be anticipated for a commercially mature CNT fibre. Models for the scale-up of this technique have been developed and suggest that a single industrial reactor tube may be able to produce up to 20 kg of fibre per day, however this estimate assumes effective scaling of the process from a reaction tube of 6.5 cm diameter to one of 1.95 m diameter with corresponding increases in gas flow rates and tube length,[132] and these assumptions may prove to be highly optimistic. Equipping a production line with multiple furnaces and spinning lines in parallel is likely to result in high capital and running costs which may prove to be a barrier to widespread commercial exploitation of this process.

2.3.3 Structure-property relationships in CNT fibres

Structure-property relationships for CNT fibres have been explored both in individual studies[105] and in wide reviews of the CNT fibre literature.[88] Across the literature, the best tensile performance has been identified in aligned CNT materials (i.e. those spun into fibres with preferred orientation) rather than unaligned materials such as buckypaper films.[88] As such this review section will focus on the aligned materials which are typically produced by the methods described in sections 2.3.1 and 2.3.2 above.

The tensile properties of CNT assemblies are driven primarily by the shear interactions between the CNTs and bundles, rather than the strong covalent bonds within each nanotube. The shear interactions are derived from van der Waals forces and are expected to be proportional to the overlap between adjacent CNTs. Following this model, the greatest load transfer capability is expected for long CNTs which can bend and deform to form contacts and increase the overlap area. A strong linear relationship between CNT length and fibre strength has been predicted in micro-mechanical models[133, 134] and observed experimentally.[96] The effective overlap area between adjacent CNTs may be increased by deformation of the circular shape of the CNT wall. This deformation has been proposed to occur by the polygonization and self-collapse of large diameter CNTs due to van der Waals interactions[135, 136] and has been predicted to result in extremely stiff and strong CNT structures.[137, 138] On the basis of this model, SW-CNTs and DW-CNTs are expected to yield fibres with better tensile properties than MW-CNTs on both an areal and mass basis. The interior walls of MW-CNTs do not aid inter-nanotube interactions whilst increasing the mass of the structure and its area. This prediction is generally reflected in the CNT fibre literature, where the best MW-CNT fibres reach tensile strengths and tenacities of 3.2 GPa and 3.1 N tex^{-1}[139] compared to 4.2 GPa and 4.1 N tex^{-1} for few-walled CNT fibres, and there is a statistically significant difference between the two groups across the whole literature base.[88] However, there is a large degree of overlap in the reported properties for MW-CNT and SW-CNT fibres and it is clear that other structural factors such as CNT length, fibre packing density and CNT alignment may have a crucial role.

Wet-spun and direct-spun CNT fibres represent two different approaches to achieving good mechanical properties. The degree of microstructural alignment is similar between the two

techniques, but they differ significantly in density and CNT length. Wet-spun CNT fibres have a high density (approaching fully packed) but shorter CNT length, resulting in a fibre with excellent areal-basis strength (4.2 GPa) but more modest specific strength (2.1 N tex^{-1}).[106] In contrast, as-spun direct-spun CNT fibres have a lower packing fraction but longer CNT length and the fibres have very impressive specific strength (3.1 N tex^{-1}) but a slightly lower tensile strength (3.5 GPa).[128] As described previously (section 2.3.2, p.41), the densification of direct-spun CNT fibres has yielded large increases in the tensile strength and as of now these fibres have the best reported properties in the literature.

Across the entire CNT fibre literature, tensile strength is correlated to the fibre density (Figure 2.10a), but the dependency is approximately linear, implying that the increase in strength is mostly due to a reduction of cross-sectional area rather than improved efficiency of the CNT network. Correspondingly, the specific strength is only weakly correlated with density across the literature of aligned CNT structures, suggesting that fibre density and packing fraction has a lesser role on the specific strength than other parameters such as CNT length (Figure 2.10b).[88] However, when separating the data sets into wet spun and direct-spun materials and making independent analyses, a more apparent correlation emerges. Higher specific strengths tend to be reported at higher densities, and this relationship is particularly strong when examining the better performing fibres which are likely to have a less defect dependent failure which better reflects the strength of the CNT network (Figure 2.11a). Examining just the direct-spun, few-walled CNTs shows this trend more strongly, and within individual studies there are several examples of a clear relationship between specific strength and density, which is particularly prominent after post-processing in chlorosulfonic acid.[7, 126, 127, 140] On this basis it can be judged that a high density is not sufficient to create a CNT fibre with a high specific strength but does tend to improve fibre properties. Consistently, the highest specific strength fibres are produced using the direct-spinning method, likely due to the higher aspect ratio of the CNTs in these fibres which leads to greater load bearing for a given mass of CNTs. As predicted in models,[133] densification of direct-spun CNT fibres leads to an improved specific strength, implying that the denser microstructure can carry more load. In order to achieve CNT fibres with the highest tensile strength and specific strength, dense fibres are needed, nearing full packing, using the longest possible CNTs.

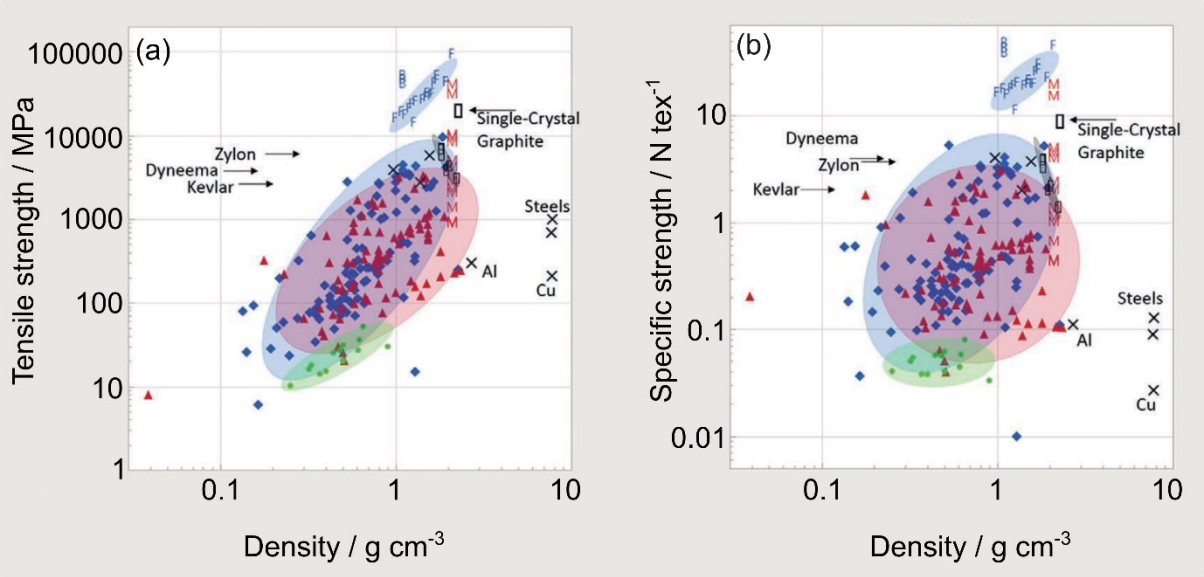


Figure 2.10. Log-log plots of (a) tensile strength and (b) specific strength against bulk density for CNT fibres across the literature. (Blue diamonds) aligned FW-CNT materials, (red triangles) aligned MW-CNT fibres, (green circles) unaligned FW-CNT materials, (blue F) individual FW-CNTs and small bundles thereof. Adapted from reference [88] under the CC-BY license.

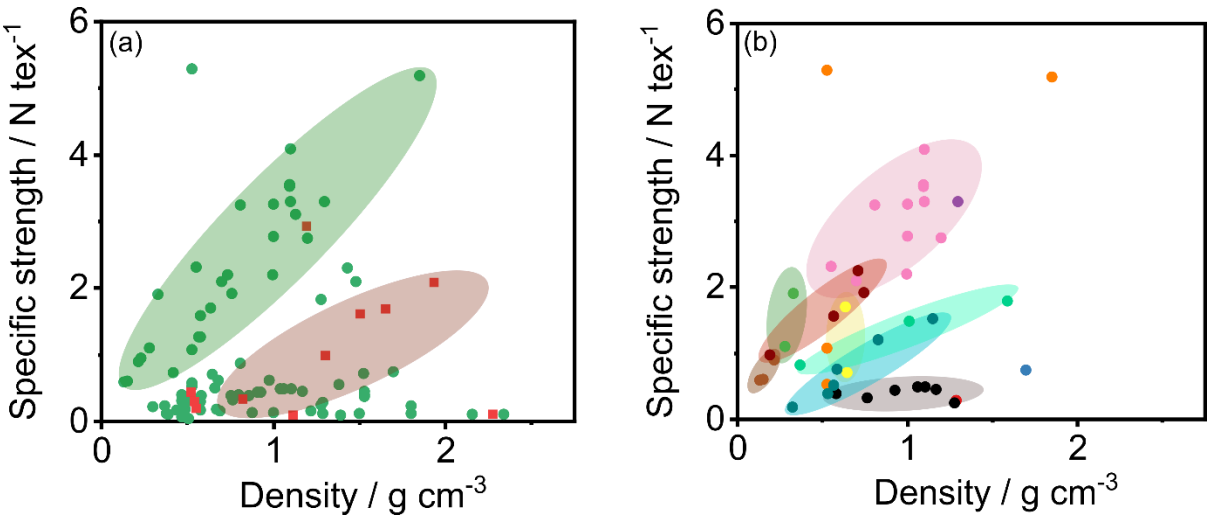


Figure 2.11. (a) Specific strength as a function of bulk density for (green) direct-spun and (red) superacid wet-spun CNT fibres. Data extracted from reference [88]. (b) Specific strength as a function of bulk density for direct-spun few-walled CNT fibres from individual studies: (brown)[114], (green)[141], (yellow)[117], (black)[142], (red)[143], (orange)[119], (blue)[144], (purple)[118], (pink)[7], (teal)[140], (cyan)[126], (burgundy)[127]. Ellipses are guides to the eye.

The effect of CNT alignment on fibre properties is more difficult to assess from the literature due to characterisation challenges. Polarised Raman spectroscopy can be used to obtain an anisotropy index which correlates with alignment, but this technique is not widely used and only samples the surface of the fibres, which is in general not representative of the bulk

microstructure. Meanwhile, X-ray diffraction can be used to determine the orientation of CNTs throughout the bulk of a fibre but the dispersity of CNT diameter and helicity in typical samples weakens the intensity of the diffracted signal, essentially necessitating synchrotron sources for studying individual CNT fibres (section 3.3.3, p.64). Due to these challenges, there is an understandable lack of consistent reporting of alignment across the literature and an analysis of the available results indicates that there is no clear correlation between strength and CNT alignment.[88]

From a theoretical perspective, there are competing theories on how alignment may affect the properties of CNT fibres. Based on the theory of both composites and linear polymers, it should be advantageous to have a perfectly aligned microstructure so that tensile load is applied directly along the stiff covalent backbone of the CNTs. In a fully packed structure with sufficient overlap between CNTs to transfer load through the shear stress, this argument should apply and a fully aligned structure is expected to be stiffer and stronger. The performance of this ideal model has been demonstrated in individual stress-relieved CNT bundles which have strengths of up to 43 GPa.[145] However, shear stress transfer between fibrillar bundles of CNTs is the limiting factor for fibre strength in most CNT yarns, as the degree of packing between bundles is evidently poorer than within each bundle (Figure 2.12). In these structures, it is expected that interweaving and branching of nanotubes between bundles plays an important role in transferring stress and preventing fibrillar failure. In this sense, a degree of misalignment in the overall structure is likely to be beneficial to fibre properties, as has been illustrated in finite element models which show improved stress transfer across the cross-section of a fibre due to misalignment.[146] From this argument, off-axis CNTs and bundles may improve the strength of fibres in the regime where shear slip dictates fibre properties. However, some forms of misalignment are likely to be purely detrimental to fibre properties. Excessive waviness of CNTs and bundles is expected to reduce the contact area between CNTs and bundles, resulting in lower strength,[147] whilst also having little beneficial effect in terms of stress transfer. Distinguishing these separate ‘types’ of misalignment is challenging and the conflation of these effects is expected to cloud the determination of fibre property-alignment relationships, making it difficult to identify an ideal degree of alignment in a CNT fibre.

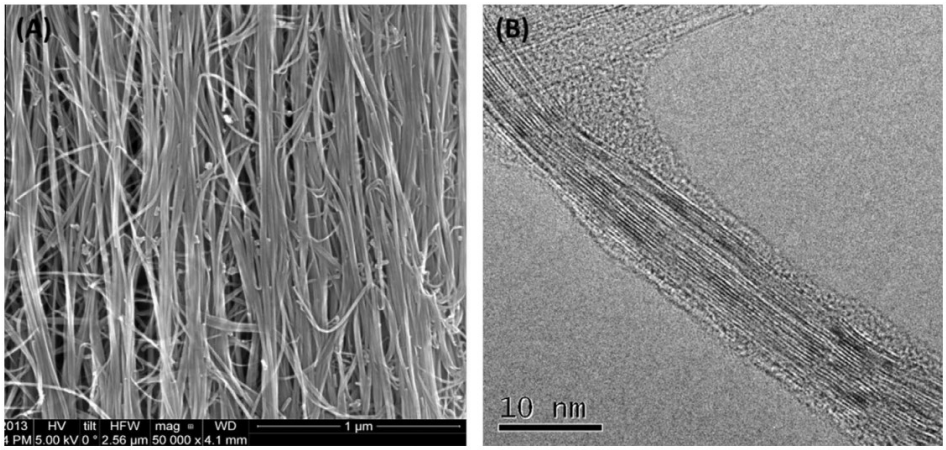


Figure 2.12. (a) SEM of solvent-densified direct-spun CNT fibre showing CNT bundles aligned along the fibre axis and (b) TEM of a CNT bundle showing highly aligned and densely packed CNTs. Reprinted from reference [146] with permission from Elsevier.

Whilst structure-property relationships are still difficult to precisely identify in CNT fibres some key guiding messages emerge from the extant literature. Firstly, further improvements to specific strength are likely to only be possible with the application of longer CNTs, likely requiring further research in CNT synthesis methods to produce suitable material in quantity. Secondly, increasing fibre density greatly improves tensile strength on an areal basis. The relationship between density and specific strength is more complex, but recent work densifying direct-spun fibres suggests that exceptional specific strength (>4 N tex^{-1}) may only be possible in CNT fibres which are both dense and contain long CNTs. Finally, increasing alignment within CNT fibres is generally desired on the basis of typical models but there is an indication that some degree of misalignment is beneficial to aid stress transfer and improve fibre properties. On this basis, densified direct-spun CNT fibres appear to be in the best position to achieve the highest performance, as the technique can create a reasonably aligned 'precursor fibre' from high aspect ratio CNTs which can later be post-processed into a more ideal, dense structure. However, there are challenges extending direct-spinning to industrial scale, particularly if additional post-processing is required, and so wet-spinning is still an attractive technique for the production of CNT fibres. The process of nanotube assembly in wet spinning and the effect of various spinning parameters is still not fully understood. The application of imogolite nanotubes as an analogue material will enable more detailed observation of the processes occurring during wet spinning, whilst an exploratory approach to using reductively charged CNT solutions in wet spinning may identify a competitive process for the superacid spinning (or post-processing) of CNT fibres.

3 Materials and methods

This chapter introduces the primary materials, experimental methods and characterisation techniques used throughout this work. In general, I performed the methods presented in this work except where specified. This project was supported by collaboration with Erwan Paineau and Pascale Launois at Université Paris-Saclay, who synthesised the INTs, provided some X-ray scattering analysis programs and collected some X-ray scattering patterns during periods when international travel was not possible. The cross-linking studies were supported by undergraduate students, Jian Bi and Jiawei Zhang, during the course of their studies at Imperial College London.

3.1 Materials

3.1.1 Imogolite nanotubes

The INTs used in this project were synthesised by collaborator Erwan Paineau, following a method previously developed to produce long, double-walled Ge-INTs.[85] Tetraethoxygermane (Sigma-Aldrich), aluminium perchlorate nonahydrate (Alfa Aesar) and urea (Sigma-Aldrich) were mixed in a PTFE beaker with a molar ratio of [Ge]:[Al]:[urea] = 1:2:2. The beaker was then placed into a PTFE-lined acid digestion bomb and treated in an autoclave at 140 °C for a variable incubation time between 5 and 40 days to enable growth of the INTs. In Chapters 5 and 6, an incubation time of 40 days was used. The INT solutions were then dialysed against ultrapure water using a membrane (Spectra/Por, 10 kDa cutoff) until the bath conductivity reduced below 0.5 mS m^{-1}. The mass concentration of the as-synthesised INT solutions was determined by heating a 2 mL aliquot in an oven at 90 °C until full dryness was achieved. Solutions of other concentrations were obtained by serial dilution of the stock solution.

3.1.2 Carbon nanotubes

In this project, multiple sources of CNTs were used. Tuball single wall CNTs (product code 01RW03.N1, batch numbers 398 and 788) were obtained from OCSiAl. Meijo eDIPS EC1.5 CNTs (batch number 8901404) were obtained from Meijo Nano Carbon Co. and Meijo eDIPS EC-DX CNTs (lot number 5R81D08C) were obtained from New Metals & Chemicals Corporation. Before use, all CNT samples were vacuum degassed. The CNTs were loaded into

a glass vial and placed into a quartz tube (one end sealed, one with metal joint) in a tube furnace (Lenton PSC 12-450-H) which was connected to a turbomolecular pump (Edwards EXT75DX). Once an ultra-high vacuum ($<10^{-7}$ mbar) was obtained, the temperature was slowly ramped up to 500 °C and then held for ten hours, followed by a slow cooling to room temperature. The evacuated quartz tube was transferred into a glovebox where the CNT samples were then stored.

3.2 Experimental methods

3.2.1 CNT dissolution

CNTs were dissolved as reduced polyelectrolytes in aprotic solvents by treating with sodium naphthalenide using a method adapted from the literature.[8]

Anhydrous N,N-dimethylacetamide (DMAc, Sigma-Aldrich, 99.8%) was transferred into a glovebox and dried twice over activated 4 Å molecular sieves. Naphthalene (Sigma-Aldrich, 99%) was dried over phosphorous pentoxide under vacuum overnight and transferred into a glovebox. Sodium metal (Sigma-Aldrich, 99.95%) was received as an ingot in a sealed glass vial which was transferred into a glovebox before opening. All glassware used in preparation was thoroughly dried before transferring into the glovebox either by baking overnight at 150 °C or flame drying with a blowtorch.

A preparation is described here with typical quantities and equipment for producing approximately 25 mL of a 5 mg_{CNT} mL^{-1} solution. It should be noted that scale-up of the quantities may affect the dissolution by impacting the physical agitation during stirring.

A solution of sodium naphthalenide in DMAc was prepared by first adding sodium metal (35.2 mg) and naphthalene (196 mg) to a 25 mL glass reagent bottle with a 24 mm glass encapsulated magnetic stir bar. DMAc (17.6 mL) was pipetted on top and the solution was stirred overnight to produce a dark green solution of sodium naphthalenide at a concentration of 2 mg_{Na} mL^{-1}.

CNTs (102 mg) were added to a 50 mL glass reagent bottle with a 24 mm glass encapsulated magnetic stir bar. The pre-prepared sodium naphthalenide solution (12 mL) was pipetted on top, with the quantity chosen to determine the final charging ratio of the CNT polyelectrolyte

(here NaC_8). The CNTs were left to rest for 10-15 minutes, until swollen into a gel. DMAc (8 mL) was then pipetted on top and the mixture stirred at 600 rpm for 24 hours to produce a CNT solution at a mass loading of 5 mg_{CNT} mL^{-1}. Lower mass loadings can be prepared by adding a greater volume of solvent to the charged CNT gel, or more preferably by serially diluting the more concentrated CNT solution with stirring.

The CNT solution was finally filtered through a 26 µm aperture stainless steel mesh (#500 mesh, 316L stainless steel, Mesh Direct) supported in a 13 mm diameter polypropylene syringe filter holder (Swinnex, Millipore) and collected in a clean glass vial.

3.2.2 Wet spinning nanotube fibres

3.2.2.1 Experimental equipment

The wet spinning equipment was developed during the course of this work and consists of a syringe pump (100 Legacy, KD Scientific, US) and two stepper motors (QSH4218-35-10-027, Trinamic) controlled *via* IC drivers (TMC2130, Trinamic) and a microcontroller (Arduino Uno). A wiring schematic for the stepper motors and the Arduino code is available in the appendix (sections A3 and A4, p.192). In a typical experiment, the extrusion rate of the syringe pump was set between 1 and 10 mL hr^{-1} and the spinning dope was injected into a coagulation bath and then collected on a motorised PTFE take-up wheel (100 mm diameter). The speed of the take-up wheel was set to determine the draw ratio in the fibre spinning, defined as the take-up velocity divided by the mean injection velocity. Depending on the processing conditions selected, the fibre filament was then either collected from the take-up wheel or passed onto a collection spool. The 'squirrel cage' collection spools are comprised of five bamboo rods regularly spaced around a circle with a rod centre separation of 42 mm (Figure 3.2). An optional washing bath was included in the spinning line with static PTFE guide rods.

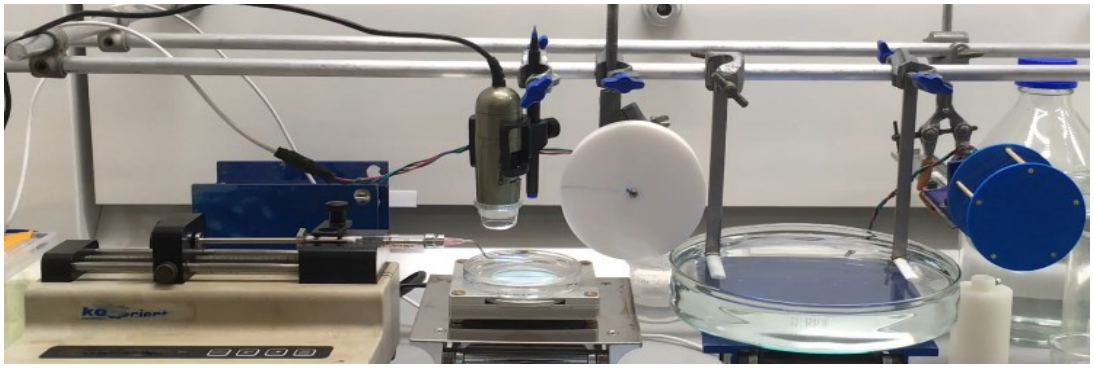


Figure 3.1. Photograph of wet spinning equipment with syringe pump, needle and glass capillary, coagulation bath, PTFE take-up wheel, washing bath and blue collection spool. Also shown are the digital microscope and lightbox used for *in situ* microscopy.

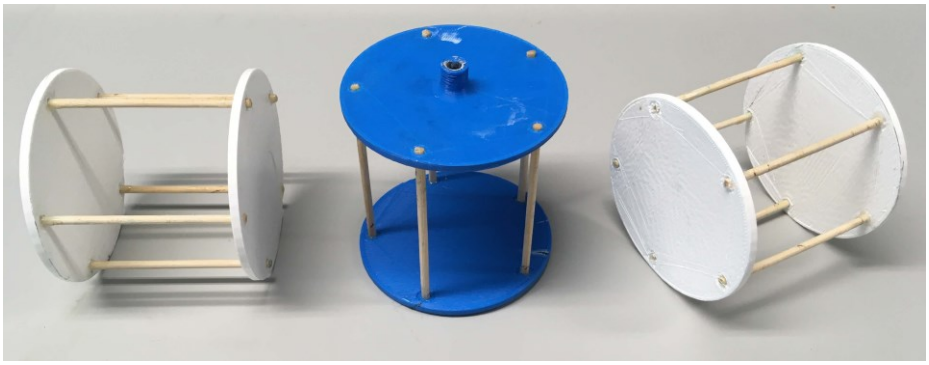


Figure 3.2. Photograph of collection spools used for in-line washed INT fibres and CNT fibres.

3.2.2.2 Preparing tapered glass spinnerets

Tapered glass spinnerets were prepared by necking soda glass capillary tubing (Samco G119/02) in a fine blowtorch flame. The tubing was rotated by hand in the flame until softened and then removed from the flame and pulled to form a neck. The necked section was carefully snapped off and the two ends were gently ground flat on P1000 silicon carbide abrasive paper. The tips are then gently flame polished in the blow torch flame to produce a tapered spinneret.

Spinnerets used for spinning CNT polyelectrolyte solutions were silanised to reduce the adhesion of CNTs to the surface, aiding both the spinning process and cleaning. A solution of 2 vol% dichlorodimethylsilane (Sigma-Aldrich, 98.5%) in toluene was prepared and flushed through a spinneret. The spinneret was then washed in pure toluene and baked in an oven at 150 °C overnight. Successful silanisation was confirmed by treating a glass microscope slide and observing an increase in water contact angle. The dimensions of the fabricated spinnerets were characterised using optical microscopy.

3.2.2.3 INT fibre spinning

In brief, INT fibres were spun by injecting aqueous INT solutions through a needle into a coagulation bath where they were then collected on the PTFE take-up wheel (100 mm diameter) with a determined draw ratio. Unless otherwise stated, the coagulation bath used was 300 g L^{-1} aqueous $CaCl_2$ prepared from calcium chloride dihydrate (Sigma-Aldrich) where, to account for the water of crystallisation, the mass loading of $CaCl_2 \cdot 2H_2O$ used was 397 g L^{-1}. The salt was weighed into a beaker and dissolved in a minimum quantity of deionised water. The solution was then transferred into a volumetric flask and made up to the desired volume to achieve the required concentration.

In Chapter 4, the INT solutions (feedstock incubation time 5-40 days, mass loading 9 mg_{INT} mL^{-1}) were injected along a 21 g stainless steel cannula (180 mm long) at a flow rate of 5 mL hr^{-1} into a $CaCl_2$ coagulation bath (8 cm long). The gel fibres were collected on a PTFE take-up wheel (100 mm diameter) at a draw ratio of 5 (rotation speed 6.4 RPM and surface linear velocity of 33.5 mm s^{-1}). Then, 15 cm lengths of the gel fibre were removed from the take-up wheel and washed by dipping in a beaker of deionised water for 3 x 2 s. A small tag of aluminium foil (~20 mg) was attached to the washed fibres by the surface tension of the liquid and they were hung vertically from a rod to dry at ambient conditions.

In section 5.2, the INT solutions (feedstock incubation time 40 days, mass loading 11 mg_{INT} mL^{-1}) were injected through a tapered glass nozzle (orifice diameter 461 µm, taper semi-angle 8°) at a flow rate of 5 mL hr^{-1} into a $CaCl_2$ coagulation bath approximately 8 cm in length. As before, the fibres were collected on a PTFE take-up wheel (100 mm diameter) at draw ratios varying between 1 and 5 and sections were removed from the wheel and then washed by dipping in deionised water (3 x 2 s) and hung to dry with a tag of aluminium foil (~20 mg) in ambient conditions.

In section 5.3, the INT fibres were initially spun as per section 5.2 with a draw ratio of 2 or 4. After initial take-up, the gel fibres were guided by static PTFE rods through an in-line washing bath of deionised water for varying washing lengths between 15 and 40 cm. The washed fibres were collected a ‘squirrel cage’ collection spool (Figure 3.2) with no additional draw The washed fibres were left to dry on the spool at ambient conditions so that they dried at constant strain.

3.2.2.4 CNT fibre spinning

CNT fibres were spun by transferring the spinning dope into a 1 mL polypropylene syringe (Normject^{TM}, Henke Sass Wolf) within a glovebox. A spinneret was then fitted using a blunt, luer-slip cannula with a small section of silicone tubing to attach the tapered glass tip. The spinneret was inserted through a pre-punctured septum (Suba-Seal) into a nitrogen filled vial and the assembly was removed from the glovebox and rapidly transferred to the spinning equipment to prevent air ingress and charge quenching. The spinneret was removed from the nitrogen filled vial and placed into the coagulant bath. The coagulant was not observed to travel up the spinneret and a buffer of nitrogen gas was present between the spinning dope in the syringe bubble and the coagulant fluid. Nonetheless, in order to prevent charge quenching spinning was started within one minute of removing the assembly from the glovebox and was conducted over a maximum of 15 minutes.

The spinning dope was injected into the coagulation bath and the gel fibre was gently guided to the surface of a submerged PTFE rod to define the length of passage in the coagulation bath and then out of the bath onto the PTFE take-up wheel (100 mm diameter) at a chosen draw ratio. The fibre was then transferred directly onto a squirrel cage collection spool (Figure 3.2) with no additional draw, where it was left to dry and densify in ambient conditions (Figure 3.3). A large variety of process parameters were varied during the spinning experiments and in a single spinning run fibres would be collected with several different processing conditions, typically varying the volumetric flow rate, draw ratio or coagulation bath length.

In section 8.6, fibres were spun from 1 mg_{CNT} mL^{-1} NaC_8 spinning dopes through a silanised tapered spinneret with orifice diameter of 346 µm (area 0.0938 mm^2) and taper semi-angle ~9° (Figure 3.4) and taken-up with a spin draw ratio of 1.2. The extrusion velocity was adjusted by varying the injection rate from 3 to 13 mL hr^{-1} and the coagulation time was adjusted by varying the length of the coagulation bath by moving the position of the spinneret tip relative to the guide rod.

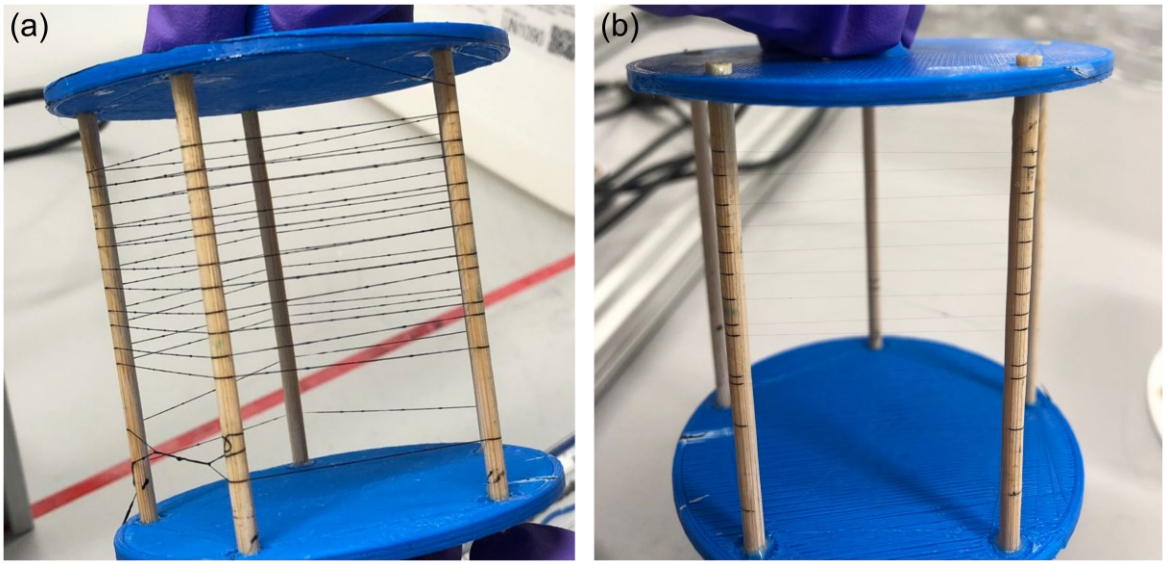


Figure 3.3. Photographs of CNT fibres on collection spool (a) immediately after collection and (b) after drying in ambient conditions for 5 minutes.



Figure 3.4. Micrographs of tapered glass spinneret used to spin CNT fibres in section 8.6 imaged (a) side-on and (b) end-on. Scale bars 500 µm.

3.2.3 Cross-linking INT fibres

3.2.3.1 Ionic cross-linking

Ionic cross-linking was conducted by washing $CaCl_2$-coagulated INT gel fibres in an aqueous solution of sodium succinate (>98%, Sigma-Aldrich). The gel fibres were prepared as per those used in section 5.2, by injecting INT solutions through a tapered glass spinneret with orifice diameter of 461 µm at 5 ml hr^{-1} followed by take-up at draw ratios varying between 1 and 5. Sections of the gel fibre were immediately cut from the take-up wheel and then held with tweezers and dipped into a beaker of 0.1 M sodium succinate (2 x 15 s) and then hung to dry at ambient conditions with a small tag of aluminium foil (~20 mg).

3.2.3.2 Dehydration reactions

This method was conducted by Jiawei Zhang during his *BSc Chemistry* course at Imperial College London.

INT fibres were spun as per section 5.3 with a draw ratio of 4 and washing bath length of 40 cm and then collected for thermal treatment.

Fibres treated at 200 °C were placed in a glass petri dish and then heated to 200 °C in a laboratory oven (Memmert VO400) for two hours, allowed to cool to room temperature and then collected for testing.

Fibres treated at 400 °C were placed into a glass vial then transferred to a quartz furnace tube and heated in a furnace (Lenton PSC 12-450-H). In order to control the heating and prevent overshoot, the furnace was first heated to 250 °C at a rate of 10 °C min^{-1} and held for 15 minutes, then ramped to 350 °C and held for 5 minutes and finally heated to 400 °C at 5 °C min^{-1} and held for two hours. The furnace was then allowed to cool to room temperature and the fibres were collected for testing.

3.2.3.3 Silanisation of INT fibres

This method was conducted by Jiawei Zhang during his *BSc Chemistry* course at Imperial College London.

INT fibres were spun as per section 5.3 with a draw ratio of 4 and washing bath length of 40 cm and then collected for silanisation.

Solutions of tetraethoxysilane (TEOS, Sigma-Aldrich, 98%) in ethanol were prepared at 0.001 and 1 M using a volumetric flask. The INT fibres were placed in polystyrene petri dishes and TEOS solution (7 mL) was carefully poured over the top to submerge the fibres. The fibres were left to react overnight (16 hours) and then removed and allowed to dry before testing.

3.2.4 Polymer infusion into INT fibres

This method was conducted by Jian Bi during his *MRes Nanomaterials* course at Imperial College London.

INT fibres were spun as per section 5.3 with a draw ratio of 4 and washing bath length of 40 cm and then collected for silanisation.

A 3 wt% solution of poly(vinyl alcohol) (PVOH, Mowiol 56-98, MW~195000, 98.0-98.8 mol% hydrolysis, Kuraray Co.) was prepared in deionised water. PVOH (3 g) was dispersed in cold deionised water (100 mL) by vigorous stirring. The mixture was then heated at 70 °C with moderate stirring for approximately 45 minutes, until the mixture was fully dissolved. The solution was then cooled to room temperature and kept in a sealed flask for up to 1 week before use.

INT fibres were attached with double-sided tape to a metal support frame constructed from a paperclip (Figure 3.5). The fibres were then immersed into a petri dish containing the polymer solution by first dipping one end of the support frame into the solution and then slowly submerging longitudinally. After soaking for between 1 and 7 minutes, the fibres were collected off the support frame using tweezers and carefully removed from the solution. The fibres were hung to dry in ambient conditions and then collected for testing.



Figure 3.5. Photograph of metal support frame used to immerse INT fibres in polymer solution.

3.2.5 Molecular dynamics simulations

Molecular dynamics simulations were conducted using NAMD[148] with the CHARMM36 all-atom forcefield. Carbon atoms within the CNTs were modelled using the CA aromatic carbon atom type, while sodium ion and dimethylacetamide atom types were assigned from the SOD and DMA residues respectively. Electrostatic energies were calculated using the Particle Mesh Ewald method. A switching distance of 10 Å was used to start tapering the van der Waals potentials smoothly to 0 at a cut-off distance of 12 Å.

The structure files for a (10,0) CNT with a length of 5 nm (0.8 nm diameter, 480 atoms) were created using the Nanotube Builder extension in VMD.[149] Atom co-ordinates for N,N-dimethylacetamide (DMAc) were taken from ligand 5Y9 in the Protein Data Bank[150] structure 5HCL.[151] These structures were then minimised at 0 K and used to construct the simulations. Two parallel CNTs with a centre-to-centre distance of 13 Å (wall separation ~5 Å) were added to a 72x72x70 Å simulation box with fractional charges applied evenly to the carbon atoms of the CNTs to attain the target charging ratio, NaC_x. The PACKMOL package[152] was used to add a stoichiometric number of sodium ions followed by 2500 DMAc molecules. Initialisation was conducted with fixed CNT positions and two cycles of minimisation and equilibration (4 ps at 300 K). An additional equilibration (20 ps) was then conducted with one CNT fixed and the other free to move to allow the CNTs to move to their equilibrium separation.

Steered molecular dynamics was performed with a dummy atom attached to the centre-of-mass of one of the CNTs with a spring with force constant 50 kcal mol^{-1} $Å^{-2}$. The other CNT was kept fixed while the dummy atom was translated at a velocity of 0.5 Å ps^{-1}. The simulation was evolved for 25 ps at 300 K and 1 atm pressure, as controlled by a Langevin piston, with a timestep of 2 fs. The force between the dummy atom and CNT recorded through the simulations to characterise the attraction/repulsion between the CNTs at varying charging ratios.

3.3 Characterisation techniques

3.3.1 (Polarised) optical microscopy

Optical microscopy is one of the most ubiquitous tools in materials characterisation due to its simplicity of use, and variety of contrast modes which enable imaging of a variety of samples. However, the application of optical microscopy to nanomaterials is typically hindered by the resolution limit of approximately 0.2 µm and the small depth of field at high magnifications. Whilst several methods have been developed to visualise the presence of individual CNTs in light microscopes such as coating with a thick ice layer,[153] tagging with fluorophores[154] or using the CNTs to catalyse surface reactions leaving visible trenches[155], these methods require significant sample preparation and are still unable to visually distinguish two or more CNTs within the resolution limit. Optical microscopy can be used to gain an impression of the bulk material on the 10-1000 µm scale. Microscopy is primarily used in this work to image nanotube fibres and solutions, including *in situ* imaging of the spinning process. Both reflection and transmission light sources can be used to image the samples, but in this project transmission imaging was preferred as more intense and uniform illumination was available on the equipment used.

After calibration with an appropriate graticule, microscope images can be used to determine the observed diameter of fibres. For non-circular fibres, the observed diameter can vary considerably depending on the orientation of the fibre in the light path such that a major or minor axis length is measured, rather than a diameter which is representative of the cross-sectional area. Assuming that all roll angles are equally likely, for elliptical fibres the mean diameter determined microscopically is typically a small over-estimate (~1%) of the representative fibre diameter.[156] This error may be greater for thick fibres with little-to-no twist as elliptical fibres can preferentially lie on their major axis on a microscope slide. Despite this potential shortcoming, optical microscopy of a transverse view is a recommended method for determining the filament diameter of carbon fibres in BS ISO standard 11567:2018.[157] Other potential methods for diameter determination are more challenging to implement for nanotube fibres. Gravimetric methods rely upon a precisely known and consistent fibre density, alongside accurate measurement of small masses (approximately 10 µg for a 10 cm section of fibre produced in this work). Laser diffraction methods require

specialist equipment and scanning electron microscopy is significantly more time consuming. Transversely mounting and cutting individual filaments for optical observation is possible with carbon fibres but is difficult with nanotube fibres due to their tendency to deform by compression or pull-out. Focused-ion beam milling in an SEM can be used to transversely cut nanotube filaments[158] but is extremely time-intensive with trial experiments in this work taking approximately 6 hours to cut a single filament.

Transmission microscopy can also be used to image nanotube solutions. Well individualised nanotube solutions are expected to be uniformly absorbing across a sample surface. Liquid samples can be prepared for imaging by dispensing a droplet on a microscope slide and then covering with a coverslip or by drawing into a capillary which is then placed on a slide or supported in the light path. Speciality capillaries (from suppliers such as Vitrocom) are available with rectangular cross-sections, which enable transmission microscopy through a sample with consistent path length and these capillaries can also be sealed with wax to prevent air ingress. Preparing and sealing these capillaries within a glovebox enables imaging of charged CNT solutions under atmospheric conditions over the course of a couple of days, after which diffusion of oxygen through the capillary wax leads to discharging.

Polarised optical microscopy is used to provide contrast based on the birefringence of samples in microscopy and is well described in a number of textbooks[159, 160] and so a brief explanation is provided here. Two polarisers (named polariser and analyser) are placed in the light path with orthogonal polarisation directions. In the absence of any sample, light from the illumination source is polarised in the direction of the polariser and then completely blocked by the analyser resulting in a dark field. Birefringent materials are characterised by having an anisotropic optical indicatrix, or equivalently the refractive index depends upon the direction of polarisation of light with a fast (low refractive index) and slow (high refractive index) direction. As light enters a birefringent material, the component rays polarised along the fast and slow directions travel at different velocities leading to the formation of phase (or path) difference between the two polarisation directions with the optical path difference (or retardation), Δ_{pd}, given as,

$$\Delta_{\mathrm{pd}} = (n_1 - n_2)\, t_{sample} \qquad (1)$$

where n_1 and n_2 are the refractive indices along the slow and fast directions and t_{sample} is the sample thickness. When linearly polarised light is passed through a birefringent sample

with polarisation direction at 45° to the fast and slow axes, the optical path difference changes the effective polarisation depending on the wavelength of the light. For an optical path difference (OPD) of an integer number of wavelengths the polarisation is unchanged and for an OPD of a half wavelength the direction of polarisation is rotated perpendicular to the initial direction. For intermediary wavelengths the light is elliptically polarised with a component of polarisation both parallel and perpendicular to the initial direction.

When a birefringent sample is placed between crossed polarisers and illuminated with white light, wavelengths which are factors of the retardation are therefore blocked by the analyser, whilst others are transmitted to a lesser or greater degree. The wavelength-dependent transmission therefore yields characteristic colours depending upon the retardation of the sample which are commonly reported on a Michel-Levy chart (Figure 3.6). Additional colour contrast can be provided to low retardation samples by introducing a plate with a known retardation to the light path between the two polarisers. This approach provides a retardation offset to the image, making the isotropic field coloured, from which the sample can add or subtract. In petrology and materials science, full-wave plates are commonly used with a typical retardation of 540 nm. The colours of images are shifted to magenta for isotropic regions, and cyan or yellow-orange for small sample retardations.

Nanotubes are inherently optically anisotropic with strongly differing polarizability parallel and perpendicular the nanotube axis. There is limited experimental data available on the value of birefringence for individual nanotubes, although first principle models have been developed for single wall CNTs which predict that the longitudinal polarisability is inversely proportional to the square of the band gap whilst the transverse refractive index is proportional to the square of the CNT radius - the longitudinal polarisability is typically a factor of 10-100 greater.[161] The highest degree of anisotropy occurs for small diameter metallic CNTs. Models have been constructed to describe the birefringence of solutions of CNTs, with the straightforward result that (to the leading term) the birefringence of the solution is proportional to the volume fraction of the CNTs, the difference in longitudinal and transverse polarisabilities, and Hermans nematic order parameter which is zero for random distributions and 1 for perfect alignment.[162] As such, the orientation of nanotube solutions can be visualised with POM, with regions of a greater birefringence corresponding to a higher degree of alignment. Direct calculation of an order parameter is not possible without further

information on the intrinsic birefringence of the nanotubes, but it is possible to make qualitative comparisons of the degree and direction of alignment using POM.

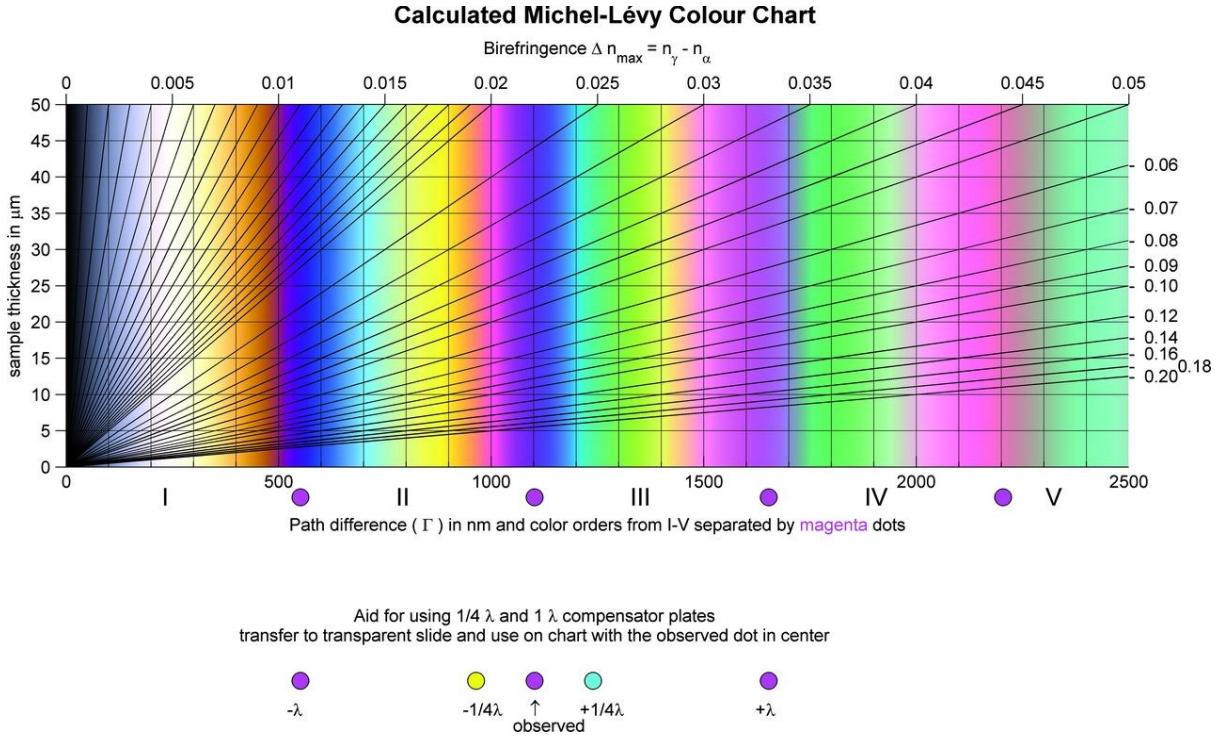


Figure 3.6. Michel-Lévy chart with markers for λ plates. Reproduced with permission from [163].

The high optical absorbance of CNTs limits the use of optical microscopy and bright light sources are required to image solutions even with a short light path (~0.2 mm) for solution mass loadings of 5 mg_{CNT} mL^{-1}. Condensed CNT fibres absorb almost all light in transmission and the surfaces have poor reflection making polarised techniques virtually impossible. In contrast, INTs are significantly less absorbing and high contrast polarised imaging is possible with relatively dim light sources which enables the use of optical microscopy to study the alignment of nanotubes both in dry fibres and in solutions during spinning.

In situ (polarised) optical microscopy of fibre spinning was conducted using a variable magnification digital microscope with a polarising filter (Dino-lite premier AM4113ZTL) and a lightbox with adjustable polariser (Dino-lite BL-ZW1). As the magnification depended upon the focal distance used, micrograph scales were set using a known reference length in each image such as the capillary diameter.

Optical microscopy of dried INT and CNT fibres was conducted using a Leica DM2500 optical microscope equipped with a camera (Basler PowerPack Ace 2.3 MP) in transmission

illumination with a 100 W halogen lamp and Leica HiPlan objectives. Polarised optical microscopy was conducted using a transmission polariser and integrated analyser oriented at 0 and 90° to the microscope head respectively. For additional colour contrast, 560 nm retardation film (Edmund Optics WP560 retarder film) was positioned between the polariser and condenser lens at 45° to the polariser and analyser directions. Fibre samples were imaged by placing fibres mounted on card frames onto a microscope slide in the light path. Nanotube solutions were collected into rectangular borosilicate capillaries (Vitrocom 3520, path length 0.2 mm, width 2 mm) and sealed with wax before imaging.

The cross-sectional area of INT and CNT fibres was determined by measuring the apparent diameter in transmission optical microscopy. Two or three images were taken of each fibre tensile specimen and the average diameter over each image was determined using an imageJ macro (appendix section A5). The macro workflow first applies a scale depending on the objective magnification and thresholds the image using the AutoThreshold method. The thresholding is then manually confirmed and used to create a mask. The diameter of the fibre at each point in the mask is determined using the Local Thickness method as 'the diameter of the largest sphere that fits inside the object and contains the point'.[164] A selection is then manually created down the centre of the fibre and the mean of the local thickness values along the selection is calculated and reported as the fibre diameter for that image. The specimen diameter is then taken as the average of the diameters from each of the images. The cross-sectional area is then calculated from the determined specimen diameter assuming a circular cross-section. For eDIPS CNT fibres, the measured diameter varied along the fibre length and to reduce the effect of sampling errors, the cross-sectional area used for tensile analysis was averaged from all the filaments for each spinning condition. For other fibres, the tensile analysis was conducted using the cross-sectional area measured for each individual filament.

3.3.2 Electron microscopy

Electron microscopy is preferred to optical microscopy for visualising nanomaterials due to the significantly improved resolution and depth of field. In electron microscopy, an electron beam is used as the illumination source. When the incident electron beam interacts with the sample both electrons and X-rays are emitted at a variety of energies. Depending on the

information and type of contrast desired, different signals are selected for detection and analysis. Secondary electron emission is highly dependent upon surface topography, whilst backscattered electron emission is primarily dependent upon the atomic number of the atoms within the sample, giving compositional contrast.[165] The energy of emitted X-rays is characteristic of the elements within a sample. Measuring the number and energy of the X-rays, in a method known as energy-dispersive X-ray spectroscopy (EDS), enables measurement of the elemental composition of a sample.

In a scanning electron microscope (SEM), a tightly focussed electron beam is rastered across a sample and the signal intensity at each point is used to construct an image. Both secondary electron and backscattered electron detectors can be used to obtain topographic and compositional contrast. The resolution is dependent upon a number of factors including the electron spot size, the beam brightness and the accelerating voltage used in the electron gun but in optimal cases can be as low as 1-2 nm.[166] In practice, this means that SEMs can image the structure of CNT materials at the bundle-level but cannot distinguish individual CNTs. The imaging of non-conductive samples in SEM is limited by the build-up of charge on the material surface which distorts the electron beam. To avoid the build-up of charge conductive coatings may be applied to non-conductive samples. Sputtered gold is commonly chosen as a coating material as it has a high conductivity and also a high secondary electron coefficient, which boosts signal for topographic imaging. However, pure gold often forms discontinuous islands and so for high resolution imaging chromium coatings are preferred, but require immediate imaging and high quality vacuum to prevent oxidation.[167] Applied coatings mask the nanoscale features and so limit the effective resolution at which a non-conductive sample can be imaged. Therefore, in the context of this project, SEM will be more useful for characterisation of CNT fibres than INT fibres.

In transmission electron microscopy (TEM), a thin specimen is illuminated with an electron beam and the transmitted electrons are detected. Various imaging modes are possible but in the most common modes, bright field and dark field TEM, contrast is provided by the absorption and scattering of electrons which generally increases with the atomic number of the atoms and the material thickness. Individual CNTs and INTs can be imaged using this technique to determine their diameter, length and number of walls.[82, 168, 169]

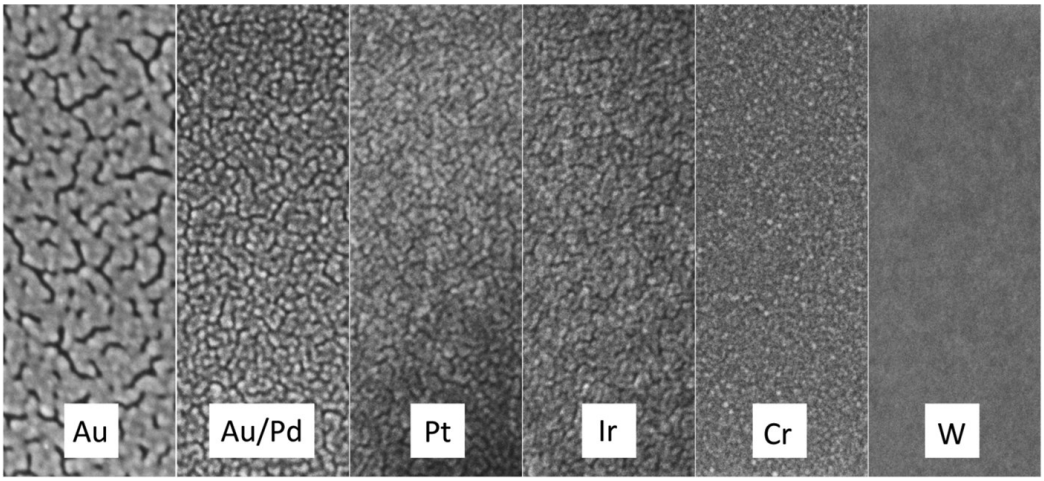


Figure 3.7. Secondary electron SEM images of various coating materials sputtered onto glass substrates with a coating thickness of 2 nm. Image widths are 140 nm. Reproduced from reference [167].

SEM images in this project were captured using microscopes and coating techniques appropriate for the samples and desired resolution. Fibre samples were fixed to aluminium stubs using conductive carbon tape. Low resolution SEM imaging was carried out using a JEOL 6010LA SEM using a gold sputtered coating for INT fibres using an Everhart-Thornley secondary electron detector at a working distance of approximately 14 mm. Higher resolution imaging was carried out with a Zeiss Auriga CrossBeam SEM equipped with a field emission gun with a 5 nm chromium coating for INT fibres using an in-lens detector at a working distance of approximately 5 mm. SEM images were generally collected at an accelerating voltage of 5 kV to obtain topographical contrast, whilst an accelerating voltage of 20 kV was used for EDS. SEM images of fibre cross-sections were prepared by milling the fibres with a 30 kV Ga^+ beam at a beam current of 30 nA. TEM images of INTs were collected by collaborator, Erwan Paineau, using a JEOL 1400 TEM operating at 80 kV. Highly dilute solutions of INTs in ethanol (1 mg L^{-1}) were drop cast onto carbon-coated copper TEM grids before imaging.

3.3.3 X-ray scattering

X-ray scattering (XRS) and diffraction techniques are widely used in materials science to probe the structure of materials from length scales of a few angstroms up to 1 µm depending upon the experimental configuration.[170] X-ray diffraction patterns are formed when a collimated beam of monochromatic X-rays is shone on a sample by the scattering of X-rays from electrons around individual atoms and the interference of these scattered rays.[171] In highly

crystalline materials, sharp peaks in X-ray intensity are observed at the diffraction angles which lead to constructive interference of the scattered X-rays. Almost no intensity is seen at other angles due to destructive interference. The diffraction angles of these peaks are known as Bragg angles and are given by Bragg's Law,

$$n\lambda = 2d\sin(\theta) \qquad (2)$$

where λ is the X-ray wavelength, d is the inter-planar spacing of the crystal lattice, 2θ is the scattering angle and n is an integer (Figure 3.8).[172]

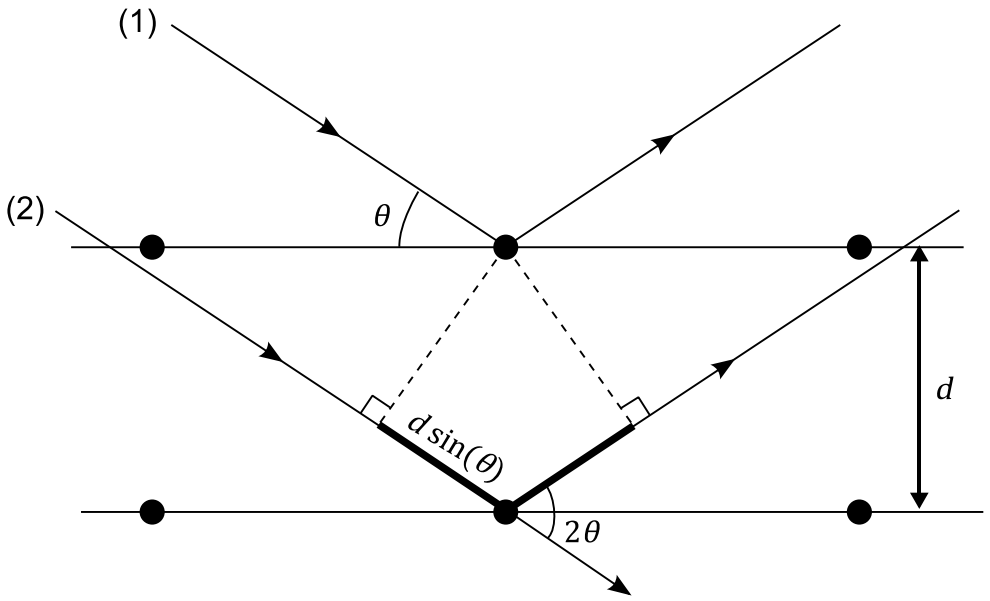


Figure 3.8. Illustration of Bragg's Law for a crystalline material. Constructive interference occurs when the path difference between scattered rays (1) and (2), $2d\sin(\theta)$, is an integer number of wavelengths.

The image formed in an X-ray diffraction pattern is in reciprocal space, representing the Fourier transform of the electron distribution of the sample. The scattering vector $\vec{Q}$ is given by difference between the wavevectors of the incident $\overrightarrow{k_i}$ and outgoing $\overrightarrow{k_o}$ X-rays (Figure 3.9). Whilst a nanotube behaves as a crystal along its axis, producing Bragg reflections corresponding to the axial period of the atomic structure, the small lateral dimensions mean no Bragg reflections are observed in the transverse directions. The X-ray scattering pattern in the equatorial plane instead arises from the shape of the electron density of a nanotube (the form factor). The form factor can be approximated for a nanotube with given diameter and wall thickness by assuming that the electron density is uniform within the nanotube walls. The calculation of scattering patterns from the form factor is carefully derived in

reference [171] and demonstrated for imogolite nanotubes in reference [173]. An alternative approach is to calculate the pattern directly from a proposed atomic structure.[174] The scattering pattern of an imogolite nanotube located in the plane perpendicular to the incident X-ray beam is therefore comprised of the scattering due to the nanotube form factor modulated by the axial periodicity (Figure 3.10a,b).

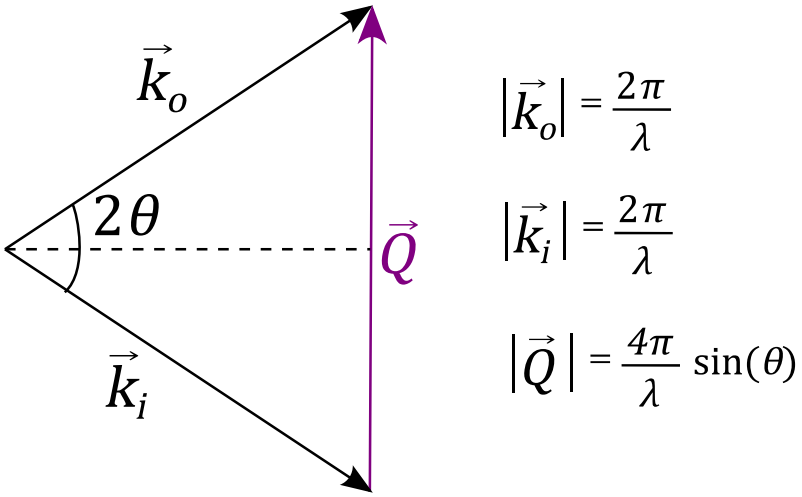


Figure 3.9. Illustration of the definition of scattering vector $\vec{Q}$.

The scattering pattern of a physical INT fibre resembles the calculated patterns for individual INTs and assemblies of perfectly aligned INTs with some distortions due to the experimental arrangement and angular spread of the scattering peaks due to imperfect alignment within the fibre (Figure 3.10c). The peak positions of the equatorial features of the XRS pattern of an INT fibre corresponds closely to that predicted from the form factor of an individual INT, although the presence of some experimental background reduces the sharpness of some of the oscillations, and the peak at 2.6 nm^{-1} is flattened (Figure 3.10d). The projection of XRS patterns onto a planar detector combined with possible tilt of the fibre axis out of the plane perpendicular to the incident beam distorts the appearance of the diffraction pattern, with the straight layer lines in reciprocal space appearing as curves on the diffraction pattern, whilst information along the meridional direction (parallel to the fibre axis) is missing.[175, 176] However, the equatorial line is broadly unchanged and may reasonably be used to characterise the orientation of nanotubes within a fibre diffraction pattern without additional computation.

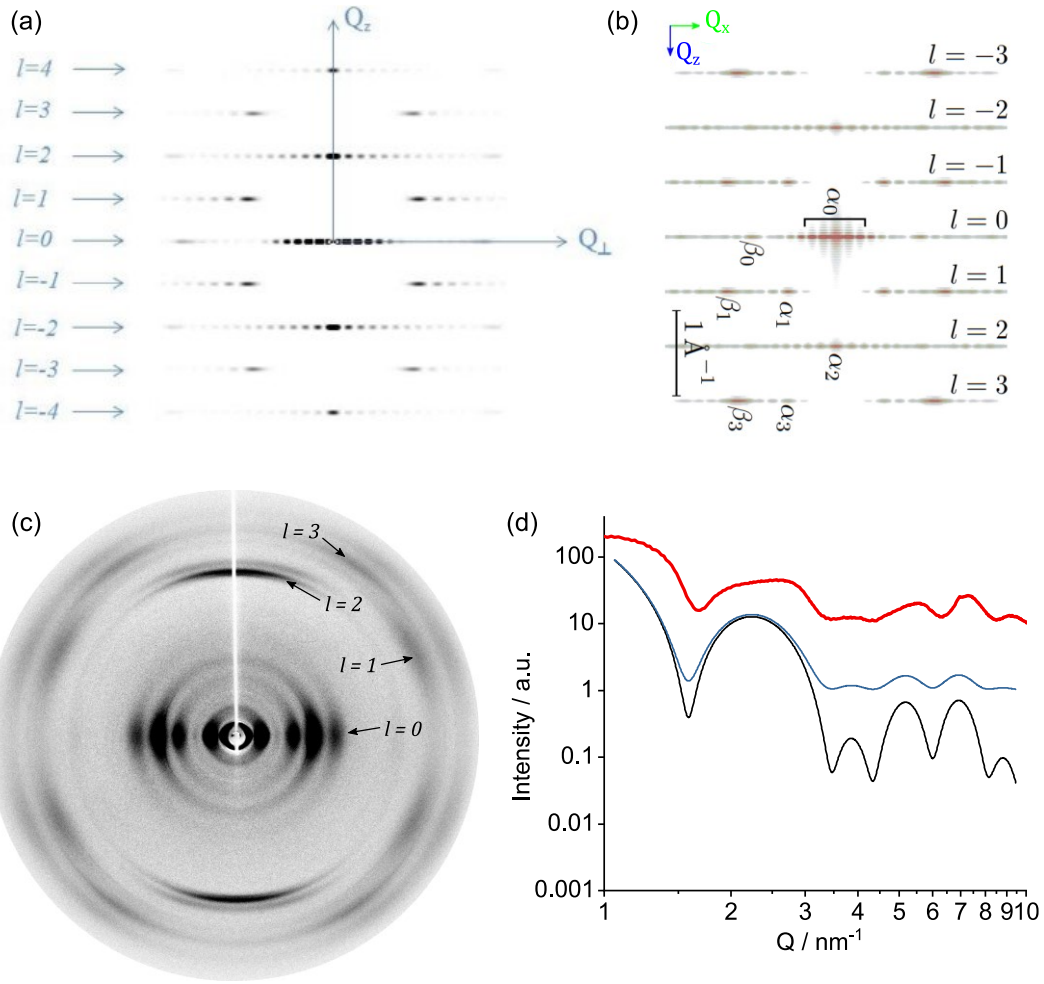


Figure 3.10. (a) Simulated diffraction pattern for an assembly of vertically oriented single walled imogolite nanotubes using the homogeneous approximation. Reproduced from reference [173]. (b) Calculated diffraction pattern for vertically oriented $SiCH_3$ single walled imogolite nanotubes. Adapted from reference [174]. (c) Experimental XRS pattern of an INT fibre. (d) Radially integrated XRS intensity as a function of scattering modulus for (red) experimental XRS pattern of an INT fibre, (black) simulated XRS pattern for double-walled Ge-INT and (blue) simulated XRS pattern for double-walled Ge-INT with addition of constant background of 1% of peak intensity. Simulation functions taken from reference [177].

For assemblies of non-parallel nanotubes, the diffraction spots are curved into arcs and the width of the arc can be used to characterise the degree of alignment of the nanotubes. A typical approach is to take the azimuthal scan of the most intense equatorial diffraction peak and which is then normalised and equated to the orientation distribution of the nanotube walls (Figure 3.11).[178] However, the azimuthal scan of the equatorial peak does not have a true one-to-one relationship with the polar angle between the fibre and nanotube axes and greater care should be taken to convert the reciprocal space azimuthal scan of intensity to a

direct space orientation distribution function. An empirically determined transformation for intensity scans with Lorentzian lineshape is described in the appendix (section A6, p.197).

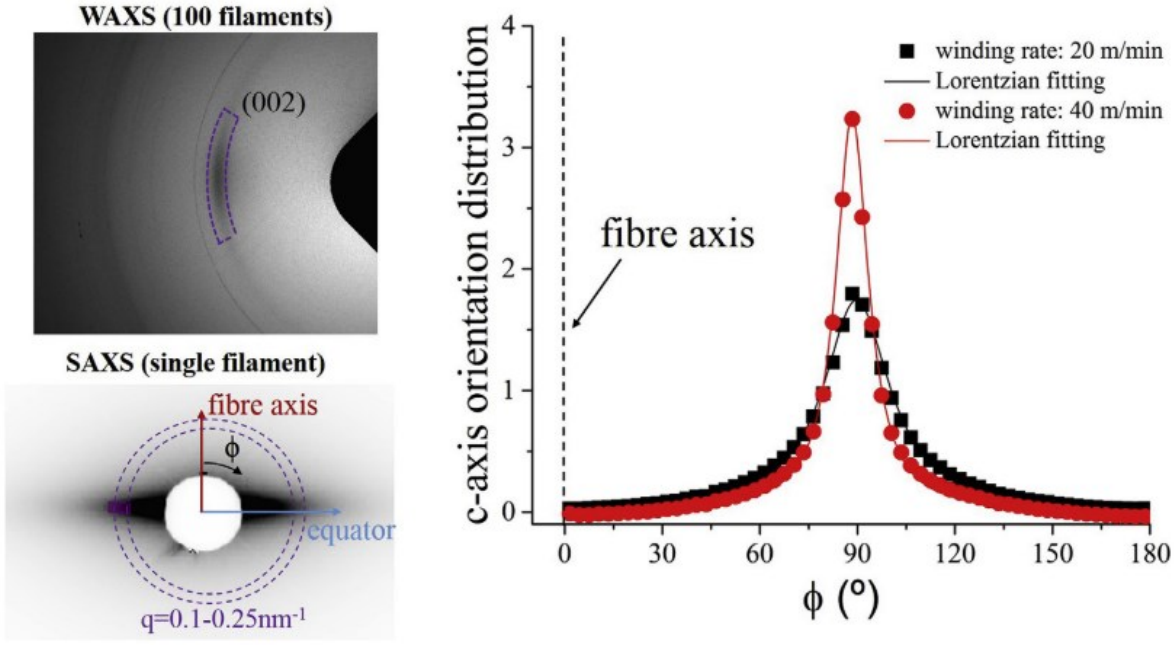


Figure 3.11. Wide angle X-ray scattering (WAXS) and small angle X-ray scattering (SAXS) patterns for CNT fibres alongside azimuthal scans of the equatorial diffraction peaks. Reprinted from reference [178] with permission from Elsevier.

XRS experiments in this work were carried out on a rotating anode (RU H3R, Rigaku Corporation) using Cu Kα radiation (wavelength 0.154 nm) delivered by a multilayer W/Si optics. Sections of single fibre filaments were mounted on cardboard struts and placed in the beam path. Some samples were imaged in a lab atmosphere (for which a background due to scattering from air was subtracted), and others were imaged using a vacuum chamber equipped with a collimator, with entrance and exit windows made of 500 µm thick Mylar films. The fiber was kept perpendicular to the incident X-ray beam. Two-dimensional patterns were recorded on a MAR345 detector (marXperts GmbH) with 150 µm pixel size and sample-detector distance of 300 mm. Extraction of the scattered intensity as a function of the scattering modulus, Q, or azimuthal angle, τ, was performed with software developed by my collaborators Pascale Launois and Erwan Paineau. Further calculation of the orientation parameter from the diffraction pattern was performed from the most intense equatorial peak which has a scattering modulus of 2.6 nm^{-1}.

3.3.4 Raman spectroscopy

Raman spectroscopy examines the vibrational states of a molecule through the inelastic scattering of light. A monochromatic laser is used to excite electrons in a sample to a higher energy state from which they subsequently relax, emitting a photon. The material may relax into the same original vibrational state (Rayleigh scattering) or into a higher or lower vibrational state (Stokes' or anti-Stokes' scattering) and the difference between the energies of the incident and scattered photons is measured and used to determine the vibrational energy levels in the material (Figure 3.12). When the laser excitation energy matches the band gap or another van Hove singularity gap of a nanotube, the greater density-of-states leads to a significantly increased probability of transitions and a Raman signal approximately a factor of 10^3 higher.[179] By varying the laser excitation, different groups of CNTs can be probed in this resonance condition and this technique has been used to selectively characterise metallic and semi-conducting CNTs at excitation wavelengths of 532 and 785 nm, respectively.[180]

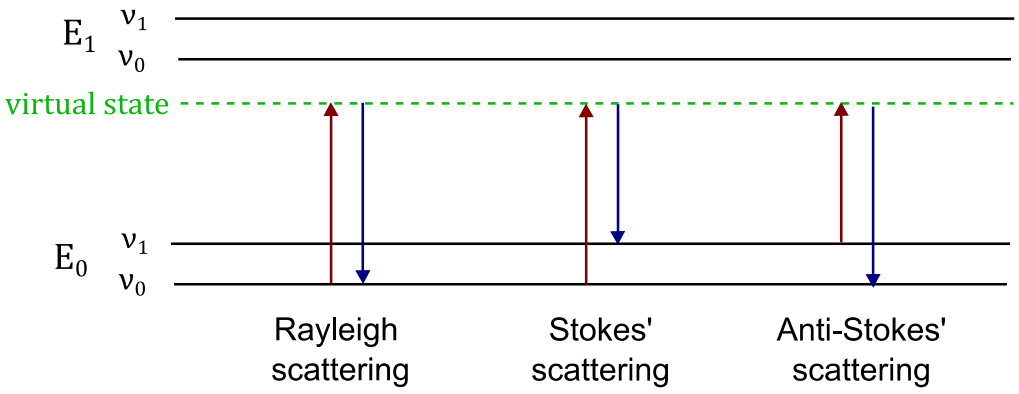


Figure 3.12. Illustration of the (red) excitation and (blue) relaxation steps of the scattering processes in non-resonant Raman spectroscopy.

The Raman spectra of CNTs are comprised of a few key vibrational bands (Figure 3.13a). The G-band is located at a Raman shift of approximately 1580 cm^{-1} and is associated with bond stretching within the graphitic plane. In CNTs, the G-band is split into two sub-bands corresponding to axial and transverse stretches. The D-band, located around 1350 cm^{-1}, is associated with defects within the CNTs and is commonly reported as an intensity ratio to the maximum intensity of the G-band (I_D/I_G). I_D/I_G is known to be dependent upon the laser excitation energy (E_L) used to collect the Raman spectrum and varies as ${E_L}^{-4}$ with lower I_D/I_G for higher excitation energy.[181] It is therefore important to compare I_D/I_G values which are

collected with the same excitation energy. I_D/I_G does not vary linearly with defect density. For CNTs with a low defect level an increased I_D/I_G indicates increased defect density, but there is ambiguity for highly defective graphitic structures with I_D/I_G greater than 1 and care should be taken in these cases (Figure 3.13b). The radial breathing mode (RBM) appears at a Raman shift of 100-500 cm^{-1} and corresponds to coherent radial deformation of the nanotube. The Raman shift of the RBM (ω_{RBM}) is dependent upon the CNT diameter (d_{CNT}) as

$$\omega_{RBM} = \frac{248\ \mathrm{cm}^{-1}}{d_{CNT}} \tag{3}$$

for individual CNTs on a SiO_2 substrate and this information can be used in combination with various laser excitation energies to assign the helicity of CNTs in a sample.[182]

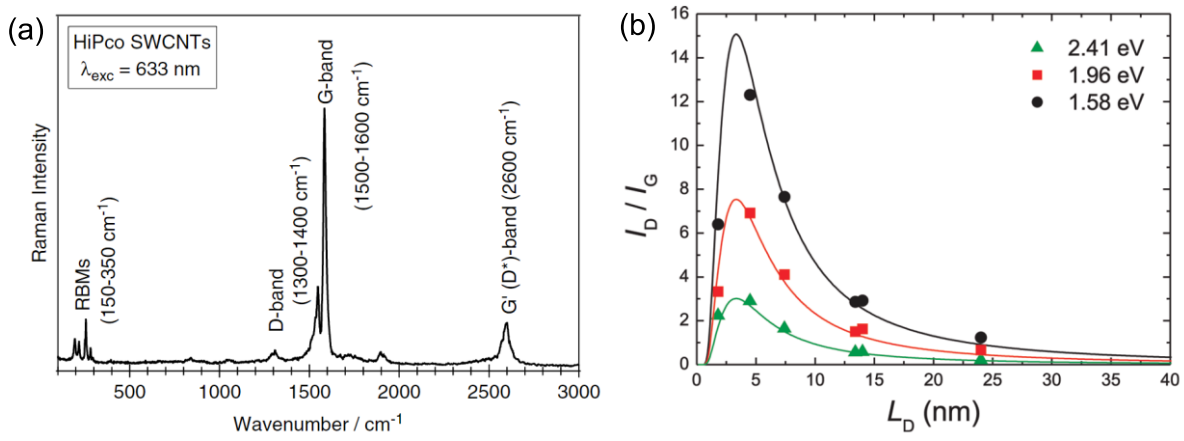


Figure 3.13. (a) Representative Raman spectrum for single-walled CNTs, with key features indicated. Reprinted from reference [183] with permission from John Wiley & Sons. (b) D/G intensity ratio (I_D/I_G) as a function of average inter-defect distance (L_D) for Ar^+ ion-bombarded graphene samples collected with varying laser excitation energy. Adapted from reference [184] with permission from The American Chemical Society.

Raman spectroscopy was conducted using a Renishaw inVia micro-Raman spectrometer via a 50x magnification lens using a 50 mW 532 nm laser at a laser power of 10% and exposure time of 2 s. For each sample, 100 Raman spectra were collected in a 10x10 grid over a 20x20 µm square by rastering the excitation laser spot. The I_D/I_G was calculated for each spectrum using a MATLAB analysis script by first subtracting a linear background from the dataset and then identifying I_G as the maximum intensity between 1550 and 1650 cm^{-1}. In some cases, the G-peak overlapped with the D-peak and so to determine I_D, a linear background was subtracted from between 1280 and 1400 cm^{-1} and I_D was identified as the maximum intensity remaining within that window. For each sample, the calculated I_D/I_G values are reported as a histogram.

3.3.5 Single filament tensile testing

Single filament tensile tests are widely used to characterise the performance of fibres for use in structural composites. In a typical tensile test, a filament is mounted in a universal testing machine and stretched at a constant cross-head speed whilst the tensile load is measured. The engineering stress (σ) and engineering strain (ϵ) in the material are calculated during the experiment from the tensile load (F), extension of the fibre (ΔL) and the initial fibre cross-sectional area ($A_{f,0}$) and length (L_0) as,

$$\sigma = \frac{F}{A_{f,0}} \quad (4)$$

$$\epsilon = \frac{\Delta L}{L_0} \quad (5)$$

Compliance in the tensile load train can lead to an over-estimate for the strain if the cross-head displacement is simply used as the extension of the fibre. This issue can be avoided by making a direct measurement of sample strain using an extensometer or digital image correlation, but these methods can be difficult to implement on a single filament. The machine compliance in the equipment used in this project is dominated by the load cell and can be corrected by calculating the load cell extension for the measured tensile force and subtracting this machine extension from the cross-head displacement to obtain the sample extension. This correction is applied within the software of the tensile testing stage used in this work, with the correction factors being provided by the manufacturer for each load cell. Various other methods exist to correct for machine compliance using multiple identical samples of differing gauge lengths or a sample of a material with a known elastic modulus.[185, 186]

A typical stress-strain curve for a CNT fibre is schematically represented in Figure 3.14 with definitions of the key mechanical properties: elastic modulus, tensile strength and strain at failure. The elastic modulus is defined here as the gradient of the initial linear section of the stress-strain curve (in this work typically taken between 0.1 and 0.2% strain). In the context of lightweight materials, it is often useful to compare the specific strength and specific modulus of fibres (the strength or modulus divided by the material density) and, in this project, these properties are determined by dividing the load (in Newtons) by the linear density of nanotubes in the fibre (in tex or $g_{CNT/INT}\,km^{-1}$) calculated from the spinning

conditions, which obtains specific stress in the non-SI but industrially standard units of N tex^{-1}. The measuring of specific strength in N tex^{-1} is popular industrially due to the greater convenience of measuring the linear density, as compared to the cross-sectional area, of yarns and tows.

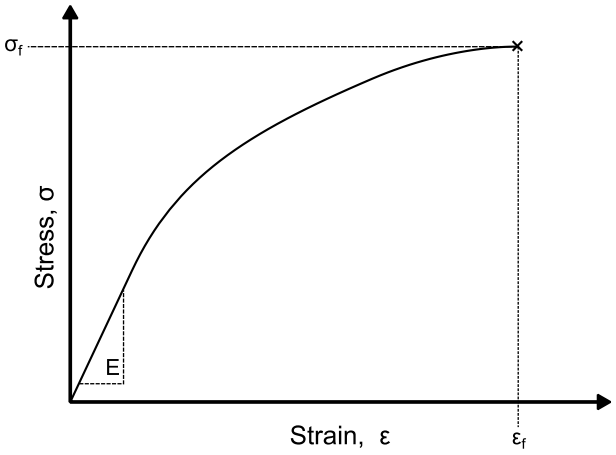


Figure 3.14. Typical stress-strain curve for CNT fibres with indicated of definitions elastic modulus (E), tensive strength (σ_f) and strain at failure (ϵ_f).

Single filament tensile tests were conducted following BS ISO 11566:1996. Single filament specimens were gently mounted on cardstock frames with a gauge length of 15 mm using double sided tape (Figure 3.15) and the ends were fixed using epoxy adhesive (Araldite Rapid, Huntsman Advanced Materials) which was left to cure overnight. Tests were conducted using a tensile testing stage (TST350, Linkam Scientific) equipped with a 2 N load cell at a crosshead speed of 1 mm min^{-1} (effective strain rate 0.0011 s^{-1}). Machine compliance was corrected for in the software using a manufacturer provided correction factor. A testing system compliance of 127 µm N^{-1} was applied for the 2 N load cell used in these tests. Testing at controlled humidity was conducted using a humidity controller (RH95, Linkam Scientific) integrated with the tensile testing stage. Samples were mounted in the testing stage and then allowed to equilibrate for 20 minutes at the target humidity before testing.

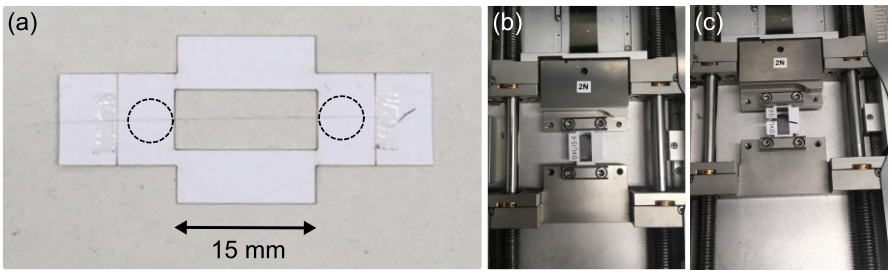


Figure 3.15. Photographs of (a) CNT fibre mounted on cardstock tensile frame before application of epoxy adhesive on the dashed circles and fibre sample mounted in tensile tester (b) before and (c) after cutting the card frame.

3.3.6 Capillary rheometry

Shear rheometry of nanotube solutions is typically conducted using rotational rheometers with a cone-plate, parallel plate or couette configuration depending upon the viscosity of the solution.[187] The key benefits of a rotational rheometer with a cone-plate arrangement are a constant shear rate throughout the sample, good temperature control and the opportunity to conduct small amplitude oscillatory measurements to determine viscoelastic properties. However, it is challenging to test air-sensitive samples in a rotational rheometer as custom inert gas enclosures are required. In comparison, capillary rheometry can successfully be conducted with air-sensitive samples provided that the material feedstock is suitably sealed and that no reactions occur within the capillary, although the technique becomes effectively destructive if conducted in a room atmosphere.

The theory for capillary rheometry is well described in the existing literature.[188, 189] A brief overview of the key equations used in this thesis are given below. For fluid flow in a cylindrical pipe, the wall shear stress, τ_w, is simply given by

$$\tau_w = \frac{\Delta P \, R_c}{2L_c} \tag{6}$$

where ΔP is the capillary pressure drop, R_c is the capillary radius and L_c is the capillary length. In general, the shear rate at the wall is not simply determined by the pressure drop and capillary dimensions and depends upon the rheology of the fluid. The *apparent* wall shear rate, $\dot{\gamma}_{a,w}$, (i.e. that of a Newtonian fluid) is given by

$$\dot{\gamma}_{a,w} = \frac{4Q}{\pi R_c^3} \tag{7}$$

where Q is the volumetric flow rate of the fluid. The true wall shear rate for non-Newtonian fluids can be determined by following the Rabinowitch correction. The true wall shear rate, $\dot{\gamma}_w$, is given by

$$\dot{\gamma}_w = \left(\frac{3+b}{4}\right) \dot{\gamma}_{a,w} \tag{8}$$

where b is determined from a plot of $\log \dot{\gamma}_{a,w}$ vs $\log \tau_w$ as

$$b = \frac{d\left(\log \dot{\gamma}_{a,w}\right)}{d(\log \tau_w)} \tag{9}$$

Capillary rheometry was conducted by injecting nanotube solutions down cylindrical capillaries and measuring the pressure drop for a variety of flow rates. A syringe pump (100 Legacy, KD Scientific) was used to control the flow rate and the capillary was selected depending upon the viscosity of the fluid under test. A 21 g stainless steel needle (514 µm ID, 180 mm length) (BD Microlance, Becton Dickinson) and PEEK HPLC tubing (178 µm ID, 500 mm length) (Trajan Scientific) were used for CNT and INT solutions respectively. The capillaries were attached to the syringe barrel and a pressure sensor (ABPDANT030PG0D3, Honeywell) using barbed polypropylene luer adapters (Colder Products Company) and short lengths of silicone tubing (1/16" ID).

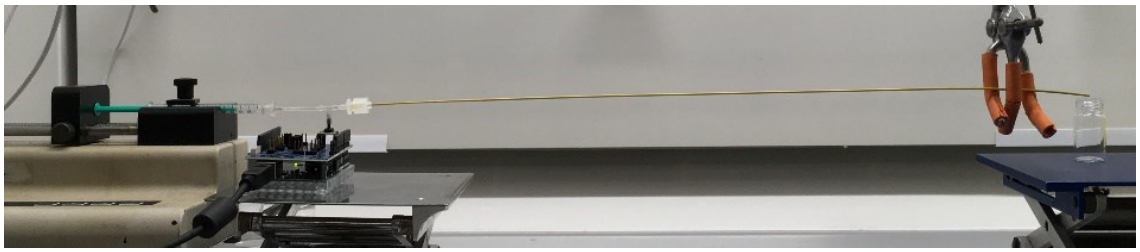


Figure 3.16. Photograph of capillary rheometry equipment with 50 cm length of PEEK tubing.

3.3.7 Thermogravimetric analysis

In thermogravimetric analysis (TGA), the mass of a sample is measured through a heating process (typically a linear ramp) in a controlled atmosphere. TGA has been used to assess the thermal stability of CNTs, their inorganic content and the mass of surface functional groups which can be thermolyzed from the CNTs. CNTs are more resistant to combustion than fullerenes, graphite and amorphous carbon, enabling some identification of the content of carbon samples.[190] In a typical TGA experiment under an air atmosphere, amorphous carbons are combusted at 200-400 °C followed by the sublimation of fullerenes at 400-600 °C and then combustion of graphite and CNTs above 600 °C, with the remaining mass comprised of metal catalysts and their oxidation products.[191] The oxidation and combustion processes typically occur over a wide range of temperatures and there is some considerable overlap between the combustion temperatures of graphite and CNTs which can hinder identification and hence TGA is only semi-quantitative for the determination of carbon allotropes. The remnant mass after combustion is more quantitative and with knowledge of the metal catalyst used in synthesis (typically Fe) and the corresponding oxidation product (Fe_2O_3), the initial mass fraction of catalyst in a CNT sample can be determined.

TGA was conducted with a Mettler Toledo TGA/DSC under either air or nitrogen gas flow of 50 mL min^{-1}. In a typical temperature profile, the samples were heated to 100 °C at which they were held for 20 minutes and then heated with a constant temperature ramp of 10 °C min^{-1} to 800 or 900 °C. Blank runs were conducted with alumina crucibles to obtain baselines to correct for the buoyancy effect. Samples (1-3 mg) were then loaded into the alumina crucibles and the heating profile was repeated and the baseline was subtracted from the experimental runs.

3.3.8 Electrical conductivity

Electrical conductivity of CNT fibres was measured using a Keithley 3706A system switch multimeter with a home-designed four point probe measurement jig (1 cm sense electrode separation). The resistance was measured three times for each sample using the in-built constant current source method on the multimeter. The specific electrical conductivity was then determined by dividing the electrode separation distance by the product of the mean resistance and linear density of each sample whilst the (areal basis) electrical conductivity was determined by dividing the electrode separation distance by the product of the resistance and cross-sectional area of each sample.

4 Exploring the spinning and properties of imogolite nanotube fibres

Parts of this chapter, including figures and text, are adapted from reference [192] previously published in *ACS Applied Materials & Interfaces* under the CC BY 4.0 license. Where relevant, the research contributions of co-authors are indicated in the text.

Imogolite nanotubes (INTs) can serve as an excellent analogue for CNTs as they have a similar morphology and aspect ratio but are considerably more convenient experimentally. In contrast to CNTs, INTs are simple to dissolve and they disperse spontaneously in deionized water[11] but similarly to CNT polyelectrolyte solutions, they form liquid crystalline mesophases which may be used to spin aligned fibres.[80, 177] As described previously (sections 2.2.2, 3.3.1 and 3.3.3), INT fibres may be characterised using a variety of methods which are challenging to apply to CNTs, particularly POM and XRS techniques. As such, spinning INT fibres may provide an opportunity to study the assembly of nanotubes into fibres more generally, gaining insights which can be applied to other materials systems.

In addition to acting as an analogue for CNTs, INT fibres may also find applications in their own right, as their uniform diameter can be used for molecular filtration, catalysis and molecular transport and release.[11] INTs have several properties complementary to CNTs; they are electrically insulating, stable to oxidation, hydrophilic, and rather notably either transparent or white depending on the scattering of light within their macroscale structure. These properties may enable possible applications as insulating separators in electrical devices, and may offer benefits in some composite applications where improved surface interaction with the matrix is advantageous.

Although INTs have previously been incorporated in polymer fibres as nanoscale reinforcements,[193] there are no reports of spinning pure, binder-free fibres from these nanotubes. In this chapter, the development of an INT fibre spinning process is described alongside an initial characterisation of these new fibres.

4.1 Synthesis of aluminogermanate INTs

Synthesis and characterisation of the INT feedstocks used in this work was conducted by collaborator Erwan Paineau. In brief, the INTs were synthesised by a sol-gel process in which an aqueous solution of aluminium perchlorate, tetraethoxygermane and urea are mixed in a digestion bomb and hydrothermally treated at 140 °C. The INTs were then separated from any remaining reactants or by-products by dialysis against ultrapure water. This synthesis method has been shown to consistently produce double-walled INTs with an outer diameter of 4.34 nm and inner diameter of 1.54 nm with wall thickness and separation of 0.6 nm and 0.2 nm respectively.[85]

The incubation time of the INT synthesis was varied from 5 to 40 days in order to create INT feedstocks (named INT-5d, INT-12d etc.) with different length distributions. The length distribution of each INT feedstock was determined by measuring the length of at least 200 nanotubes over several TEM images (Figure 4.1).

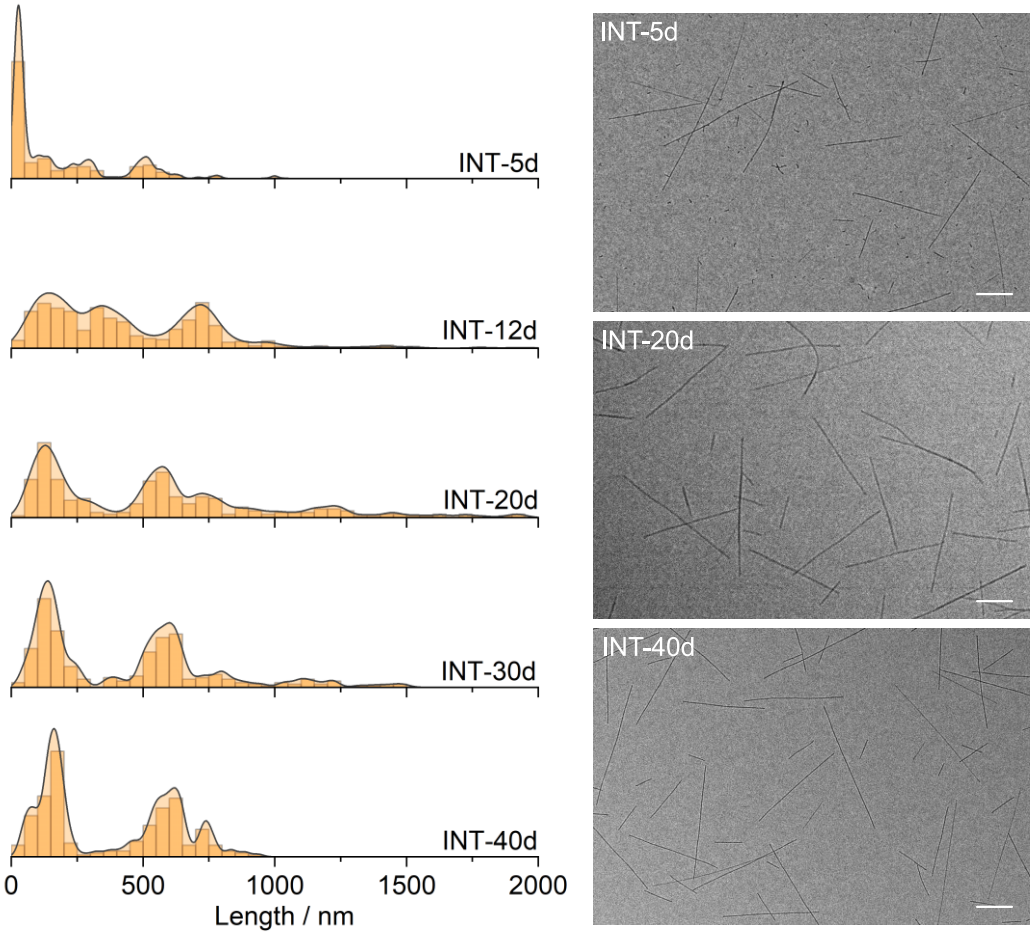


Figure 4.1. Length number distributions of synthesised INT feedstocks alongside representative TEM images. Scale bars 200 nm.

INT-5d is dominated by short nanotubes with lengths less than 100 nm. After further incubation, these short nanotubes are consumed to produce a bimodal distribution with average lengths centred at 150 and 600 nm. Beyond 20 days of incubation, little further change to the distribution was observed. The growth of INTs is theorised to occur via an oriented attachment mechanism.[194, 195] This growth mechanism is expected to occur slowly at larger nanotube lengths due to the L^{-4} dependency of tip-tip collision frequency,[196] explaining the lack of meaningful growth after 20 days of incubation. Fourier transform infrared spectra were collected and found to be consistent across the INT feedstocks (Figure A1).

4.2 Spinning INT fibres

INTs spontaneously form colloidal solutions in deionised water because of the development of a weak positive charge on the outer walls (with a corresponding negative charge on the inner walls).[197, 198] Following Derjaguin-Landau-Verwey-Overbeek (DLVO) theory, the electrostatic repulsions between the INTs stabilises the colloidal solution. However, these solutions are expected to become unstable at higher pH (where the outer walls reach their isoelectronic point) or in the presence of counterions which screen the electrostatic repulsions between INTs, leading to their aggregation as a gel.

INT fibres have been produced using a solution spinning technique in which an aqueous solution of INTs (typically 9-13 mg mL^{-1}) is injected into a coagulation bath *via* a needle or designed nozzle. The gelled proto-fibres are then collected on a take-up wheel, washed and dried to form pure, binder-free imogolite nanotube fibres.

4.2.1 Initial coagulation and washing trials

Coagulation of INTs into a gel-like proto-fibre can be induced by destabilising the colloidal suspension of the spinning dope. The electrostatic repulsion between the positively charged outer walls of the INTs can be screened using high ionic strength solutions. In the first case, highly concentrated aqueous solutions of calcium chloride (300 g L^{-1}) were used, however, other salts are also able to screen the repulsions and gel the INT fibres. Gel fibres coagulated in calcium chloride cannot not fully dry under ambient conditions when removed from the coagulation bath due to the presence of hygroscopic salt, which absorbs moisture from the

air at typical room humidity levels. If these wet fibres are dried at elevated temperature, they become brittle and challenging to handle, possibly due to the formation of brittle salt crystallites within the fibres. To enable drying and densification of these fibres, excess salt in the gel fibre can be removed by washing in deionised water. When dipping INT fibres in and out of a washing bath, swirling regions can be seen with a higher refractive index around the fibre, indicating where salt has diffused from the fibre into the washing bath. When removed from the bath, the washed fibres could then dry fully into a translucent-white, robust and handleable fibre.

Prolonged washing with water leads to solubilisation of the fibre, initially seen as swelling; after washing for between 30 s and 1 minute, the gel fibre became too fragile to handle and remove from the washing bath. In order to wash the fibres whilst preventing weakening due to solubilisation, a washing strategy was developed in which the INT fibres were dipped into a beaker of deionised water (3 x 2 s) and then hung to dry in ambient conditions with a small tag of aluminium foil (~20 mg) attached to the end.

The collected dry fibres had an average diameter of ~20 µm, textured surfaces and irregular cross-sections typical of nanomaterial fibres (Figure 4.2a-c).[10] Polarised optical microscopy (POM) observations indicated strong birefringence in the INT fibres, with a maximum of intensity observed with the fibre axis at 45° to the crossed polarisers (Figure 4.2d,e). The use of a full-wave retardation plate (530 nm) showed that the nanotubes are aligned along the fibre axis. A blue colour (retardation ~700 nm) is obtained when the fibre is parallel to the slow axis of the retardation plate, whilst a yellow colour (retardation ~350 nm) is obtained when the fibre is perpendicular to the slow axis of the plate (Figure 4.2f,g). As the dielectric constant is higher in the axial direction of the INTs, the summative retardation when the fibre is parallel to the slow axis of the plate demonstrates that the INTs are preferentially aligned along the fibre axis.

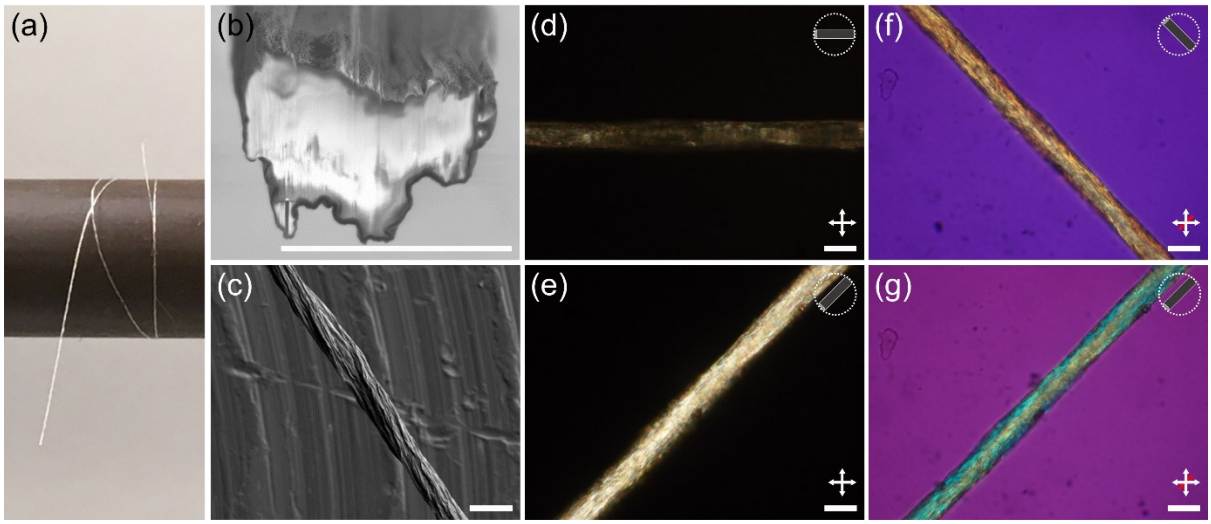


Figure 4.2. (a) Photograph of fibre section on spool, (b) SEM image of focused ion beam milled cross-section of Au-coated fibre, (c) SEM image of Au-coated fibre on aluminium stub, (d-g) Polarized optical micrographs for INT fibre without (d, e) and with (f, g) retardation plate (530 nm). White arrows indicate the polariser and analyser directions, and red lines indicate the slow axis direction of a retardation plate. Scale bars 20 μm.

Energy-dispersive X-ray spectroscopy confirmed that the dry fibres mostly comprised of aluminium, germanium and oxygen with a small residue of calcium (3 at%) and chlorine (6 at%). As expected from the Ge-INT structural formula ($GeAl_2O_7H_4$), the measured atomic ratio of aluminium to germanium was 2:1 (Figure A4). The packing density (ϕ) of the fibres can be estimated from the dope concentration (c_{dope} = 9 mg mL^{-1}), needle area (A_{nozz} = 0.207 mm^2), draw ratio (DR = 5), fibre diameter (d_f) and the density of a double-walled germanium INT (ρ_{INT} = 2.7 g cm^{-3}) as

$$\phi = \frac{4\, c_{dope}\, A_{nozz}}{\pi\, d_f^2\, \rho_{INT}\, DR} \tag{10}$$

This estimate yields packing densities of around 45-55%, similar to that of as-spun FC-CVD CNT fibres (~35-60%),[199] but lower than highly optimised solution spun CNT fibres (~75%).[96]

4.2.2 Spinnability of INT fibres

The spinnability of nanomaterial fibres is expected to depend upon the aspect ratio of the constituent nanomaterials, as previously observed in the literature on solution spinning both CNTs and nanocellulose.[96, 200] Fibres were easily spun from the longer INT feedstocks (INT-12d to INT-40d). However, spinning fibres from the INT-5d feedstock was more challenging and the gel-like proto-fibre was found to fracture repeatedly at the air-coagulant

interface when being withdrawn from the coagulation bath. This failure location indicates that the surface tension of the coagulant imparts sufficient force to overcome the gel strength of the fibre. By considering a modification of the Wilhelmy plate method, the stress in a cylindrical fibre being withdrawn from a liquid is found to be inversely proportional to the fibre radius (Figure A2). With knowledge of the surface tension of the coagulation bath (82 mJ m^{-2} [201]) and the assumption that the fibre-coagulant contact angle is small, the gel strength of the INT fibres can be loosely quantified by determining the fibre radius at which fracture occurs.

INT-5d was found to be unspinnable using a 24 gauge needle (internal diameter, ID 311 µm) but spinnable using a 21 gauge needle (ID 514 µm). The gel strength was, therefore, estimated to be approximately 500 Pa. The other feedstocks, from INT-12d to INT-40d, were all successfully collected from the coagulant without breakage using a 27 gauge needle (ID 210 µm) implying a gel strength of at least 1.5 kPa. These gel strengths are all relatively low, necessitating careful handling of the proto-fibres before collection, washing and drying.

4.3 INT fibre mechanical properties

4.3.1 Impact of INT length on mechanical properties

The mechanical properties of the pure INT fibres were measured using a conventional single filament tensile test. The tensile strength of the dry fibres across the INT feedstocks follows the same trend observed in the gel strengths, with a higher strength for feedstocks INT-12d to INT-40d and a lower strength for INT-5d. The data are quite scattered for these small batch fibres which have been manually processed, however, within error, the strengths and stiffnesses of fibres produced from feedstocks INT-12d to INT-40d were similar, with tensile strength and elastic modulus in ambient conditions (40% RH) of approximately 100 MPa and 15 GPa respectively (Table 3). A lower failure stress was measured for the shorter INT-5d sample of approximately 60 MPa. The stress-strain curves exhibit a shape typically seen in nanomaterial fibers. There is a short initial take-up related to the straightening of fiber followed by an elastic region and then plastic deformation characteristic of inter-nanotube slip, which arises as a prominent ‘elbow’ at around 25 MPa in most cases (Figure 4.3).

Table 3. Properties of wet spun and manually washed INT fibres.

Feedstock	Tensile strength	Elastic modulus	Specific strength	Specific modulus	Density	Failure strain
	MPa	GPa	N tex^{-1}	N tex^{-1}	g_{INT} cm^{-3}	%
INT-5d	70 ± 20	9 ± 2	0.047 ± 0.013	6.1 ± 1.3	1.5 ± 0.3	1.0 ± 0.3
INT-12d	110 ± 13	20 ± 4	0.073 ± 0.018	14 ± 3	1.5 ± 0.2	0.7 ± 0.2
INT-20d	95 ± 10	15 ± 4	0.065 ± 0.016	10 ± 3	1.44 ± 0.07	1.1 ± 0.3
INT-30d	120 ± 30	16 ± 5	0.08 ± 0.04	11 ± 3	1.58 ± 0.08	1.1 ± 0.3
INT-40d	100 ± 20	12 ± 3	0.07 ± 0.03	9 ± 3	1.38 ± 0.14	1.5 ± 0.6

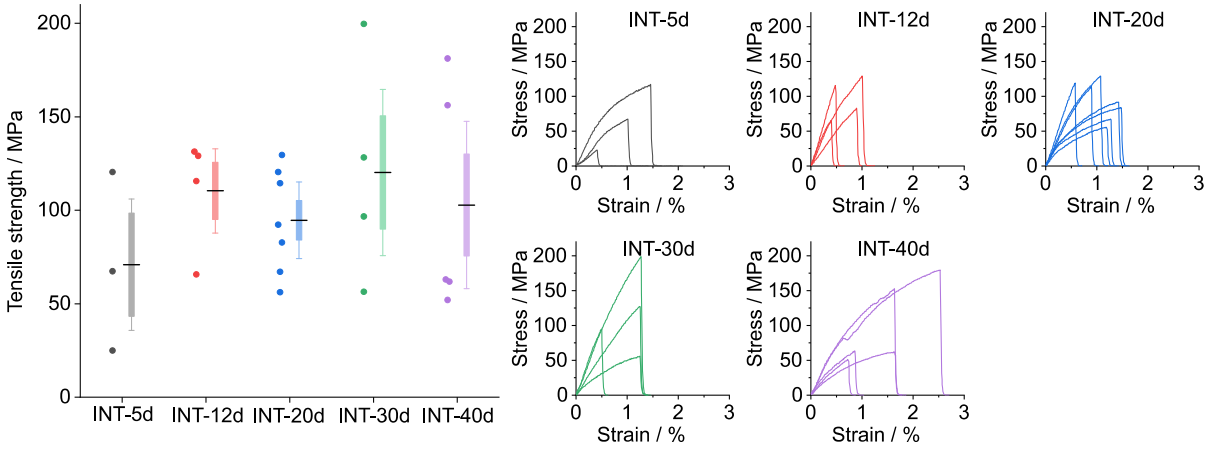


Figure 4.3. Tensile strength and corresponding stress-strain curves for fibres made from (grey) INT-5d, (red) INT-12d, (blue) INT-20d, (green) INT-30d and (purple) INT-40d feedstocks.

4.3.2 Impact of humidity on mechanical properties

INT fibres were found to be highly hygroscopic with moisture uptake of up to 150% at 90% relative humidity (Figure 4.4). At high humidity, the fibres visibly swell and glisten with the uptaken moisture. This moisture uptake is likely to be partially driven by the $CaCl_2$ remaining even after washing (Ca: 3 at%, Cl: 6 at%), although based on the large mass change with humidity, there is almost certainly a contribution due to the hydrophilic INTs, which are expected to adsorb moisture.

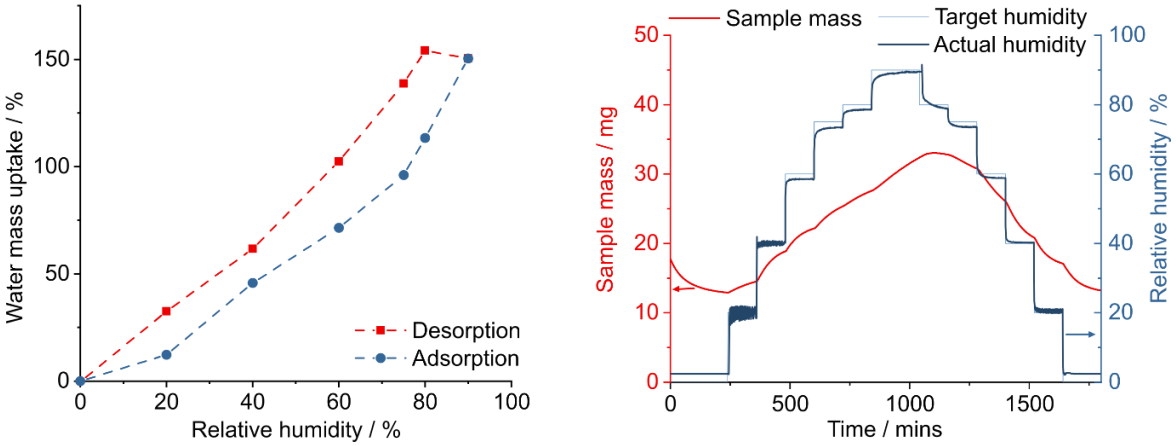


Figure 4.4. Dynamic vapour sorption isotherm of INT fibre at 25°C showing water mass uptake for adsorption and desorption cycles.

The mechanical properties of the INT fibres are influenced by the relative humidity during the tensile test. The modulus in particular is strongly dependent upon the humidity with a modulus of 30 GPa at 10% RH compared to 2.8 GPa at 85% RH. The tenfold decrease in tensile strength and modulus with increasing humidity indicates that the INT fibre properties are

chiefly driven by inter-nanotube interactions, which are weakened by the incorporation of water into the fibre structure.

The presence of water in the fibre is expected to modify interactions between the surface hydroxyl groups of neighbouring INTs in the fibre, leading to a reduction of the both the shear strength and shear modulus of the inter-nanotube interactions. It is expected that such a reduction in the shear interactions with increased humidity will lead to greater plastic slip and a change in failure mode, as indeed observed in the fracture surfaces of fibres tested at different humidity (Figure 4.5). Fibres tested at low relative humidity show a flat brittle fracture surface. As humidity is increased more pull-out is evident at the fracture site and at high relative humidity local necking and shear deformation is visible. The humidity dependence is broadly reversible, with fibres conditioned at 85% RH and then tested at 40% RH showing similar tensile behaviour to those simply conditioned at 40% RH (Figure A3). The humidity dependence of INT fibre properties may be seen as a disadvantage of this nanotube fibre system, especially considering the ease of INT slip and ductile failure at high humidity (85% RH), which is likely to appear as creep for a naked fibre used in typical environmental conditions. As a result, structural use of INT fibres will almost certainly be limited to composites where a polymer matrix can inhibit the uptake of water and protect the fibres from environmental conditions.

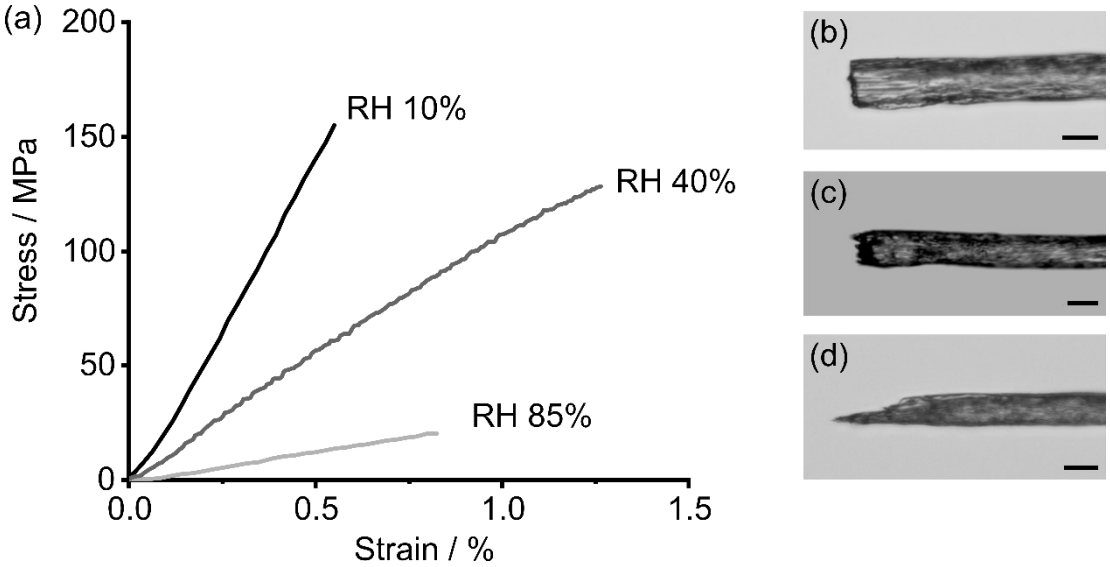


Figure 4.5. (a) Stress-strain curves for fibre samples of INT-30d tested at various controlled humidity, (b-d) optical micrographs of fibres fractured at (b) 10%, (c) 40% and (d) 85% relative humidity. Scale bars 20 μm.

4.3.3 Impact of alignment on mechanical properties

In order to identify the root cause of the intra-batch scatter in mechanical properties, a larger number of tensile samples were tested for fibres produced from INT-20d (Figure 4.3). X-ray scattering patterns were collected on a small section of each fibre sample and used to quantify the orientation of INTs within the fibres as described in the appendix (section A6, p.197). Hermans order parameter is calculated from the ODF and used to characterise the orientation of the fibres between perfectly uniaxial ($S = 1$) and randomly oriented ($S = 0$). The calculated values of S range from 0.49 to 0.74 for the eight fibre samples studied by XRS, indicating some significant variation in alignment between samples despite attempts to use consistent processing conditions. Measurements performed at varying positions along the length of a single 5 mm fibre section indicated that the degree of alignment is constant along each individual section and hence the differences in orientation between fibre samples likely arises from the manual handling of each section.

Somewhat surprisingly, higher degrees of alignment correlate with lower elastic modulus and a higher strain-at-failure (Figure 4.6a,b). This result initially seems counter-intuitive, particularly when considering typical short-fibre composite models which predict that stiffness and strength should increase with alignment.[178, 202] However, this trend can be explained by considering the microstructure and load transfer within these relatively porous fibres. These fibres do not contain a matrix and are comprised of stiff, straight nanotubes with relatively low interfacial shear strengths. In highly aligned fibres, the load must be transferred between the nanotubes by frictional shear interactions at nanotube contacts. In the aligned case, these contact points can slide relatively easily without arrest leading to a lower stiffness, more ductile behaviour and a higher strain-to-failure. However, in less aligned packings of high aspect ratio rods, load may also be supported by mechanical interlocking. This interlocking occurs at a jamming transition when the number of independent contacts per rod exceeds a critical value of approximately ten.[203, 204] As the number of contacts between rigid rods increases with increased misorientation,[205] it is expected that jamming occurs more frequently in the less aligned INT fibres. The resulting interlocked structure for the fibres with lower alignment is therefore stiffer and undergoes less plastic deformation before failure, leading to a lower strain-at-failure.

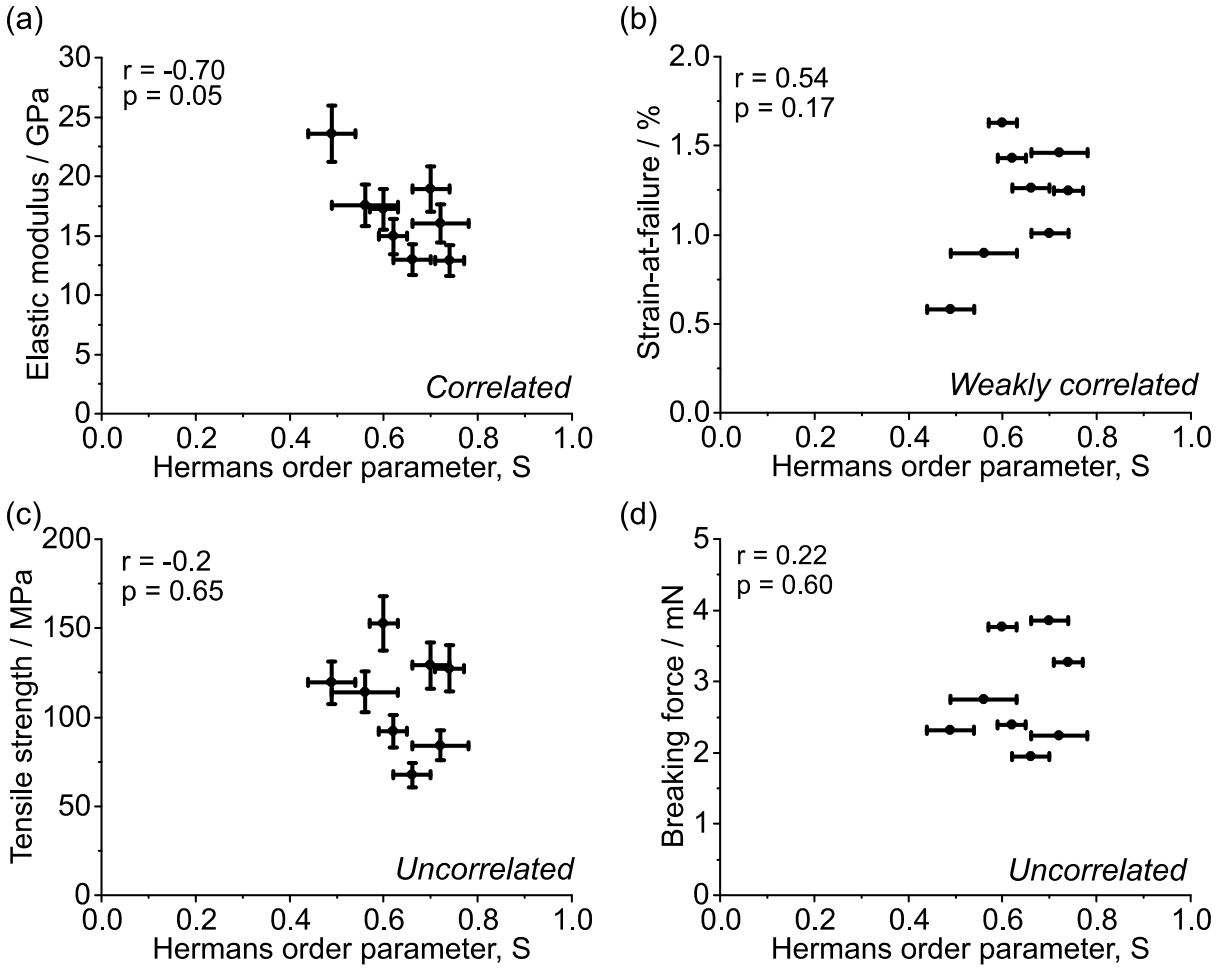


Figure 4.6. Fibre mechanical properties as a function of Hermans order parameter, S, with Pearsons correlation coefficients, r, and corresponding p-values.

This mechanism of load transfer has been observed in systems across a variety of length scales from entangled twigs in birds' nests to the formation of stiff networks of bamboo skewers and colloidal glasses.[206] A similar behaviour can be visualised by considering the low tensile stiffness of an aligned sheaf of hay, in which individual strands can easily slide past one another, compared to a randomly packed bale where the network of interlocking strands leads to more efficient stress transfer and a higher effective elastic modulus (Figure 4.7a,b).

A complementary picture of this mechanical model can be constructed from the shear of granular assemblies of rigid rods. Such assemblies are modelled to undergo extensive shear alignment in order to reduce inter-particle contact and reduce the stress required for deformation.[207] As the solid volume fraction of these models increases above 50% (noting that INT fibre packing density is approximately 45-55%), a rapid increase in shear stress occurs due to mechanical percolation through the formation of rigid clusters. Previous modelling has

found that percolation thresholds for rod assemblies increase with alignment[208] and by corollary, at a constant volume fraction, less oriented systems are more networked. A two-dimensional picture of this behaviour is found in log driving where aligned logs can easily flow, whereas misorientated groups can form stiff, rigid clusters leading to jams (Figure 4.7c,d).



Figure 4.7. Photographic analogies of stress transfer models in rod and fibre assemblies. (a) Bundles of aligned straw, which can be easily pulled apart along their axis in tension and (b) a randomly packed straw bale which has a stiffer network structure. (c) Shear aligned logs flowing freely in a river and (d) a log jam forming a rigid cluster due to misorientation. Sources: (a) adapted from *Covoni di grano* by Monica Arellano-Ongpin under the CC BY 2.0 license. (b) adapted from *Hay Bales* by leppre under the CC BY 2.0 license. (c) *Log Drive by Coos Bay LC on E Fork Coquille River* by U.S. Forest Service released to the public domain. (d) *St. Croix River log jam* by Sargen released under the CC BY-ND 4.0 license.

Despite the relationship between alignment and elastic modulus, there is no discernible correlation between alignment and tensile strength or ultimate breaking force. This lack of correlation implies that the final failure is less related to the overall microstructure of the

fibres and may instead be driven by point defects created during manual handling or from instabilities in the spinning process.

This orientational dependence is likely more prevalent in these INT fibres than in similar CNT of nanocellulose fibres due to the comparably short aspect ratio and high rigidity of the double-walled INTs. The individual nanotubes are less able to bend and form the necessary links and contacts for frictional load transfer and do not fibrillate in the manner of CNT or nanocellulose bundles. In addition, the coagulation process inherently delivers porous fibres near the mechanical percolation threshold and due to the lack of a matrix, the jamming behaviour is most important to the fibre mechanical properties.

4.4 Summary

A wet spinning technique was developed to produce pure binder-free fibres from imogolite nanotubes, which are analogous but complementary to CNT fibres. A collaborator has worked to develop a synthesis process to produce longer INTs, which have improved spinnability. The absolute mechanical properties of these early-stage fibres are relatively modest (strength ~ 100 MPa, modulus ~ 10 GPa), however they serve as a valuable model for the behaviour of nanomaterial fibres in general.

The importance of shear interactions in load transfer is illustrated by the reduction in stiffness and strength and the change failure mode with increased humidity. A somewhat surprising trend was discovered that fibre stiffnesses were higher in less aligned fibres. This finding can be attributed to the relatively low aspect ratio and high rigidity of the INTs, which makes them unable to bend and form contacts. As such, a degree of misalignment is required for INTs to entangle and interlock to form a stiff network in the relatively porous fibres.

INTs are an experimentally convenient analogue for CNTs, as the larger X-ray scattering cross-sections and their diametral uniformity aids the use of X-ray techniques to study the fibre structure. Additionally, they are optically transparent enabling (polarised) optical techniques to image fibres throughout processing. This possibility for *in situ* imaging is explored in the next chapter as a method to optimise the solution spinning process.

5 *In situ* investigation of INT fibre spinning

Parts of this chapter, including figures and text, are adapted from a manuscript currently in preparation. Where relevant, the research contributions of co-authors are indicated in the text.

Following from the development of a wet spinning process for INTs and the characterisation of these new fibres in Chapter 4, it is desired to use INTs as an analogue material to further understand the solution phase processing of nanotubes. In this chapter, *in situ* POM is used to visualise INT spinning using various spinnerets and flow rates, obtaining an understanding of how the rheology of the nanotube solutions and the flow patterns in a spinneret affects the alignment of nanotubes in wet spinning.

In addition, improvements to the wet spinning process are sought to increase the consistency of fibre properties. The washing step in particular is investigated in detail and found to have a critical role in the fibre properties, due to its effects on INT packing density and alignment.

5.1 Rheology and flow alignment of INT solutions

5.1.1 INT rheology

INT solutions were prepared with a range of concentrations varying from 1 to 11 mg mL^{-1} (volume fraction 0.037% to 0.41%). This range of concentrations represents the full range from isotropic to fully liquid crystalline phases (Figure 5.1). At 1 mg mL^{-1} the solution is completely isotropic with no birefringence visible between crossed polars, whilst at 3 mg mL^{-1} the presence of small birefringent tactoids can be faintly identified within the INT solution. At 5.5 and 11 mg mL^{-1} widescale orientational ordering can be seen. The optical textures of the are challenging to interpret but may be that of a nematic or a columnar phase which has been previously observed in INT solutions.[177] Small angle X-ray scattering experiments conducted by collaborator, Erwan Paineau, confirmed that the 5 mg mL^{-1} solution is a nematic phase, whilst at 11 mg mL^{-1} a columnar phase forms (Figure A5). It is unclear how quickly these phases form and when initially loading into a capillary the liquid crystalline solutions appeared to flow align along the capillary axis, with the domain structures forming over the course of a few days. Following this observation, it is likely that the particular columnar or nematic phases

are disrupted during loading of the spinning dope in the syringe barrel and may have little impact on the downstream spinning.

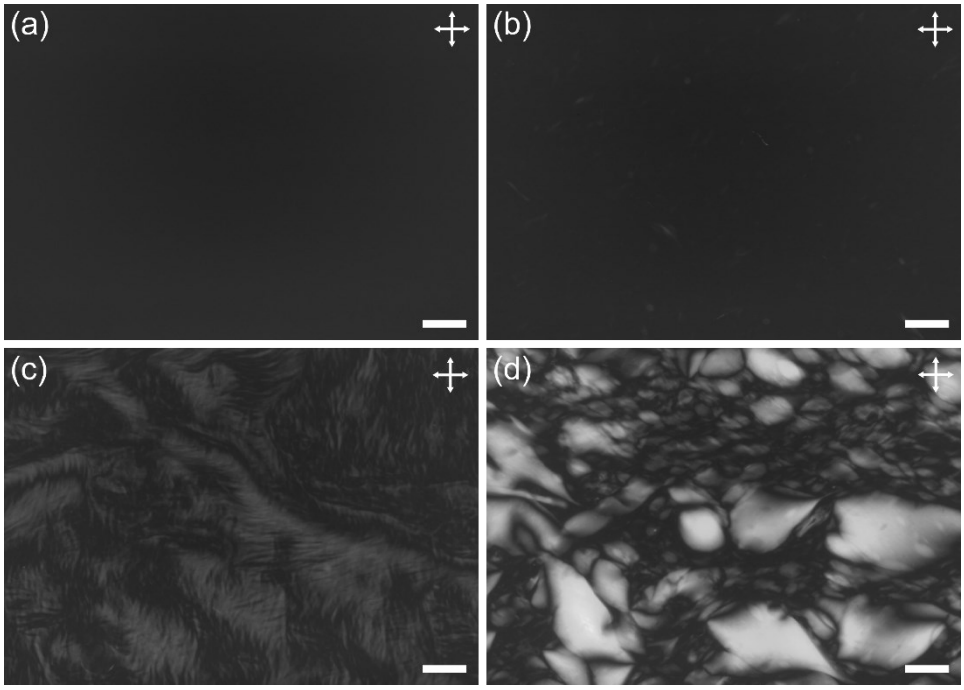


Figure 5.1. Polarised optical micrographs of INT solutions with mass loading of (a) 1, (b) 3, (c) 5.5 and (d) 11 mg_{INT} mL^{-1}. Samples were collected in rectangular capillaries (thickness 200 µm) and allowed to relax for 1 month. White arrows indicate polariser and analyser directions. Scale bars 200 µm.

The rheological flow curves of these INT solutions were determined by capillary rheometry using the equipment developed during this work (section 3.3.6, p.73). The pressure drop across a PEEK capillary tube (inner diameter 178 µm, length 50 cm) was measured at various flow rates between 0.025 and 2 mL hr^{-1}. The Rabinowitch correction was applied to determine the wall shear rate and viscosity.

All of the INT solutions are shear thinning and exhibited power-law behaviour in the shear range relevant for wet spinning (100 to 1000 s^{-1}) which can be modelled as

$$\eta = K\,\dot{\gamma}^{n_i-1} \tag{11}$$

where η is the shear viscosity, $\dot{\gamma}$ is the shear rate, K is a flow consistency index and n_i is a flow behaviour index where values of n_i less than unity correspond to shear thinning.

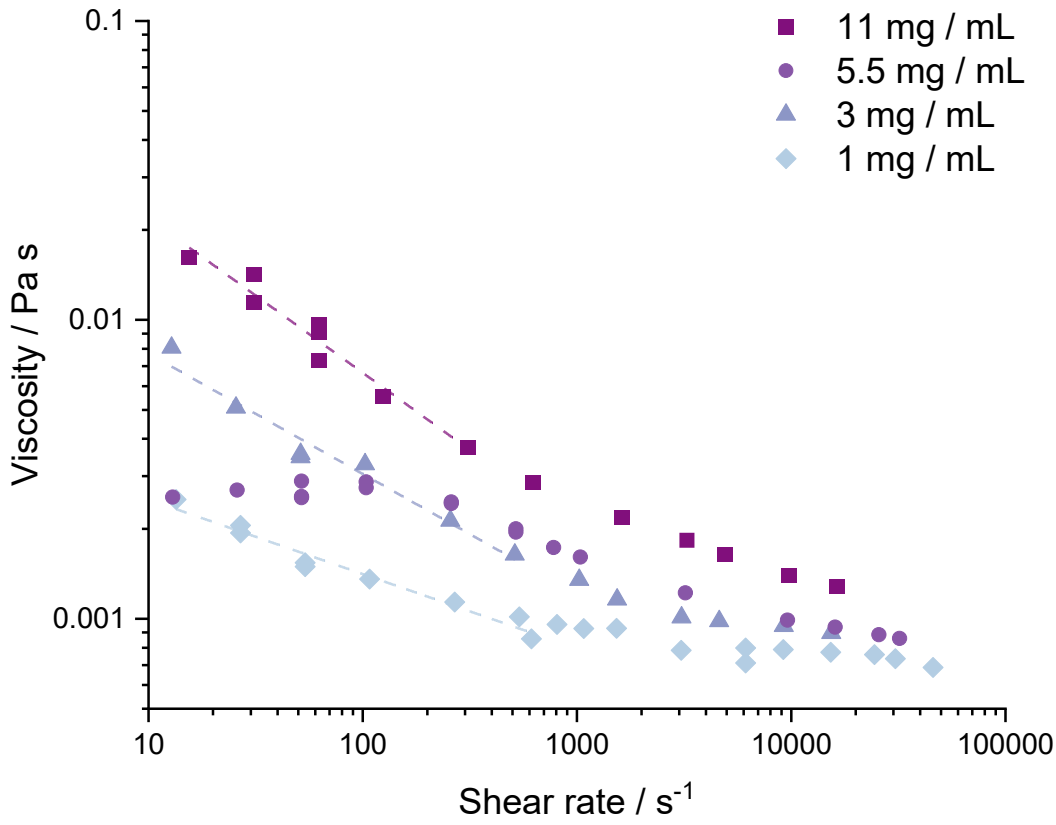


Figure 5.2. Flow curves of INT solutions determined by capillary rheometry. Dashed lines are generated by linear fits to the straight line parts of the log-log data, corresponding to a power law fluid.

The velocity profile of power law fluids flowing through cylindrical pipes is given by[209]

$$v_z(r) = \left(\frac{3n_i + 1}{n_i + 1}\right) U \left[1 - \left(\frac{r}{R_c}\right)^{\frac{n_i+1}{n_i}}\right] \quad (12)$$

where $v_z(r)$ is the fluid velocity in the flow direction at a radius r from the centre of a cylindrical pipe with radius R_c, U is the mean fluid velocity and n_i is the flow behaviour index from equation (11). For the nematic 11 mg_{INT} mL^{-1} solution, a power law fit is obtained for shear rates between 10 and 1000 s^{-1} with a flow behaviour index, n_i, of 0.48 (Figure 5.3a). The corresponding velocity profile approaches plug flow with minimal shear occurring in the core of the capillary and extensive shear at the capillary walls (Figure 5.3b).

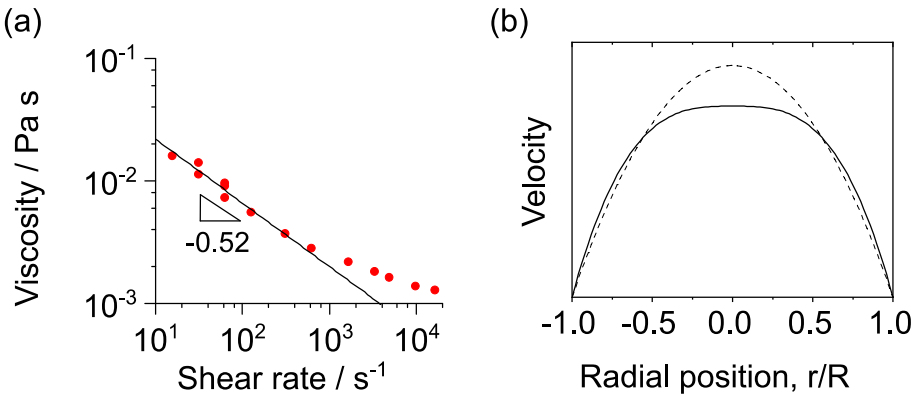


Figure 5.3. (a) Viscosity of 11 mg mL^{-1} solution of INTs in water. (b) Predicted velocity profile of 11 mg mL^{-1} INT solution flowing in a cylindrical pipe (solid line) compared to a Newtonian fluid (dashed line).

5.1.2 Flow alignment in cylindrical channels

The alignment of INTs in a solution injected through a capillary can be visualised using polarised optical microscopy. When the polariser and analyser are crossed at 45° to the capillary axis, INTs aligned either along or perpendicular to the capillary axis will produce a bright birefringent signal whilst isotropic regions and those aligned with either the polariser or the analyser will remain dark.

In cylindrical capillaries, bright regions of aligned INTs are clearly visible at the capillary walls, whilst a less aligned core translates down the centre of the channel with no visible shear (Figure 5.4). This flow behaviour was observed across the range of flow rates from 0.5 to 10 mL hr^{-1}. The alignment was not consistent and likely contains some history of the domain structure of the nematic solution in the syringe barrel. In general, the core of the flow was dark to varying degrees, indicating misalignment, but more aligned regions can sporadically be seen.

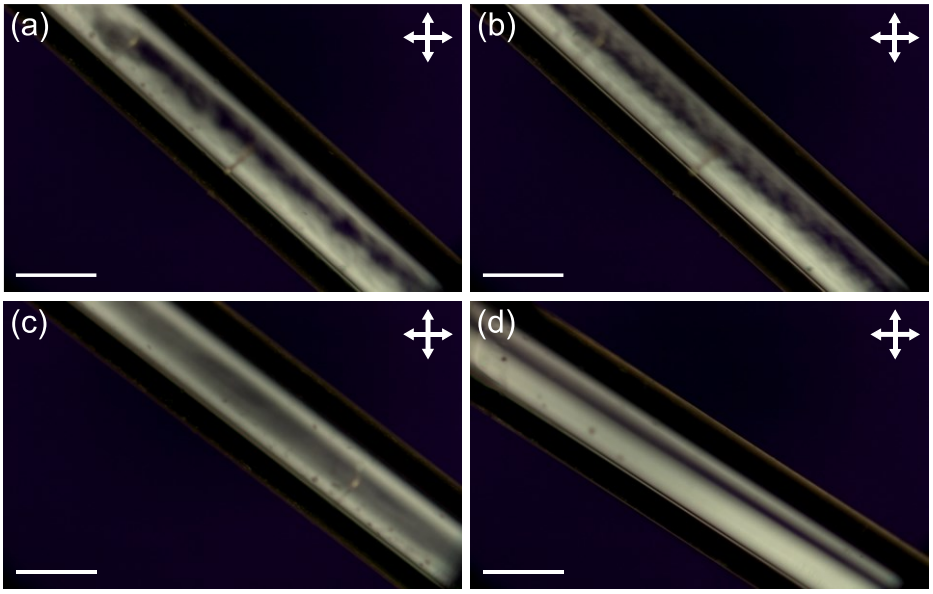


Figure 5.4. Polarised optical micrographs of INT solution flowing through a cylindrical capillary with an inner diameter of 390 μm at (a) 0.5, (b) 1, (c) 3 and (d) 10 mL hr^{-1}. Note that at higher flow rates distinct regions appear as streaks due to exposure time and frame rate limitations of the microscopy videos. White arrows indicate polariser and analyser directions. Scale bars 500 μm.

5.1.3 Flow alignment in tapered channels

In order to obtain a more uniform and consistent mesostructured spinning dope, a tapered channel was implemented. The tapered channel leads to a complex blend of shear and extensional flows as the fluid is sheared by the capillary walls whilst simultaneously being accelerated axially in the taper due to the decreasing channel cross-section. Two tapered glass capillaries were prepared with similar taper semi-angles (~8°) but different taper lengths (4 and 7 mm). In order to further identify the flow alignment of the INTs, a full-wave λ plate was added to the optical path with the slow axis perpendicular to the capillary axis (Figure 5.5a). This optical arrangement produces colour contrast in the optical micrographs such that the isotropic material is magenta pink, regions with INTs aligned along the capillary axis are yellow and regions with INTs aligned perpendicular to the capillary are blue. The colours seen can be interpreted to retardation values using a Michel-Lévy chart (Figure 3.6, p.61).[163] When the slow axes of the INTs (the INT cylindrical axis) and the λ plate are aligned, the overall retardation of the sample increases producing a blue colour. When the INTs are perpendicular to the slow axis of the λ plate, the overall retardation is reduced, and the colour shifts to yellow.

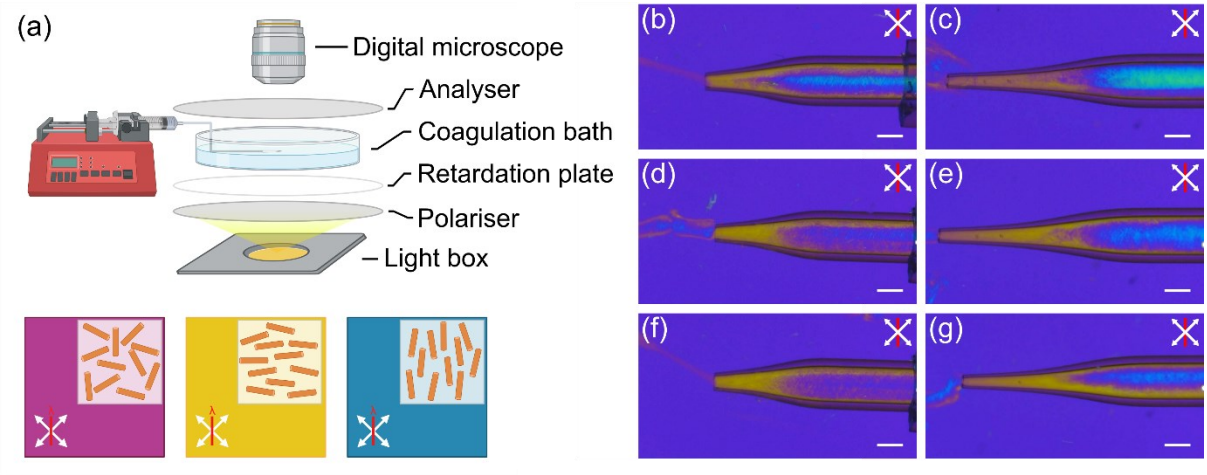


Figure 5.5. (a) Schematic of optical arrangement for *in situ* observation of INT alignment and illustration of magenta, yellow and cyan colour contrast for isotropic INTs, and INTs aligned parallel and perpendicular to the slow axis of the retardation plate. Created with BioRender.com. (b-g) Polarised optical micrographs of INT solutions flowing through tapered glass nozzles at (b,c) 1, (d,e) 5 and (f,g) 10 mL hr^{-1}. White arrows indicate the polariser and analyser directions and red lines indicate the slow axis direction of a 560 nm retardation plate. Scale bars 1 mm.

In the parallel section before the taper, the edges are bright yellow indicating alignment along the capillary axis due to the high shear (Figure 5.5b-g). Meanwhile, the core undergoes plug flow with some tendency to align perpendicular to the capillary. At the taper, extensional flow commences and deformation can be seen throughout the capillary section which leads to flow alignment throughout the spinning dope. The whole of the INT solution emerges as a bright yellow region which is visibly homogeneous and consistent with time. INT alignment occurs within the taper region in all cases, although at higher flow rates the alignment occurs over a shorter channel length.

The elongational strain rate in the taper of the capillary, $\dot{\epsilon}_z$, is given by[210]

$$\dot{\epsilon}_z = \frac{2\,Q\tan(\alpha)}{\pi\,{R_c}^3} \tag{13}$$

where Q is the volumetric flow rate of spinning dope, α is the taper semi-angle and R_c is the radius of the capillary. The elongational strain rate therefore increases as the spinning dope travels along the taper due to the decreasing diameter. A critical elongational strain rate for full flow alignment can be estimated by identifying the diameter of the capillary at the point where the spinning dope is uniformly yellow. Across the range of flow rates studied, the critical elongational strain rate was between 1 and 2 s^{-1}.

Table 4. Estimated elongational strain rate for complete flow alignment of INT solutions at varying flow rates.

Flow rate / mL hr^{-1}	Diameter at full alignment / mm	Critical elongational strain rate / s^{-1}
1	0.58 ± 0.02	1.03 ± 0.11
5	0.96 ± 0.04	1.13 ± 0.14
10	1.04 ± 0.10	1.8 ± 0.5

The diameter at the orifice of the 4 mm long taper is 0.45 mm, resulting in elongational strain rates between approximately 2 and 20 s^{-1}. The 4 mm long nozzle was selected for future fibre spinning experiments, as it was sufficiently long to induce complete alignment and more robust for repeated use.

It may be possible to further study the effect of elongational strain on flow alignment by using carefully designed nozzles. The elongational strain rate in hyperbolic nozzles is consistent along their length[210] and so the effect of a constant elongation rate may be assessed and simply manipulated by varying the volumetric flow rate. However, fabricating nozzles with carefully controlled taper angles is challenging and the creation of custom taper profiles was not possible in this work.

5.1.4 Impact of draw on INT alignment during spinning

Without draw, the proto-fibre decelerates rapidly on entering the static coagulation bath. This inertial effect in combination with die swell leads to a sudden misalignment of the INTs, which can be clearly seen as a colour change in the POM images (Figure 5.6a). Applying draw with a take-up roller prevents the deceleration and maintains a tensile stress in the proto-fibre during coagulation which preserves the alignment of the INTs (Figure 5.6b-d). Take-up at higher draw ratios leads to deformation and thinning of the fibre close to the spinneret nozzle. After the INT proto-fibre has exited the spinneret, it is more difficult to identify the optical retardation due to light scattering at the edges of the fibre and imperfect alignment of the drawn thread with the capillary axis. In addition, as the fibre thins the optical retardation is reduced for a given birefringence, making quantification more challenging.

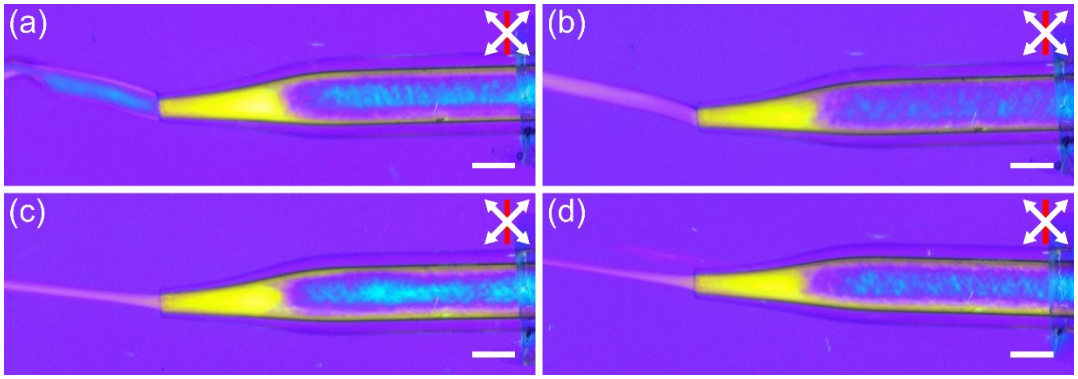


Figure 5.6. *In situ* polarised optical micrographs of INT fibre spinning with (a) no draw applied and (b-d) a draw ratio of (b) 1, (c) 3 and (d) 5. White arrows indicate the polariser and analyser directions, and red lines indicate the slow axis direction of a 560 nm full-wave retardation plate.
Scale bars 1 mm.

5.2 Properties of INT fibres with varied draw ratio and constant washing time

INT fibres were spun with draw ratios of 1, 2, 3, 4 and 5 and then washed in deionised water by dipping the fibres into a beaker two times for 3 s. The fibres were then hung to dry with a small weight (~20 mg) under ambient conditions. The mechanical properties of the resulting fibres were assessed using a single filament tensile test at controlled humidity of 10% and 40% RH.

As expected, the diameter of the fibres was smaller for higher draw ratios, but the packing density was not uniform across the series (Figure 5.7a,b). The packing density for DR 1 was around 25%, rising to 60% for DR 4 and then decreasing to 47% for DR 5. It was observed that the fibres prepared at DR 1 appeared wet and glistened under laboratory illumination, showing that the $CaCl_2$ coagulant was not fully removed during the washing. For gel fibres with different diameters, a consistent washing time does not have equivalent impact due to the longer diffusion distances required to remove salt from the core of the larger fibres. Hence, the fibres spun with the higher draw ratios have had a greater 'effective wash' which then leads them to dry and densify to a greater degree as they contain less remnant hygroscopic salt.

As observed in previous experiments (section 4.3.2, p.83) the stiffness is higher and the strain at failure is lower at 10% RH compared to 40% RH, due to the reduction in moisture mediated sliding. The tensile strength, tenacity and modulus follow the trend in packing density across

the draw ratios, whilst the strain at failure shows the inverse relationship (Figure 5.7c-f). The densification of the INT fibres during drying is critically important to their mechanical properties with denser arrangements being stronger and stiffer but failing at a lower strain, being less able to undergo plastic deformation. It is striking that the tenacity of the fibers increases with packing density. This correlation shows that the increased strength of the more highly packed fibres is not simply due to a reduction in the cross-sectional area but due to an improved efficiency of load transfer within the INT network.

Although this experiment shows that achieving a high packing density is crucial to attaining good fibre properties, it is not possible to identify an optimal draw ratio as the efficiency of washing changes across the draw ratio series. In order to make a fair comparison between fibres spun with differing draw ratios, it was necessary to characterise the washing process and identify conditions which lead to equivalent degrees of washing.

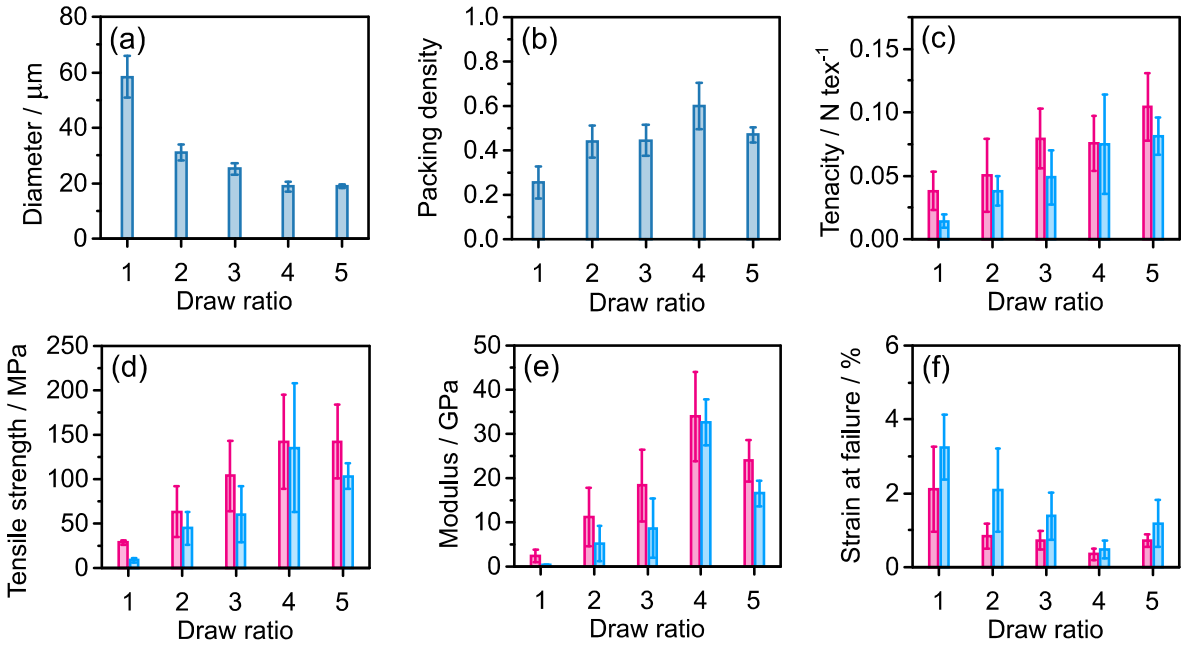


Figure 5.7. Structural and mechanical parameters of INT fibres prepared by coagulation in $CaCl_2$ with a tapered spinneret at varying draw ratio followed by washing in DI water (2 x 3 s). Magenta bars indicate samples tested at 10% RH, cyan bars for samples tested at 40% RH. Error bars show ± 1 standard deviation.

5.3 Washing strategies for microstructural control of INT fibres

5.3.1 Impact of washing on densification and alignment in INT fibres

Fibres collected directly from a $CaCl_2$ coagulation bath cannot fully dry under ambient conditions due to the presence of the hygroscopic salt within them (Figure 5.8a). The unwashed fibres are visibly wet with a glistening surface and are relatively fragile to handle. As described in Chapter 4, washing with water can be used to remove salt from the gel fibres, enabling full drying and densification. However, washing in water was found to solubilise the INTs in the gel fibres leading to swelling and defibrillation which causes the fibres to become significantly weaker and more challenging to handle. Preliminary trials indicated that after 1 minute of soaking, it is not possible to remove a continuous piece of fibre from a washing bath and after 10 minutes the fibre is almost completely dissolved. In order to further understand microstructural changes during washing, more detailed observations of the fibre during washing were made using *in situ* POM (Figure 5.9). After just 10 s of immersion the gel fibres swell compared to their initial state, and this swelling further increases over time with defibrillation of the fibre visibly occurring after 5 minutes. During this washing process, the intensity of the birefringence colours decreases, indicating a reduction in retardation which is likely contributed to by both an increase in the fibre diameter (and corresponding decrease in INTs in the light path) and a reduction in alignment.

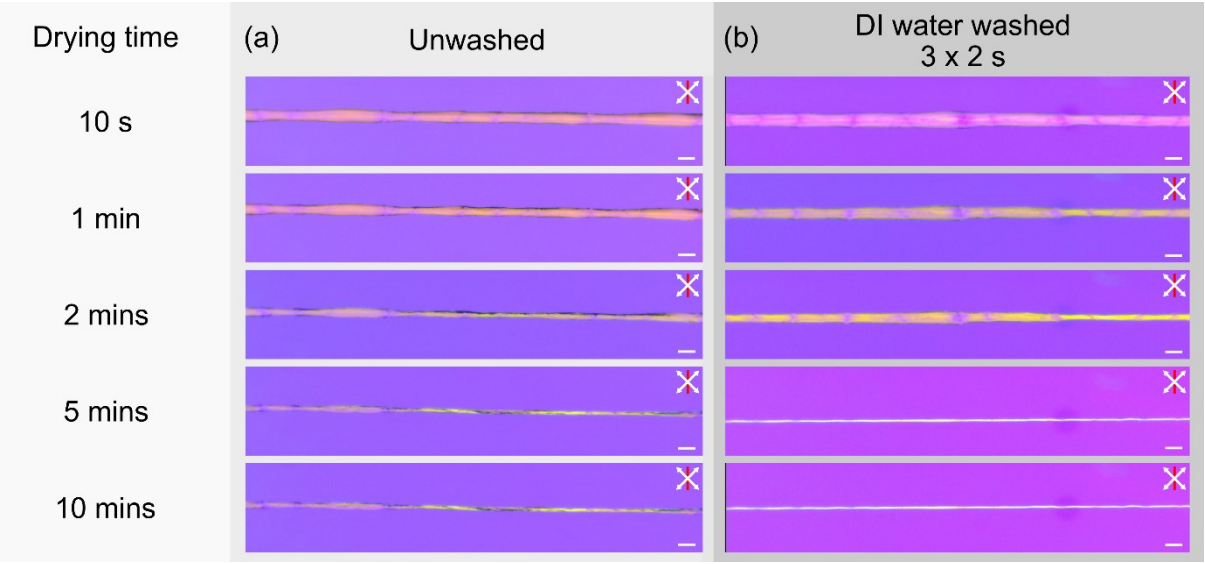


Figure 5.8. *In situ* polarised optical micrographs of INT fibres drying in ambient conditions (a) with no washing and (b) after washing by immersion in DI water for 3 x 2 s. White arrows indicate polariser and analyser directions and red lines indicate the slow axis direction of a 560 nm full-wave retardation plate. Scale bars 500 µm.

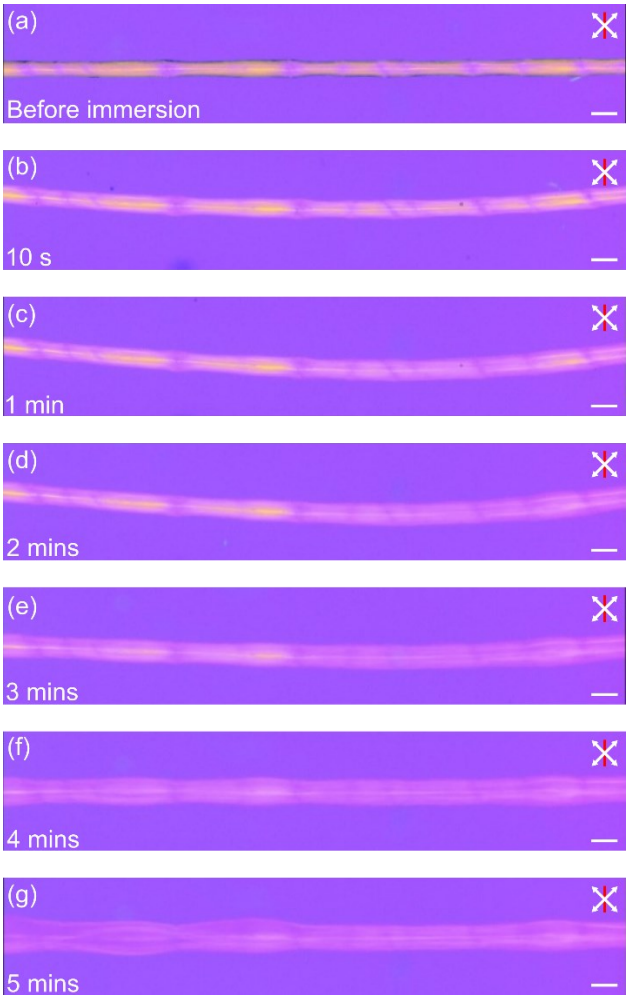


Figure 5.9. Polarised optical micrographs of INT fibre spun with a draw ratio 2 during immersion in DI water. White arrows indicate polariser and analyser directions and red lines indicate the slow axis direction of a 560 nm full wave retardation plate. Scale bars 500 μm.

To observe the impact of varying washing times on the densification and final microstructure, INT fibres were spun at two different draw ratios (DR 2 and DR 4), washed by dipping into DI water for varying times, dried in ambient conditions, and then imaged using POM (Figure 5.10). Fibres washed for 5 s did not completely dry and had a larger diameter and a glistening wet appearance under the microscope. For longer washing times the fibres were able to better densify during drying, resulting in a smaller dry fibre diameter. Distinctive changes to the birefringence colours occur at 20 s for DR 2 (Figure 5.10a) and 10 s for DR 4 (Figure 5.10b). As the washing time is increased the total retardation with the fibre positioned at 45° to the crossed polars increases from ~200 to ~500 nm. The increase in retardation likely arises due to the improved densification at longer washes, where a greater quantity of INTs are in the light path for the thinner, more highly packed fibres. At the same time, after longer washes there is significantly more birefringent signal when the fibre is positioned parallel to

the analyser, indicating a greater number of INTs misaligned with the fibre axis. These changes show two conflicting effects that, with longer washing times, the dried fibres reach increased INT packing density but may have a greater number of INT misaligned to the fibre axis.

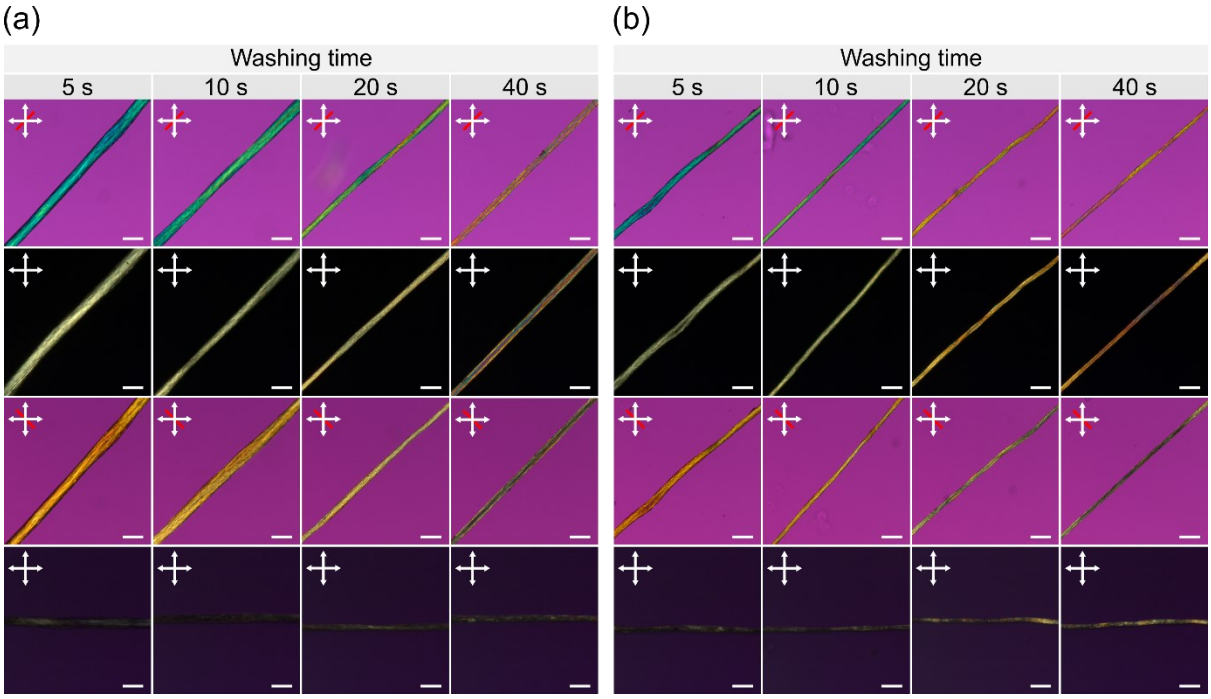


Figure 5.10. Polarised optical micrographs of dry INT fibres produced with (a) DR 2 and (b) DR 4 washed by immersion in water for varying periods of time. White arrows indicate the polariser and analyser directions, and red lines indicate the slow axis direction of a 560 nm retardation plate. Scale bars 100 μm.

The simultaneous increase in packing density and decrease in alignment may seem counter-intuitive, as it is known that aligned rigid rods can pack more efficiently than random arrangements. However, it is important in this case to recognise that the orientational rearrangement of the INTs occurs alongside the removal of highly hygroscopic salt from the fibres. The more aligned fibres from shorter washing times are swollen with adsorbed water which leads to their lower packing density.

The POM observations indicate that two key processes may be occurring during washing: the diffusion of $CaCl_2$ out of the gel fibre and structural rearrangement of the INTs during their solubilisation. The relative balance of these processes may be compared by considering the characteristic time scales over which they occur.

The characteristic diffusion time for calcium and chloride ions to be removed from the gel fibre can be estimated by modelling the diffusion of the salt as the random walk of a Brownian

particle in 2 dimensions (corresponding to the radial plane of the fibre). The root mean squared displacement for this random walk is given by,[211]

$$\langle x^2 \rangle^{\frac{1}{2}} = \sqrt{4\,D\,t} \tag{14}$$

where D is the diffusion coefficient and t is the diffusion time. We can estimate the characteristic time as that required for the root mean squared displacement to be equal to the initial gel fibre diameter (319 and 226 µm for DR 2 and DR 4 respectively). Using 1.2×10^{-9} m^2 s^{-1} as the diffusion coefficient for $CaCl_2$ yields characteristic diffusion times of 21 and 11 s for DR 2 and DR 4.

The characteristic timescale for orientational rearrangement can be estimated as $1/D_r$ where D_r is the rotational diffusion coefficient for the INTs in the fibre. The rotational diffusion coefficient for a semi-dilute suspension of thin rigid rods has been derived by Doi[212] as,

$$D_r = \frac{k_B T \ln\left(\frac{L_r}{d_r}\right)}{\eta_s\, {c_n}^2\, {L_r}^9} \tag{15}$$

where k_BT is the Boltzmann constant multiplied by temperature, L_r and d_r are the length and diameter of the rods, η_s is the solvent viscosity and c_n is the number concentration of the rods. In this case, we consider that the solvent viscosity is 1 mPa s (water) and the rod concentration is equivalent to that of the spinning dope. The rod number concentration for a given INT mass loading, c_{dope}, depends on the assumed length of the INTs as,

$$c_n = \frac{4\,c_{dope}}{\rho_{INT}\,\pi\,{d_r}^2\,L_r} \tag{16}$$

where ρ_{INT} is the envelope density of the INTs (2.7 g cm^{-3}[192]). The rotational diffusion coefficient can then be written in the form,

$$D_r = \frac{k_B T\,{\rho_{INT}}^2\,\pi^2 {d_r}^4 \ln\left(\frac{L_r}{d_r}\right)}{16\,\eta_s\,{c_{dope}}^2\,{L_r}^7} \tag{17}$$

This expression is strongly dependent upon the INT length. For 600 nm long INTs, the rotational relaxation time is around 120 s whilst for shorter INTs (250 nm) the relaxation time is around 0.3 s. Although there is a very large spread in these estimated relaxation times it is clear that the orientational rearrangement of the INTs in the fibres may occur over similar timescales to the washing process.

These estimates show that the diffusion of salt from the gel fibres and orientational rearrangement occur over very similar timescales and as such it is challenging to decouple these two processes experimentally. In addition, the solubilisation of the INTs which enables the structural rearrangement may only occur alongside the removal of the coagulating salt, further linking the two effects.

As the degree of washing is intrinsically linked to the diffusion of $CaCl_2$ from the gel fibres, the degree of washing can be represented by the diffusion distance divided by the gel fibre diameter. Following equation (14) the root mean squared diffusion distance is given by,

$$\langle x^2 \rangle^{\frac{1}{2}} = \sqrt{4\,D\,\left(\frac{A_{nozz}\,L_{bath}}{Q\;\;DR}\right)} \tag{18}$$

where A_{nozz} is the nozzle orifice area, L_{bath} is the length of the washing bath, Q is the volumetric flow rate of spinning dope and "DR" is the spin draw ratio. Meanwhile the gel fibre diameter is given by,

$$d_{gf} = \sqrt{\frac{4\,A_{nozz}}{\pi\;DR}} \tag{19}$$

As such, in this washing arrangement, the degree of washing is explicitly controlled by the length of the washing bath and the extrusion rate of the spinning dope as,

$$\frac{\langle x^2 \rangle^{\frac{1}{2}}}{d_{gf}} = \sqrt{\frac{L_{bath}\,\pi}{Q}} \tag{20}$$

which is independent of the spin draw ratio enabling fair comparison between different draw ratios.

Hence to obtain more consistent fibre properties, an in-line washing bath with controlled length was introduced to the wet spinning apparatus (Figure 3.1). In order to change the washing time, the length of the washing bath could be varied by adjusting the guide rods. Additionally, a take-up spool consisting of five rods separated 42 mm apart was used to collect the washed fibres, such that they dried at constant strain.

Fibres were spun using this arrangement with a tapered spinneret nozzle (451 µm orifice diameter) at draw ratios of DR 2 and DR 4 and washing bath lengths of 15, 30 and 40 cm. These lengths correspond to washing times varying between 8 and 23 s for DR 2 and 4 and

11.5 s for DR 4. It was not possible to use longer washing baths due to weakening of the gel fibre and subsequent filament breakage on the line. The fibres were characterised by X-ray scattering and the INT alignment was quantified with Hermans' orientation parameter as before (section A6, p.197). Although there is some considerable uncertainty in the measurement of alignment, for both draw ratios the degree of orientation tends to decrease with longer washing times, confirming the misaligning effect of washing in DI water (Figure 5.11). When plotted as a function of washing time, it can be seen that the thinner DR 4 fibres misalign more quickly than the thicker DR 2 gel fibres. By instead quantifying the degree of washing as the diffusion distance divided by the initial gel fibre diameter, the data reduces to a master curve suggesting that the degree of structural rearrangement in the fibres is intrinsically linked to the $CaCl_2$ diffusion (Figure 5.11b). It should be noted here that the initial spin draw ratio appears to have little impact on the degree of alignment within the fibres, with the exception of affecting the downstream washing process. This independence may be because the extensional deformation of the gel fibre once it has exited the spinneret is predominately driven by longitudinal slip of the already aligned INTs, rather than some affine deformation which reorients the nanotubes.

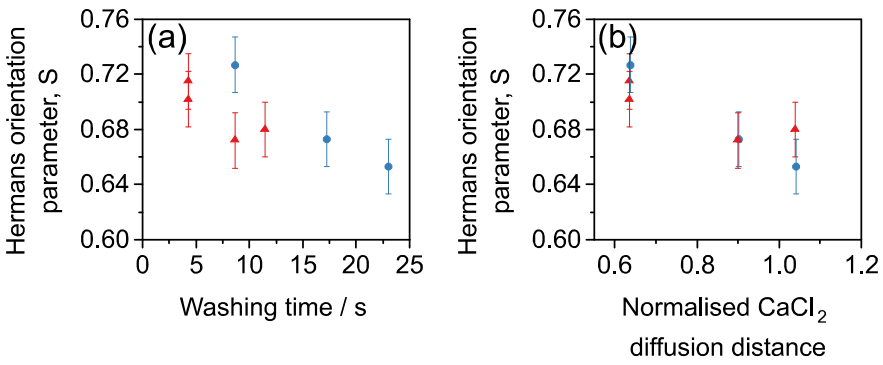


Figure 5.11. Hermans orientation parameter for INT fibres spun with a tapered spinneret at (blue circles) DR 2 and (red triangles) DR 4 as a function of (a) the washing time and (b) the $CaCl_2$ diffusion distance divided by the initial gel fibre diameter.

5.3.2 Mechanical properties of washed INT fibres

The mechanical properties of these INT fibres were strongly related to the degree of washing. Using longer washing baths resulted in significantly stiffer and stronger fibres, which tended to have smaller strains to failure (Figure 5.12). For DR 4, the elastic modulus increased from 4.3 ± 1.7 to 23 ± 2 GPa and the strain at failure decreased from 1.8 ± 0.7 to 1.3 ± 0.3% as the

washing bath length increased from 15 to 40 cm (Table 5). As the bath length increased from 15 cm to 30 cm, the packing density increased from ~20% to ~40% but further increases to the washing length did not result in greater packing density, nor did it have a measurable effect on the alignment. The increase in stiffness and strength from 30 to 40 cm washing lengths cannot be easily ascribed to any particular structural parameter but may be due to a further reduction in moisture content of the dried fibres. These data agree with the previous observations that less aligned INT fibres are stiffer but now illustrate how the washing step can be used influence the fibre microstructure and its properties. Stress transfer is limited within these fibres which are comprised of short, rigid nanotubes and in highly aligned fibres, ductile sliding can occur easily without arrest. In contrast, the less aligned structures can more easily form a jammed network as described previously (section 4.3.3, p.85).

The trends of packing density, alignment, stiffness, strength, tenacity and strain-at-failure with the washing bath length are similar between the two draw ratios, further supporting that the length of the bath, which controls the degree of washing as in equation (20), is the crucial process factor and by comparison the actual draw ratio is less influential. Although a minor effect compared to the degree of washing, the DR 4 fibres had higher strength and modulus for most spinning conditions. It was qualitatively found that it was easier to produce the 40 cm washing bath fibres at DR 4 than DR 2 as the faster line speed was easier to handle manually. This easier processing may lead to more consistent fibres with fewer defects and hence improved strength.

In an attempt to decouple the effect of alignment and packing fraction, some INT fibres were spun using a cylindrical capillary for the spinneret. As the *in situ* imaging of INT flow in cylindrical capillaries showed a core of misaligned spinning dope (Figure 5.4), it was expected that fibres spun from cylindrical spinnerets would have a lower average degree of alignment compared to those spun through tapered nozzles, particularly at short washing lengths. For comparison, these fibres were spun through a cylindrical channel (diameter 377 µm, length 20 mm) using the same experimental conditions. The properties of fibres spun with the cylindrical spinnerets did not have the strong washing length dependence as previously seen and there was significantly more variation in mechanical properties within each sample set compared to the fibres spun using the tapered spinneret (Figure 5.13). The inconsistency of the properties is likely due to inhomogeneity of the spinning dope during spinning. The

alignment of the spinning dope in the capillary is highly variable and is likely influenced by the initial domain structure within the syringe barrel as previously shown using POM (section 5.1.2, p.92). As such, some regions of the spun fibre are expected to be highly aligned and others highly misaligned, explaining why the tensile properties are so variable between samples spun using the same conditions. Surprisingly, the degree of alignment in these fibres was similar to those spun with tapered spinnerets with calculated order parameters between 0.66 and 0.72 compared to 0.65 to 0.73. The alignment may have arisen from the extensional draw which, although seemingly ineffective on the uniformly aligned proto-fibres from the tapered spinnerets, could lead to some alignment in this case. The calculated order parameters did not follow the expected trend with washing time and instead were higher for longer washing times (Figure 5.13c). This outcome may be due to statistical sampling as the XRS patterns were only collected at one position on these fibres but further study may be justified to more clearly understand this result. The packing density of these samples was also more variable, perhaps indicating that the inhomogeneous alignment along the fibres influences the washing and drying processes, leading to variable densification.

The absolute properties of the best cylindrical spinneret fibres were lower than those spun with the tapered spinneret with a tensile strength of 125 ± 27 MPa for DR 4, 30 cm bath compared to 170 ± 30 MPa for DR 4, 40 cm with the tapered spinneret. These results illustrate the importance of controlling the alignment of INTs in the spinning dope. With the cylindrical spinneret there is limited control of the microstructure of the INT fibres and as a result the fibre properties are highly variable. Using a tapered spinneret results in a significantly more consistent and homogeneous microstructure in the proto-fibre which can then be modified by a careful washing treatment to yield optimum properties.

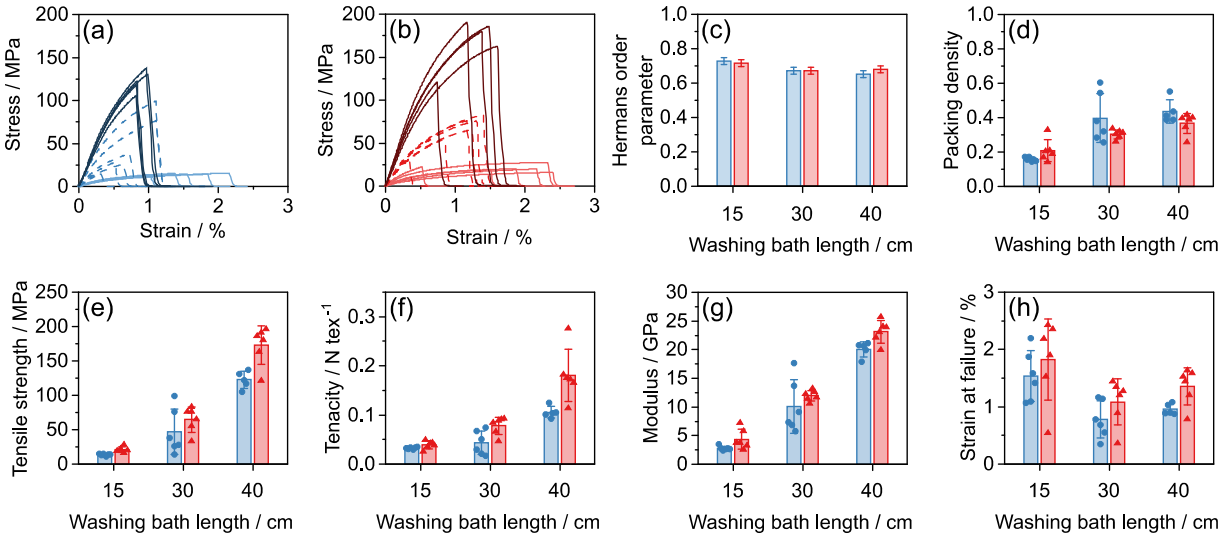


Figure 5.12. (a,b) Stress strain curves for INT fibres spun at (a) DR 2, (b) DR 4 using a tapered spinneret. Dark solid lines 40 cm washing bath, medium dashed lines 30 cm washing bath, light solid lines 15 cm washing bath. (c-h) Structural and mechanical parameters for (blue) DR 2 fibres and (red) DR 4 fibres with varying washing bath lengths. Error bars indicate 1 standard deviation.

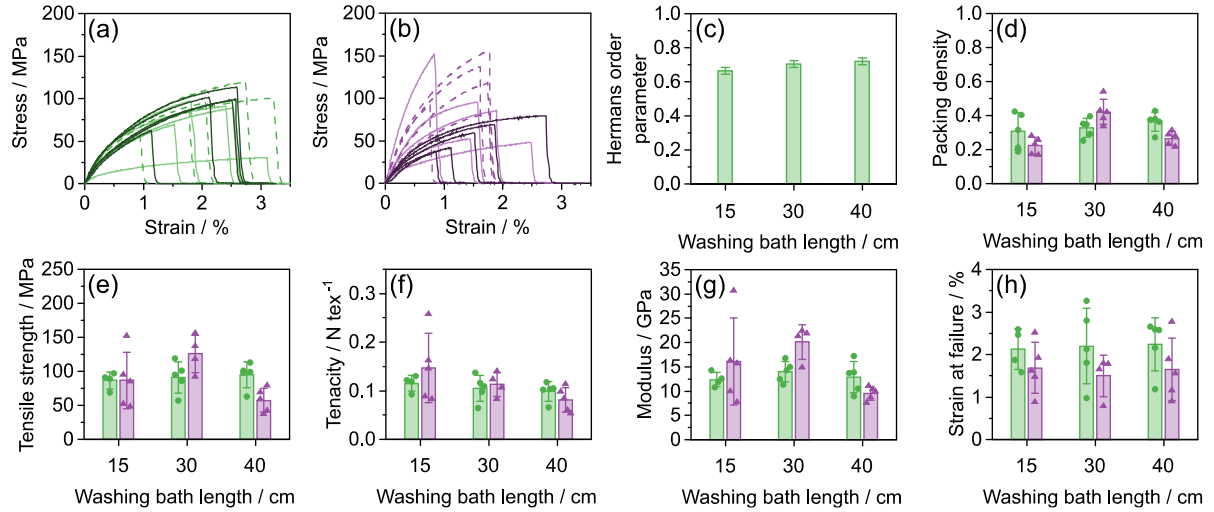


Figure 5.13. (a,b) Stress strain curves for INT fibres spun at (a) DR 2, (b) DR 4 using a cylindrical spinneret. Dark solid lines 40 cm washing bath, medium dashed lines 30 cm washing bath, light solid lines 15 cm washing bath. (c-h) Structural and mechanical parameters for (green) DR 2 fibres and (purple) DR 4 fibres with varying washing bath lengths. Error bars indicate 1 standard deviation.

Table 5. Properties of wet spun and in-line washed INT fibres produced with tapered spinneret

Draw ratio	Washing bath length	Tensile strength	Elastic modulus	Specific strength	Specific modulus	Density	Failure strain
	cm	MPa	GPa	N tex^{-1}	N tex^{-1}	g_{INT} cm^{-3}	%
2	15	13.5 ± 1.5	2.8 ± 0.4	0.032 ± 0.002	6.5 ± 0.9	0.43 ± 0.03	1.5 ± 0.4
2	30	50 ± 30	10 ± 5	0.04 ± 0.02	9 ± 4	1.1 ± 0.4	0.8 ± 0.3
2	40	123 ± 12	20.0 ± 1.2	0.105 ± 0.012	17.2 ± 1.1	1.18 ± 0.18	0.96 ± 0.09
4	15	21 ± 4	4.3 ± 1.7	0.039 ± 0.008	8 ± 3	0.56 ± 0.17	1.8 ± 0.7
4	30	65 ± 19	11.9 ± 0.9	0.078 ± 0.018	14.4 ± 1.1	0.82 ± 0.07	1.1 ± 0.4
4	40	170 ± 30	23 ± 2	0.18 ± 0.05	24 ± 2	0.99 ± 0.16	1.3 ± 0.3

5.4 Summary

In situ polarised optical microscopy has been used to investigate the alignment of INTs throughout the wet spinning process. The shear thinning nature of INT solutions has been shown to affect flow alignment within cylindrical channels. Significant shear occurs at the capillary walls leading to strong alignment in the flow direction, but limited shear in the centre of the channel means that no flow alignment occurs in this region and instead the orientation of the core of the flow reflects the domain structure of the initial spinning dope. Elongational flow in a tapered channel can efficiently align the INT solutions throughout the cross-section of the fluid, with an elongational strain rate of 1-2 s^{-1} being sufficient to achieve good alignment.

The washing step has been found to be critical to the structure and properties of INT fibres with longer washing times increasing packing density and reducing alignment. The solubilisation of the INT fibres in the washing bath leads to a practical limit to the length of the washing process due to filament breakage; in this case, washing lengths longer than 40 cm were unattainable. Comparisons across fibres with different diameters indicates that the diffusion of $CaCl_2$ out of the gel fibre is the critical process during washing, and smaller diameter fibres therefore need shorter washing times to attain the same structure and properties. Consistent properties in INT fibres are only possible with careful control of the washing process (here with an in-line washing bath) and homogeneous alignment of the spinning dope with a tapered spinneret. The best INT fibres spun in this work have tensile strength of 170 MPa, elastic modulus of 23 GPa, specific strength of 0.18 N tex^{-1}, specific modulus of 24 N tex^{-1} and a failure strain of 1.5%. It is challenging to determine the relative impacts of packing density and alignment on the INT fibre properties as these structural parameters change at similar timescales in the washing process, but it is expected that both will have a strong effect on the formation of networks which aid stress transfer between the relatively short rigid rods in these INT fibres.

6 Cross-linking INT fibres

In previous chapters it was identified that less aligned INT fibres are stiffer than more aligned fibres and this response can be explained by the limited stress transfer between nanotubes in the binder-free fibres. There are distinct benefits to binder-free fibres for applications requiring access to the individual nanotubes such as catalysis, or molecular transport and release. However, it is expected that the mechanical properties of INT fibres may be improved by either adding a matrix binder or by cross-linking the INT network. These locked networks may show the opposite stiffness response with alignment, which is more similar to the standard composite models.

In this chapter, a variety of different linking techniques are tested including ionic (physical) cross-linking, covalent cross-linking by silanisation and dehydration reactions and matrix infusion with polymers.

6.1 Ionic cross-linking of INT fibres

Inspiration for ionic cross-linking was taken from sodium alginate gels which can be cross-linked using salts with divalent cations such as Ca^{2+}. The cross-linked gels form stiffer networks which are more robust and insoluble in water.[213] As the outer surface of the INTs are positively charged it was expected that multivalent anions would induce a similar physical cross-linking process. The presence of ionic cross-linking was tested by injecting a small quantity of INT spinning dope (11 mg mL^{-1}) by hand through a 21 g needle into a vial of coagulant solution prepared from different salts (1 M). The gel fibres were than collected and submerged into a petri dish of deionised water. The robustness of the gel fibres was assessed by gently handling the fibres with tweezers at varying time intervals and the fibres were recorded as either robust or fragile (Table 6). Fibres coagulated using salts with monovalent anions (NaCl and $CaCl_2$) weakened significantly when immersed in water and fractured easily after soaking for 30 seconds and 1 minute respectively. In comparison fibres coagulated using salts with multivalent anions were robust even after prolonged soaking of 30 minutes. The resistance of these fibres to redissolution in water demonstrates the successful physical cross-linking.

Table 6. Stability of INT fibres prepared with various coagulants after washing in water. At each washing time the fibres were recorded as either robust (✓) or fragile (×).

Coagulant	Washing time / minutes				
	0.5	1	5	10	30
Sodium chloride	×				
Calcium chloride	✓	×			
Sodium citrate	✓	✓	✓	✓	✓
Sodium succinate	✓	✓	✓	✓	✓
Sodium tripolyphosphate	✓	✓	✓	✓	✓
Sodium sulfate	✓	✓	✓	✓	✓

Attempts were made to spin INT fibres directly into a sodium succinate coagulation bath, however several challenges occurred during spinning which prevented stable drawing of the fibres. The concentration of the coagulant was varied from 0.001 to 1 M (compared to 2.7 M $CaCl_2$ used previously). The Hardy-Schulze rule predicts that the critical coagulation concentration of an electrolyte is given by the inverse sixth power of the valency of the dominant ion.[214] As such, a sodium succinate concentration of 0.04 M (=$2.7/2^6$ M) is expected to have similar coagulating power as the $CaCl_2$ bath used previously. At high coagulant concentrations (0.1-1 M) rapid coagulation at the spinneret exit led to clogging which disrupted the spinning process. At very low coagulant concentrations (0.001-0.005 M) the proto-fibre coagulated very slowly and underwent significant die swell when exiting the nozzle. The proto-fibres also have a very low gel strength leading to sudden necking during drawing and poor spinning stability. Intermediate concentrations (~0.01 M) were extruded more stably; however the flow from the spinneret was not consistent, with the proto-fibre being drawn with a pulsatile flow causing frequent fracture. The difficulty of spinning with these cross-linking coagulants is probably related to the formation of a stiff, undeformable surface to the proto-fibres which may not occur uniformly along the fibre length. Regions which are rapidly cross-linked cannot deform under the draw and so areas which are less linked are drawn significantly more, leading to the necking and fracture which has been observed. In comparison, spinning in $CaCl_2$ baths is significantly more stable. Using a non-cross-linking coagulant simply destabilises the INT solution and promotes the osmotic

removal of water from the gel fibre without rigidly linking any INTs. As such, the gel fibre can flow and deform readily, enabling stable and uniform draw. These trials indicate that a non-cross-linking coagulant must be used for stable spinning of INT fibres and cross-linking must be performed in a later processing step.

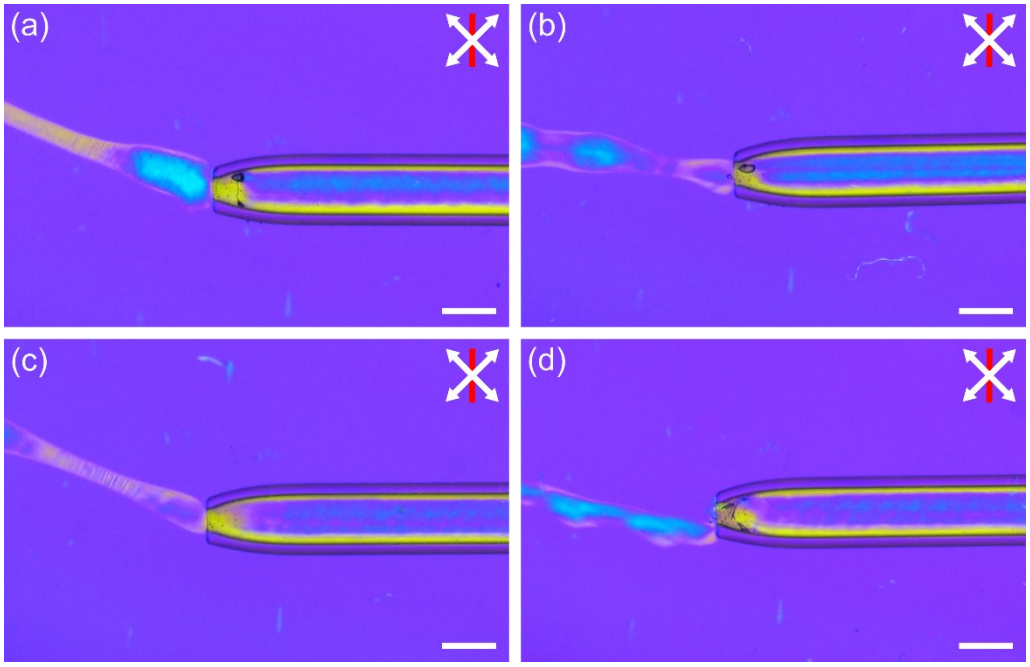


Figure 6.1. *In situ* POM of spinning INT fibres in a sodium succinate coagulation bath with a salt concentration of (a) 1, (b) 5, (c) 10 and (d) 100 mM. At low concentrations (a,b) there is large die swell and weak gel strength leading to necking and failure. At intermediate concentrations (c) the flow is pulsatile with periodic increases and decreases in diameter. At high concentrations (d), the spinneret clogs rapidly disrupting the extrusion. White arrows indicate the polariser and analyser directions, and red lines indicate the slow axis direction of a 560 nm retardation plate. Scale bars 2 mm.

Cross-linking was instead attempted by washing $CaCl_2$-coagulated gel fibres in a sodium succinate solution (0.1 M), rather than the deionised water used in Chapters 4 and 5. As the fibres did not swell excessively in the cross-linking wash, longer washing times could be used with the dipping method and fibres were dipped into the washing solution two times for 15 s before drying in ambient conditions. These gel cross-linked (GCL) fibres were prepared under the same conditions as the water washed (WW) INT fibres in section 5.2 (p.96) by spinning them at varying draw ratio between 1 and 5 and tensile testing at relative humidity of 10 and 40% RH (Figure 6.2). The cross-sectional area of the GCL fibres was consistently higher than the WW fibres, leading to lower packing densities of 0.15-0.3 compared to 0.25-0.67 for the WW fibres. The tensile strengths and moduli of the GCL fibres were considerably lower than

the WW fibres, giving a maximum of ~25 MPa and ~10 GPa respectively compared to ~150 MPa and ~35 GPa. The better performance of the WW fibres is not simply due to the smaller cross-sectional area, since the absolute breaking force and tenacity were both also higher for the denser WW fibres (Figure 6.2d).

In this process, the ionic cross-links are formed whilst the fibres are in their gel state with an INT volume fraction assumed to be similar to the initial spinning dope concentration (~0.41%). The cross-links therefore lock in a relatively expanded structure which cannot densify fully during drying, resulting in the lower final packing density. Even if the cross-links can help transfer load between the INTs, the lower packing results in fewer INT interactions and thus an overall weaker fibre. Although the statistical power is weak in this experiment with only 2-6 samples per condition, a similar trend is observed with humidity as in section 4.3.2 (p.83), where a higher modulus and lower strain-at-failure was observed at 10% RH compared to 40% RH. If the cross-links are active to restrict INT sliding in the fibres, it would be expected that the GCL fibres should be less sensitive to humidity. In fact, there is no clear difference between the GCL and WW fibres in this experiment, indicating that the ionic cross-links are not sufficiently effective at preventing INT sliding, or that these ionic cross-links may themselves be softened by the hydration. The implications of these experiments are that cross-linking whilst the fibre is in its expanded gel state inhibits densification and worsens the properties of the final fibre. Although the results are not totally conclusive, it also appears that the ionic cross-links added in this process are not sufficient to prevent deformation in the INT fibres and are hence unlikely to greatly improve fibre properties.

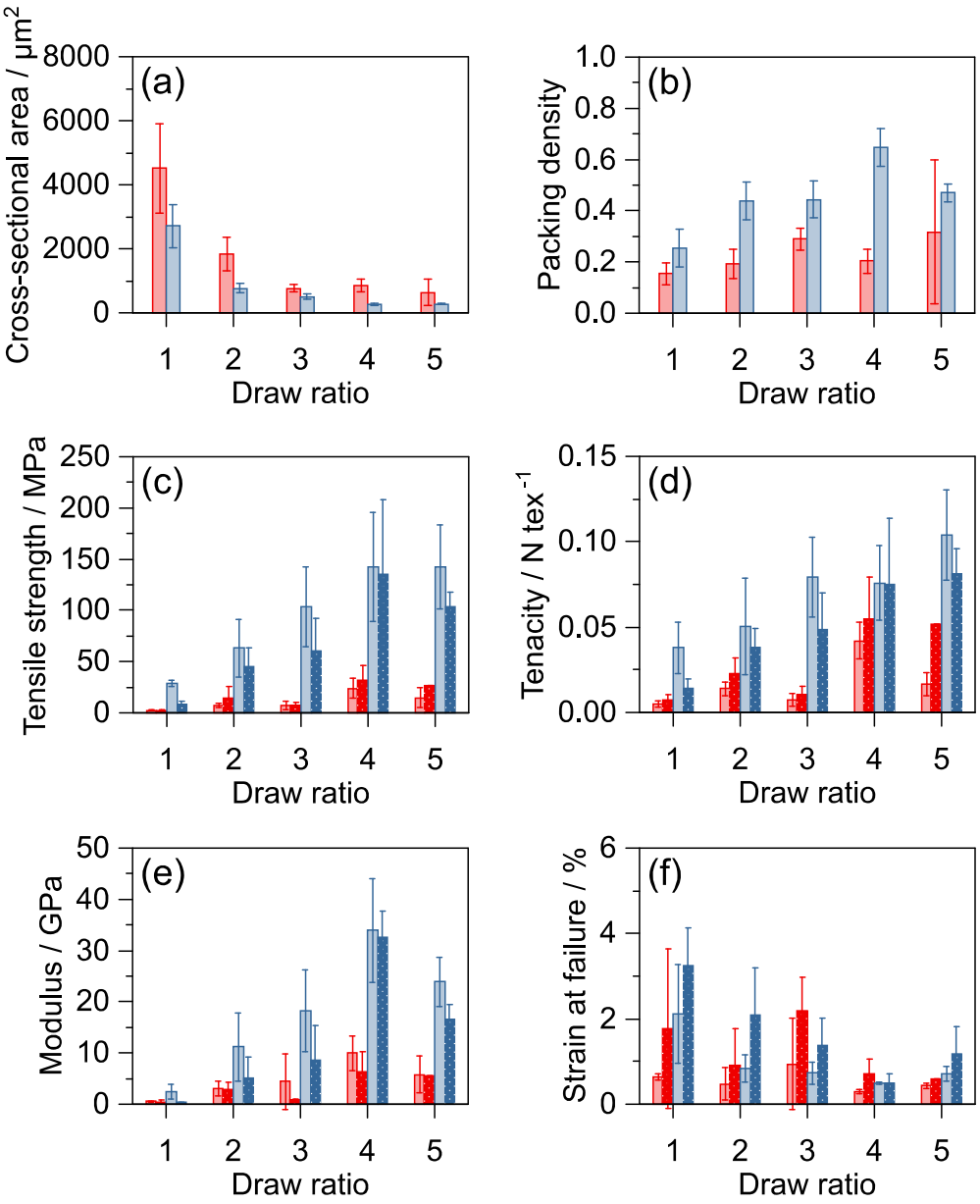


Figure 6.2. (a,b) Structural and (c-f) mechanical properties of (red) gel cross-linked and (blue) water washed INT fibres. Mechanical properties at 10% and 40% RH are shown with light and dark bars respectively. Error bars indicate 1 standard deviation.

6.2 Covalent cross-linking of INT fibres

The experimental work in this section was conducted by Jiawei Zhang, with my support, during his *BSc Chemistry* course at Imperial College London. The discussions here are my own.

Cross-linking INT fibres whilst in their gel state leads to poorer mechanical properties due to the inhibition of densification. In order to increase the inter-nanotube shear stress without impacting densification, covalent cross-linking strategies for the dry, densified fibres have been investigated. Two key reaction schemes have been explored: dehydration and silanisation reactions.

6.2.1 Dehydration reactions

When heated, clay materials undergo structural changes which are typically separated into three phases: dehydration, dehydroxylation and recrystallisation.[215] In the first of these stages, adsorbed water is removed from the clay, typically leading to the collapse of pores and the reduction of interlayer spacing. During the dehydroxylation stage, significant changes to the crystalline structure occur as surface hydroxyls on the clay minerals condense, liberating water. At even higher temperatures, new phases can crystallise.

In imogolite, all of these structural arrangements occur, with initial dehydration occurring at around 100-120 °C, dehydroxylation around 300-400 °C and finally the crystallisation of a mullite phase at temperatures above 900 °C.[216] The dehydroxylation has been predicted to be complete, with both inner and outer hydroxyls reacting,[217] and a series of mechanisms have been proposed which involve fracture of the INT walls and subsequent collapse to a lamellar structure.[218, 219] The formation of these lamellar structures is likely to occur alongside the formation of Ge-O-Ge and Al-O-Al bridges which may act to covalently link the now distorted INTs in the fibre, effectively forming a linked ceramic network.

The dehydroxylation of the INT fibres was first examined using thermal gravimetric analysis (TGA). A bundle of INT fibre was added to a sample pan and heated to 70 °C and held for 30 minutes and then the temperature was increased at 10 °C min^{-1} up to 600 °C. The initial desorption of physisorbed water occurred both during and after the isothermal step at 70 °C, finishing at around 130 °C. The dehydroxylation mass loss was seen to occur between 310 and 410 °C, with a peak in the derivative sample weight at 360 °C (Figure 6.3a). The reversibility

of these mass losses was explored by performing heating and cooling cycles to first 200 °C to induce dehydration of adsorbed water and then 400 °C for dehydroxylation. Over the course of the experiment, no significant reversion of the mass loss was observed, indicating that these structural changes are preserved at least over a short time scale.

In order to test the effect of dehydration and dehydroxylation on mechanical properties, INT fibres were treated by heating in air at either 200 °C or 400 °C for two hours, and then allowed to slowly cool before mounting for single filament tensile tests. The treated fibres were noticeably brittle compared to the as-spun fibres, making them more challenging to mount and test. The fibres treated at 400 °C were especially difficult to handle and of the eight samples prepared, it was only possible to successfully test three. The mechanical properties of the as-spun fibres were consistent with those prepared previously (section 5.3.2, tapered nozzle, DR 4, 40 cm washing bath) with tensile strength of 140 ± 20 MPa and elastic modulus of 24 ± 3 GPa. The thermally treated fibres had higher elastic moduli but significantly lower failure strains leading to lower tensile strengths (Table 7). Compared to the as-spun fibres, the heat treated fibres are almost entirely brittle, with virtually no plastic deformation visible in the stress-strain curve. Although the improvement to the elastic modulus through this heat treatment is encouraging, the drastic increase in brittleness is an extreme disadvantage, especially in making the fibres extremely challenging to handle. The 400 °C treatment is shown to be very detrimental to fibre performance with a severe reduction of tensile strength to approximately 40 MPa. The poor performance of these thermally treated fibres likely arises due to the formation of an unfavourable microstructure consisting of stiff, brittle covalent network with significant porosity. The low compliance and inhibition of plastic deformation in this network likely leads to flaw driven failure, which can occur at low tensile stresses.

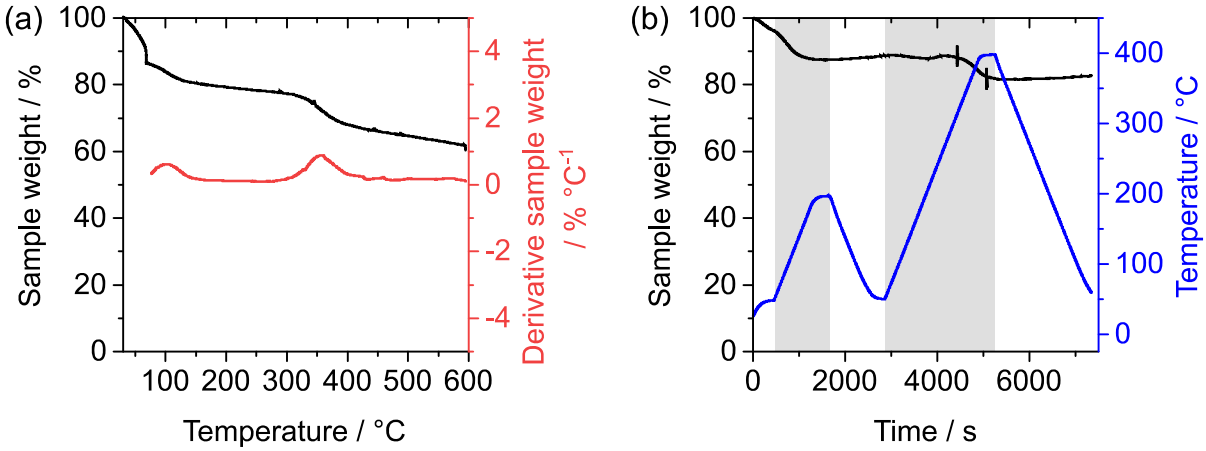


Figure 6.3. TGA traces of INT fibres at (a) constant heating of 10 °C min^{-1} and (b) heating and cooling cycles to 200 °C and 400 °C at a rate of 10 °C min^{-1}.

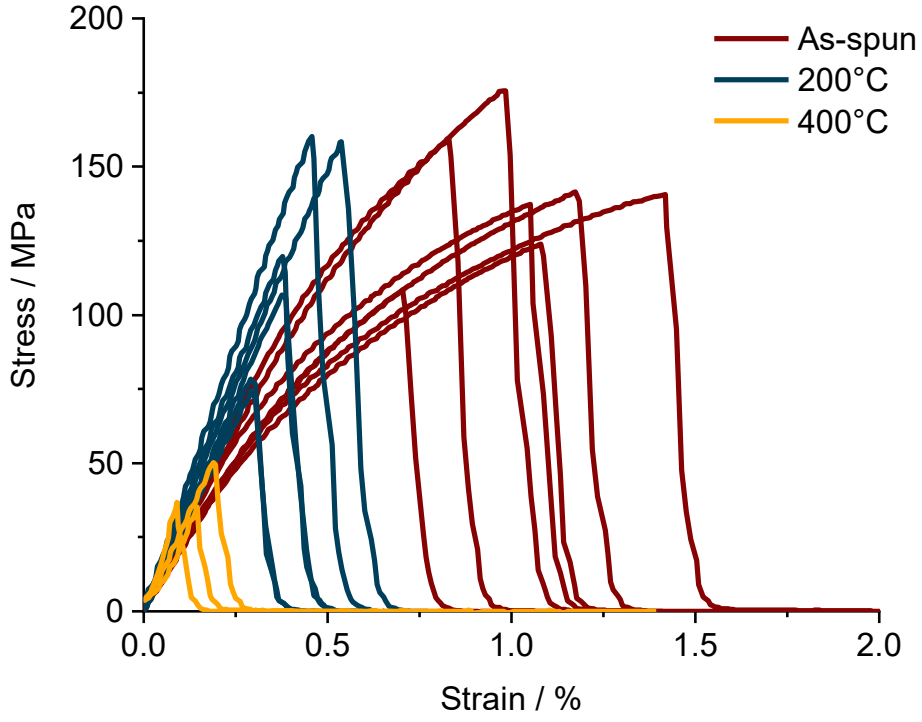


Figure 6.4. Stress-strain curves for INT fibres (red) as-spun and (blue, yellow) after heat treatment at 200°C and 400°C for 2 hours.

Table 7. Mechanical properties of as-spun and thermally treated INT fibres.

Sample	Tensile strength / MPa	Strain at failure / %	Elastic modulus / GPa
As-spun	140 ± 20	1.1 ± 0.2	24 ± 3
200°C treatment	120 ± 40	0.4 ± 0.1	31 ± 4
400°C treatment	40 ± 8	0.17 ± 0.05	31 ± 7

6.2.2 Silanisation reactions

The INT outer surface is coated with hydroxyl groups which may be used for reactions to create covalent linkages between the nanotubes. In the literature, oxysilanes and in particular γ-aminopropyltriethoxysilane (APS) have been used to functionalise INTs to increase their compatibility with organic solvents.[220, 221] APS is reported to react at multiple places on the imogolite surface, with the ^{29}Si NMR spectrum showing that the majority of the APS molecules graft at three points.[221] A similar functionalisation process can be envisaged using tetraethoxysilane (TEOS), where the TEOS may graft at up to four points, potentially creating links between adjacent INTs.

Silanisation of the INTs was conducted by soaking the INT fibres in a solution of TEOS in ethanol (1-1000 mM) overnight (approx. 16 hours). Additional control samples were prepared by soaking the fibres in pure ethanol. Silanisation of the INT fibres was confirmed using SEM and energy dispersive spectroscopy (EDS). In general, little difference was observed in the SEM images of as-spun, ethanol-soaked and TEOS-treated fibres (Figure 6.5), although some small regions of the TEOS soaked fibres appeared to have a coating on the surface (Figure 6.5c inset). EDS elemental analysis of the samples (Table 8) shows that the ethanol soaking of the INT fibres removes remnant $CaCl_2$. The Si content of the TEOS treated fibre (0.77 mol%) is greater than the as-spun and ethanol soaked fibres (0.19 and 0.33 mol%). The degree of grafting may be estimated by considering the fraction of surface hydroxyls which have been reacted. Only the outer wall of the double-walled INT, which comprises 69% of the total mass, is likely to participate in the reaction. Following the stoichiometry of the INT, $(OH)_3Al_2O_3Ge(OH)$, there are three outer surface hydroxyl groups for every two outer-wall Al atoms. As the TEOS is able to bind at four sites, for full surface modification, a maximum of one silicon atom is expected for every 3.9 aluminium atoms, corresponding to approximately 5 mol% in the fibre. In reality, the amount of Si measured in EDS is far lower indicating that the TEOS surface modification, although possibly present, is not complete.

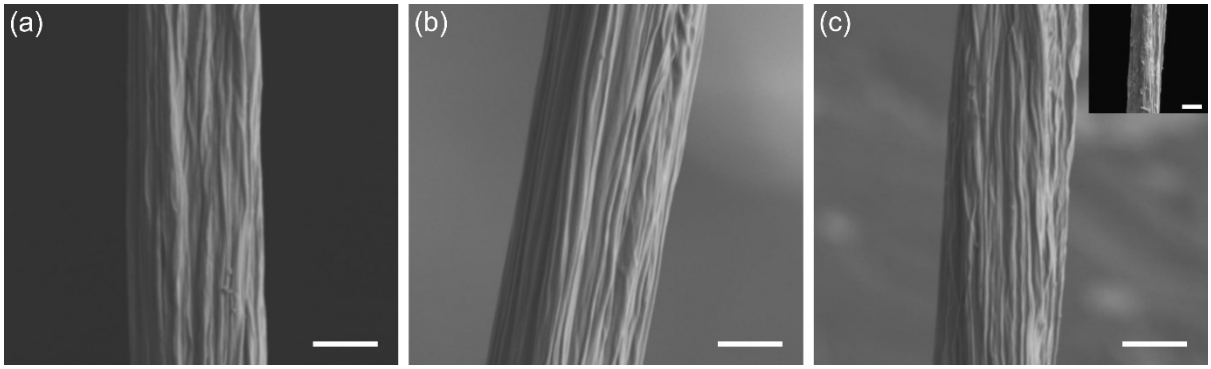


Figure 6.5. SEM micrographs of (a) as-spun, (b) ethanol soaked and (c) 1 M TEOS treated INT fibres. Inset is a region of (c) which has a visible coating on the surface of the fibre. Scale bars 10 μm.

Table 8. EDS elemental analysis of as-spun, ethanol soaked and 1 M TEOS treated INT fibres.

Sample	Al / mol%	Ge / mol%	O / mol%	Si / mol%	Ca / mol%	Cl / mol%
As-spun	19.5 ± 0.9	9.7 ± 1.6	63 ± 3	0.19 ± 0.05	3.5 ± 0.5	4.4 ± 0.3
Ethanol soaked	23.1 ± 0.3	11.6 ± 0.8	63 ± 1	0.33 ± 0.04	0.57 ± 0.05	1.45 ± 0.1
TEOS treated	22.9 ± 1.6	12.1 ± 1.6	63 ± 3	0.77 ± 0.11	0.53 ± 0.05	1.18 ± 0.06

The mechanical properties of the treated fibres were assessed by single filament tensile tests (Figure 6.6). The ethanol soaked controls, showed very poor tensile strengths (35 MPa) and failed at a low strain (0.2 %). In comparison, the fibres treated with TEOS had improved properties with tensile strengths of 150 and 170 MPa for TEOS concentrations of 0.001 and 1 M respectively, confirming the presence of some successful cross-linking. Similarly to the thermally treated fibres, the TEOS cross-linked fibres have a stress-strain curve characteristic of a brittle material, with no observable plastic deformation. The TEOS treated fibres have marginally higher elastic moduli than the as-spun fibres, but a lower strain-at-failure. The values of elastic modulus for these covalently-linked fibres are very similar to those that underwent the thermal treatment at approximately 31 GPa. It is possible that this is the limiting value for the network of INTs in this fibre, considering the intrinsic nanotube stiffness, the porosity and the alignment in the fibre.

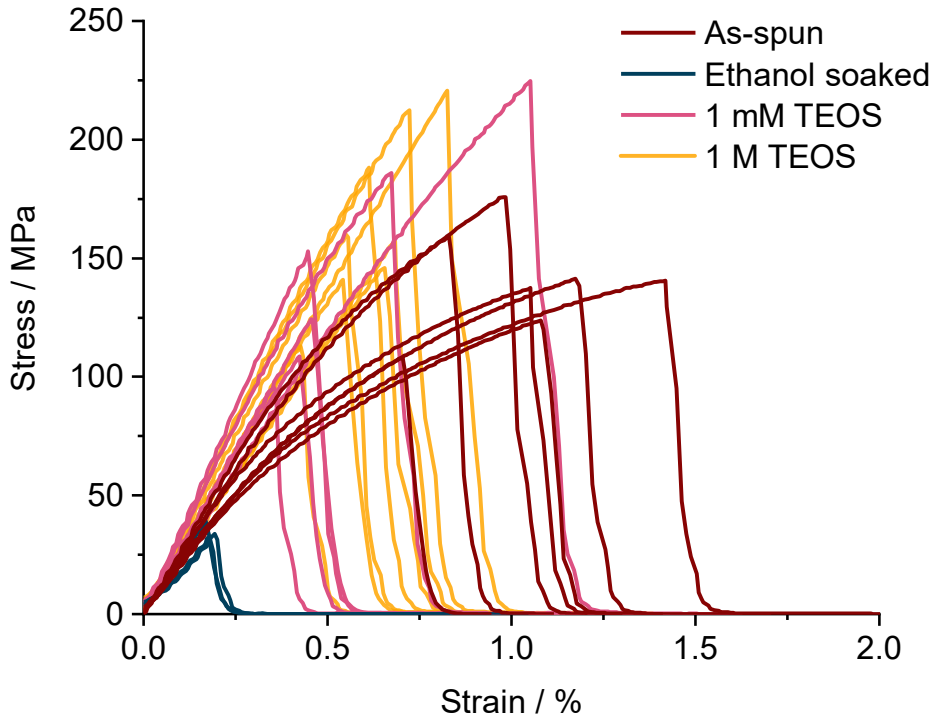


Figure 6.6. Stress-strain curves for INT fibres (red) as-spun, (blue) after soaking overnight in ethanol and (pink, yellow) after soaking overnight in solutions of TEOS in ethanol.

Table 9. Mechanical properties of as-spun, ethanol soaked and TEOS treated INT fibres.

Sample	Tensile strength / MPa	Strain at failure / %	Elastic modulus / GPa
As-spun	140 ± 20	1.1 ± 0.2	24 ± 3
Ethanol soaked	35 ± 4	0.21 ± 0.01	20 ± 3
1 mM TEOS	150 ± 50	0.6 ± 0.2	30 ± 4
1 M TEOS	170 ± 30	0.6 ± 0.1	28 ± 4

6.3 Polymer infusion into INT fibres

The experimental work in this section was conducted by Jian Bi, with my support, during his *MRes Nanomaterials* course at Imperial College London. The discussions here are my own.

Infusing a polymer matrix into the INT fibres may improve the properties by improving the stress transfer between the constituent nanotubes. In the literature, poly(vinyl alcohol) (PVOH) / INT nanocomposite fibres have previously been developed which show good compatibility between the nanotubes and the matrix.[193] To infuse the polymer into the INT

fibres, firstly an aqueous solution of PVOH was prepared at 3 wt% and the fibres were attached to a support frame and then carefully submerged in the polymer solution. The fibres were introduced to the polymer solution vertically in order to break the surface tension without removing the fibre from the support. Fibres were soaked for between 1 and 6 minutes and then removed from the solution to dry at constant strain under ambient conditions.

A polymer coating can be seen on the outside of the infused fibres in SEM (Figure 6.7a), compared to the as-spun fibres which have a corrugated texture within which INT bundles can be identified (Figure 6.7b). The mechanical properties of the INT fibres were improved with polymer infusion, with the tensile strength increasing from 170 MPa to a maximum of 350 MPa, whilst the elastic modulus increased from 24 to 71 GPa. However, the strain at failure was significantly lower for the infused fibres, decreasing from around 1.5% to ~0.7%. The mechanical properties steadily improved with longer infusion times up to 5 minutes, whilst no further improvement was seen with a 6 minute infusion. It is difficult to be confident in the significance of this result, as only one sample was tested for each infusion time, however it seems that roughly 5 minutes is required to enable full diffusion of the polymer into the INT fibre. Further study of the effect of infusion time on the structure and make up of these polymer infused fibres is warranted. Gravimetric methods, whether measuring the mass before and after infusion or *via* TGA, are limited by the small masses of the samples and so it is expected that further study would require the use of imaging methods perhaps using focused ion beam milling in an SEM to study the interior of the fibres.

These results provide an initial proof-of-concept that infusing a matrix into the INT fibres can improve their properties and are promising for composite applications where the matrix will ideally infuse into and around these fibre reinforcements. In particular, the elastic modulus of the network is greatly increased, likely due to improved stress transfer in the fibre. It is not clear from these experiments exactly how deeply the polymer is able to diffuse, although it is unlikely that the strength improvements arise purely due to the sub-micron thickness surface layer observed in SEM (which would require the polymer surface layer to have a tensile strength of the order of 1.6 GPa, higher than the 1.4 GPa of optimised PVOH fibres[222]). The final polymer loading fraction in the fibre is expected to be relatively low, as the infusion solution is only 3 wt% PVOH. It may be possible to further improve this process by increasing

the initial polymer content of the infusing solution and by exploring a variety of polymers and molecular weights (MW). There is likely to be a competition between using a high MW polymer for their superior intrinsic mechanical properties and a lower MW polymer which is easier to infuse into the fibre.

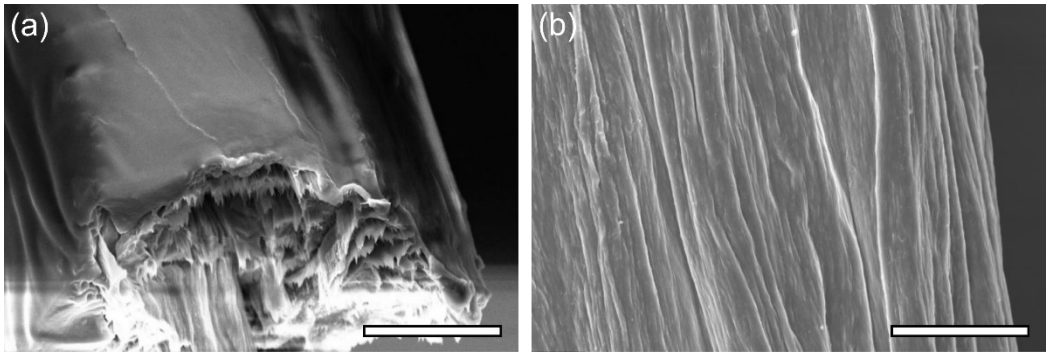


Figure 6.7. SEM images of (a) polymer-infused and (b) as-spun INT fibres. Scale bars 5 µm.

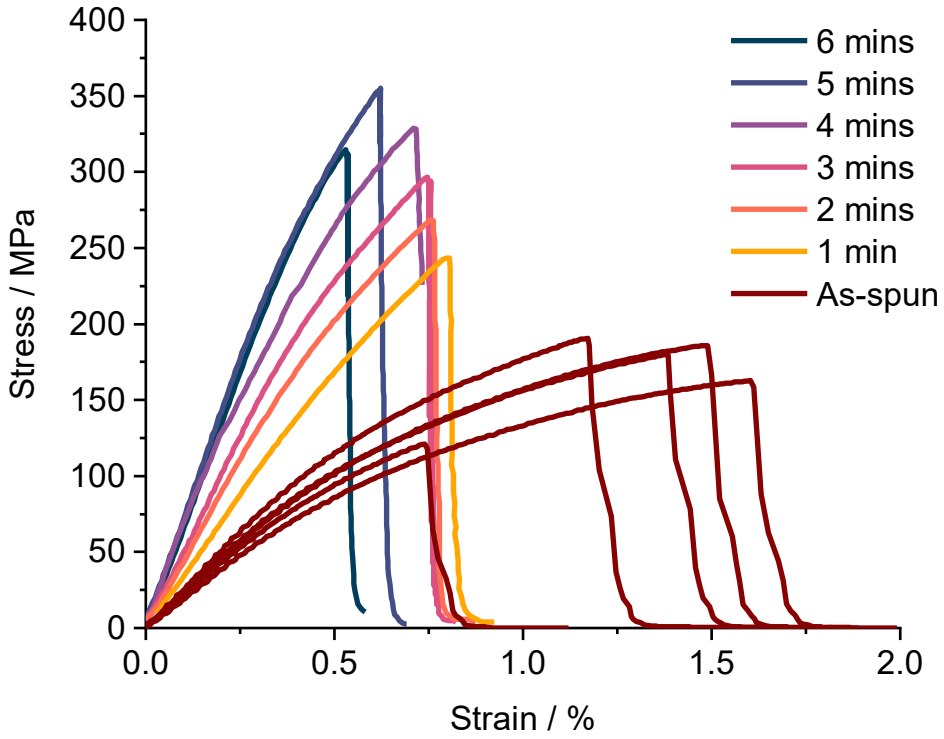


Figure 6.8. Stress-strain curves for polymer infused INT fibres with varying infusion times compared to as-spun controls.

6.4 Summary

INT fibres were successfully cross-linked using a range of strategies including physical ionic cross-links and covalent cross-links induced by dehydroxylation and siloxy networking. It was found that cross-linking while the fibre is in its gel state leads to poorer mechanical properties, due to the inhibition of densification leading to more porous fibres with lower strength and modulus. The absolute breaking force and tenacity of these cross-linked fibres were lower than the as-spun controls, showing that the reduction in strength and stiffness are not just due to the larger area of the gel cross-linked fibres, but also due to poorer stress transfer through the poorly densified network.

Covalent cross-linking has been demonstrated using dehydration reactions *via* thermal treatment and solution-phase silanisation with TEOS. In both cases, the treated fibres are more brittle than the as-spun fibres and have a similar failure strength. The elastic modulus is the same for both of the covalent cross-linking strategies and is slightly greater than the as-spun controls (~30 GPa compared to ~24 GPa).

Polymer infusion appears to be the most promising method for improving stress transfer of the INT fibres and the best infusion conditions tested significantly improved the tensile strength (from 170 to 350 MPa) and the elastic modulus (from 24 to 71 GPa). Further optimisation of the polymer infusion, by increasing the polymer content of the infusion solution and identifying the ideal polymer molecular weight, may yield further improvement,. It may be that the optimum INT microstructures are different for as-spun and infused fibres. In particular, it could be expected that with a stress transferring matrix, a more aligned microstructure would offer the best performance.

7 Dissolution of reduced CNT polyelectrolytes

7.1 Introduction

In this work, the reductive charging method for dispersing carbon nanotubes has been investigated to identify the required conditions for creating homogeneous spinning dopes. Firstly, a theoretical framework is presented for the required conditions to spontaneously disperse CNTs, followed by molecular dynamics simulations to illustrate the process. This analysis is then followed with an experimental study to identify the interplay between CNT mass loading and degree of charging on the homogeneity of CNT solutions.

7.2 Theoretical framework for CNT polyelectrolyte solutions

The debundling of CNT polyelectrolytes is driven by the balance of attractive intertubular van der Waals interactions and electrostatic repulsion, which may be screened by the presence of condensed or mobile counterions. A smaller energetic contribution may also arise due to solvent structuring, which leads to greater adhesion between nanotubes.

7.2.1 Van der Waals energy

The Lennard-Jones potential (U_{LJ}) is commonly used to describe the short range repulsive and longer range attractive forces between two non-bonded atoms as a function of their separation x and is given by

$$U_{LJ}(x) = -\frac{A}{x^6} + \frac{B}{x^{12}} \tag{21}$$

where A and B are positive constants which describe the potential well depth and equilibrium separation of the atoms. The overall van der Waals interactions (ϕ_{vdW}) between two single-walled nanotubes as a function of the nanotube separation (R_{sep}) can be calculated by integrating the Lennard-Jones potential over the two cylindrical surfaces with a mean atom surface density, σ_a. The potential is given by

$$\phi_{vdW}(R_{sep}) = \iint {\sigma_a}^2 \, U_{LJ}(x) \, \mathrm{d}\Sigma_1 \, \mathrm{d}\Sigma_2 \tag{22}$$

where x is the distance between the surface elements Σ_1 and Σ_2 on the CNTs 1 and 2. This integral has been evaluated for a range of infinitely long identical tubes by Girifalco et al[223]

and, through comparison to a group of other carbon systems, was used to identify a universal graphitic potential given by,

$$\frac{\phi_{VDW}(\tilde{R})}{|\phi_{VDW}(R_0)|} = -\frac{1}{0.6}\left[\left(\frac{3.41}{3.13\tilde{R}+0.28}\right)^4 - 0.4\left(\frac{3.41}{3.13\tilde{R}+0.28}\right)^{10}\right] \quad (23)$$

where $|\phi(R_0)|$ is the well depth of the potential and $\tilde{R}$ is a reduced distance parameter, which for a pair of nanotubes is equal to the CNT wall separation, g, divided by the equilibrium tube wall separation, g_0.

The applicability of this potential was developed further by Sun et al[224] who determined the potential well depths and equilibrium wall separations for interactions between nanotubes of a range of diameters. For a pair of 1.2 nm diameter nanotubes, similar to the average for the Tuball CNTs used in this thesis, a well depth of 85 meV Å^{-1} and tube wall separation distance of 3.15 Å was obtained.

7.2.2 Electrostatic energy

Electrostatic interactions between two infinitely long charged nanotubes can be calculated by considering the potential of an infinitesimal length of one nanotube with an infinite nanotube.

Due to the conjugated π orbitals, the charge on a CNT may be considered to be uniformly distributed over the nanotube walls. Applying Gauss' law - that the electric flux from a closed surface is proportional to the enclosed charge - and recognising symmetry, the system can be simplified. The interaction can be modelled as an infinitesimal point charge interacting with an infinite line charge, as illustrated in Figure 7.1. The effective linear charge density, λ_{cd}, of a CNT can be calculated as

$$\lambda_{cd} = \frac{\sigma_a \, \pi \, d_{CNT} \, \mathrm{e}}{n_c} \quad (24)$$

where σ_a = 0.382 Å^{-2} is the areal density of carbon atoms in a graphene sheet, d_{CNT} is the CNT diameter, e is the elementary charge and n_c is the charging ratio given as the number of carbon atoms per elementary charge.

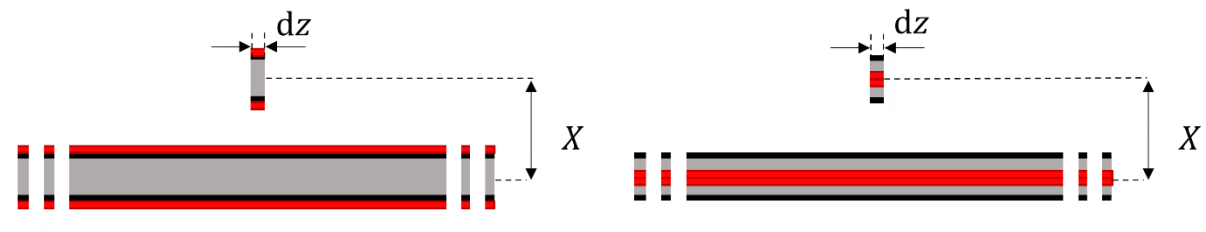


Figure 7.1. Illustration of assumed charge density on a CNT. (Left) A tube of charge on the outer surface of the CNT. (Right) A line of charge down the CNT axis.

The electric field at a distance x from an infinite line of charge density λ_{cd} in a medium with relative permittivity of ϵ_r is given from Gauss' Law by,

$$E = \frac{\lambda_{cd}}{2\pi x \epsilon_0 \epsilon_r} \tag{25}$$

where ϵ_0 is the permittivity of free space. The electrical potential energy $\phi_E(X)$ of the infinitesimal length segment δz with charge $\lambda_{cd}\,\delta z$ can then be calculated relative to a reference distance, x^*, by integrating along a radial path from x^* to X

$$\phi_E(X) = -\int_{x^*}^{X} (\lambda_{cd}\,\delta z)\frac{\lambda_{cd}}{2\pi x \epsilon_0 \epsilon_r}\mathrm{d}x = \frac{{\lambda_{cd}}^2}{2\pi \epsilon_0 \epsilon_r}\,(\ln x^* - \ln X)\,\delta z \tag{26}$$

In this calculation, the electric potential energy of our infinitesimal length segment is infinite relative to a charge initially located at infinity (a result which arises from the fact that our 'stationary' CNT is infinite in length). However, as we are seeking to model the *change* in potential energy with CNT separation, the absolute value of the energy is unimportant and we can use any reference position to obtain finite values of potential energy. In this case, the electrical potential energy is simply given by,

$$\phi_E(X) = -\frac{{\lambda_{cd}}^2}{2\pi \epsilon_0 \epsilon_r}\ln(X)\,\delta z \tag{27}$$

This formulation is naïve in that it does not consider the charge screening due to the sodium counterions in a typical nanotubide dispersion, which may be present in either a condensed Stern layer or in a diffuse Gouy-Chapman layer. These charge layers are expected to reduce the electrostatic repulsion between the charged CNTs, so this calculation can be used to indicate a minimum degree of charging for dissolution.

7.2.3 Charging conditions for spontaneous dissolution

In sections 7.2.1 and 7.2.2, the energetic contributions of van der Waals interactions and electrostatic repulsion have been derived for a pair of CNT polyelectrolytes in a medium with dielectric constant, ε_r, of 37.8 equivalent to that of the DMAc solvent used for nanotubides.[225] Plotting the total interaction energy as a function of nanotube wall separation indicates the stability of CNT bundles and is illustrated for varying charging ratios with two different types of CNTs in Figure 7.2 using the parameters in Table 10.

Table 10. Van der Waals interaction parameters for a pair of 1.2 and 2.4 nm diameter CNTs, taken from reference [224]

CNT	Diameter / nm	Van der Waals well depth / meV Å^{-1}	Van der Waals equilibrium wall separation / Å
A	1.2	85	3.15
B	2.4	121	3.16

The van der Waals energy contribution can be observed in the uncharged case, with a strong short-ranged repulsive interaction and longer ranged attractive interaction leading to a potential well at an equilibrium separation distance. Initial charging of the CNTs (NaC_{40} to NaC_{20}) leads to CNT individualisation becoming energetically favourable at large distances, although an energy barrier to bundle separation exists at small inter-wall distances. As the charge density of the CNTs increases further, the energy barrier is reduced until spontaneous dissolution can occur at some critical charging ratio (Figure 7.3).

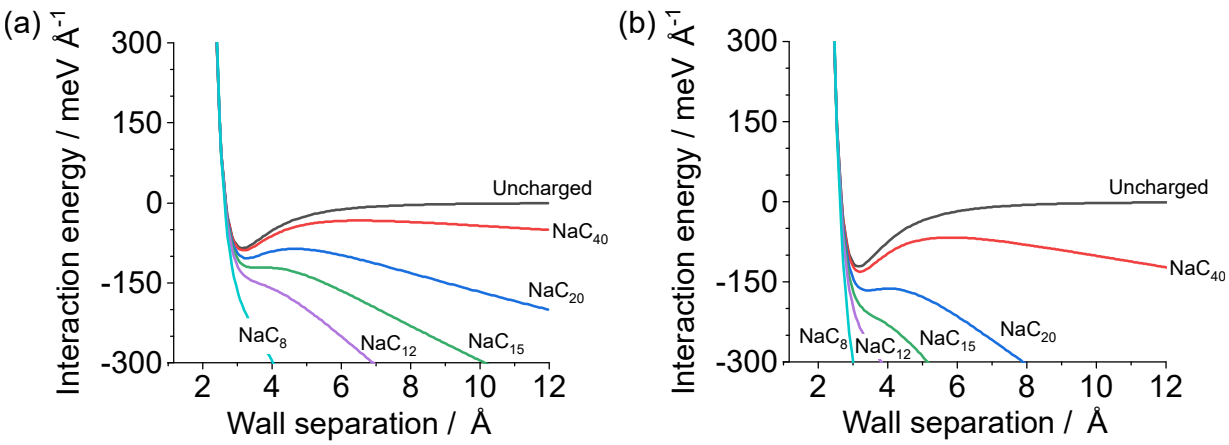


Figure 7.2. Calculated interaction energies for a pair of (a) 1.2 nm and (b) 2.4 nm diameter CNTs in a vacuum for varying degrees of CNT charging stoichiometry using equations (23) and (27). Curves have been offset vertically for clarity.

The critical charging ratio to enable spontaneous dissolution for the 1.2 nm CNTs is NaC_{15}, whereas it is NaC_{19} for the 2.4 nm CNTs. As the calculation neglects the effects of charge screening and condensation by counter-ions, this result provides only a lower bound for the degree of charge required to dissolve CNT bundles. It may be anticipated that higher charge densities are required to experimentally dissolve the CNTs.

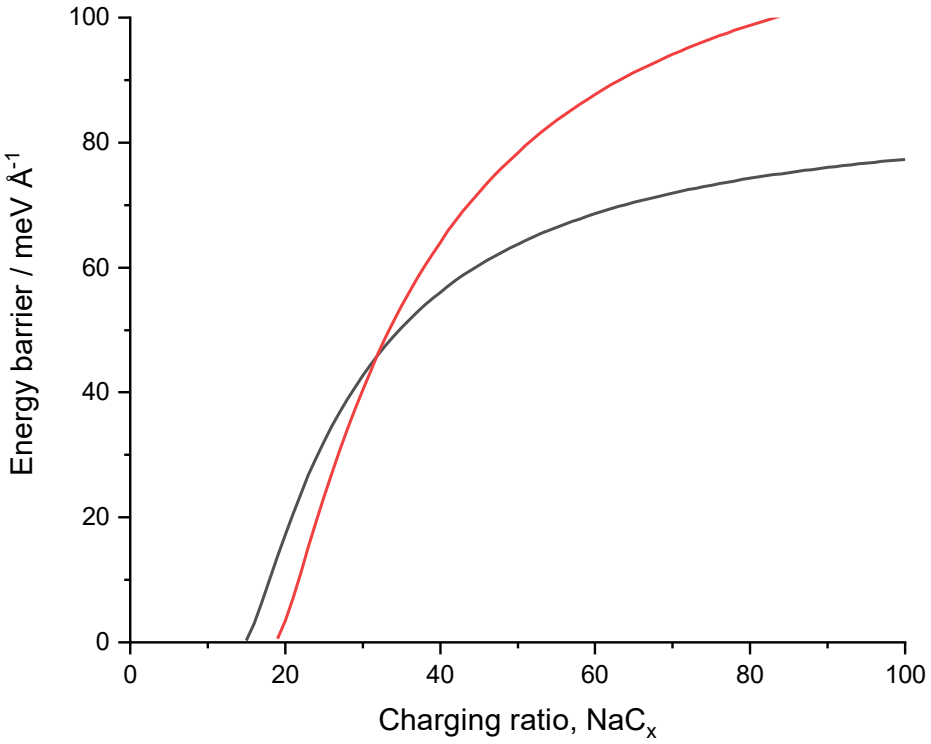


Figure 7.3. Calculated energy barrier for separation of pairs of charged CNTs in vacuum with (grey) 1.2 nm and (red) 2.4 nm diameter.

7.2.4 Counter-ion condensation

When CNTs are chemically charged, as in the alkali metal reductive route, counter-ions are produced and persist in the system. At low concentrations and degrees of charging these counter-ions are expected to be 'free', however as the concentration and charge of the polyelectrolyte increases, increased electrostatic attraction between the counter-ions and the polyelectrolyte results in the condensation of the counter-ions, which then become localised at the polyelectrolyte surface. These condensed counter-ions screen the electrostatic repulsion between the CNTs and in extreme cases where a CNT bundle is fully intercalated may also provide attractive interaction between layers of negatively charged CNTs and positively charged counter-ions.

The Oosawa-Manning two-state model, which has previously been applied to CNT polyelectrolytes,[226] describes the counter-ions as either localised with the polyelectrolyte or free to move. A condensation parameter ξ describes the degree of charge condensation[227] where ξ is given by,

$$\xi = \frac{e^2}{\epsilon_0 \epsilon_r k_B T} \lambda_{cd} \quad (28)$$

where λ_{cd} is the linear charge density of the polyelectrolyte. Above a critical value of $\xi = 1$, counterions are condensed onto the polyelectrolyte surface to achieve an effective screened charged density corresponding to a ξ of unity.

Considering a 12 Å diameter CNT in DMAc at room temperature, the condensation parameter is given by,

$$\xi = \frac{21.3}{n_c} \quad (29)$$

where n_c is the charging ratio, or the number of carbon atoms per elementary charge on the CNT. It is clear that for typical dissolution conditions of NaC_4 to NaC_{20} charge condensation is likely to take place and may reduce the stability of CNT solutions.

7.3 Molecular dynamics simulations of CNT solutions

The theoretical description of CNT polyelectrolyte solutions in terms of van der Waals and electrostatic interactions identified a critical charging ratio to enable spontaneous CNT dissolution between NaC_{15} and NaC_{19} depending on the CNT diameter.

In order to investigate the additional contributions of solvent-CNT interactions and counterion condensation, molecular dynamics simulations were conducted using NAMD[148] with the CHARMM36 all-atom forcefield.[228] The CHARMM forcefield is comprised of harmonic bond, angle and improper energies and sinusoidal dihedral potentials for bonded atoms, alongside van der Waals and electrostatic non-bonded interactions.

Two parallel CNTs with a centre-to-centre distance of 13 Å were added to a simulation box alongside a stoichiometric number of sodium ions and DMAc molecules and then initialised with two cycles of minimisation and equilibration (4 ps at 300 K) with fixed CNT positions. An additional equilibration (20 ps) was then conducted with one CNT fixed and the other free to move (Figure 7.4). The conditions used are required to minimise the number of atoms in the

simulation box and hence reduce computation times, however they correspond to extremely large effective CNT and sodium ion concentrations (500 mg_{CNT} mL^{-1} and [Na]~2-6 M). At these concentrations the entropic penalty for charge condensation is reduced leading to extensive condensation for most conditions (Figure 7.4f-j).

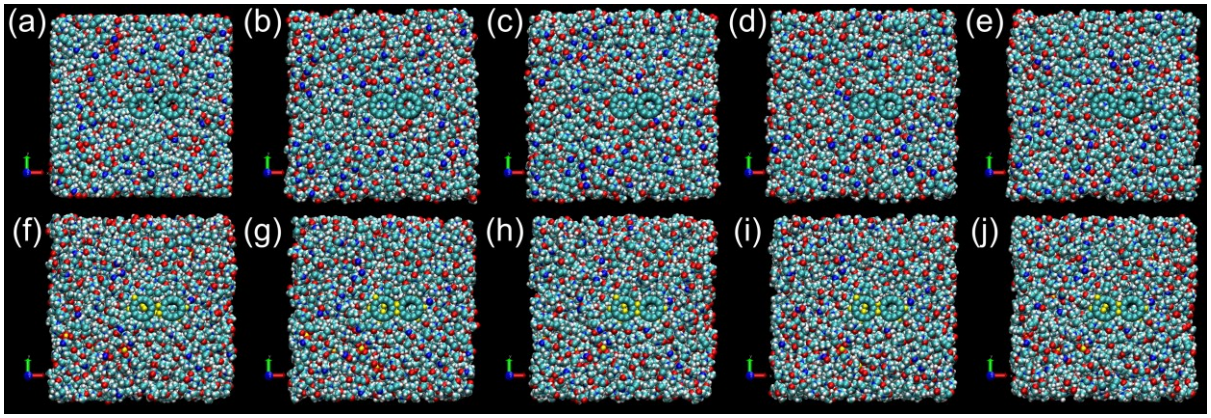


Figure 7.4. Snapshots of cut-throughs of the simulation box during equilibration for (a-e) uncharged and (f-j) NaC_8 CNTs at (a,f) 0 ps, (b,g) 5 ps, (c,h) 10 ps, (d,i) 15 ps, (e,j) 20 ps. Carbon: light blue, sodium: yellow, oxygen: red, nitrogen: dark blue, hydrogen: white

As the diffusion rate is slow for large molecules, it was required to use steered molecular dynamics (SMD) to study the force profile for separating the CNTs. A dummy atom was attached to the centre-of-mass of one of the CNTs and translated while the other CNT was kept fixed, providing a force to separate the two CNTs. The simulation workflow from initialisation and equilibration through to SMD simulation was repeated 5 times for CNTs charged at charging ratios, NaC_x, of 8, 10, 12, 20 and for uncharged CNTs (Figure 7.5).

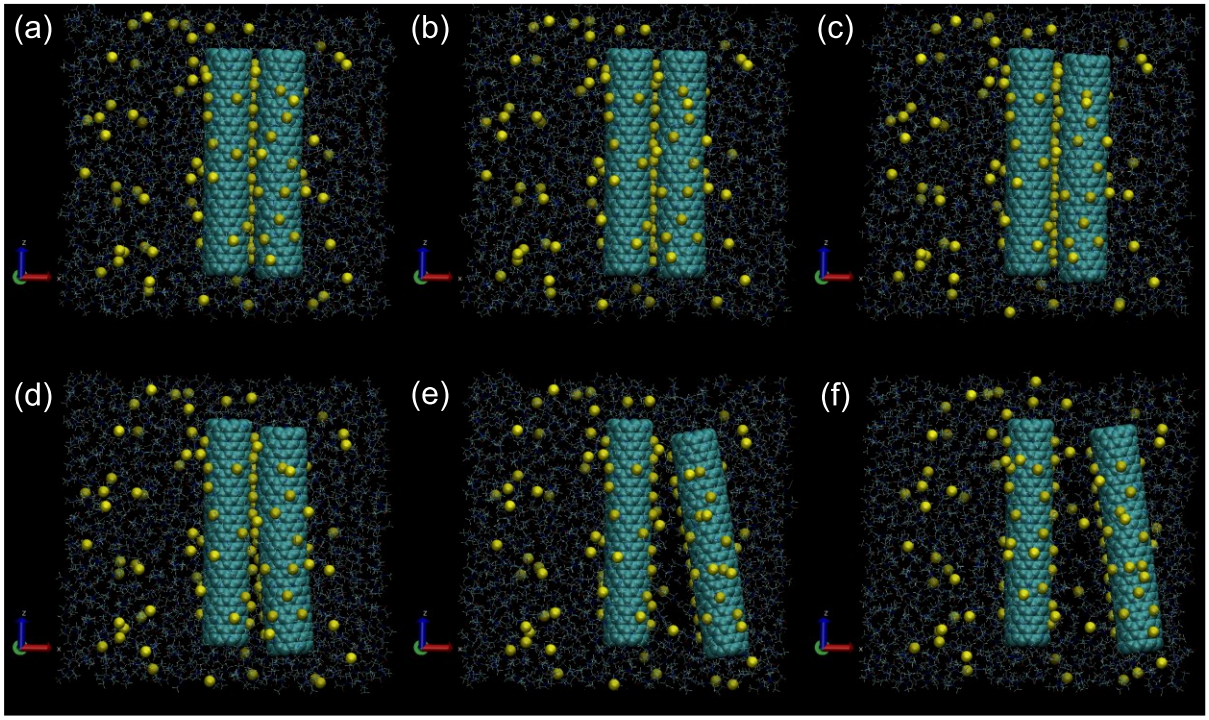


Figure 7.5. Snapshots of cut-throughs of the simulation box during steered molecular dynamics for NaC_8 CNTs at (a) 0 ps, (b) 5 ps, (c) 10 ps, (d) 13 ps, (e) 15 ps, (f) 20 ps. CNT carbon atoms and sodium ions are shown as spheres. Explicit solvent molecules are shown as lines.

The SMD force plotted as a function of the simulation time (Figure 7.6) indicates whether separation of the CNTs is spontaneous (negative force) or requires energy input (positive force). In the uncharged case, a small force is required to initially overcome an energy barrier. For CNTs with a charging ratio of NaC_{20} the separation is spontaneous, however CNTs with larger charging ratios require significant force for separation. This effect is due to the charge condensation in the highly concentrated conditions used for the simulation, which leads to a cohesive ionic interaction between the CNTs and the interstitial sodium ions. It is notable here that the contribution of the van der Waals interactions to CNT bundling is greatly reduced for CNTs in solvent compared to a vacuum. The formation of solvent-CNT interactions offsets the energy required to separate the CNTs, meaning that lower charging ratios are required to dissolve the CNTs relative to those in the vacuum case.

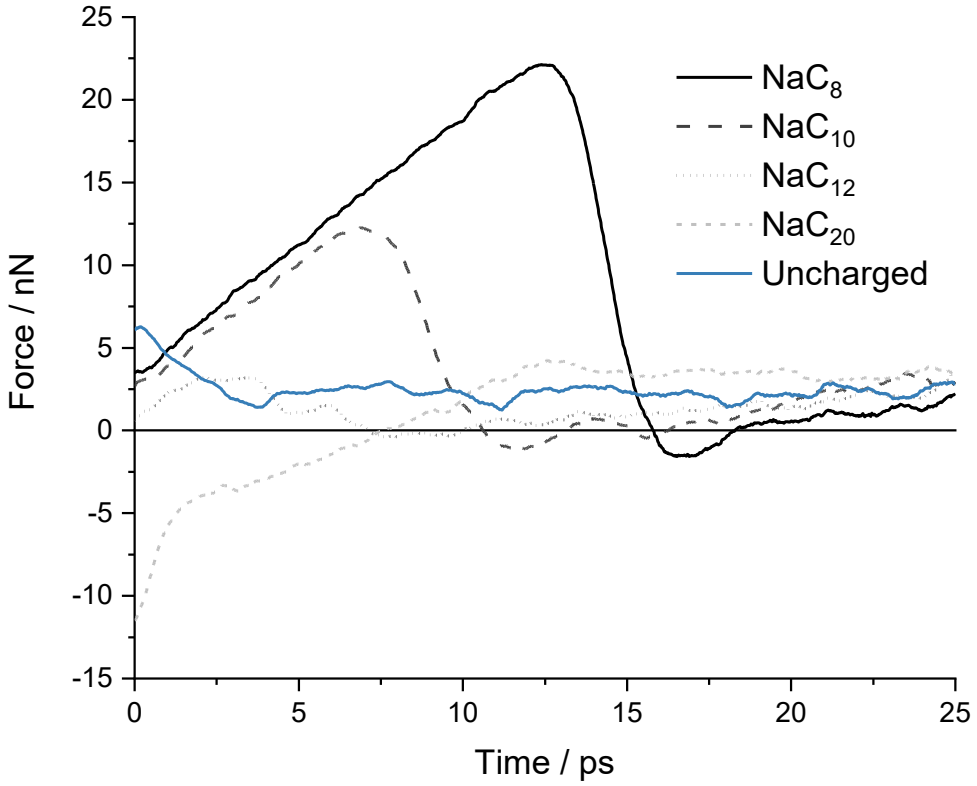


Figure 7.6. Force profiles for separating a pair of CNTs calculated using steered molecular dynamics.

7.4 Experimental determination of optimal CNT dissolution conditions

In sections 7.2 and 7.3, the key variables and phenomena affecting the dissolution of CNT polyelectrolytes were explored. It was shown that, in a vacuum, a charging ratio of at least NaC_{15} is required to separated CNTs of typical diameters (2.4 nm), although this value may be reduced in a solvent due to the presence of favourable solvent-CNT interactions. At high charging ratios and concentrations, charge condensation can lead to attractive ionic forces between the CNTs mediated by the condensed sodium ions.

In practice, the dissolution of CNTs is further complicated by the mixture of helicities and corresponding electronic density of states present in typical CNT feedstocks. At a given nominal charging ratio it is expected that metallic and semi-conducting CNTs will have different degrees of charge. In addition, dissolution may be inhibited by the presence of physical entanglements between CNTs in the dry powder feedstocks.

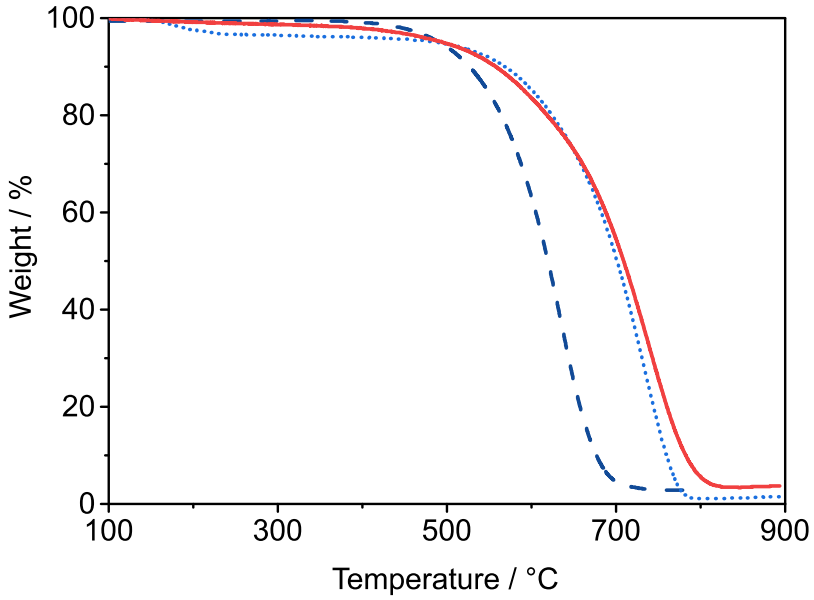
The ideal CNT dissolution conditions were identified empirically using a series of optimisation experiments. Initial work indicated that a charging stoichiometry of NaC_{20} and higher led to

poor dissolution with large agglomerates visible by eye. Indeed, charging at these levels has been used within the research group to purify CNT feedstocks by preferentially dissolving carbonaceous impurities leaving the pristine CNTs as an undissolved sediment.[8] Centrifugation steps to remove undissolved material from spinning dopes hinder the economical application of reduced CNT solutions, and high agglomerate contents make filtration challenging, so it is essential to identify dissolution conditions which minimise the agglomerate content of the spin dopes.

7.4.1 CNT feedstock characterisation

The work in this thesis primarily uses two different CNT feedstocks; OCSiAl Tuball 01RW03 (batch numbers 398 and 788) and Meijo eDIPS EC1.5 (lot number 8901404) CNTs. Both manufacturers report that these CNTs are primarily single-walled CNTs with diameters in the range of 1.2-2 nm, and low metallic catalyst impurities. The degree of metallic impurities of the batches used in this work was assessed experimentally using TGA under a steady flow of air at a temperature ramp of 10 °C min^{-1} with the remnant mass after complete combustion assumed to be comprised of fully oxidised iron catalyst (Fe_2O_3). For the Tuball CNTs, the remnant mass was 1.1-2.8% corresponding to an initial iron mass content of 0.8-2.0%, whilst the eDIPS CNTs have an initial iron mass content of 2.4% (Figure 7.7). Surprisingly, the two Tuball batches had markedly different TGA traces despite being ostensibly the product code. The earlier received batch 398 has a much lower combustion onset and peak degradation temperature, typically indicative of less pure and more defective CNTs which may also contain more amorphous carbon.[229] It should be noted here that whilst both batches 398 and 788 have been used in dissolution experiments, only batch 788 was used in fibre spinning. The thermal stability of the eDIPS EC1.5 and Tuball (batch 788) samples are remarkably similar and correspond to highly pure CNT samples.

The presence of amorphous carbon and defects on CNTs is also commonly quantified using Raman spectroscopy (section 3.3.4, p.69), using the intensity ratio of the D (~1350 cm^{-1}) and G (~1600 cm^{-1}) peaks (I_D/I_G). All the CNT batches used in this work have very low I_D/I_G (~0.01) indicative of highly pristine CNTs with few defect sites (Figure 7.8).



	T_{onset} / °C	T_{peak} / °C	M_{Fe2O3} / %
Tuball (batch 398)	559	637	2.8
Tuball (batch 788)	645	731	1.1
eDIPS EC1.5	639	742	3.4

Figure 7.7. TGA traces for (blue) Tuball 01RW03 and (red) eDIPS EC1.5 CNTs with decomposition onset and peak temperatures and remnant mass of oxidised metal catalyst.

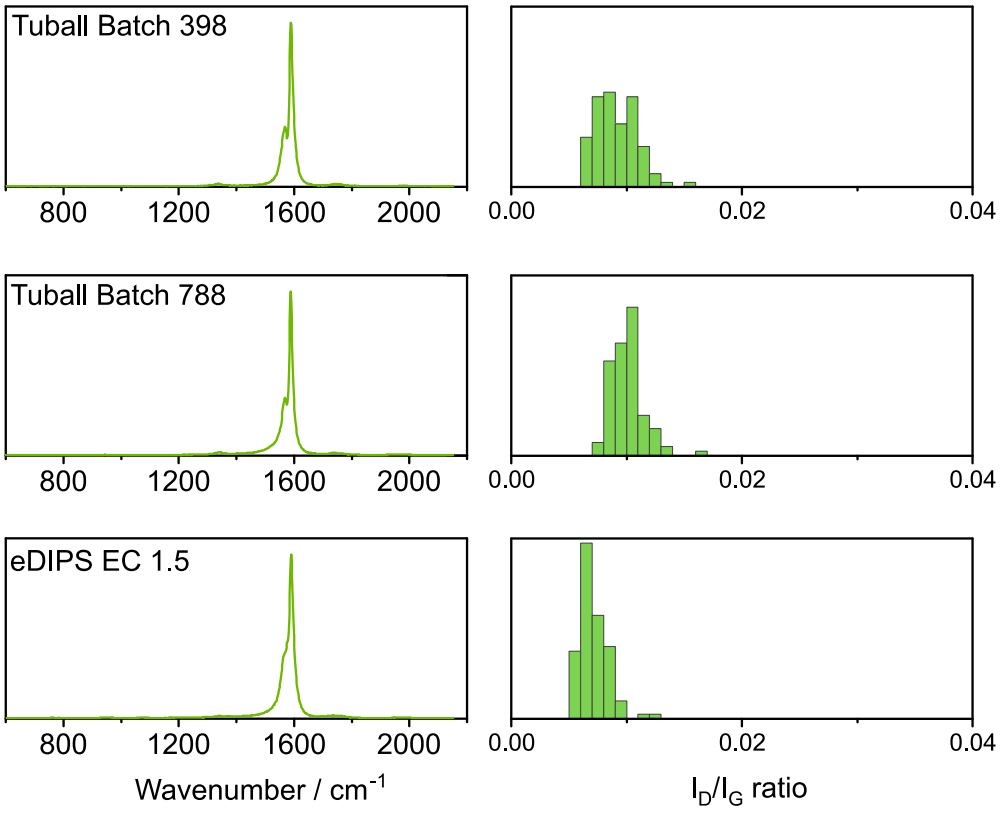


Figure 7.8. Representative Raman spectra and histograms of I_D/I_G values obtained across 10x10 maps of each sample for Tuball and eDIPS EC1.5 CNTs. Laser wavelength 532 nm.

The length distribution and aspect ratio of these CNT feedstocks is not precisely specified by the manufacturers (although OCSiAl state that Tuball CNTs are >5 µm long). It can be challenging to measure length distributions, particularly for longer CNTs. Methods have been developed to estimate the average length using TEM images, despite CNTs traversing across multiple images.[169] However, these methods are liable to sampling errors as the smaller CNTs are less likely to be collected and recognised on a typical holey carbon film. Instead, a method of determining a 'viscosity-averaged' aspect ratio using extensional viscosity has been developed by Tsentalovich et al.[230] Whilst a suitable extensional rheometer was not available to study the particular batches used in this work, the aspect ratios of a large number of CNT sources have been reported in the literature.[96] For each of the CNT sources, there is a notable batch-to-batch variation in the measured aspect ratio, although despite this range it is apparent that the true aspect ratio of the Tuball CNTs (~1000-3000) is somewhat lower than that suggested by the manufacturer data sheet (>3000). No value for aspect ratio of the eDIPS EC1.5 CNTs is reported by Meijo Nano Carbon, but based on the literature results[96] these CNTs appear to have a higher aspect ratio than the Tuball CNTs at ~4000-6000.

Table 11. Technical specifications of Tuball 01RW03 and eDIPS EC1.5 CNTs used in this work. **Bold** indicates values obtained experimentally, (*italic)** indicates values obtained from manufacturer data sheets and references are given for values obtained from the literature.

Specification	Tuball 01RW03	eDIPS EC1.5
Synthesis method	Plasma enhanced CVD	Direct injection pyrolytic synthesis
SWCNT content / %	*(99 ± 0.5)**	*(>90)**
Metal impurities / %	**0.8-2.0** *(0.8)**	**2.4**
Raman D/G ratio (532 nm)	**~0.006-0.0015** *(<0.025)**	**~0.07** *(<0.01)**
SWCNT diameter / nm	*(1.6 ± 0.4)**	*(~ 2)**
Aspect ratio	~1000-3000 [96] (*>3000)**	~4000-6000 [96]

7.4.2 Stirring and mechanical agitation

Stirring is qualitatively seen to be important to the dissolution of reduced CNTs. With no stirring a cloudy black supernatant slowly forms whilst the majority of CNTs remain as a swollen gel towards the bottom of the dissolution flask. Agitation by stirring can first incorporate the gel into the solvent and then help to break up larger agglomerates through viscous shear.

The agglomerate content of a CNT dispersion can be reduced by stirring more vigorously. The size and quantity of agglomerates in a CNT dope has been shown to be reduced by increasing the stirring speed from 250 rpm to 400 rpm (Figure 7.9a,b). Inefficiencies can arise when stirring CNT solutions in poorly sized vials. Using too small a vial for the solution volume can result in intense stirring at the bottom of the vial, whilst the viscoelasticity of the liquid above means the majority of the fluid remains stagnant above. The effect of the poorer stirring can be seen in optical micrographs of the CNT solutions prepared with solution volumes of 4 mL and 25 mL in a 25 mL vial (Figure 7.9c,d).

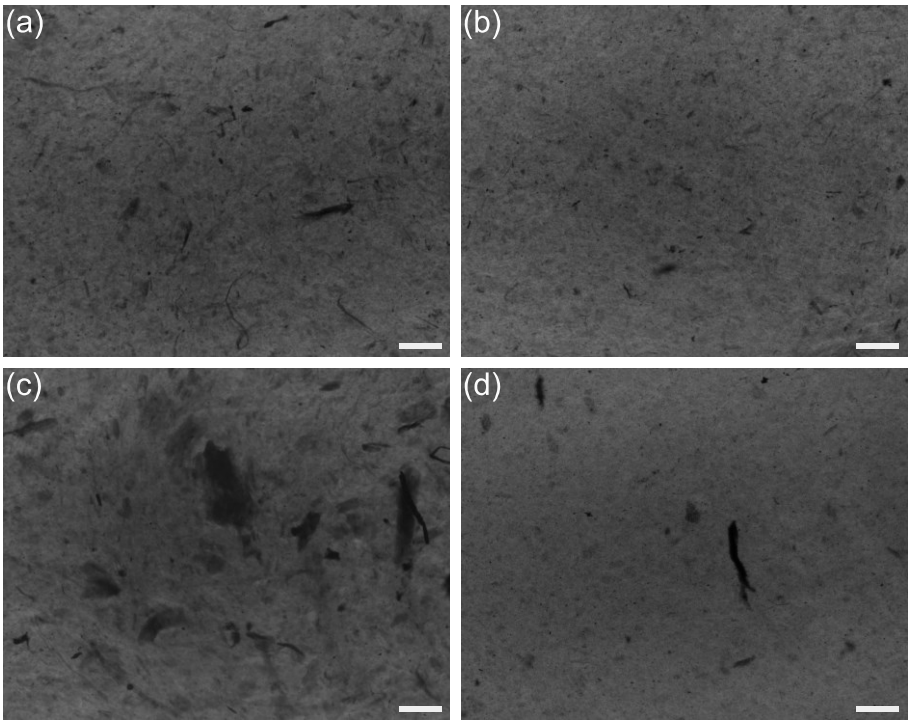


Figure 7.9. Transmission optical microscopy images of reduced CNT solutions prepared at (a,b) 4 mg_{CNT} mL^{-1} NaC_8 with stirring at (a) 250 rpm and (b) 400 rpm and (c,d) 5 mg_{CNT} mL^{-1} NaC_8 with a solution volume of (c) 25 mL and (d) 4 mL. All preparations were conducted in a 25 mL vial. Scale bars 200 µm.

7.4.3 Charging ratio and CNT mass loading

Solutions of reduced CNTs (Tuball 01RW03, batch 398) in DMAc were prepared at mass loadings of 3, 4 and 5 mg_{CNT} mL^{-1} at charging ratios of NaC_6, NaC_8 and NaC_{10} with a volume of 4 mL and overnight stirring at 400 rpm. Qualitative comparison of the spin dopes, imaged with optical microscopy, indicates that, for all mass loadings, a charging ratio of NaC_8 leads to optimal dissolution (Figure 7.10). For each mass loading at charging levels either side of this

optimum, a mottled texture appears due to the presence of small regions of poorly dissolved CNTs.

The quality of the CNT solutions can be quantified by using a segmentation algorithm to threshold the optical micrographs. A figure for the aggregate content is obtained from the area fraction of the micrograph which is segmented. To correct for inconsistent illumination due to scattering from capillary edges, an adaptive thresholding algorithm was chosen. The Phansalkar local thresholding algorithm,[231] initially developed to identify cell nuclei in dark, low contrast regions of cytology smears is ideal for segmenting the CNT agglomerates within these dark, relatively low contrast micrographs. The algorithm was applied using the Auto Local Thresholding plugin from the FIJI distribution of imageJ[232] with a background radius of 15 pixels. The agglomerate content increased with increasing mass loading of CNTs but at all mass loadings the lowest agglomerate content was obtained for a charging ratio of NaC_8 (Figure 7.11).

This change in agglomerate content indicates that there may be an upper limit to CNT dissolution and that CNT spinning at mass loadings at 3 $mg_{CNT}\,mL^{-1}$ is likely to be more successful than higher mass loadings. NaC_8 represents the charging ratio with the best compromise between achieving sufficient charge on the CNTs to lead to electrostatic repulsion and dissolution whilst limiting the amount of charge condensation, which in the extreme case promotes agglomerate formation. This balance of effects, leading to an optimum charging ratio, has been explored previously in the literature for both nanotubide and graphenide solutions and a variety of different values for the optimum charging ratio are reported from $(Na/K)C_7$ to $(Na/K)C_{25}$. [8, 99, 226, 233]

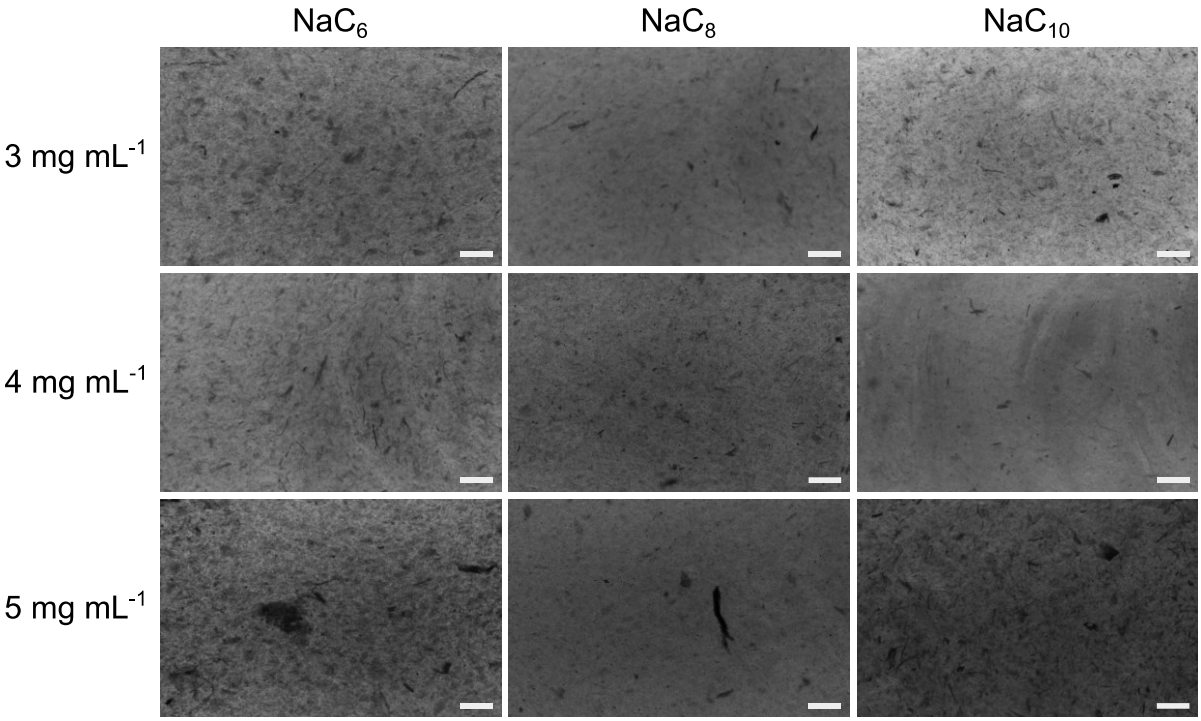


Figure 7.10. Transmission optical micrographs of reduced CNT solutions in DMAc at varying charging ratios and mass loadings prepared from Tuball 01RW03 CNTs (batch 398). Scale bars 200 µm

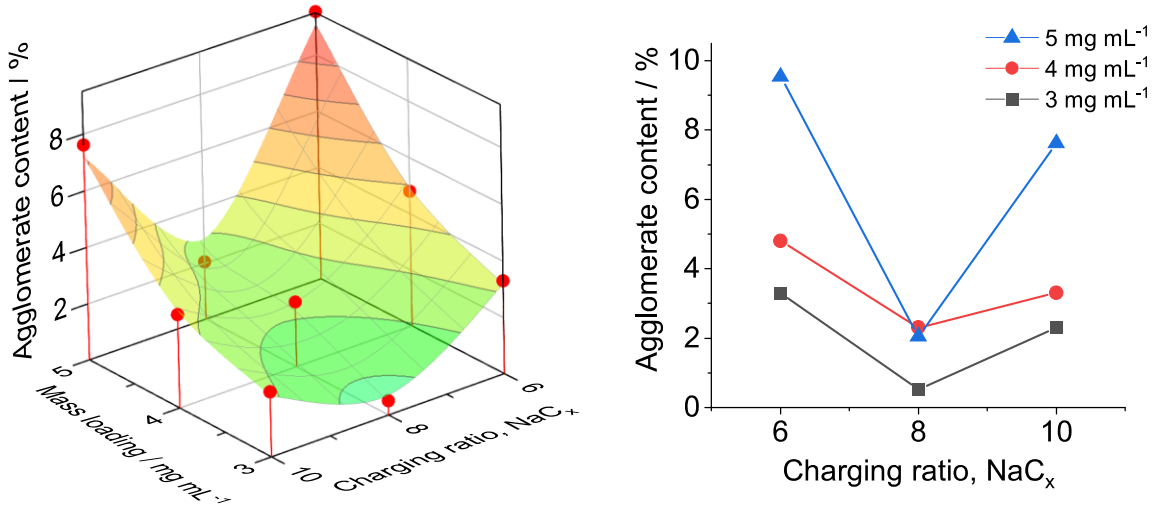


Figure 7.11. Agglomerate content of reduced CNT solutions from Tuball 01RW03 batch 398 as a function of CNT mass loading and charging ratio as determined by Phansalkar local thresholding of optical micrographs.

This process was repeated across a wider range of charging ratios and mass loadings using a later batch of the same CNT product (Tuball 01RW03, batch 788). Solutions for each charging ratio were first prepared at 5 mg_{CNT} mL^{-1} with a solution volume of 4 mL in a 25 mL vial and stirred overnight at 800 rpm. Samples were collected in rectangular capillaries (Vitrocom 3520-050), sealed with wax and transferred out the glovebox for immediate observation. The

solutions were then diluted to 3 mg_{CNT} mL^{-1}, stirred overnight then observed followed by dilution, stirring and observation at 1 mg_{CNT} mL^{-1}. In this case, coloured optical micrographs were captured (Figure 7.12) with consistent illumination and colour balance conditions used across the micrographs and exposure times selected to achieve good contrast. In general exposure times of 2 ms, 1 ms and 0.1 ms were used for mass loadings of 5, 3 and 1 mg_{CNT} mL^{-1} respectively, however samples collected at charging ratios of NaC_{15} and NaC_{20} were noticeably darker at higher mass loadings (Figure 7.12, insets) and hence higher exposure times were required to obtain good contrast in these cases.

It can be clearly seen that the quality of dispersion is strongly driven by the charging ratio. At particularly high charging ratios (NaC_6) there is a mottled appearance of agglomerates. As the degree of charging decreases to NaC_{10} the agglomerate size and number is refined to achieve a relatively uniform dispersion. At lower degrees of charging, incomplete dissolution is observed with large agglomerates in poor quality dispersions. There is a noticeable transition in the colour of the CNT solutions with charging ratio. At high degrees of charging, the solution takes on a distinctly orange colour, which disappears when solutions are quenched by exposure to atmospheric air. This colour is likely to occur due to a change in the electronic transitions available in charged CNTs due to the change in Fermi level.

A similar local thresholding algorithm can be used to quantify the solution quality, however because of the higher image contrast in this case, the Sauvola algorithm generates better thresholding results. Similarly to Figure 7.11, an optimal charging ratio can be identified, although in this case it appears at NaC_{10} rather than NaC_8 (Figure 7.13). It is clear from this study of a wider range of charging ratios that the impact of having insufficient charge for dissolution is more significant than having an excess of charge leading to condensation. It is not clear why the optimum ratio is different in this case, although it may be due to differences between the CNT batches, such as amorphous carbon contents or composition of semi-conducting or metallic CNTs.

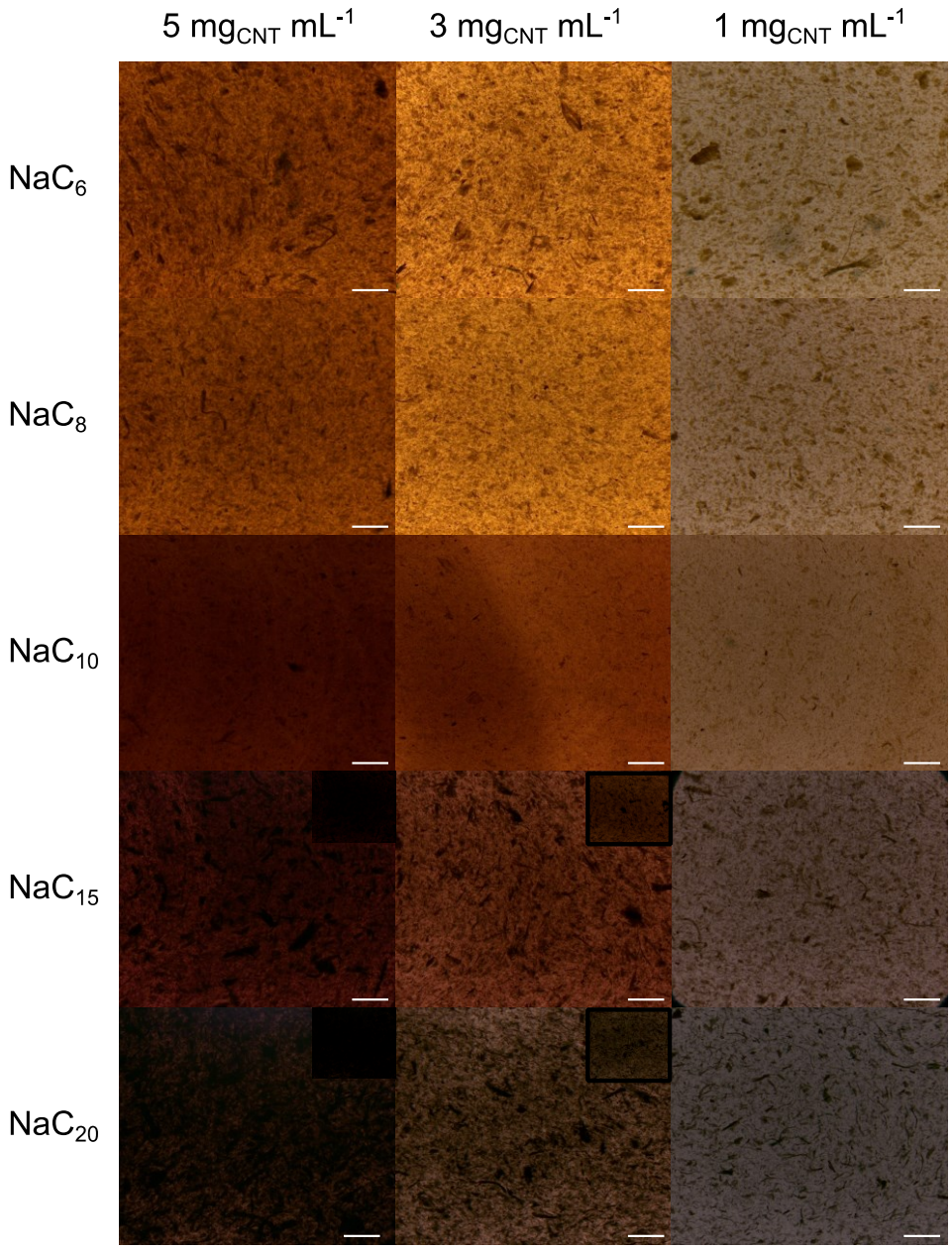


Figure 7.12. Optical micrographs of reduced CNT solutions at charging ratios between NaC_6 and NaC_{20} and mass loadings from 5 mg mL^{-1} to 1 mg mL^{-1} prepared from Tuball 01RW03 CNTs (batch 788). Images are collected with consistent illumination and colour balance. Exposure time was varied for different mass loadings: 5 mg mL^{-1}, 2 ms; 3 mg mL^{-1}, 1 ms; 1 mg mL^{-1}, 0.1 ms. Higher exposures were required for certain conditions, for which the consistent exposure image is shown inset. Scale bars 200 µm.

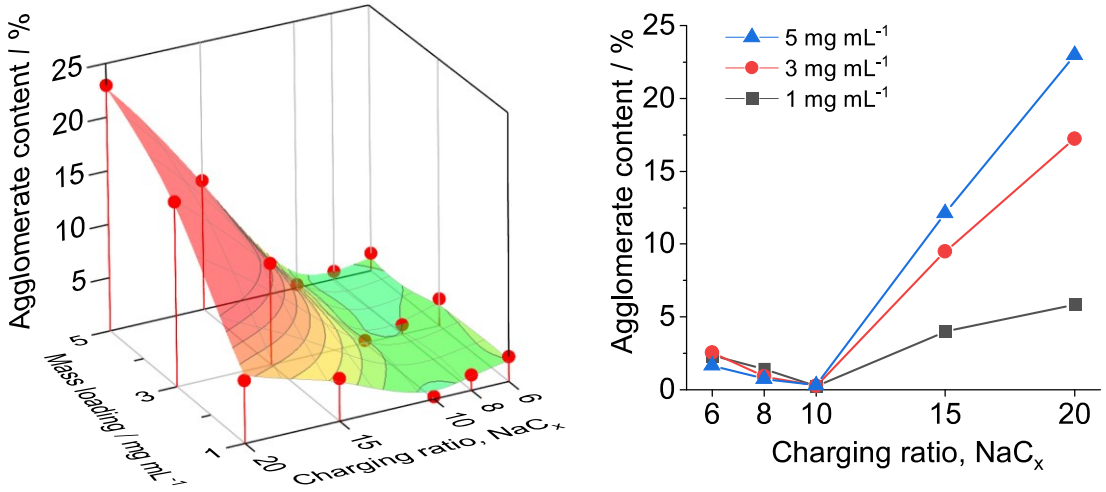


Figure 7.13. Agglomerate content of reduced CNT solutions from Tuball 01RW03 CNTs (batch 788) as a function of CNT mass loading and charging ratio as determined by Sauvola local thresholding of optical micrographs.

7.4.4 Filtration of CNT solutions

The requirement for high intensity stirring to disaggregate agglomerates in CNT solutions presents a limit on the batch size and throughput of dissolution. Filtration through a metal mesh can help reduce the agglomerate content by sieving out larger undissolved agglomerates and by subjecting the solution to shear as it passes through the small apertures.

Custom syringe filters were created by combining Swinnex filter holders (Sigma-Aldrich, 13 mm, polypropylene) with a #500 stainless steel mesh (The Mesh Company, 26 µm aperture, 37% open area). The solutions were first collected into a syringe, the filter was fitted and then extruded through into a collection vial. The resulting filtered dope was imaged in transmission optical microscopy (Figure 7.14).

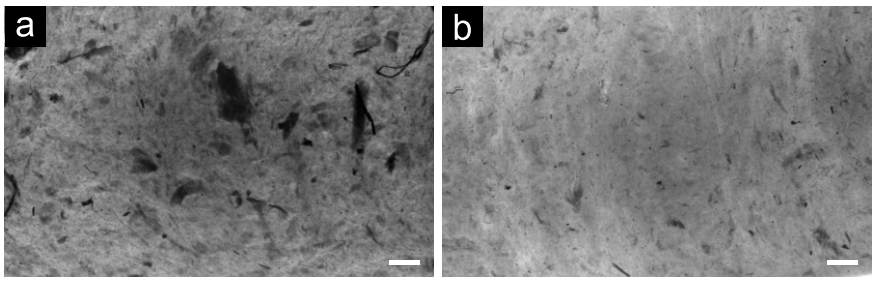


Figure 7.14. Transmission optical microscopy images of reduced CNT solutions prepared at 5 mg_{CNT} mL^{-1} NaC_8 with a solution volume of 25 mL (a) before and (b) after filtration through a 26 µm aperture stainless steel mesh. Scale bars 200 µm.

Filtration through the mesh leads to a significant reduction in agglomerate content with the effective removal of almost all large undissolved CNTs. This presents an opportunity to prepare larger batches of CNT solutions with magnetic stirring. Due to the retention of some fluid (~1 mL) within the filter holder, it was not possible to estimate the filtration yield but it is expected that some of the CNT agglomerates are sieved out, whilst some may be disentangled by the shear at the mesh and pass through. As such, the final mass loading of the filtered spinning dope is not as well controlled but, despite this disadvantage, filtration was used for the work described in Chapter 8, in order to achieve more homogeneous and consistent spin dopes.

7.5 Summary

Through considering the processes affecting dissolution of reduced CNTs, the charging ratio of the CNTs was found to be the most critical factor. Sufficient charge is required to overcome the van der Waal's interactions between CNTs in bundles in order to yield spontaneous dissolution (section 7.2.3, p.126). However, under most charging conditions used in practice, charge condensation can be expected, leading to the (partial) immobilisation of counter-ions on the CNT walls. Molecular dynamics simulations of pairs of charged CNTs indicate that these counter-ions can mediate attractive electrostatic interactions between the CNTs and may prove detrimental to dissolution. Hence, it is expected that an optimal charging condition will exist in which sufficient but not excess charge is added to CNTs, as has been previously explored in the literature.

The optimum charging ratio for the dissolution process used in this work has been determined empirically by quantifying the agglomerate content in the solutions observed by optical microscopy. The optimum charging ratio was found to be independent of the mass loading between 1 and 5 mg_{CNT} mL^{-1} and is between NaC_8 and NaC_{10}. The penalty for under-charging the CNTs is significantly greater than that for applying excess charge. Therefore, to ensure that good quality dissolutions are achieved consistently, further work in this thesis used NaC_8 as the preferred charging ratio. Using this ratio means that, even with changes of composition and purity across different feedstocks, sufficient charge is used. In addition, a small excess of charge may help to accommodate charge quenching from air leaks in downstream processing, or any remaining moisture or oxygen trapped in the feedstocks or reagents.

Experiments have also shown that the intensity of physical mixing is important during dissolution. Care was taken in further work to use consistent volumes of solution, vials and stirring rates to achieve consistent spin dope qualities. In addition, filtration through a 26 µm aperture stainless steel mesh was used to further improve spin dope homogeneity and consistency.

8 Wet spinning CNT fibres

In order to use INTs as a useful analogue for CNTs it is important to understand how the characteristics of the two materials compare. Following guidance from the literature,[88] it was chosen to use single-walled CNTs in this work as they tended to produce the fibres with the highest strengths. In general, the single-walled CNT feedstocks are somewhat longer than the synthesised INTs, with typical lengths of 1-20 µm compared to 200-700 nm.[230] In addition, the diameters of SWCNTs are smaller at 1-2 nm, resulting in overall higher aspect ratios. The persistence lengths of CNTs, while still large at ~1-100 µm,[234-236] is significantly less than the double-walled Ge-INTs used earlier in this work, which have very high bending stiffnesses due to their larger diameter and the greater number of covalent bonds within each wall. As such, CNTs more readily form fibrillated bundles where the individual CNTs bend and deform to form networks (Figure 2.9).

In addition, although both species are stabilised in solution by coulombic repulsion, the nature of the charge is different. In the case of INTs, the surface charge is permanent and localised, arising from the inherent structure of the INT due to variations of bond valency in the tube wall.[197] In contrast, the charge on the CNTs is transferred from a reducing agent as free electrons. This CNT charge is mobile and highly reactive, as illustrated by the range of functionalisation reactions which are known, and may be easily quenched.[9] The differences between CNTs and INTS are likely to strongly influence the coagulation kinetics.

8.1 Rheology of CNT solutions

Despite these distinctions, as solutions of high aspect ratio nanomaterials, CNT and INT solutions should have broadly related rheological behaviour. However, differences in the solvent viscosity, nanotube aspect ratio, feedstock size-dispersity and rigidity will have significant influence. CNT polyelectrolyte solutions are extremely sensitive to air, making typical rheometers unsuitable. A simplified, home-built capillary rheometer was, therefore, used to characterise the fluids. Essentially, the pressure drop was measured for a constant flow of unquenched material passing through a capillary. The CNT solutions are significantly more viscous than INT solutions, even at low mass loadings of just 0.5 mg mL^{-1} (Figure 8.1a). In the range of shear rates studied (~10-1000 s^{-1}) the flow curves closely follow a power law model, as given previously in equation (11) (p.90), and a power law index can be used to

describe the flow curve where an index less than 1 indicates shear thinning behaviour. The CNT solutions are more shear thinning than the INT solutions with power law indices of 0.19 and 0.08 for CNT mass loadings of 1 and 5 mg mL^{-1} respectively compared to 0.48 for aqueous INT solutions at 11 mg mL^{-1} (section 5.1.1). Similarly to the INT solutions, the degree of shear thinning increases with the mass loading of the nanomaterial, showing that as concentrations are increased, greater care may be required to process the dope uniformly during wet spinning (Figure 8.1b). The velocity profiles of these solutions flowing in a cylindrical pipe can be predicted, as before, using equation (12) (p.91). In both 1 and 5 mg mL^{-1} solutions, there is almost no shear in the central region of the pipe. As shown previously using INTs (section 5.1.2, p.92), this lack of shear could lead to inhomogeneous fibres, where the fibre microstructure is influenced by the domain structure of the spinning dope, and inconsistent properties. Due to the opacity of the spinning dopes and the diameter of the spinneret at the start of the taper (~1.4 mm), it was not possible to visualise the alignment of the CNTs using transmission POM with either a polarised lightbox and digital microscope or a 100 W halogen lamp and benchtop microscope.

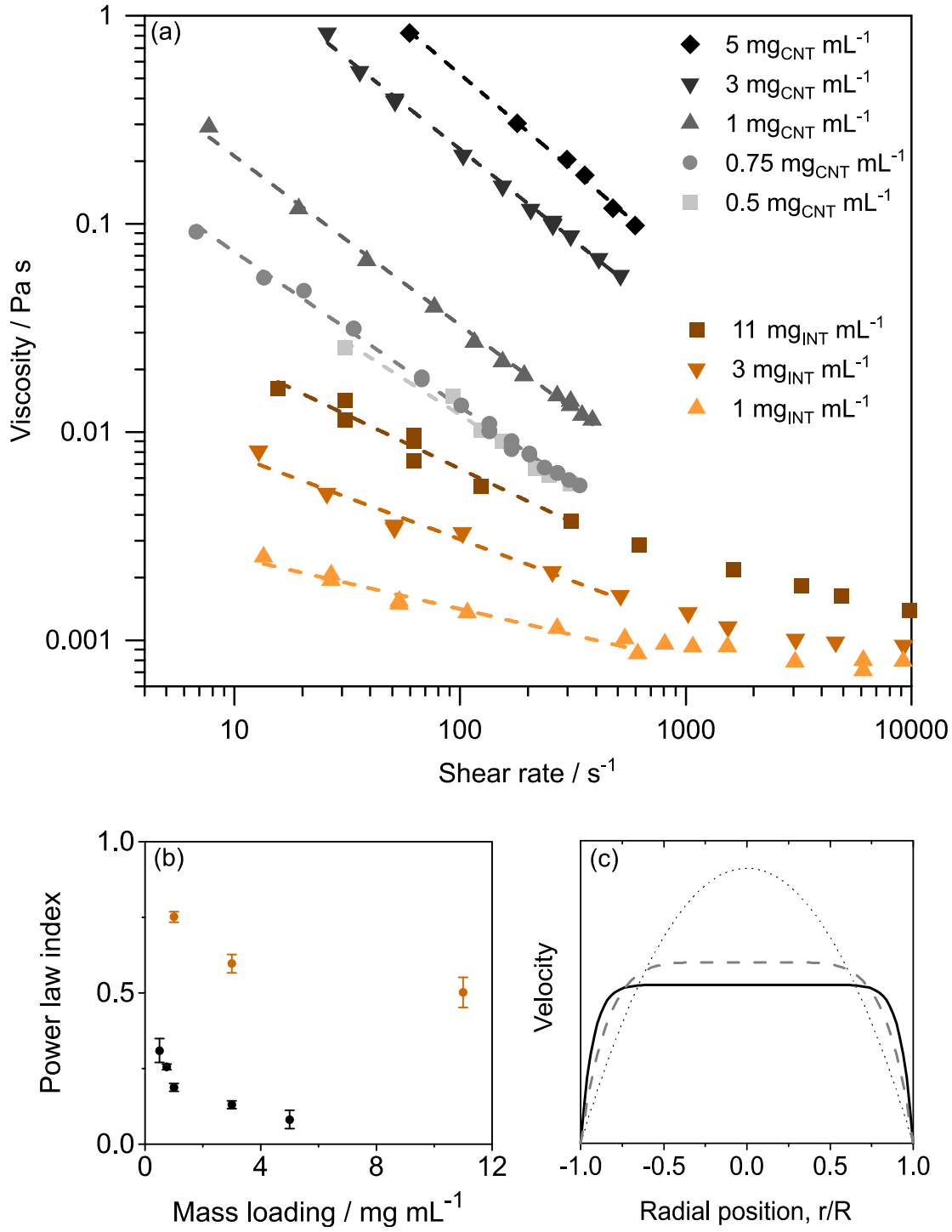


Figure 8.1. (a) Flow curves for (black/grey) Tuball CNT and (brown/orange) INT solutions as determined by capillary rheometry. (b) Power law indices for the straight line fits to the flow curves for (black) CNT and (orange) INT solutions as a function of nanotube mass loading. (c) Predicted velocity profiles for (black solid line) 5 mg mL^{-1} and (grey dashed line) 1 mg mL^{-1} CNT solutions flowing in a cylindrical pipe compared to the (dotted line) parabolic profile of a Newtonian fluid.

8.2 Preparation of CNT spinning dopes

Spinning dopes were prepared using Tuball 01RW03 and eDIPS EC1.5 CNTs following the best identified conditions in section 7.4 (p.131). In order to ensure the spinning dopes remained in the optimal charged state, and were protected against small amounts of quenching from air ingress or incompletely dry solvents, they were prepared at a charging ratio of NaC_8. A typical batch size of 25 mL was used with vigorous stirring. The eDIPS CNT solutions were qualitatively very different to the Tuball solutions. They appeared to be more viscous and also optically less homogeneous. Whilst the Tuball spinning dopes were generally uniform on the 10-100 µm length scale, the eDIPS solutions had a strongly mottled texture with large variation in optical absorbance across the micrograph (Figure 8.2). This texture shows that the CNTs are not homogeneously distributed throughout the spinning dope, and there are signs of the presence of long connected bundles in the micrographs. It is likely that the longer CNTs in the eDIPS feedstocks (section 7.4.1, p.132) are more entangled and therefore more difficult to individualise via reductive charging. POM images of the CNT spinning dopes are difficult to interpret due to the opacity of the CNT solutions limiting the amount of transmitted light (Figure 8.3). The domain structure of the solutions is less apparent than for the INT solutions, and may indicate that the formation of mesophases may be kinetically hindered by the viscosity of the solution and CNT entanglements. Nonetheless, regions of orientational ordering can be seen as bright birefringent areas in the micrographs, showing that CNTs do preferentially align in these solutions.

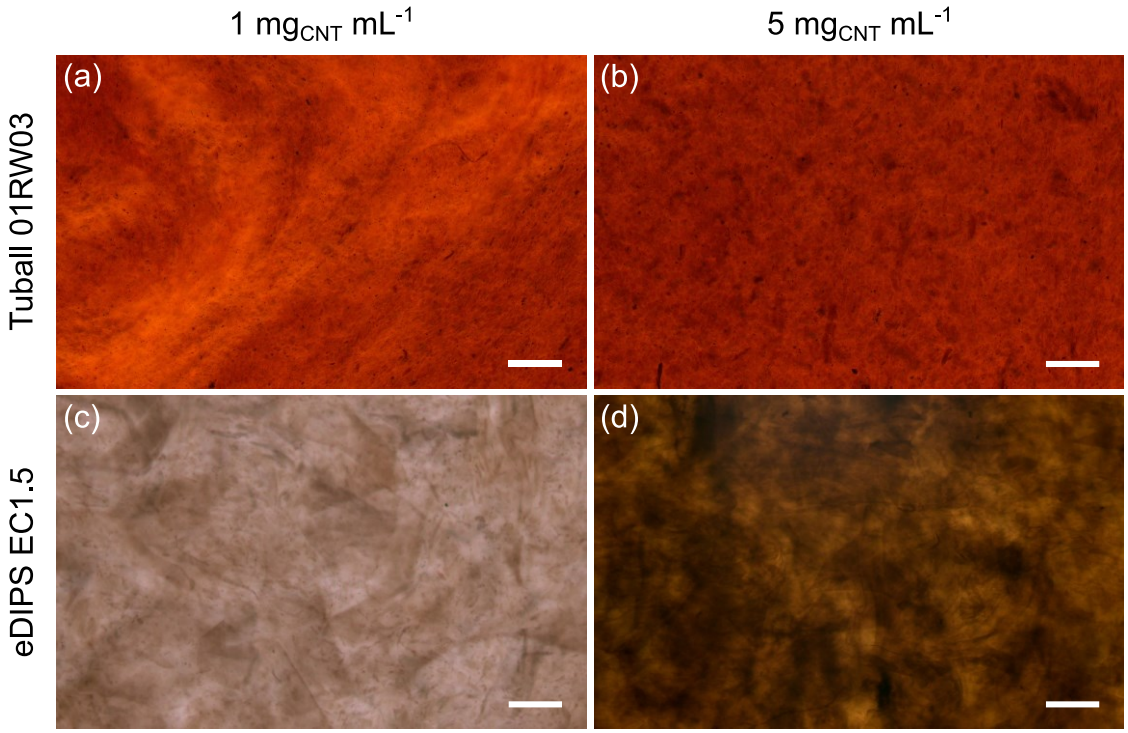


Figure 8.2. Transmission optical micrographs of CNT spinning dopes collected in 0.2 mm thick rectangular capillaries prepared at a charging ratio of NaC_8 from (a,b) Tuball 01RW03 and (c,d) eDIPS EC1.5 CNTs at mass loadings of 1 and 5 mg_{CNT} mL^{-1}. Note: colour and brightness of images should not be compared as different illumination and image acquisition conditions were used in each case. Scale bars 200 μm.

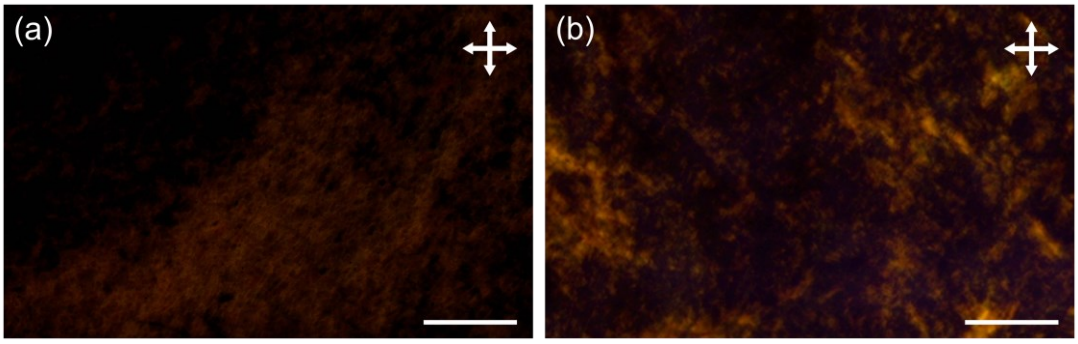


Figure 8.3. Transmission polarised optical micrographs of CNT spinning dopes collected in 0.2 mm thick rectangular capillaries prepared at a charging ratio of NaC_8 at mass loading of 5 mg_{CNT} mL^{-1} from (a) Tuball 01RW03 and (b) eDIPS EC1.5 CNTs. White arrows indicate polariser and analyser directions. Scale bars 200 μm.

8.3 Identifying the CNT spinning processing window

The charged CNT polyelectrolytes are highly reactive and are known to react with oxygen present in air and a variety of chemical reagents.[97] The discharging process occurs relatively quickly and a 30 mL vial of reduced CNT solution can gellate within seconds of exposure to ambient conditions. This behaviour can create challenges for spinning CNT fibres and requires careful choice of coagulant and spinning conditions to achieve stable spinning. In early experiments, it was observed that the tapered glass spinnerets used to spin INT fibres frequently clogged during CNT spinning and were challenging to clean. A silanisation treatment with dichlorodimethylsilane was found to greatly reduce the adhesion of CNTs to the glass surface, reducing the occurrence of nozzle fouling and enabling them to be easily cleaned by flushing with solvent. In order to explore the CNT processing window, a variety of conditions were studied, using different coagulants, spinning dope concentrations, nozzle sizes, injection rates and draw ratios. Videos were collected of the spin dope emerging from the spinneret for a mixture of conditions. These videos were compared to identify the key conditions that affect the stability of CNT spinning, minimise nozzle fouling and enable the stable extrusion of a consistent filament.

8.3.1 Coagulant

The coagulant for wet spinning must typically be an antisolvent for the solute but miscible with the spinning dope solvent so that the solvent diffuses into the coagulation bath whilst the solute solidifies into a fibre. In the case of these CNT solutions, any chemical species which can remove charge from (quench) the CNTs can act as an effective antisolvent. In principle, the rate of coagulation can be adjusted by varying the concentration of the quenching agent in an inert solvent.

Using the pure polar aprotic solvents, DMAc or THF, as the coagulation bath leads to very poor extrusion of the spinning dope. As the dope leaves the spinneret orifice, there is significant swelling and the solution then tends to adhere to the outer surface of the spinneret. As a result, further extrusion of more CNT solution created large ‘bubbles’ at the spinneret rather than a useful filament (Figure 8.4a,b). The INT fibres were successfully coagulated using a salt solution with a high ionic strength as the coagulation bath, where the counterions screen the electrostatic repulsions (Chapters 4 and 5). A similar approach was,

therefore, attempted using these CNT solutions, although the choice of salts was limited by poor solubility of inorganic salts in polar aprotic solvents.[237] Spinning into a 1 M solution of LiBr in DMAc was not significantly better than the pure solvents, with the formation of large globs of poorly coagulated CNTs at the spinneret orifice (Figure 8.4c). More uniform filaments were occasionally formed when spinning in the salt solution, however, the fibre gel strength was extremely low, resulting in fracture when even gentle tension was applied (Figure 8.4d).

Adding ethanol to these polar aprotic solvents, to act as an explicit quenching agent, led to significantly improved extrusion. At 5% (v/v) ethanol in DMAc, a continuous filament could be extracted from the spinneret, although it was very distorted with a large die swell and extremely inconsistent diameter (Figure 8.5a). Increasing the concentration of ethanol to 20% enabled the spinning of a uniform filament which was stable over time, with significantly less die swell (Figure 8.5b). Successful extrusion was also obtained using pure ethanol as the coagulation bath (Figure 8.5c), although it was seen that over time 'hair-like' CNT deposits formed around the spinneret orifice which eventually disrupted the extrusion (Figure 8.5d). The introduction of protic ethanol into the coagulation bath rapidly quenches the spinning dope, forming sodium ethoxide and either hydrogen gas or hydrogenated CNTs. The loss of charge increases the net attractive interactions between the CNTs which imparts strength and some rigidity to the gel fibre. The more rigid proto-fibres swell less as they exit the spinneret, were less likely to adhere to the spinneret and maintained their uniform filamentous shape whilst being 'pushed along' by further material during free flow extrusion.

Empirically, acetone behaves as an ideal coagulant, with smooth, uniform extrusion of a consistent filament. Reactions between reduced CNTs and carbonyl compounds to produce functionalised CNTs have previously been studied[238] and functionalisation with carbon dioxide has also been observed.[239] Similarly, acetone may also react with the reduced CNTs in solution, quenching their charge and causing them to coagulate out of solution. However, the reaction pathway of acetone and nanotubide is not well understood, and may proceed with deprotonation of acetone followed by base-catalysed aldol condensation or potentially simply by nucleophilic addition at the carbonyl carbon. However the reaction proceeds, we would expect to produce some oligomerised or cyclised acetone-derivatives[240] which may, or may not, be grafted to the CNTs. The kinetics of coagulation with acetone qualitatively appear to be slower than with ethanol, potentially due to a longer reaction pathway. Even

using acetone as a coagulant, the gel strength of the fibre remained relatively low causing failure near the spinneret orifice when under draw (Figure 8.6).

In summary, some charge quenching reactivity was needed in the coagulant to stably extrude consistent CNT filaments. Stable extrusion was achieved with acetone and with mixtures of ethanol in DMAc with concentrations varying between 20 and 100% ethanol.

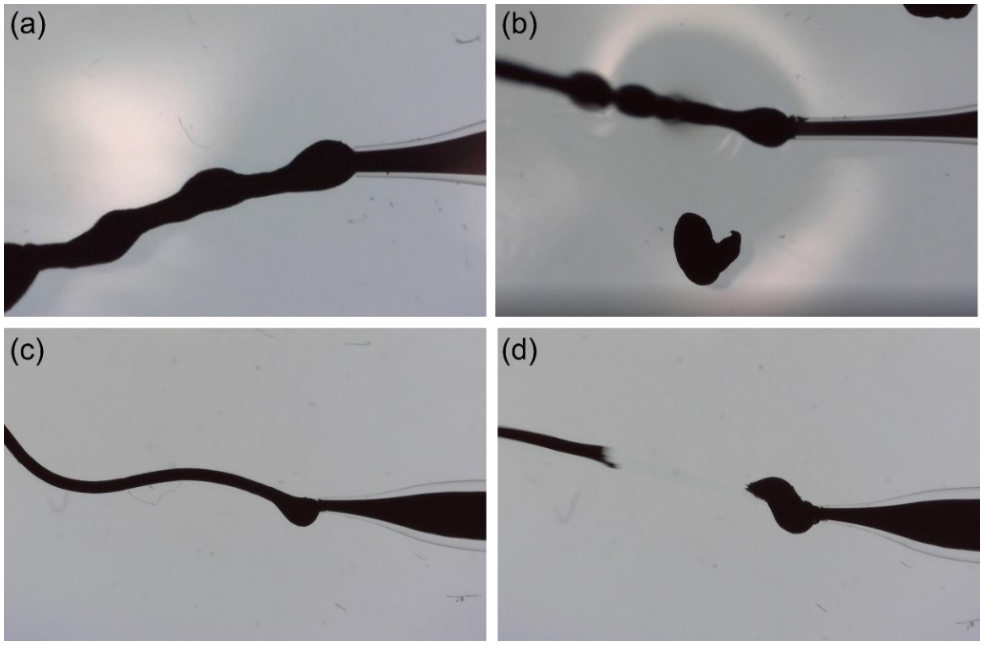


Figure 8.4. Microscope images of CNT solutions extruded into polar aprotic solvents; (a) DMAc, (b) THF and (c,d) 1 M LiBr in DMAc, (c) before and (d) after gentle tension was applied by hand.

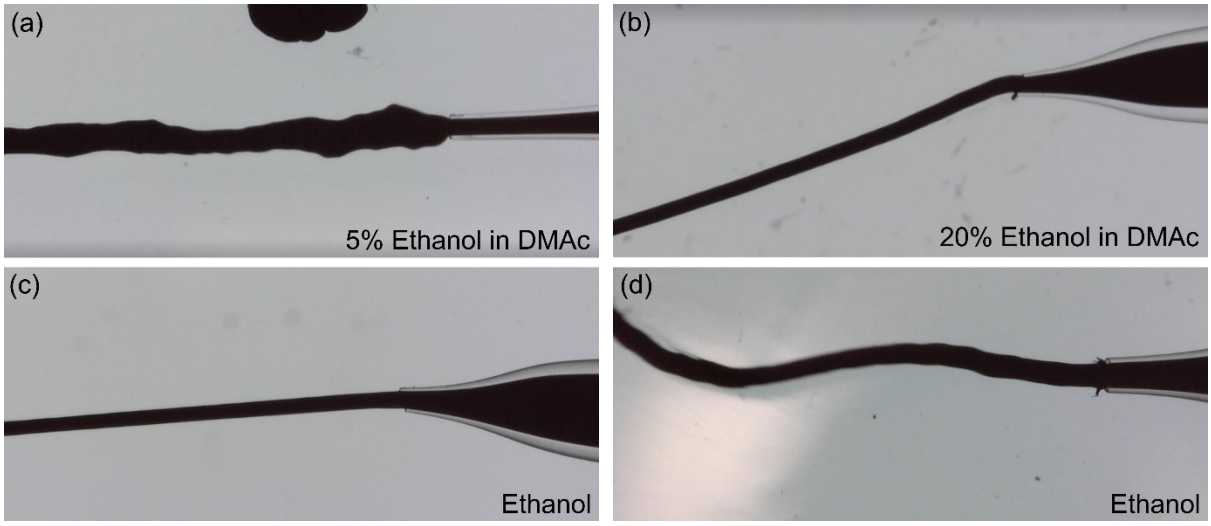


Figure 8.5. Microscope images of CNT solutions extruded into (a) 5% ethanol in DMAc, (b) 20% ethanol in DMAc and (c,d) ethanol.



Figure 8.6. Microscope images of CNT solutions extruded into acetone showing necking and filament fracture under excessive draw.

8.3.2 Dope concentration

The effect of dope concentration on extrusion stability was investigated by comparing identical extrusion conditions with spinning dopes of 2.5 and 5 mg_{CNT} mL^{-1}. In all cases, extrusion was poorer at the lower dope concentration, with significantly less stable flow. Despite these apparent instabilities, continuous filaments were still collected at the lower dope concentration.

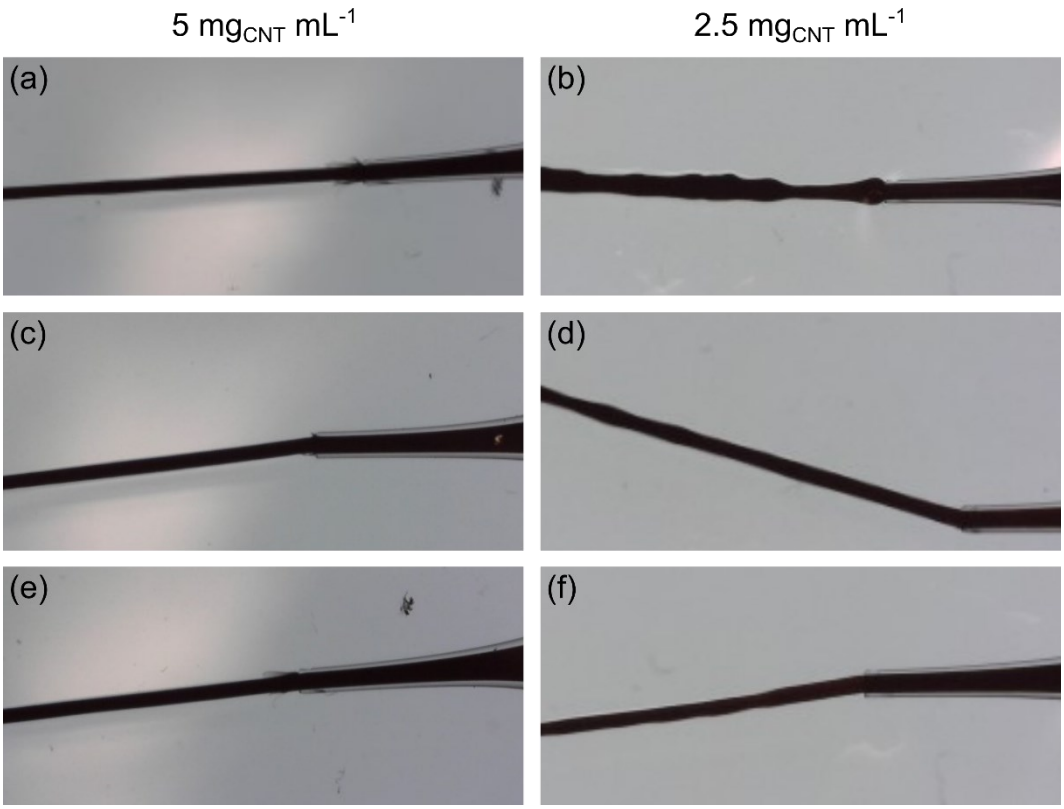


Figure 8.7. Microscope images of CNT solutions with dope concentration of 5 and 2.5 mg mL^{-1} extruded into (a,b) acetone at 5 mL hr^{-1}, (c,d) acetone at 10 mL hr^{-1} and (e,f) ethanol at 5 mL hr^{-1}.

8.3.3 Extrusion velocity

Qualitatively, it was seen that nozzle fouling occurred most frequently when extruding at relatively slow injection rates, with the formation of deposits at the spinneret orifice. In some cases, these deposits could be removed by rapidly increasing the flow rate, displacing them from the tip. However, on return to the lower flow rates they would form again and start to disrupt the flow after approximately 1 minute.

The formation of these deposits was reduced by increasing the velocity of injection, by either reducing the size of the spinneret orifice or increasing the flow rate of the injection. Two different spinneret nozzles (orifice diameter 511 and 329 µm, Figure A6) and two different flow rates (5 and 10 mL hr^{-1}) were used to explore this fouling in both acetone and ethanol coagulation baths. The spinning dope was injected into a static coagulation bath under free-flow conditions (i.e. with no take-up) and, for each case, the extrusion was categorised as unstable, poor or satisfactory (Figure 8.8). In all cases, the quality of the extrusion was improved by increasing the extrusion velocity. Satisfactory extrusion was achieved in acetone at a velocity of 13.5 mm s^{-1}, whilst a higher velocity of 16 mm s^{-1} was required when spinning into ethanol. These trends follow the previous observations (section 8.3.1, p.148) that the coagulants which more rapidly quench the CNT solution are most prone to spinneret fouling and therefore require a higher extrusion velocity.

The relationship between coagulation speed and extrusion velocity was investigated further using binary mixtures of ethanol and DMAc, where the speed of coagulation was expected to be proportional to the concentration of ethanol in the coagulation bath. A consistent spinneret was used throughout this experiment (orifice diameter 281 µm) with the extrusion velocity varied between 2 and 58 mm s^{-1} by adjusting the injection rate on the syringe pump. As before, extrusion was unstable in pure DMAc, and improved significantly when using a coagulation bath containing ethanol (Figure 8.9a). Increasing the concentration of ethanol in the coagulation bath improved the extrusion stability with the best performance over the widest range of extrusion velocities for coagulation baths containing 50% and 75% ethanol by volume. Extrusion was poorer using pure ethanol as the coagulant, predominately due to the formation of the previously noted hair-like deposits at the spinneret tip (Figure 8.9c).

Low extrusion velocities resulted in a kinked proto-fibre with a diameter which varied along the fibre length (Figure 8.8b and Figure 8.9d,f). When the spinning dope is injected at a slow rate, the coagulation can occur before it is extruded from the nozzle, forming a plug. The plug is then pushed out by the following material, leading to a region with a smaller diameter and the process repeats with the pattern resulting in kinks and diametral variations with a distinct periodicity. Extruding at a faster rate reduced this behaviour in all the coagulants, resulting in better quality extrusion at higher extrusion velocities.

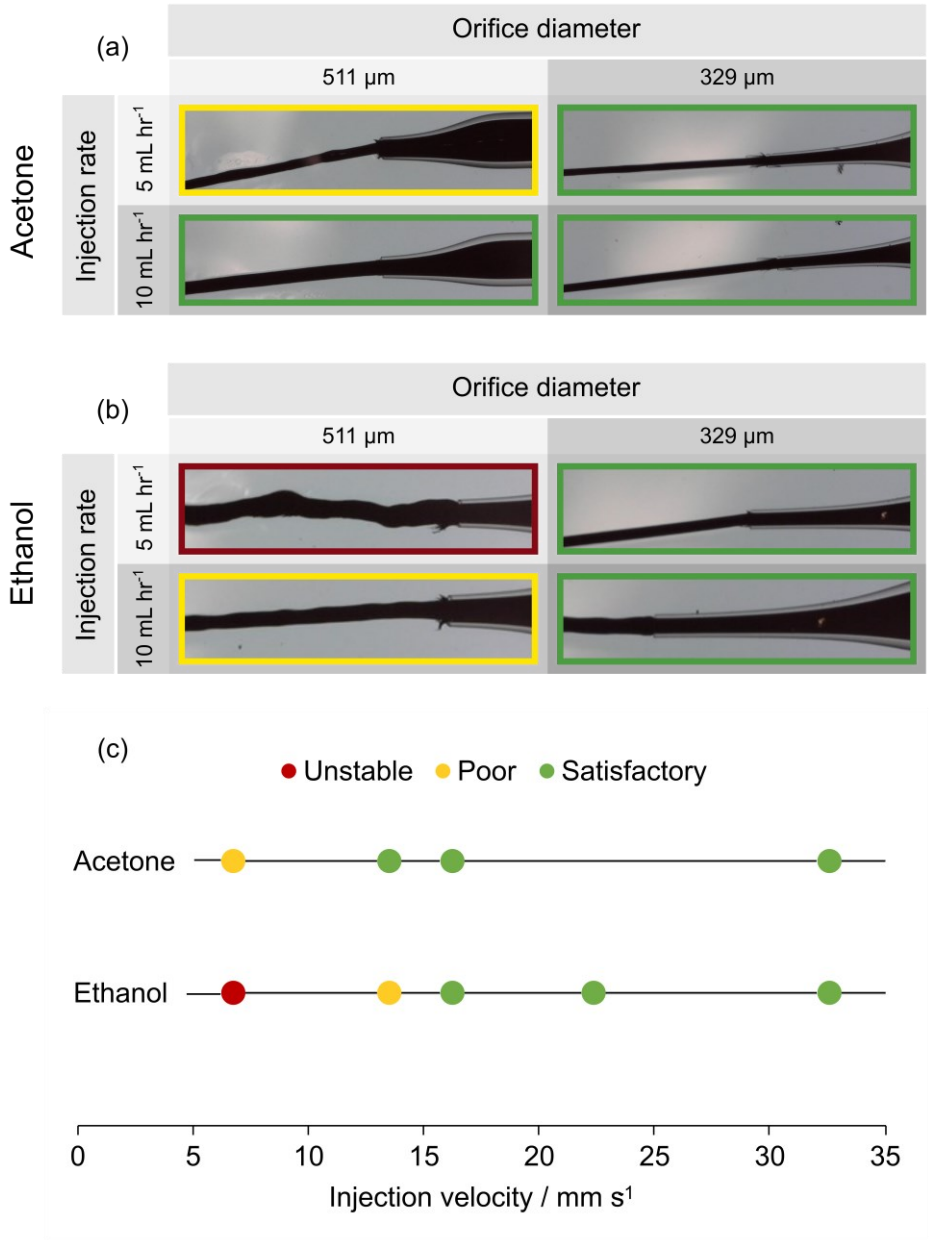


Figure 8.8. Microscope images of CNT solutions extruded into (a) acetone and (b) ethanol at a range of velocities varied by changing the spinneret orifice diameter and the injection rate. (c) Extrusion was categorised as (red) unstable, (yellow) poor and (green) satisfactory for each condition.

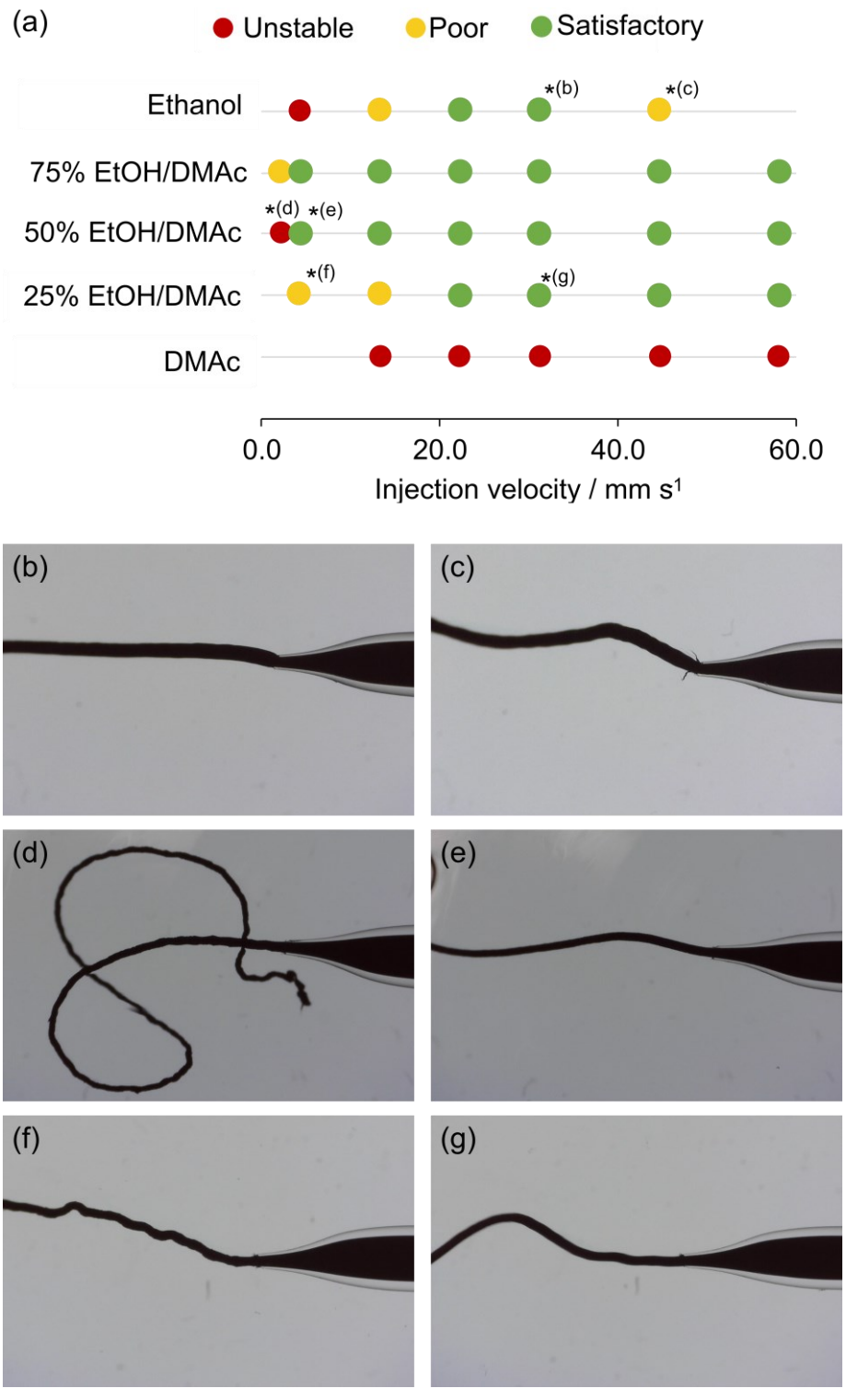


Figure 8.9. (a) Processing window for extrusion of CNT spinning dope into binary mixtures of ethanol and DMAc with (b-g) microscope images of selected process conditions.

8.3.4 Draw ratio

For the INT fibres, it was crucial to apply even a small amount of draw to maintain uniform alignment after leaving the spinneret (section 5.1.4, p.95). Draw ratio was similarly expected to be important when spinning CNT fibres.

As the draw ratio was increased, instabilities were observed on the proto-fibres with a periodic variation in the diameter characteristic of draw resonance.[241] Draw resonance is typically found to occur at a critical draw ratio, which can be as low as 3 for shear thinning polymer melts.[242] The CNT spinning line has been modelled by Jeong and Kim et al.,[243] identifying the stability window of the spinning process as a function of the Deborah number (rotational relaxation time divided by residence time in the spin line) for solutions of CNTs in chlorosulfonic acid coagulated in acetone. The maximum stable draw ratio varied from approximately 1.5-4 with the critical draw ratio decreasing as Deborah number (and hence flow rate) increased.

The stable draw ratio window for spinning CNT fibres, using the reductive approach, was determined for acetone and ethanol at two different extrusion velocities. Similarly to the model by Jeong and Kim, when coagulating in acetone, the maximum stable draw ratio was lower at higher extrusion velocities. Onset of resonance was visible at draw ratios of 1.5 and 1.3 for extrusion velocities of 16 and 32 mm s^{-1} respectively and increasing the draw ratios further (to 1.8 and 1.5) led to filament failure. Stable spinning with no observable signs of draw resonance was possible at a draw ratio of 1.2 for both extrusion velocities. In comparison, the proto-fibres are much less drawable in ethanol than acetone, with filament failure occurring at draw ratios of 1.1 and 1.2 for extrusion velocities of 16 and 22 mm s^{-1}. This trend with flow rate deviates from that expected in draw resonance models,[243] suggesting that filament failure in pure ethanol coagulants is driven by the poor extrusion at low flow rates (as discussed in section 8.3.3, p.152) rather than draw resonance.

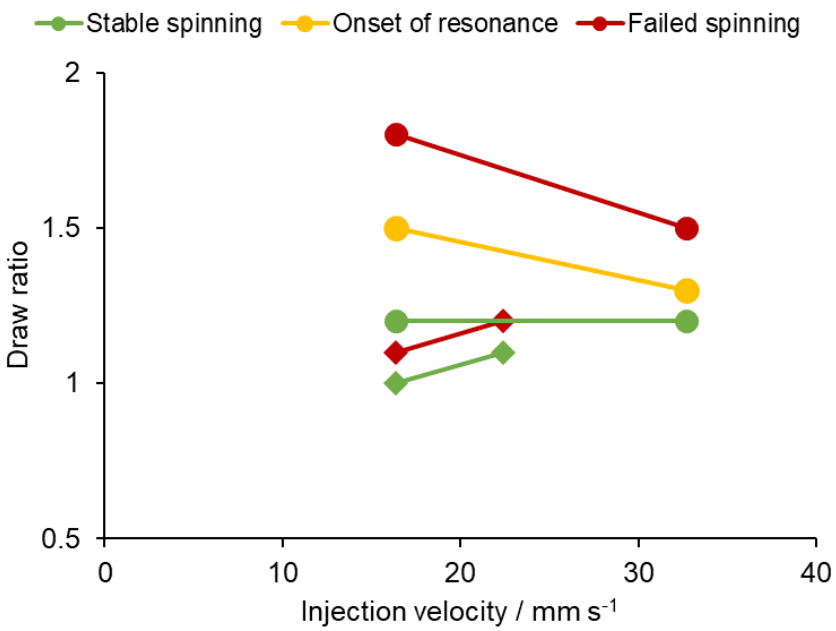


Figure 8.10. Critical draw ratios for draw resonance instabilities for spinning in (circles) acetone and (diamonds) ethanol.

8.3.5 CNT feedstock

In addition to the OCSiAl Tuball 01RW03 CNTs used above, spinning experiments were trialled with Meijo eDIPS EC1.5 CNTs. Compared to Tuball, the extrusion of eDIPS spinning dopes was visibly less stable and the proto-fibre emerged with a variable diameter which appeared to be due to inhomogeneities in the spinning dope (Figure 8.11). As seen in the images of the CNT solutions where the eDIPS CNTs are less well dissolved (section 8.2, p.146), the CNTs in the spinning dope do not appear to uniformly distributed resulting in a 'lumpy' proto-fibre due to the extrusion of regions with more and less CNTs. This behaviour was consistent across a range of extrusion velocities and appeared to be characteristic of the spinning dope, although in general a better quality extrusion was observed at higher injection rates. Despite the irregular appearance of these proto-fibres it was possible to consistently spin fibres from these feedstocks, and in the conditions tested (50% ethanol in DMAc), no issues with nozzle fouling were observed.



Figure 8.11. Microscope images of 5 mg mL^{-1} eDIPS CNT solutions extruded into a 50% ethanol/DMAc coagulation bath at a velocity of (a) 11, (b) 22 and (c) 41 mm s^{-1}.

8.4 Effect of process parameters on CNT fibre tensile properties

Whilst exploring the process parameter window for stable spinning, fibres were collected where possible and the mechanical properties were determined by a single filament tensile test. As a large number of process variables were changed throughout this experiment, directly comparable data are not always available for each parameter. However, grouping the mechanical properties as a function of the key process variables provides an initial comparison. Firstly, the tensile data is compared for Tuball CNT fibres spun using a variety of coagulants and then Tuball CNT fibres are compared to eDIPS CNT fibres. Where possible, properties are explored as a function of the draw ratio, the mass loading of the CNT dope and the extrusion velocity.

8.4.1 Coagulant

For the Tuball CNT fibres, there is significant scatter within the tensile results for each of the coagulants used and, as a result, no statistically significant differences were identified between the coagulants (Figure 8.12). These data suggest that there is no singularly ideal coagulant, and instead strong (and weak) fibres may be produced with each coagulant depending upon the other process parameters; furthermore, batch-to-batch variability has a significant impact on the fibre properties. However, some of the best performing fibres were coagulated in the 50% ethanol coagulant, with the specific strength values falling into two distinct groupings (Figure 8.12c). The weaker grouping, with a specific strength of approximately 0.2 N tex^{-1}, were extruded at significantly higher extrusion velocities (60-90 mm s^{-1}) compared to the stronger grouping, centred around 0.35 N tex^{-1}, extruded at more moderate velocities (20-30 mm s^{-1}). A potential conflating factor is that these groups were also spun from different batches of CNT solutions. Without a control between these groups it is not possible to rule out variation in the quality of the spinning dope, perhaps by oxygen infiltration in the glovebox or other experimental variation.

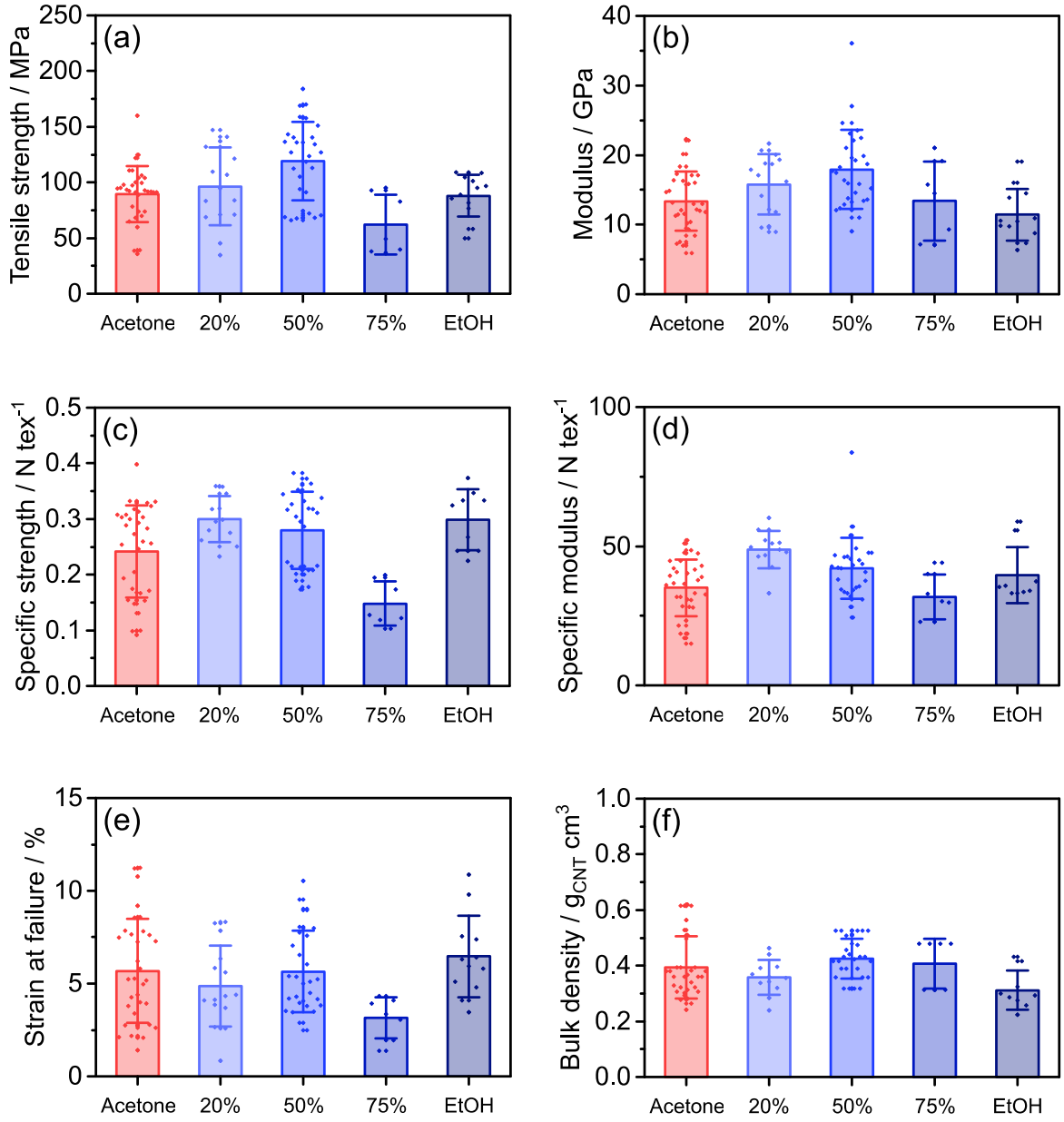


Figure 8.12. Mechanical and structural properties for Tuball CNT fibres spun with a variety of process conditions into (red) acetone and (blue) ethanol/DMAc coagulation baths. The concentration of the ethanol/DMAc mixtures is given as the volume percentage of ethanol. Error bars indicate 1 standard deviation.

8.4.2 Draw ratio

More directly comparable data are available for exploring the effect of draw ratio, as fibres were sometimes collected at different draw ratios during the same spinning experiment. Within each experiment, there was no significant difference in tensile strength or specific strength, however there was consistently a higher elastic modulus and lower strain at failure for fibres spun with a higher draw ratio (Figure 8.13). This outcome indicates that the characteristics of the CNT fibres are modified by the draw ratio, but that the intrinsic strength is more greatly affected by the other processing parameters. A possible interpretation is that higher draw ratios result in more aligned fibres, with increased stiffness but reduced ductility. It was difficult to verify this hypothesis due to the difficulties of determining CNT alignment without synchrotron X-ray sources (section 3.3.3, p.64), but it is consistent with such measurements made elsewhere in the literature.[178, 244] Whilst this argument runs counter to the results obtained for INTs in Chapters 4 and 5, the nature of the nanotubes and their networks are quite different (Figure 2.9, p.36 and section 8, p.143). There is, therefore, an opportunity to create a series of grades of CNT fibres, with some designed for higher stiffness and others designed for higher strain applications.

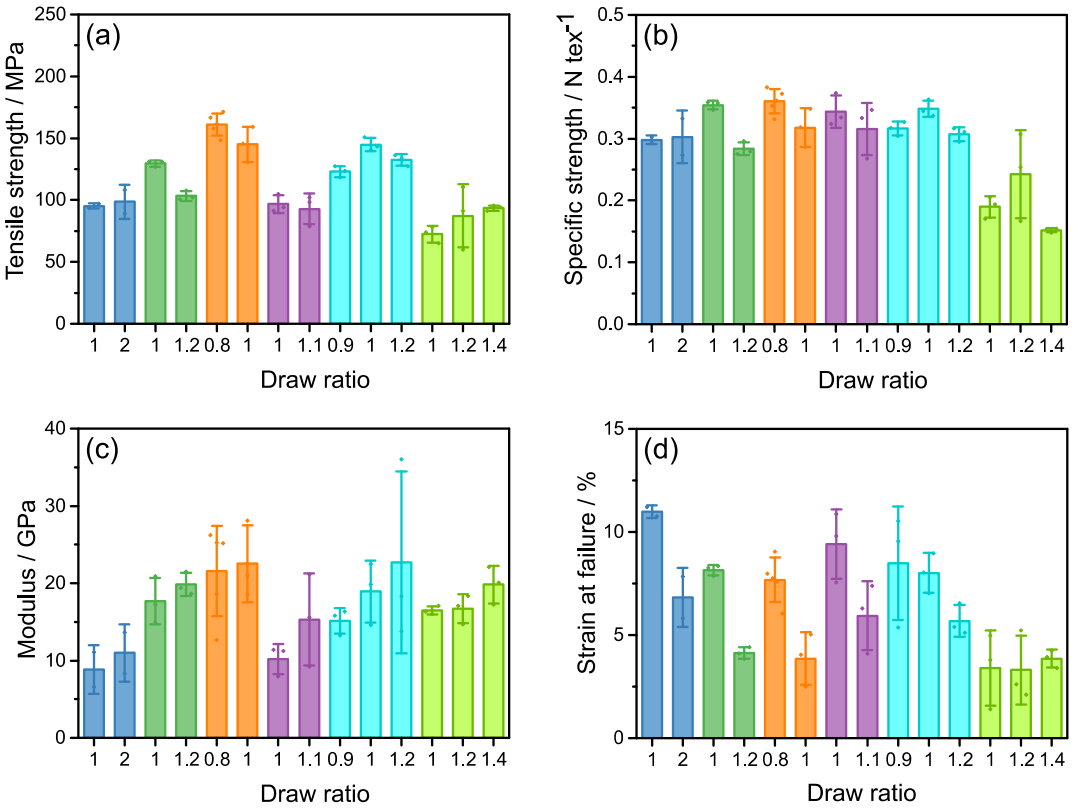


Figure 8.13. Mechanical properties of fibres spun at various draw ratios, with otherwise identical conditions.

8.4.3 CNT feedstock

Despite the apparent instabilities seen when extruding fibres from the eDIPS spinning dopes, the fibres show remarkably good mechanical properties with significantly higher strength (~170 MPa and ~0.4 N tex^{-1}) than the Tuball fibres (~120 MPa and ~0.35 N tex^{-1}) despite having similar bulk density (Figure 8.14). The difference between the fibre properties is driven by a higher yield strength of the eDIPS fibres, as seen on the stress strain curves (Figure 8.14g). The behaviour of the fibres is qualitatively the same, with an initial stiff elastic response followed by yield with plastic deformation, but with quantitatively superior properties for the eDIPS fibres. In this case, the higher aspect ratio of the eDIPS CNTs likely leads to a more entangled network in which more CNTs are loaded efficiently, which requires a higher overall stress before plastic deformation can occur. The initial modulus of the fibres is less strongly affected by the length of the CNTs, as it pertains to a loading condition below the critical shear stress in both sets of fibres, although the eDIPS fibres appear to have a slightly higher stiffness. As the bulk densities for these fibres are equivalent within error, this increased stiffness must relate to improved network efficiency in the eDIPS fibres, in a similar way to the jammed networks in INT fibres (section 4.3.3, p.85).

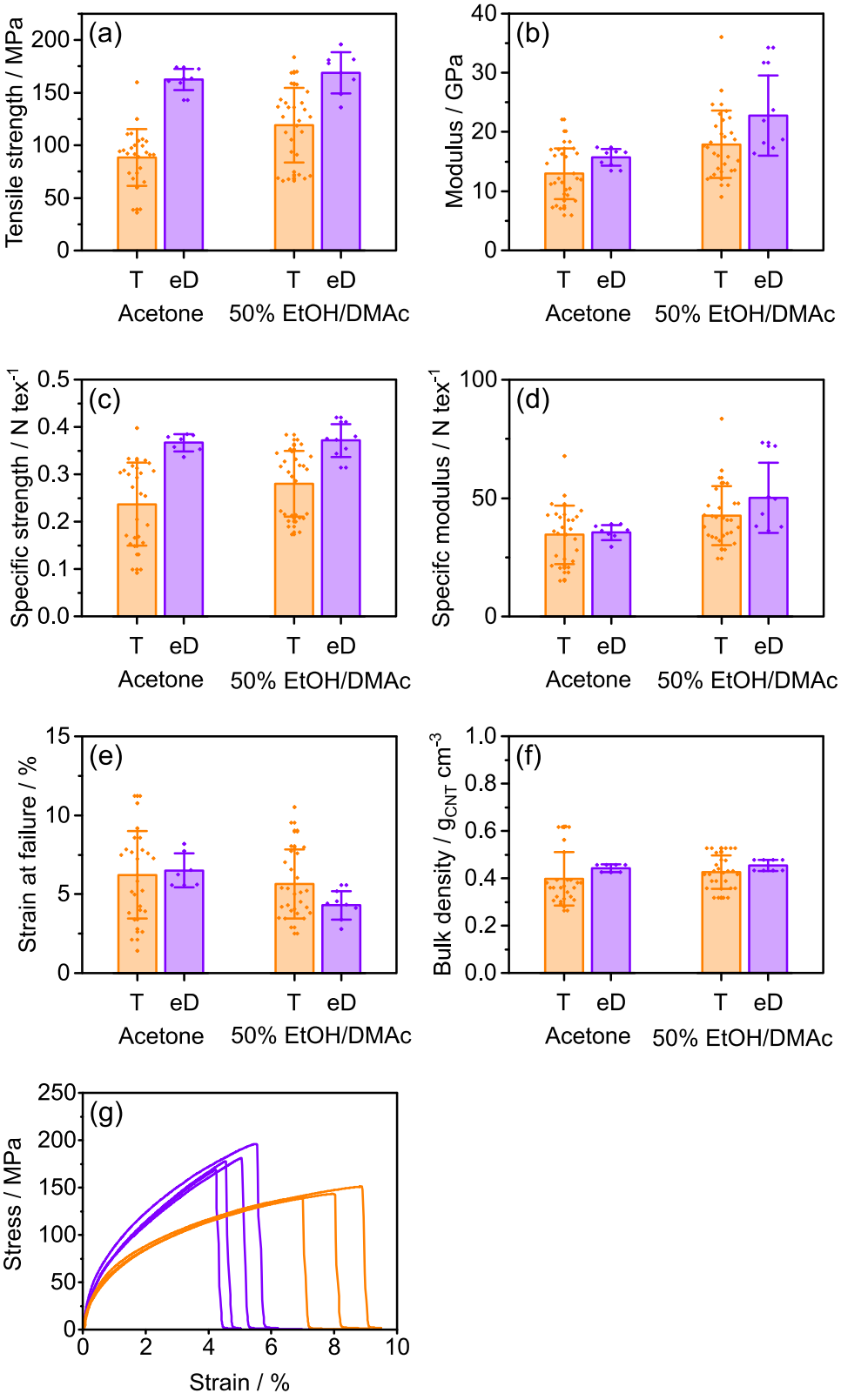


Figure 8.14. (a-f) Mechanical and structural properties of CNT fibres spun from 5 mg mL^{-1} (orange, T) Tuball and (purple, eD) eDIPS spinning dopes. Error bars indicate 1 standard deviation. (g) Stress-strain curves for CNT fibres spun from (orange) Tuball and (purple) eDIPS spinning dopes in 50% EtOH/DMAc coagulant with 22 mm s^{-1} extrusion velocity and draw ratio 1.

8.4.4 Dope concentration and extrusion velocity

As the mechanical properties of Tuball and eDIPS CNT fibres are significantly different, it is important to separate them when exploring the data to identify the influence of extrusion rate, extrusion velocity and spin dope mass loading. For the Tuball CNT fibres, there were comparable data available for fibres spun from spinning dopes with CNT mass loadings of 2.5 and 5 mg_{CNT} mL^{-1} for acetone and ethanol coagulation baths (Figure 8.15). Across these data, there is no significant difference between the sets of fibres. For each mechanical property the values for 2.5 mg mL^{-1} exists within the range of values for 5 mg mL^{-1} suggesting that across this range of values, the mass loading of the CNT spinning dope has, at most, a minor impact on the fibre properties.

For the eDIPS fibres, a series of experiments were conducted using spin dope mass loadings of 1 and 5 mg mL^{-1}, at a range of extrusion velocities, with an acetone coagulation bath and consistent spinneret and draw ratio (Figure 8.16). It is immediately apparent that for extrusion velocities greater than 20 mm s^{-1}, the fibres spun from the 1 mg mL^{-1} dope are significantly stronger than those spun from the 5 mg mL^{-1} dope on both an area and a mass basis (Figure 8.16a,c). The higher strength coincides with a higher CNT bulk density (and hence packing density), which may partly explain the difference in strength. However, the bulk density does not vary significantly with extrusion velocity (Figure 8.16f), whereas the strength increases sharply above a critical rate. This trend follows the observations that the stability and consistency of extrusion is highly dependent on the velocity (section 8.3.3, p.152), and it therefore follows that strength, which is a highly defect dependent property, improves for conditions with more stable spinning. The effects of varying the mass loading and extrusion velocity can be observed in the specific stress-strain curves (Figure 8.16g). The fibres spun at an extrusion velocity of 9 mm s^{-1} undergo significantly more plastic deformation at lower stresses, whilst higher stresses are required to plastically deform those extruded at higher velocity. The instabilities in extrusion at low velocities may result in regions with a more deformable microstructure, potentially due to areas with lower local density and variations in alignment.

In summary, the key process factors affecting the CNT fibre properties appear to be the type of CNT, and the parameters affecting solution quality and extrusion stability, for a given set of other conditions. The eDIPS CNTs showed significantly improved mechanical properties

compared to Tuball CNTs (specific strength 0.4 vs 0.35 N tex^{-1}) when tested with an equivalent spinning dope mass loading of 5 mg mL^{-1}, despite the comparably poorer extrusion stability (section 8.3.5, p.156). Reducing the eDIPS CNT mass loading to achieve a more homogeneous spinning dope and increasing the extrusion velocity to obtain more stable extrusion results in further significant improvement in tensile properties to a specific strength of 0.8 N tex^{-1}. In comparison, the homogeneity of Tuball CNT spinning dopes is not significantly affected by mass loading and hence the fibre properties are similarly insensitive to this parameter. Although the importance of achieving a stable extrusion with long, high quality CNTs has been demonstrated here, it is still unclear how changing the coagulation process affects the CNT fibres. No significant difference was apparent between acetone and a variety of ethanol/DMAc coagulation baths despite the expectation that coagulation kinetics and the time allowed for coagulation and diffusion should affect the fibre microstructure.

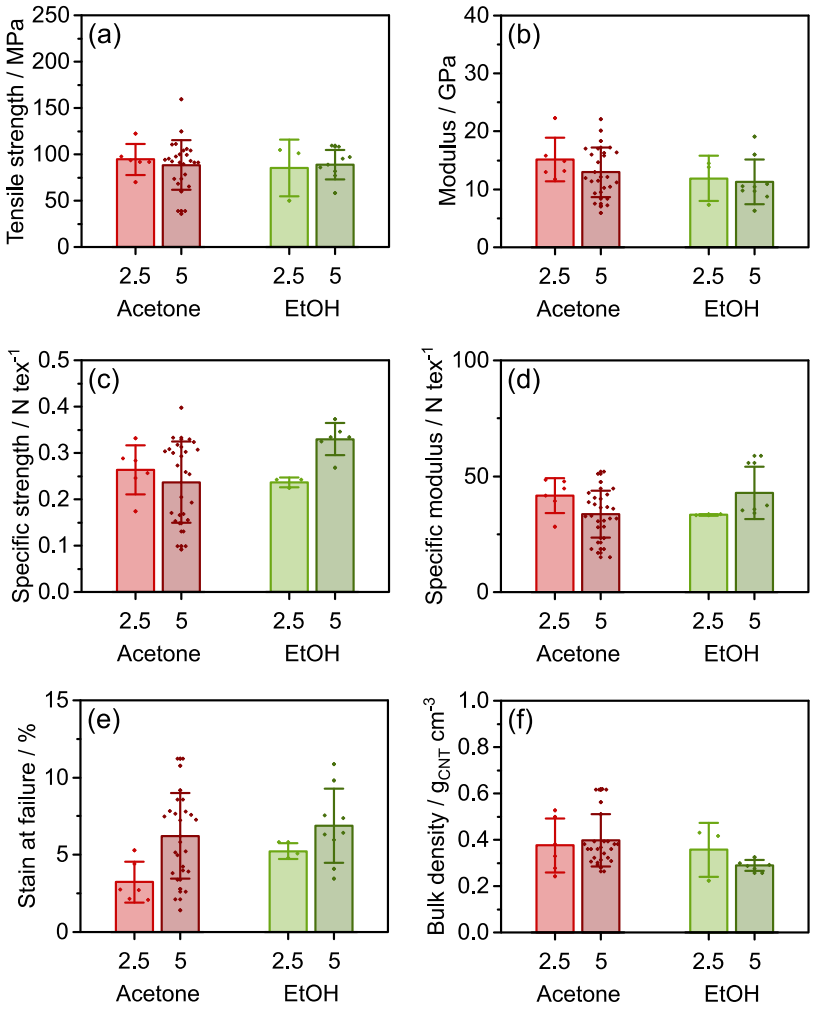


Figure 8.15. Mechanical and structural properties of Tuball CNT fibres coagulated in (red) acetone and (green) ethanol coagulation baths with spinning dope mass loadings of 2.5 and 5 mg_{CNT} mL^{-1}. Error bars indicate 1 standard deviation.

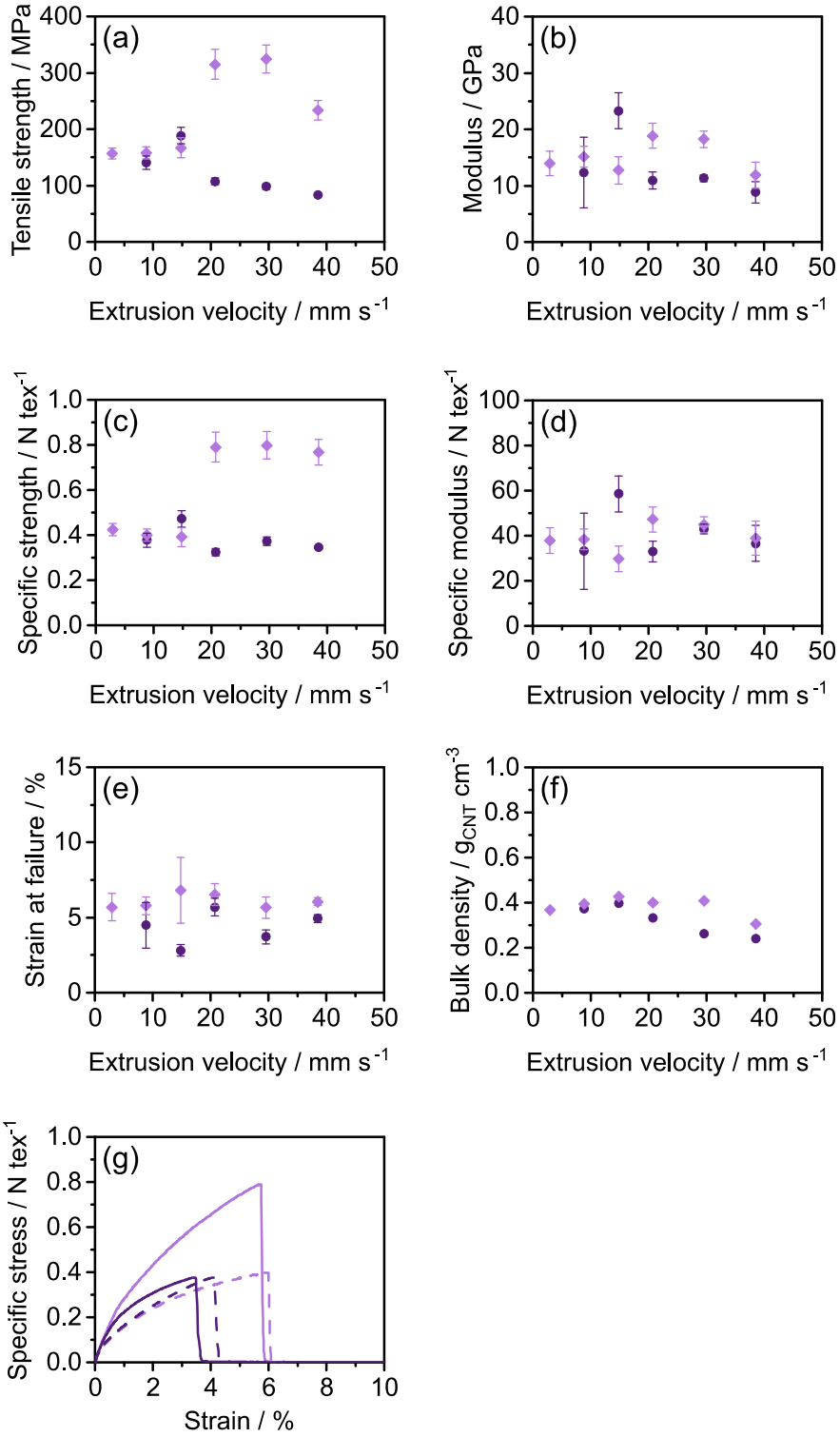


Figure 8.16. Mechanical and structural properties of eDIPS CNT fibres coagulated in acetone with spinning dope mass loadings of (light diamonds) 1 and (dark circles) 5 mg_{CNT} mL^{-1} and a draw ratio of 1.2. Error bars indicate 1 standard deviation. (g) Representative specific stress-strain curves for CNT fibres spun from (light) 1 and (dark) 5 mg mL^{-1} spinning dopes at extrusion velocities of (dashed) 9 and (solid) 30 mm s^{-1}.

8.5 Batch-to-batch variation in CNT fibre properties

In order to explore the batch-to-batch variation of CNT fibre properties across identical conditions, the best initial fibre conditions (eDIPS 1 mg mL^{-1}, acetone coagulant, DR 1.2, varied extrusion velocity) were repeated three times over the course of several months using separately prepared CNT spinning dopes.

There was a significant error in determining the cross-sectional area of the fibres by transmission microscopy due to diametral variation along the fibre length and, although this was mitigated somewhat by averaging over the cross-sections for the individual filaments, there was significant batch-to-batch variation (Figure 8.17a). The random sampling along the length of the tensile specimens resulted in large variations in the measured diameter and this error was magnified in the calculation of the cross-sectional area. Due to this random error, there was considerable scatter in the calculated tensile strength and elastic modulus of the fibres; fibres with a smaller measured cross-section had a significantly larger calculated strength (Figure 8.17c,d). Unfortunately, this uncertainty also affected calculations of the fibre density, making comparisons of packing fraction across different conditions extremely challenging. Instead, in order to obtain an estimate for the tensile strength of the produced fibres, the average breaking force for each condition can be divided by an approximate cross-sectional area averaged over the whole data set.

It was found that the breaking force of the fibres was surprisingly consistent across batches for each spinning condition. Using the spinning conditions to calculate the CNT linear density (which is constant for all these fibres at 0.078 g_{CNT} km^{-1}) allows us to determine the specific strength which provides us a metric for fibre strength which is consistent across the batches (Figure 8.17e). Ignoring some outliers, which may have arisen due to some experimental error, the difference in the mean values between batches is at most 10% and more typically less than 5%. Incidentally, removing these outliers reinforces the trend of specific strength with extrusion velocity discussed in section 8.4.4. It might be expected that the specific modulus should provide a similarly useful indicator, however intra-batch scatter for the modulus is significantly higher making comparison more difficult across different conditions. In this work it was not possible to measure the linear density of individual tensile specimens in a conventional manner due to their extremely low mass (~1.5 μg), although vibroscopic

techniques may be used in future work. In order to justify the calculation of linear density from the spinning parameters a 1.66 m length of fibre (with a calculated linear density of 0.098 g km^{-1}) was weighed using a TGA balance. The determined linear density (0.138 ± 0.004 g km^{-1}) is somewhat higher than the calculated value, perhaps indicating the presence of some remnant reagents such as trapped solvent or naphthalene within the fibres. As such, the true specific strength of these fibres may be ~30% lower than those reported here in units of N g_{CNT}^{-1} km, however, the calculated strengths are still suitable for comparison within the sample sets.

The strain at failure is independent of other measurements and can be confidently identified for each tensile sample with an estimated error of 0.1%, although as with the specific modulus there is a significant intra-batch variation, which may limit its utility as a comparative metric (Figure 8.17b). Increasing the consistency of the strain at failure and specific modulus would likely be possible by more tightly controlling some of the extraneous experimental parameters in further development of this lab scale batch process.

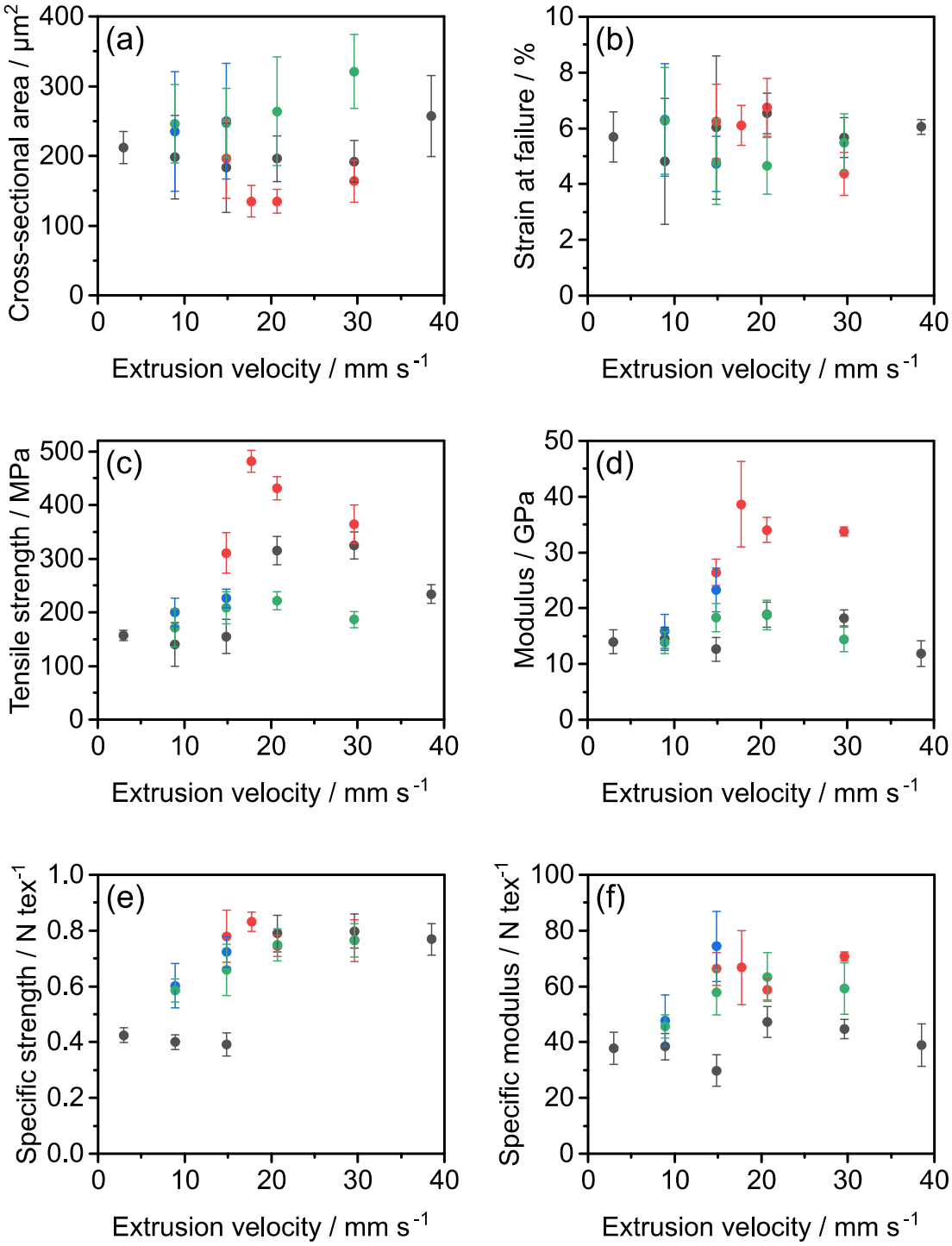


Figure 8.17. Batch-to-batch variation in CNT fibre properties prepared from 1 mg mL-1 eDIPS CNT dopes coagulated in acetone with DR 1.2. Separate colours indicate different batches. Error bars indicate 1 standard deviation.

8.6 Optimising CNT fibre spinning

With an understanding of the key parameters which result in stable spinning, the CNT spinning process can be optimised. Following the conditions which previously yielded the best properties, the process was explored further using eDIPS CNT spinning dopes with a mass loading of 1 mg mL^{-1} and a draw ratio of 1.2. The same spinneret was used throughout these experiments with an orifice diameter of 346 µm and taper semi-angle of ~9° (Figure 3.4, p.54). For three different coagulants (acetone, 25% ethanol/THF and 75% ethanol/THF), the mechanical properties are measured across a range of extrusion velocities and coagulation bath lengths. This approach enables a comparison of the coagulants across a wide processing window and illustrates how the optimal processing parameters and peak fibre properties differ between the coagulants. A total of 60 different conditions were tested with at least 5 fibre specimens per condition. The specific strength and specific modulus for each condition was calculated and plotted as a function of extrusion velocity and coagulation time, and then fitted with surface in OriginPro 2020 smoothed with a Thin Plate Spline method using a smoothing parameter of 0.1.[245, 246]

Acetone has a relatively wide processing window, with specific strength greater than 0.7 N tex^{-1} for all conditions with an extrusion velocity greater than 15 mm s^{-1} and a coagulation time less than 6 s; this group has a mean strength of 0.76 N tex^{-1} (Figure 8.18a). In contrast, when using 25% ethanol/THF coagulation baths the fibre strength tends to be weaker but is significantly improved with longer coagulation times whilst there is little dependence upon extrusion velocity; fibres with a coagulation time less than 6 s have an average strength of 0.51 N tex^{-1} compared to 0.67 N tex^{-1} for coagulation times greater than 6 s (Figure 8.18b). For 75% ethanol/THF baths, extrusion velocity appears as the most important factor, with improved properties for extrusion velocities greater than 15 mm s^{-1} (Figure 8.18c).

The poorer properties at lower extrusion velocities are almost certainly related to the less stable extrusion under those conditions. It is interesting to note that the more aggressive coagulants (acetone and 75% ethanol/THF) are more sensitive to the extrusion velocity. For faster acting coagulants, the spinning dopes are more likely to have some charge quenched whilst still in the spinneret leading to the formation of fouling deposits and less consistent

spinning and hence a higher extrusion velocity is required to prevent that effect. In comparison, the 25% ethanol/THF fibres are relatively unaffected by the extrusion velocity within this range under study (10-40 mm s^{-1}). It should be noted that instabilities had previously been observed when extruding CNT fibres into weaker coagulants at low velocities (section 8.3.3, p.152) but it is possible that those instabilities have a lesser impact on the CNT properties than those with stronger coagulants which appear with a 'stick-slip' morphology.

The results as a function of coagulation time suggest that there is an optimal 'degree of coagulation' or 'degree of charge quenching' for the fibres before removing from the coagulation bath and allowing to dry and densify. For the stronger coagulants, the required coagulation time is relatively short and good fibre properties were obtained with a residence time of just 0.9 s for acetone and 75% ethanol/THF. In comparison, at least 4 s and preferably greater than 6 s bath residence times are required to achieve good fibre strengths in 25% ethanol/THF. This difference of a factor of 4-6 is approximately in line with the relative concentrations of ethanol in the coagulation bath (a factor of 3) given some of the uncertainties around the experiment. In the case of acetone, there is some evidence of over-coagulation at times longer than 10 s, at which point the specific strength is noticeably lower than for shorter coagulation times. The coagulation process is complex, involving both charge quenching, possible surface reactions and the diffusion of solvents in and out of the fibre. It is important to note that at the end of the coagulation bath the diameter of the gel fibre is not substantially different to the point of injection and that extensive densification only occurs as the CNTs dry after removing from the coagulation bath (Figure 3.3). In a condition with long residence times the gel fibre may completely quench of charge, locking in a low volume fraction state (initially ~0.05%) which then does not densify as efficiently in a manner analogous to the issues observed when gel cross-linking INT fibres (section 6.1, p.109).

As noted previously, there is significantly more intra- and inter-batch variation in specific modulus which makes comparison more challenging and prone to over-fitting, especially due to the presence of some distinct outliers within the data sets (e.g. Figure 8.19b at 15 mm s^{-1}, 8 s). However, some trends are apparent and in general the specific modulus and specific strength follow similar dependencies upon the extrusion velocity and coagulation time for each coagulant (Figure 8.19). For acetone baths, the fibres tend to be stiffer for higher

extrusion velocities and shorter coagulation times and for 25% ethanol/THF longer coagulation times tend to be stiffer. For 75% ethanol/THF the trends are less clear and the specific stiffness is relatively uniform across the process space.

The effect of coagulation time on the fibre microstructure was investigated by taking some select samples for SEM imaging. Samples were selected with an intermediate extrusion velocity of 21 mm s^{-1} and coagulation times of 1.6 and 12-14 s (Figure 8.20-Figure 8.22). All the CNT fibres possess the same general appearance with diameter of 10-12 µm and a ridged morphology, which presumably develops during densification as a rigid skin layer of the gel fibre folds. Higher magnification images show that the fibres are primarily comprised of bundles of CNTs with lateral sizes of 10-50 nm. The bundle level microstructures are not particularly distinctive across the different conditions imaged and most show some degree of preferential alignment along the fibre axis. In general, bundles aligned along the fibre axis are thicker and appear continuous at the length scale imaged here. These major bundles are connected by smaller intermediary bundles which weave across the structure. It is clear from the SEM images that the fibres are not particularly densely packed on the bundle length scale, with a large amount of interstitial space visible on these fibre surfaces. Qualitatively, the nanostructure of the 12 s acetone coagulated fibre appears to be significantly more isotropic than the other fibre samples (Figure 8.20b). This fibre also had a lower specific modulus than the sample with the 1.6 s coagulation time (44 ± 4 vs. 56 ± 9 N tex^{-1}). These observations support the hypothesis that long coagulation times in acetone are detrimental to fibre properties due to fixing in a low volume fraction structure, which cannot effectively densify.

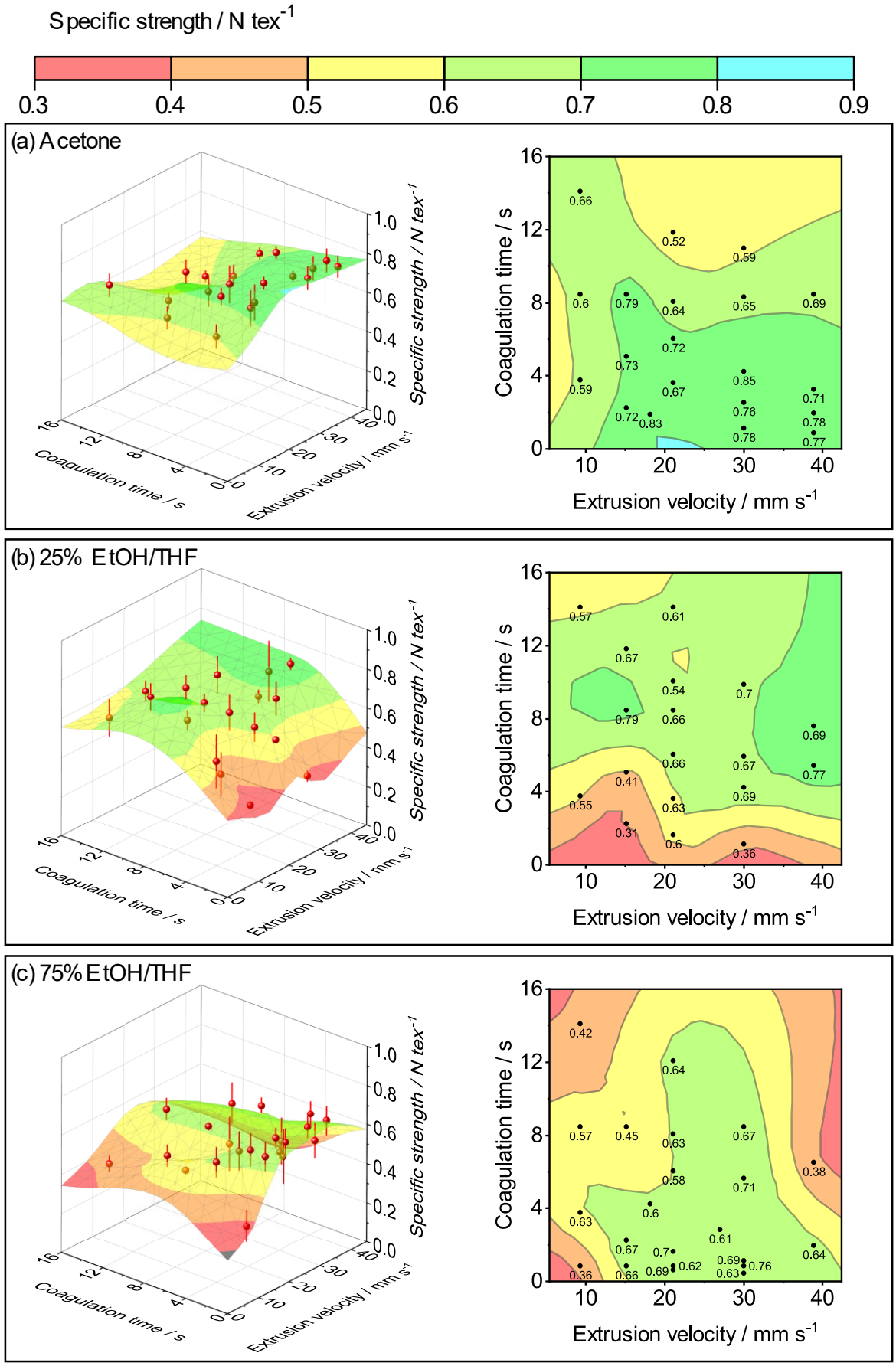


Figure 8.18. Surface plots and contour maps of specific strength of CNT fibres as a function of coagulation time and extrusion velocity for (a) acetone, (b) 25% ethanol/THF and (c) 75% ethanol/THF coagulation baths. Error bars indicate 1 standard deviation.

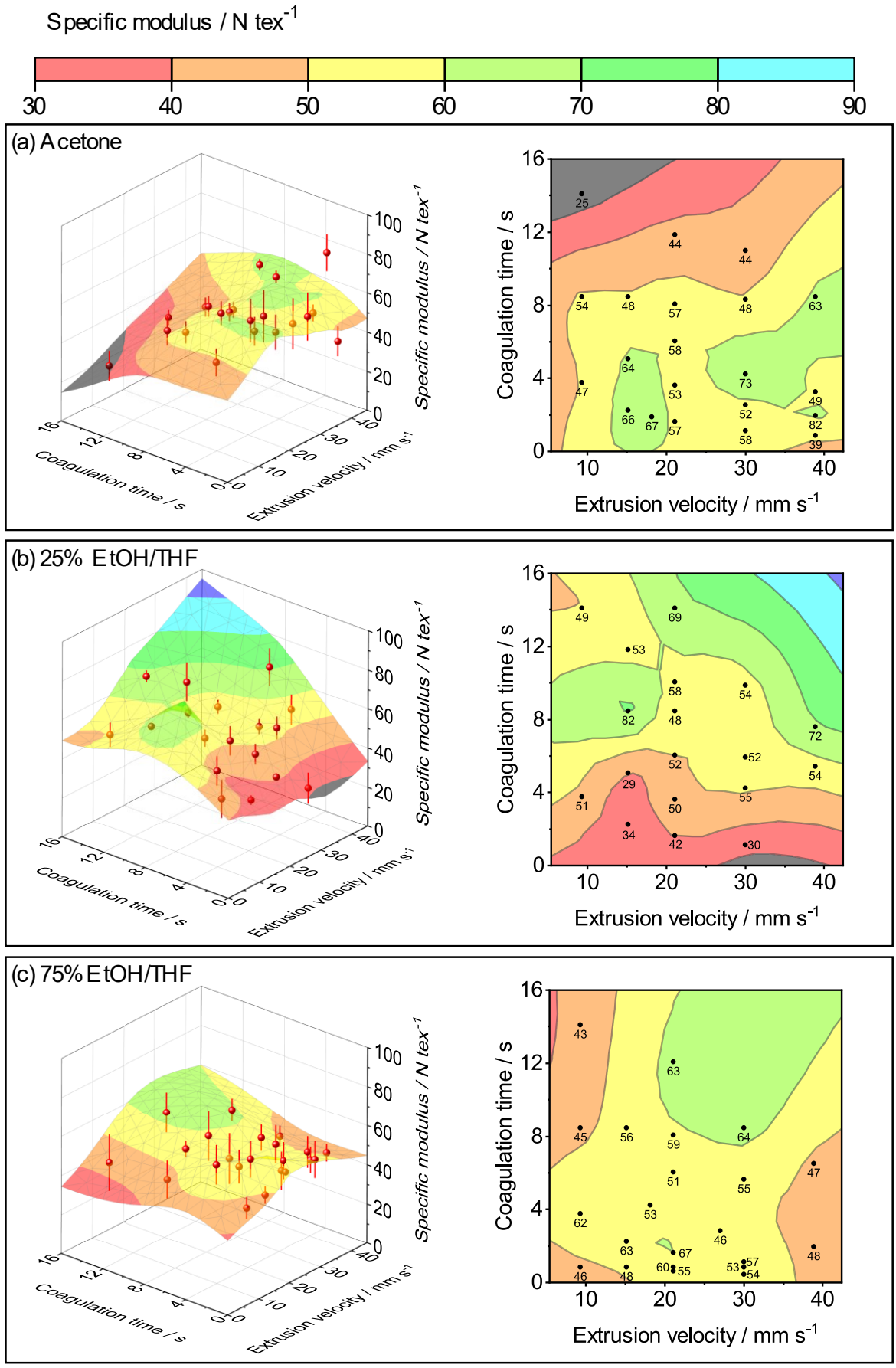


Figure 8.19. Surface plots and contour maps of specific modulus of CNT fibres as a function of coagulation time and extrusion velocity for (a) acetone, (b) 25% ethanol/THF and (c) 75% ethanol/THF coagulation baths. Error bars indicate 1 standard deviation.

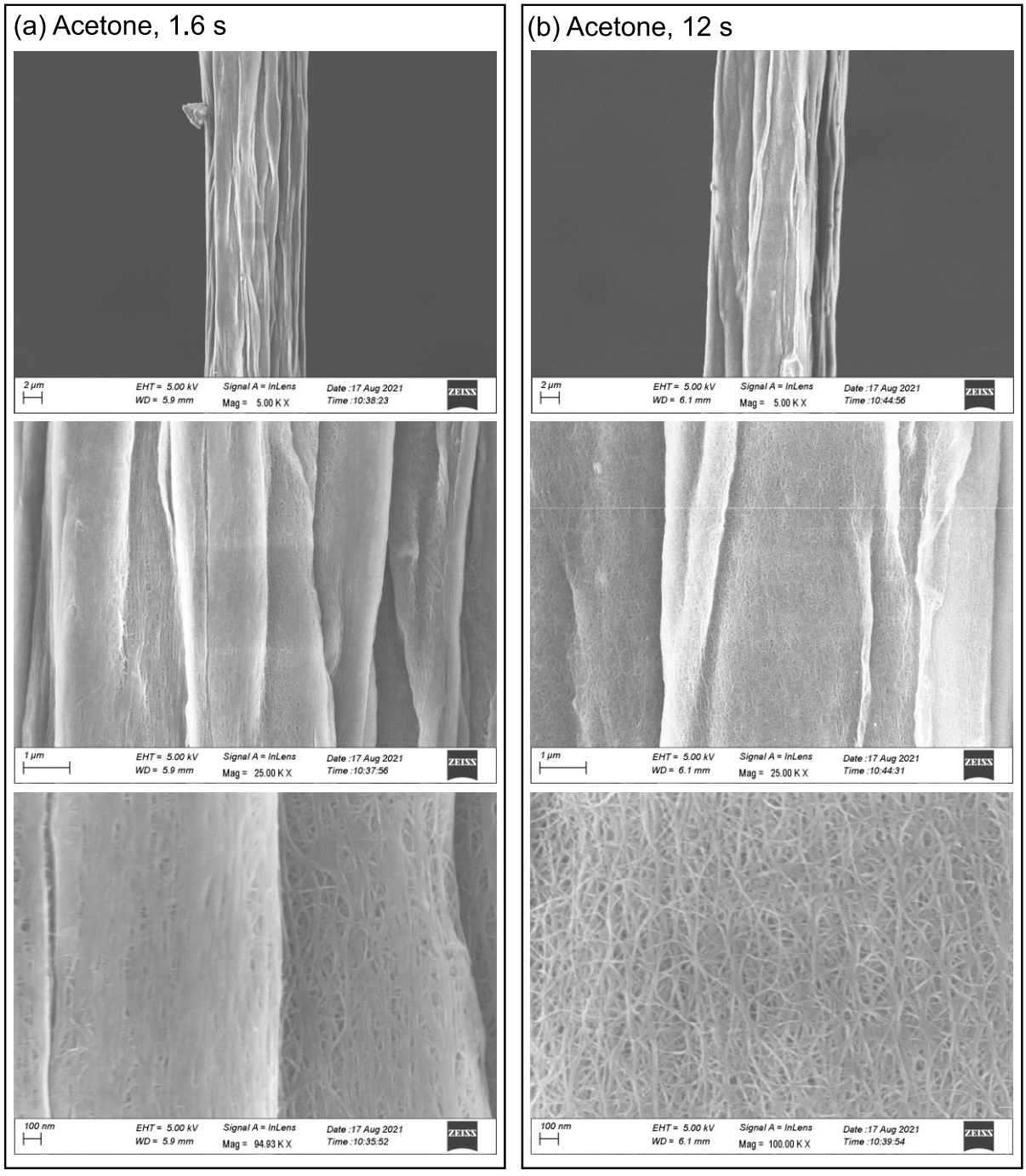


Figure 8.20. SEM images of fibres spun in acetone with an extrusion velocity of 21 mm s^{-1} and coagulation time of (a) 1.6 and (b) 12 s.

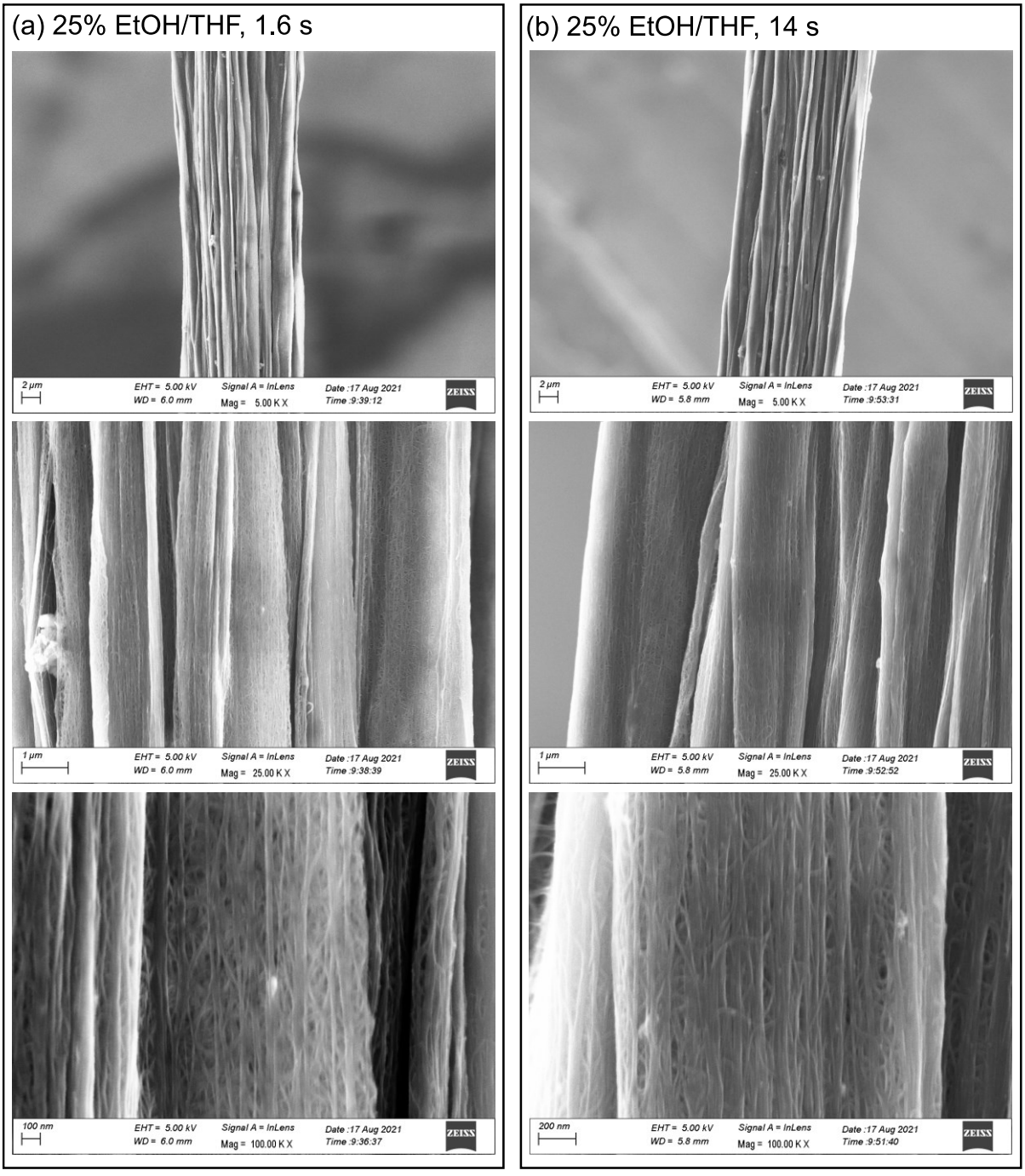


Figure 8.21. SEM images of fibres spun in 25% ethanol/THF with an extrusion velocity of 21 mm s^{-1} and coagulation time of (a) 1.6 and (b) 14 s.

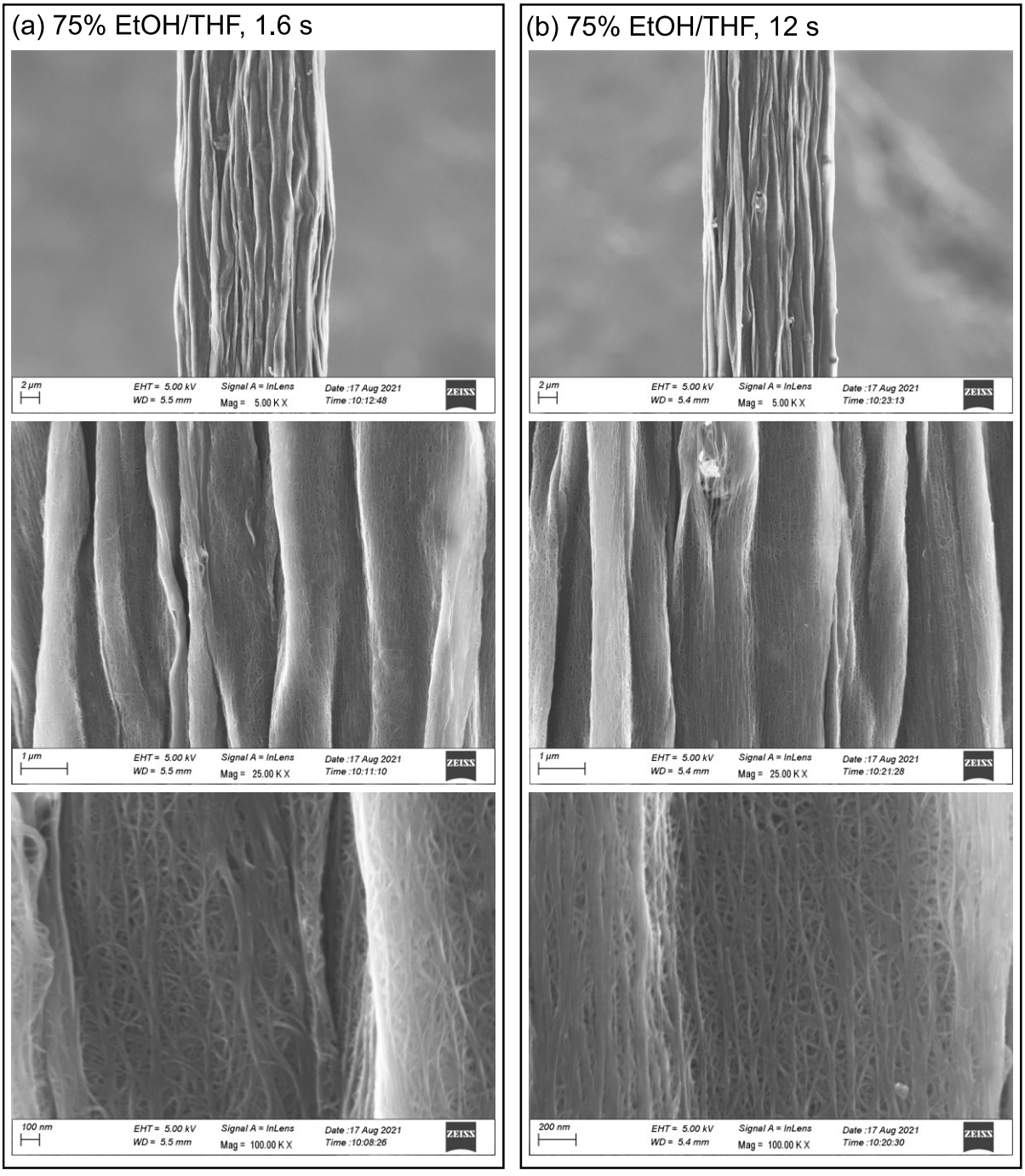


Figure 8.22. SEM images of fibres spun in 75% ethanol/THF with an extrusion velocity of 21 mm s^{-1} and coagulation time of (a) 1.6 and (b) 12 s. .

The specific conductivity, measured using a four point probe arrangement, was found to range between 0.31 and 0.43 kS m^2 kg^{-1} for these fibres. The specific modulus is correlated to the specific conductivity at the 90% confidence level (Figure 8.23a). As such, within this dataset there is evidence for a positive relationship between the degree of CNT orientation, specific modulus and specific conductivity, which agrees with literature meta-analysis.[88] The measured specific conductivity corresponds to an areal-basis conductivity of approximately 0.1-0.2 MS m^{-1}, which is within the typical range of reported results for undoped CNT fibres (0.02-0.6 MS m^{-1}). The highest conductivity fibres in the literature are almost exclusively doped typically with acid, which arises naturally during either solution spinning or acid post-processing of direct-spun CNT fibres (Figure 8.23b,c). If multifunctional performance is desired, doping methods should be investigated to increase the electrical conductivity of the fibres produced in this work.

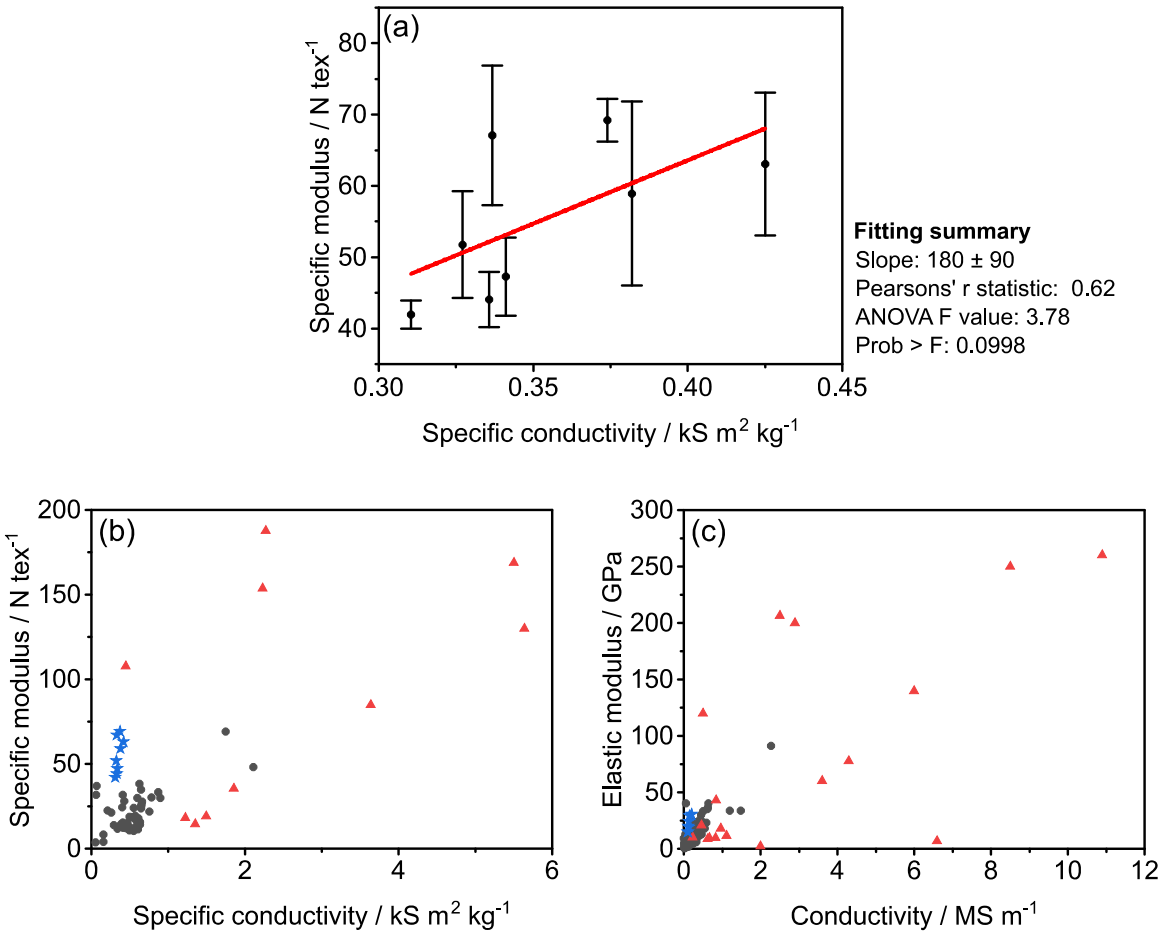


Figure 8.23. (a) Scatter plot of specific modulus against specific conductivity with linear regression. Error bars indicate 1 standard deviation. (b,c) (Specific) conductivity and modulus for aligned FW-CNT fibres from literature database:[88] (grey circles) undoped, (red triangles) doped and (blue stars) this work.

8.7 Spinning higher aspect ratio CNTs

The greatest effect on CNT strength identified has been the CNT feedstock used, with fibres produced from Tuball CNTs reaching a maximum specific strength of 0.4 N tex^{-1} compared to 0.8 N tex^{-1} for Meijo eDIPS EC1.5 CNTs. In order to improve the fibre properties further it was therefore attempted to spin fibres from the highest aspect ratio CNTs that were commercially available. Although reliable length data is typically not available for the majority of CNTs, reports from other groups suggest that the (difficult to source) Meijo eDIPS EC-DX range of CNTs may be significantly longer than the more available EC1.5 feedstocks and in the literature a batch of EC-DX CNTs with an estimated aspect ratio of 6700 has been used to produce some of the highest performing CNT fibres to date with a tensile strength of 4.2 GPa and modulus of 260 GPa (specific strength 2.1 N tex^{-1}).[106]

8.7.1 Dissolving higher aspect ratio CNTs

The EC-DX CNTs are supplied in a slightly different morphology to both the OCSiAl Tuball and eDIPS EC1.5 CNTs used elsewhere in this project (Figure 8.24). The Tuball CNTs were received as a fluffy powder, whereas the eDIPS EC1.5 CNTs were a tangled film. The EC-DX CNTs are more densely packed and entangled and were received as a pressed puck from which pieces were manually removed for experiments.

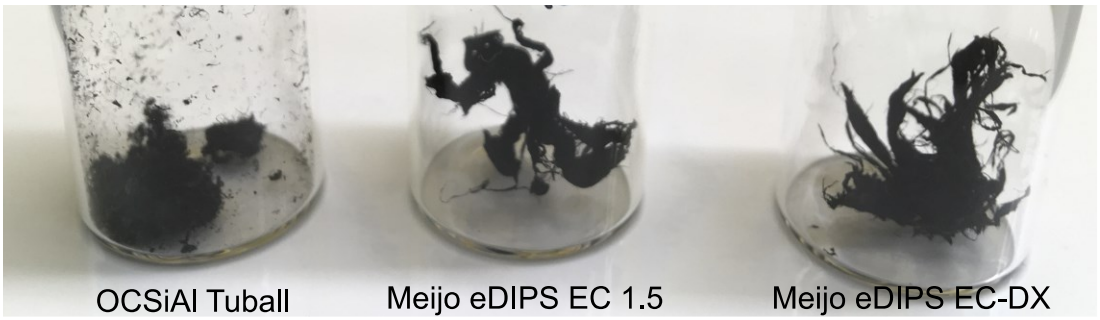


Figure 8.24. Photograph of as-received Tuball, eDIPS EC1.5 and eDIPS EC-DX CNTs.

Dissolving the EC-DX CNTs proved more challenging than both Tuball and EC1.5 CNTs with large, entangled agglomerates up to 1 mm long in solutions prepared at 1 mg_{CNT} mL^{-1} (Figure 8.25a). Stirring with a higher viscosity fluid is expected to be more efficient and so to aid breaking up the aggregates, a solution was first prepared at 2 mg_{CNT} mL^{-1} and then diluted back to 1 mg mL^{-1}. The resulting solution had a distinctly finer texture, but significant numbers of large agglomerates were still present (Figure 8.25b).

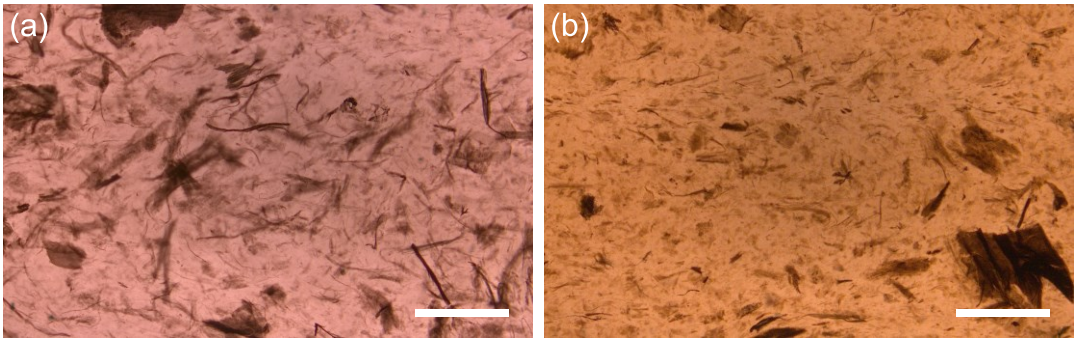


Figure 8.25. Transmission optical micrographs of EC-DX NaC_8 CNT solutions prepared at (a) 1 mg_{CNT} mL^{-1} and (b) 2 mg_{CNT} mL^{-1} followed by dilution to 1 mg mL^{-1}. Scale bars 500 µm.

Further improvement was sought by preparing and then serially diluting 5 mg mL^{-1} solutions followed by filtration through a 26 µm stainless steel mesh in a Swinnex filter holder. When filtering these solutions a large back pressure was required and the solution eventually leaked around the mesh filter, leading to a modest reduction in the number of agglomerates (Figure 8.26a). Attempts to disaggregate the agglomerates by bath sonication were unsuccessful, with no observable change to the solutions (Figure 8.26b). Despite the presence of the undissolved material, it is clear that a significant portion of the CNTs is dissolved. The solutions appear uniformly dark when observed by eye and polarised optical microscopy shows large regions of birefringence around the agglomerates. The birefringent solution flow aligns along the axis of the rectangular capillary after loading by capillary action, as seen in the significantly higher birefringent signal when the capillary axis is aligned at 45° to the polariser and analyser (Figure 8.26c,d).

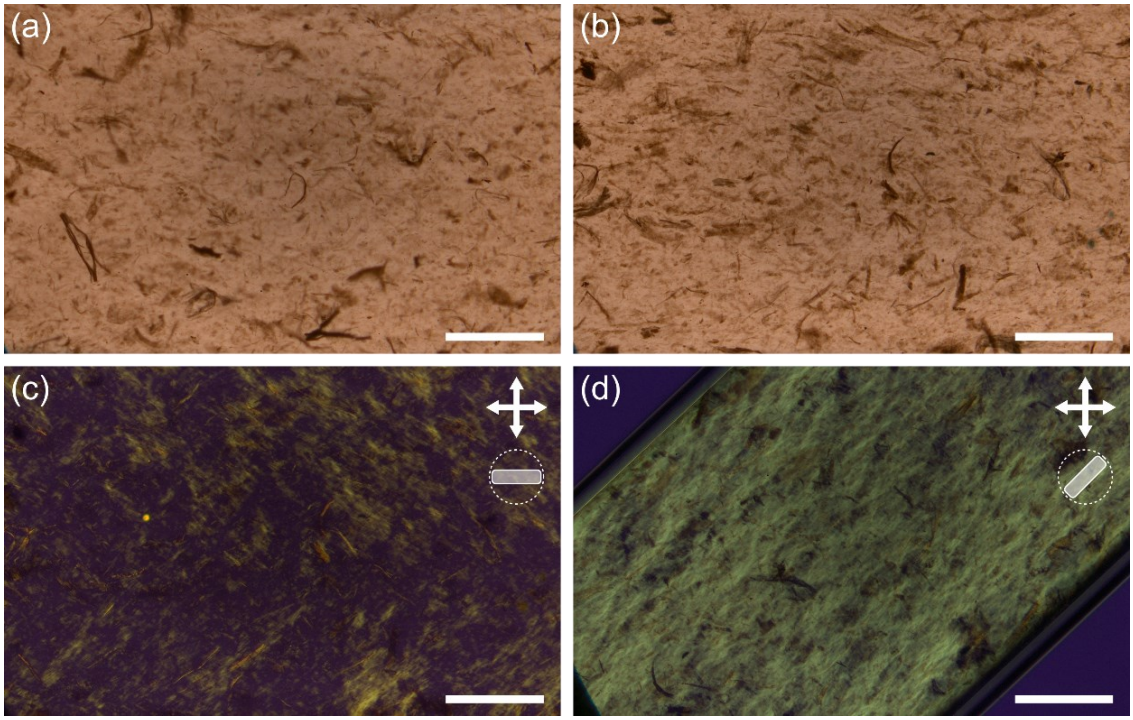


Figure 8.26. Transmission (polarised) optical micrographs of EC-DX CNT solutions prepared at 1 mg_{CNT} mL^{-1} and NaC_8 after filtration and (a) before and (b-d) after bath sonication. (c,d) Polariser and analyser directions are indicated by white arrows and capillary orientation by the diagram. Scale bars 500 µm.

8.7.2 Tensile properties of higher aspect ratio CNT fibres

Fibres were spun from the solutions using two of the best identified conditions with the EC1.5 CNTs: acetone coagulant, coagulation bath length 15 cm, draw ratio 1.2, extrusion velocities 21 and 38 mm s^{-1} and corresponding coagulation times of 6 and 3.2 s respectively. Disappointingly, the properties of these fibres were poorer than the equivalent conditions with EC1.5 CNTs. The mean specific strengths for the EC-DX fibres are 0.58 and 0.63 N tex^{-1} for extrusion velocities of 21 and 38 mm s^{-1} compared to 0.72 and 0.71 N tex^{-1} for the EC1.5 fibres (Figure 8.27a), whilst an even greater difference was observed in the specific moduli with 33 and 27 N tex^{-1} for EC-DX compared to 58 and 48 N tex^{-1} for EC1.5. However, promisingly the strain-at-failure for the EC-DX samples tended to be greater. It is expected that improving the dissolution of these higher aspect ratio CNTs should lead to better mechanical properties and further research may be directed towards higher shear mixing processes, such as centrifugal or rotor-stator mixers, to disentangle the undissolved CNTs.

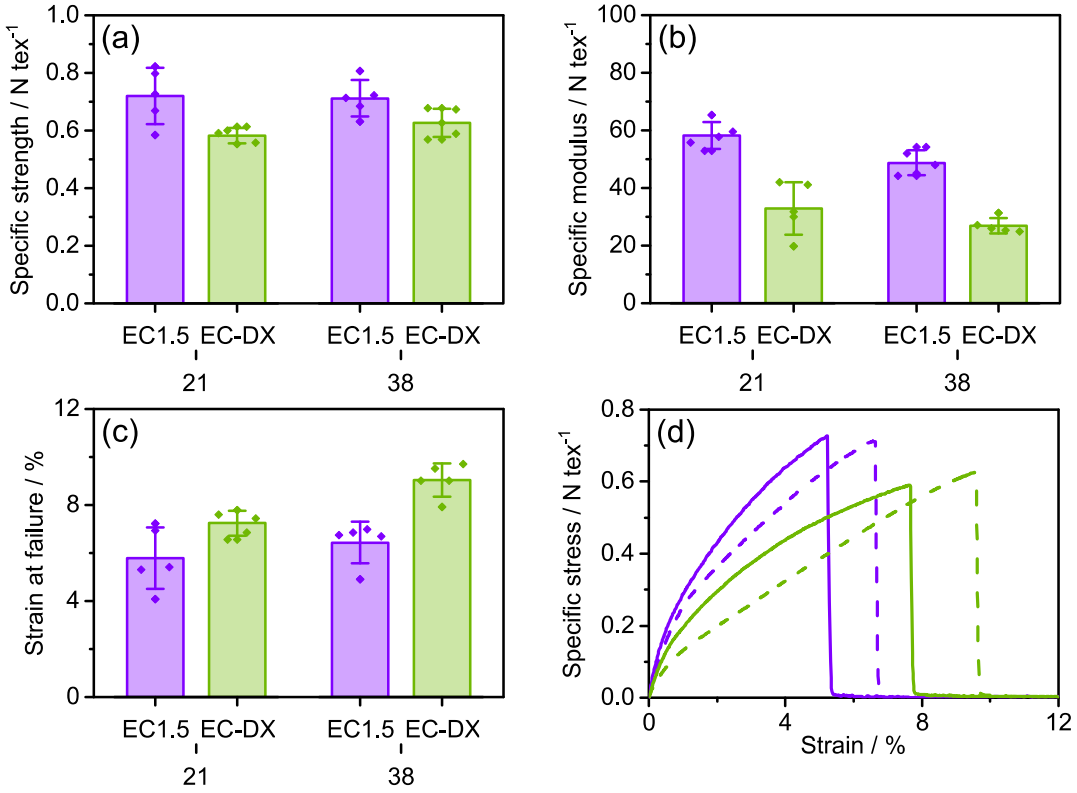


Figure 8.27. (a-c) Mechanical properties and (d) representative specific stress-strain curves for (purple) EC1.5 and (green) EC-DX CNT fibres coagulated in a 15 cm acetone bath with extrusion velocity of (solid line) 21 and (dashed line) 38 mm s^{-1}. Error bars indicate 1 standard deviation.

8.8 Summary

Wet spinning from CNT polyelectrolyte solutions has been demonstrated and the key process parameters have been identified. Stable extrusion into a coagulation bath requires a sufficiently high coagulant reactivity, and a sufficiently high extrusion velocity. Specific strength is strongly dependent upon the chosen CNTs, with the longer eDIPS EC1.5 outperforming Tuball 01RW03 CNTs by a factor of two (0.8 N tex^{-1} compared to 0.35 N tex^{-1}). However, using even higher aspect ratio feedstocks has challenges with large agglomerates (>500 µm) present in solutions of eDIPS EC-DX CNTs, resulting in disappointing mechanical properties for fibres produced from this feedstock. The solutions prepared in this study were mixed using a magnetic stirrer bar, which is relatively inefficient for the shear thinning solutions and so it is recommended to investigate high shear mixing or centrifugal mixing to attain high quality spin dopes from higher aspect ratio feedstocks to attain better mechanical properties. The ideal injection velocity and residence time in the coagulation bath during spinning is related to the coagulant composition with more reactive coagulants requiring a

higher injection velocity to avoid nozzle fouling, whilst less reactive coagulants need a longer residence time. The widest processing window and best fibre properties have been attained using acetone as a coagulant, and spinning is recommended with a 1 mg_{CNT} mL^{-1} spinning dope, 346 µm diameter tapered spinneret, injection velocity between 15 and 40 mm s^{-1} and a coagulation time between 2 and 6 s. The best fibres produced using this process had specific strength of ~0.8 N tex^{-1} and specific modulus of ~60 N tex^{-1} and a failure strain between 4 and 8%. There are difficulties with accurately measuring the cross-sectional area of the fibres, but a conservative over-estimate of 250 μm^2 predicts a tensile strength and modulus of 250 MPa and 19 GPa respectively and a bulk density of 0.31 g cm^{-3}. A more optimistic estimate for the cross-sectional area of 150 μm^2 predicts strength, modulus and density of 420 MPa, 32 GPa and 0.52 g cm^{-3}. The density of all the fibres produced from the reduced CNTs is relatively low, which may be due to the high reactivity of the spinning dope, in which a relatively low density network is formed before significant diffusion of the initial solvent can occur. Following guidance from other wet spinning processes, this challenge may be alleviated by using a higher temperature coagulation bath to aid diffusion. Unfortunately, using less reactive coagulants seems to have a negative effect on extrusion stability. Whilst the properties of the fibres produced in this work lag somewhat behind those demonstrated via the extensively optimised superacid wet spinning process (4.2 GPa and 2.1 N tex^{-1} tensile strength and specific strength), that has had over a decade of development, for an early exploratory study they are encouragingly high.

9 Conclusions and further work

This work has investigated the assembly of nanotubes into fibres *via* wet spinning processes. Firstly, a method to spin fibres purely from imogolite nanotubes (INTs) was developed and the properties of these fibres were explored (Chapter 4). The resulting fibres consisted of partially oriented (± 9-12°), low density (packing fraction 40-60%) networks of rigid INTs. High aspect ratio INT feedstocks were required for stable fibre spinning, in particular to draw the relatively weak gel fibre from the coagulation bath. Spinning a larger diameter fibre helped to reduce the stress in the fibre from surface tension mediated drag and improved the stability of spinning. The INT fibres are intrinsically sensitive to humidity due to their hygroscopic nature, an effect which is magnified by the presence of remnant salts from the coagulation processes. Interestingly, less aligned INT fibres were stiffer than more aligned fibres, in contradiction to conventional assumptions. The effect is attributed to the more efficient formation of a jammed network at lower degrees of alignment that aids stress transfer within the fibre and reduces intertube sliding.

The INT fibre spinning process was then developed further to achieve more consistent processing, using *in situ* polarised optical microscopy to study the alignment of INTs during flow (Chapter 5). The shear thinning solutions displayed plug flow in cylindrical channels, which led to inhomogeneous alignment along the fibre length. The extensional flow in a tapered spinneret induced flow alignment throughout the bulk of the spinning dope prior to extrusion, producing fibres with more consistent properties. Whilst a complete study of the effect of various spinneret shape parameters was not possible in the scope of this project, tapered spinnerets can be strongly recommended for wet spinning nanomaterial fibres with shear thinning spin dopes. The washing required to remove the coagulation salt from the INT proto-fibres leads to two critical changes to the fibre microstructure. Longer washing times led to an increased packing density, due to salt removal, and decreased alignment in the fibres. The combination of these two effects led not only to significantly stronger and stiffer fibres at higher washing times, but also higher specific strength implying improved network efficiency. The properties of these fibres (strength 170 MPa, stiffness 23 GPa) are surprisingly good considering the relatively low aspect ratio of the INTs (~50-300). There is significant scope to improve performance using higher aspect ratio INTs. Using aluminosilicate rather than aluminogermanate INTs would increase specific properties (although decrease the X-ray

scattering intensity used for characterisation). The greater flexibility of single wall, rather than double wall, INTs might help to improve the packing density and increase the number of intertube contacts in more aligned fibres. Especially in the case of higher aspect ratio INTs, this may lead to a return towards a more typical stress transfer mechanism, rather than a reliance on jammed networks.

Alternatively, other means of improving stress transfer within the INT fibre could be applied as explored in Chapter 6. Cross-linking the INT fibres in their gel state (before densification through drying) lowered the mechanical properties of the subsequent fibres by inhibiting densification. This result is generally useful to consider when wet spinning nanomaterial fibres, since it demonstrates that densification is crucial to obtain good mechanical properties and that cross-linking must be applied after any post-processing used for densification. In the overall context of this project, the discovery that gel state cross-linking is detrimental to properties is disappointing, as one of the key potential benefits of the reduced CNT system is to enable cross-linking reactions during fibre spinning. Covalent cross-linking of densified INT fibres was then attempted through dehydration and silanisation reactions. In both cases, the cross-linking led to a modest increase in elastic modulus to 31 GPa but a reduction in the failure strain to 0.4-0.6% and a more brittle failure mode, with no significant increase in tensile strength. Infiltrating a PVA matrix into the INT fibre increased both strength and modulus of the fibres, providing a general strategy to improve the mechanical properties of these relatively porous fibres. This approach to producing polymer/INT fibres can attain higher INT mass loadings compared to the direct spinning from PVA/INT dopes (limited to ~13% INT) resulting in stiffer, stronger fibres.

The INT fibres represent a new nanomaterial system, readily studied by X-ray scattering and polarised microscopy. The understanding of load transfer in loosely packed nanorod or nanotube fibres has general relevance, and due to their high rigidity the double walled Ge-INTs may act as an excellent experimental analogue for mechanical models of stiff rods. In addition, INT fibres may prove to be useful in their own right, given their complementary properties to CNT fibres, including electrical insulation, low optical absorbance and hydrophilicity. With development, the mechanical properties could be significantly improved. In the same way that glass fibres are used in preference to carbon fibres for lower cost applications, it is possible that INT fibres could be commercially competitive as structural

reinforcements due to their low temperature synthesis and relatively straightforward aqueous processing. However, similarly to glass, the specific mechanical properties of INT fibres are unlikely to ever compete with CNT or carbon fibres due to the relatively high mass of the inorganic nanotubes.

Wet spinning CNT fibres from reduced polyelectrolyte solutions was explored broadly. Firstly, dissolution conditions were optimised to achieve an agglomerate free solution of well dissolved CNTs (Chapter 7). Optimal dissolution was observed at a charging ratio of NaC_{10}, however the optimum appears narrow, with CNTs remaining significantly agglomerated when even slightly less charged. Considering that adventitious air or moisture can easily quench some of the charge, NaC_8 was chosen as the ideal charging ratio to provide some buffer during downstream processing and maintain high quality solutions.

Next, a variety of wet spinning conditions were assessed to attain stable extrusion of a CNT fibre and then optimised to achieve the best possible fibre properties (Chapter 8). Similarly to INTs, CNT solutions are shear thinning but to a much greater degree and are significantly more viscous at around 300 mPa s compared to 4 mPa s at a mass loading of 3 mg mL^{-1} and shear rate of 100 s^{-1}, likely due to their higher aspect ratio. Drawing on the learning from the INT system, tapered glass spinnerets were used to spin CNT fibres, and it was found that silanising the glass surfaces greatly simplified cleaning and reduced the adhesion of CNTs to the nozzle during spinning. Although initially considered to be a potential benefit of the system, the high reactivity of the charged CNT solutions poses some challenges with the fibre spinning process. In the INT system, gel cross-linking was shown to be detrimental to the fibre properties and balancing the rate of coagulation of the CNT fibres with the solvent diffusion rates in wet spinning is difficult. Reactive, charge quenching coagulants are required to enable stable extrusion with a minimum ethanol content of 20% (v/v), but fibres spun from these coagulants still exhibit the non-circular cross-sections symptomatic of wet spinning with too fast a coagulation rate relative to diffusion. This rapid coagulation is likely also a contributing factor to the relatively low density of the CNT fibres produced in this work (~0.3-0.5 g cm^{-3}) with estimated packing fractions as low as 15-25%. Despite these challenges, the properties of the CNT fibres are relatively encouraging given the early stage of development with specific strength and modulus of 0.8 and 60 N tex^{-1} respectively and tensile strength and modulus of

approximately 250 MPa and 19 GPa. For comparison in 2009, five years after first publication, super-acid spun CNT fibres had tensile strength of ~300 MPa.[106]

Improving the properties of fibres produced from reduced CNT polyelectrolytes will require further research in two distinct areas. Firstly, the dissolution process for higher aspect ratio CNTs will need to be optimised. Whilst it is believed that the identified charging ratio of NaC_8 should enable the initial debundling of CNTs of any length, physical mixing methods will need to be adjusted to reflect the differences in rheology as CNT aspect ratio increases. Suggested methods include high shear rotor-stator mixers, centrifugal mixers, resonant acoustic mixers or high pressure homogenisers. Meanwhile, identifying and sourcing the highest aspect ratio CNT feedstocks is difficult and a wide study investigating different suppliers and manufacturers may be justified. Measuring the aspect ratio of CNTs is not straightforward but qualitative comparisons may be made via measurements of viscosity. The theory relating extensional viscosity and CNT aspect ratio is well established[230] but capillary rheometry as described in this work may also be used to rank prospective CNT sources. For industrial scale-up, more concentrated spinning dopes will be needed to improve production rates and reduce costs. Significantly more powerful pumps and higher pressures will be needed to explore this regime.

Secondly, further investigations are required into the coagulation and densification of the CNT fibres. Reducing the coagulation speed and increasing the solvent diffusion rate may both enable improved densification of the CNT fibres. Reducing the coagulation speed will require stabilising the extrusion of the CNT spinning dopes in less reactive coagulants. Possible options include using directed flows in the coagulation bath or a co-flowing spinneret to support the fibre during its initial extrusion. Further optimisation of spinneret shapes and surfaces may also prevent the nozzle fouling and adhesion problems which reduce the stability of the extrusion process. Meanwhile, temperature control of the coagulation bath would allow the diffusion rates during coagulation to be adjusted, potentially finding an optimum balance as has been sought in wet spinning processes for polymer fibres. Exploring these effects will require some scale-up beyond the fibre spinning equipment used in this project but may be found within a pilot line research facility. However, the highly air-sensitive spinning dopes will create additional challenges and demands on facilities.

Finally, in analogy to chlorosulfonic acid treatments on direct-spun CNT fibres, reductive charging may be useful to post-process pre-existing CNT materials, for example those produced by dry spinning. As these materials are already in fibre form, difficulties of extrusion into weaker coagulants are no longer a problem, and careful gentle discharging may provide some opportunities for microstructural modification or covalent cross-linking in a more densified state.

Nanomaterial fibres are a broad family of materials which may be useful for their structural performance or multifunctional characteristics. Whilst in many cases the processing is analogous to that of polymer fibres, the size, shape and rigidity of nanotubes creates some unique challenges in spinning which necessitates extensive research and development. The commercialisation of a fibre material is a long process, with most mature technologies taking decades to go from conception to wide-scale application. Nanotube fibres have shown very promising results at this early stage of development and are now starting to attain properties competitive with commercial materials. This work has demonstrated one method of accelerating development, by using INTs as an analogue to improve CNT fibre spinning, but has also widened the known field of nanomaterial fibres to include straight, rigid inorganic nanotubes with uniform structure.

Despite the range of possible nanomaterial fibres, CNTs are likely to remain a key research focus due to their high strength, low density and favourable analogy to strategically valuable carbon fibres. CNTs may provide a route to make carbonaceous fibres with a fundamentally lower environmental impact and more sustainable sources of CNTs are being developed, from the reformation of natural gas or production from the CO_2 in flue gases. Several routes have been identified to produce CNT fibres. At this early stage it is difficult to conclusively identify which route will be most successful. Although the best specific fibre properties are currently obtained through a combination of direct spinning and superacid post-processing, this method has the most scale-up challenges and development risk due to the low production rate from direct spinning and the potential detrimental effects of remnant acid. An alternative route of wet spinning from reduced CNT solutions was explored in this project, and a number of processing challenges were identified and overcome. A potential research route to further improve the properties of these fibres has been suggested, which will help determine whether they can be a true future competitor to carbon fibres.

Appendix

A1 Technical fibres properties

Name	Type	Sub-type	Tensile strength / GPa	Elastic modulus / GPa	Density / g cm^{-3}	Specific strength / N tex^{-1}	Specific modulus / N tex^{-1}	Failure strain / %
Saint-Gobain E-glass fibres	Glass		2.4	73	2.6	0.9	28	2.3
S-glass fibre	Glass		3.5	87	2.5	1.4	35	4.0
Toray T300	Carbon		3.53	230	1.76	2.0	131	1.5
Toray T1000G	Carbon		6.37	294	1.8	3.5	163	2.2
Toray M55J	Carbon		4.02	540	1.91	1.2	282	0.8
HexTow IM7	Carbon		5.5	276	1.78	3.1	155	1.8
HexTow HM63	Carbon		4.82	434	1.83	2.6	237	1.0
HexTow AS4	Carbon		4.72	231	1.79	2.6	129	1.8
Kevlar 29	Polymer	Aramid	2.92	70	1.44	2.0	49	3.6
Kevlar 49	Polymer	Aramid	3	112	1.44	2.1	78	2.4
Zylon AS	Polymer	PBO	5.8	180	1.54	3.8	117	3.4
Zylon HM	Polymer	PBO	5.8	270	1.56	3.7	173	2.5
Twaron 1000	Polymer	Aramid	2.9	78	1.44	2.0	54	3.4
Spectra 2000	Polymer	UHMWPE	3.25	113	0.97	3.4	117	2.8
Spectra 900	Polymer	UHMWPE	2.59	79	0.97	2.7	81	3.6
Dyneema SK60	Polymer	UHMWPE	2.7	88	0.97	2.8	91	3.5
Dyneema SK76	Polymer	UHMWPE	3.6	116	0.97	3.7	120	3.5
Vectran HT	Polymer	Thermotropic LC	3.2	75	1.4	2.3	54	3.8
Vectran UM	Polymer	Thermotropic LC	3	103	1.4	2.1	74	2.8

A2 Appendix figures

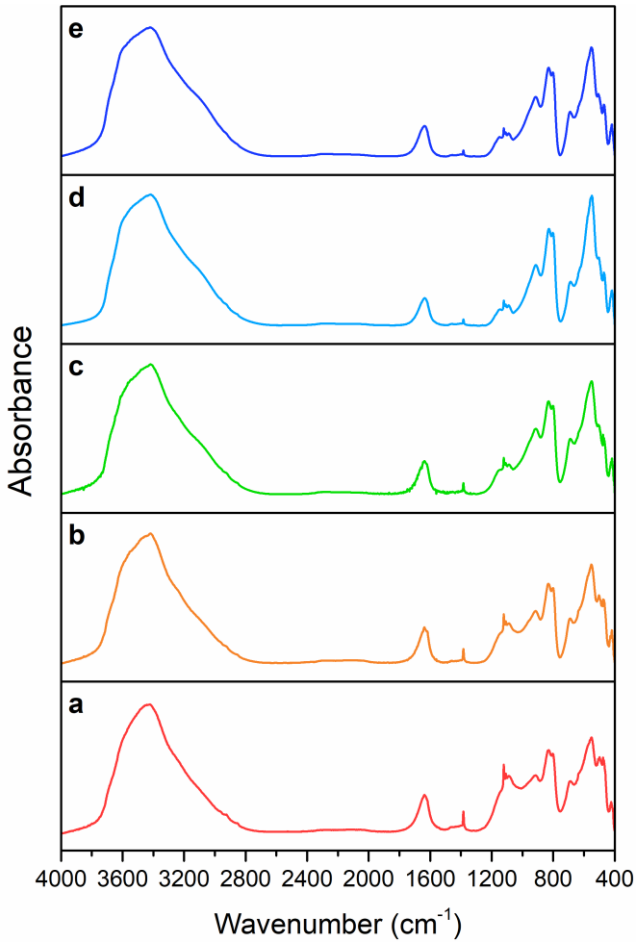


Figure A1. Infrared spectra of INT feedstocks as a function of growth time. (a) 5 days, (b) 12 days, (c) 20 days, (d) 30 days, (e) 40 days. Peaks at 1635 cm^{-1} correspond to H2O bending mode. Vibrational bands at 915, 835 and 805 cm-1 are related to Ge-O stretching and the broad peak around 555 cm^{-1} corresponds to Al-O stretching. Collected by collaborator, Erwan Paineau, and reproduced from [192].

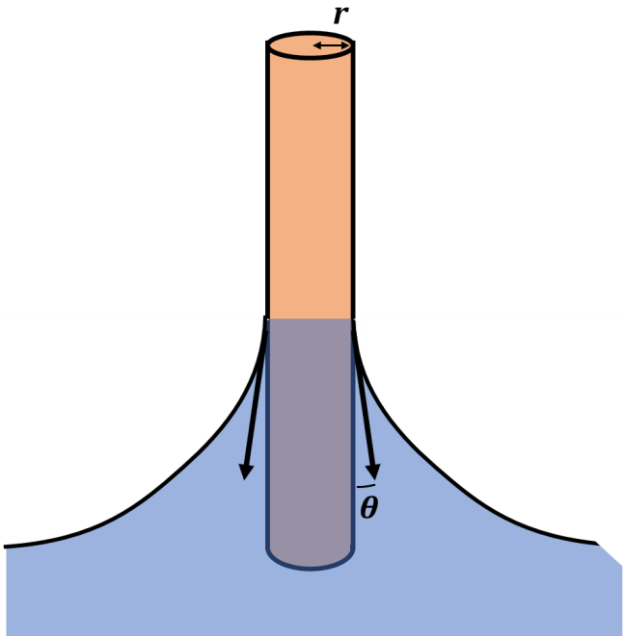


Figure A2. Illustration of modified Wilhelmy method to estimate fibre gel strengths. The stress within the fibre is given by $\sigma = \frac{F}{A} = \frac{2\pi r\,\gamma\,cos\theta}{\pi r^2} = \frac{2\,\gamma\,cos\theta}{r}$ where γ is the coagulant surface tension (83 mJ m^{-2}), r is the radius of the gel fibre and θ is the angle between the fibre axis and coagulant surface. The approximation that θ is small is used to determine the fibre stress as $\sigma \sim 2\gamma/r$. Reproduced from [192].

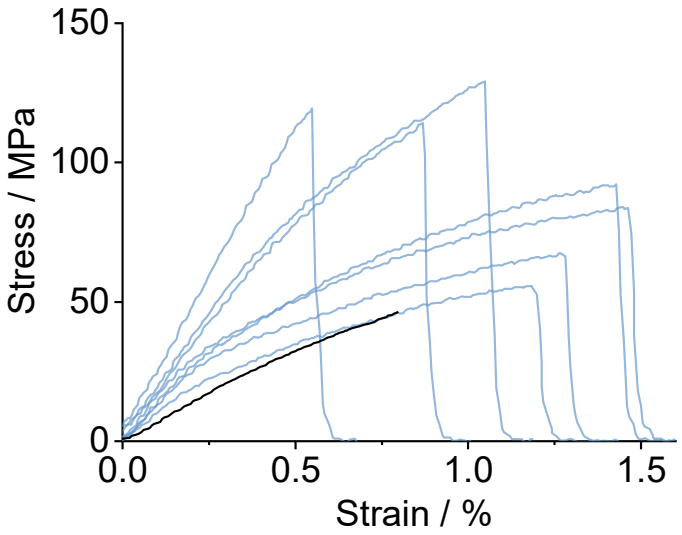
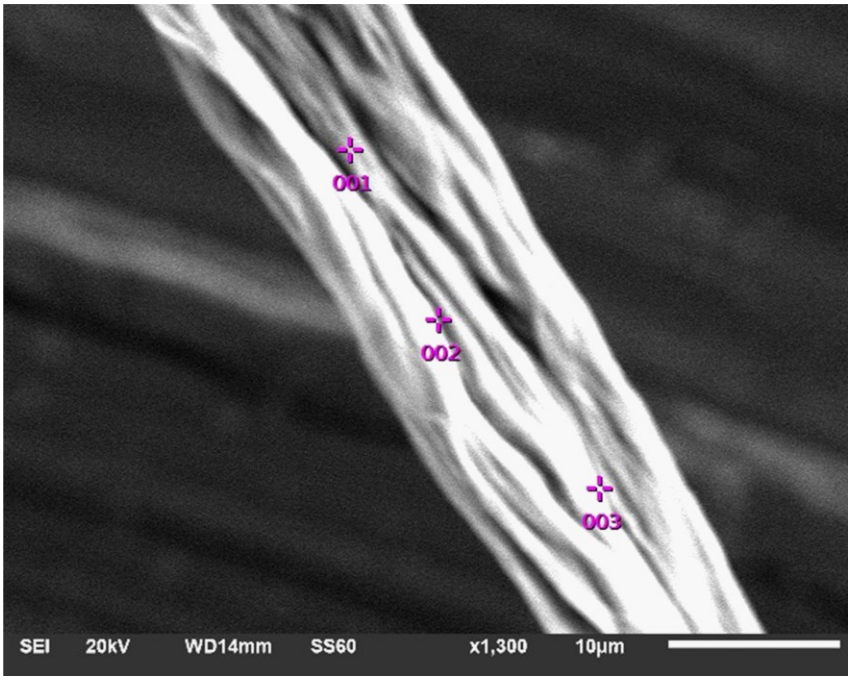


Figure A3. Stress strain curves of fibers from INT-20d tested at 40% RH with no prior conditioning (light blue) or with initial conditioning at 85% RH for two hours (black). Reproduced from [192].



Spot	O / at %	Al / at %	Ge / at %	Ca / at %	Cl / at %
001	62.1	20.8	8.7	2.9	5.4
002	60.3	21.1	9.8	3.3	5.6
003	59.5	21.4	9.8	3.4	5.9
Average	60.6	21.1	9.4	3.2	5.6

Figure A4. SEM image of INT fibre with corresponding elemental composition as calculated by energy dispersive spectroscopy. Scale bar 10 µm. Adapted from [192].

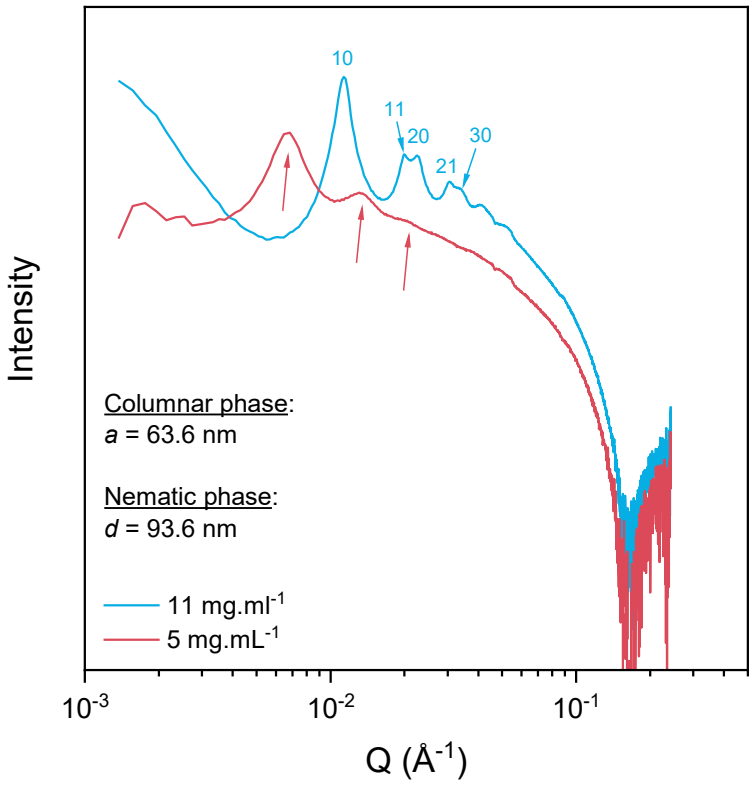


Figure A5. Small angle X-ray scattering diffractogram for INT solutions at mass loadings of 5 and 11 mg mL^{-1} with indexed peaks for nematic and columnar phase respectively. Collected and interpreted by collaborator, Erwan Paineau.

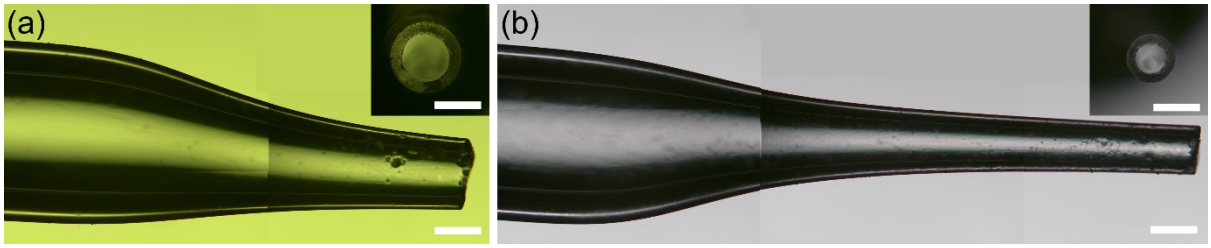
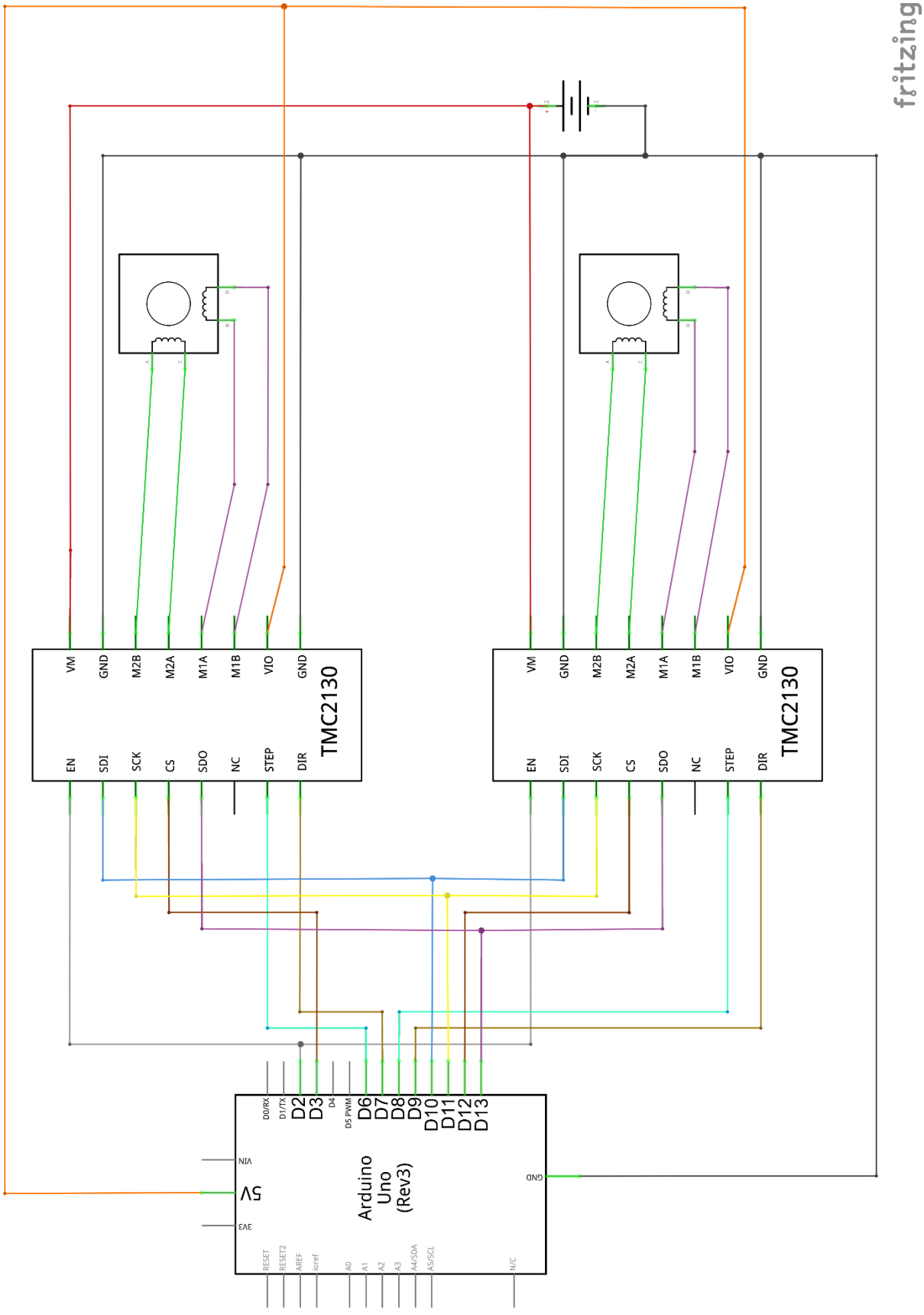


Figure A6. Stitched optical micrographs of tapered glass spinnerets used to assess impact of extrusion velocity on CNT extrusion stability. Nozzles have orifice diameters of (a) 511 and (b) 329 µm. Scale bars 500 µm.

A3 Stepper motor wiring schematic



A4 Spinning rig code

```
/**
 * INSTALL TMC2130Stepper library by teemuatlut
 *
 * Author Joe Moore
 * Uses TMC2130Stepper library to run two drivers at RPM_1 and RPM_2
*/

// Motor parameters
const int ms =32; //set number of microsteps
float RPM_1_init = 0.7; //set initial RPM for wheel 1
float RPM_2_init = 0.20039186; //set initial RPM for wheel 2
float DR = 1; //set initial draw ratio at start up

//Pin definitions
#define EN_PIN  2  // enable (CFG6)
#define DIR_PIN_1  9  //  direction pin 1
#define STEP_PIN_1  8  //   step pin 1
#define DIR_PIN_2  7 // direction pin 2
#define STEP_PIN_2  6 // step pin 2
#define CS_PIN_1  12  //  chip select of driver 1
#define CS_PIN_2  3 //chip select of driver 2
#define MOSI_PIN  10 // connect to SDI on chip
#define MISO_PIN 13 // connect to SDO on chip
#define SCK_PIN  11 // connect to SCK on chip

// Initialisation values
const int steps_per_rev = 200;
unsigned long last_step_time_1 =0;
unsigned long last_step_time_2 =0;
unsigned long step_period_1=0;
unsigned long step_period_2=0;
const int numChars = 32;
char receivedChars[numChars];   // an array to store the received data
bool newData = false;
float dataNumber = 0;             // new for this version



#include <TMC2130Stepper.h>
#include <Arduino.h>


TMC2130Stepper driver_1 = TMC2130Stepper(EN_PIN, DIR_PIN_1, STEP_PIN_1,
CS_PIN_1, MOSI_PIN, MISO_PIN, SCK_PIN);
TMC2130Stepper driver_2 = TMC2130Stepper(EN_PIN, DIR_PIN_2, STEP_PIN_2,
CS_PIN_2, MOSI_PIN, MISO_PIN, SCK_PIN);

void setup() {
      //Start serial communication with PC
      Serial.begin(9600);

      //Set up drivers
      init_driver_1();
      init_driver_2();
      digitalWrite(EN_PIN, HIGH);
      digitalWrite(DIR_PIN_2,HIGH);
      digitalWrite(DIR_PIN_1,HIGH);
```

```
  // Calculate periods between steps for each motor
  set_step_period();
}

void loop() {

      unsigned long micro = micros();
  //Check if driver_1 needs stepping
  if (micro - last_step_time_1 > step_period_1)
  {
    digitalWrite(STEP_PIN_1, HIGH);
    delayMicroseconds(10);
    digitalWrite(STEP_PIN_1, LOW);
    delayMicroseconds(10);
    last_step_time_1 += step_period_1;
    }

  //Check if driver_2 needs stepping
  if (micro - last_step_time_2 > step_period_2)
  {
    digitalWrite(STEP_PIN_2, HIGH);
    delayMicroseconds(10);
    digitalWrite(STEP_PIN_2, LOW);
    delayMicroseconds(10);
    last_step_time_2 += step_period_2;
    }

  //Check for draw ratio update via Serial monitor
  recvWithEndMarker();
  updateDR();
}

void init_driver_1() {
  Serial.println("Start driver 1 set up...");
  driver_1.begin();                 // Initiate pins and registeries
  driver_1.setCurrent(400, 0.11, 0.5);      // Set stepper current to 400mA
  driver_1.stealthChop(1);          // Enable extremely quiet stepping
  driver_1.microsteps(ms);
  Serial.println("DRV_STATUS_1=0b");
  Serial.println(driver_1.DRV_STATUS(), BIN);
  Serial.println("Set-up driver 1 complete...");
}

void init_driver_2() {
  Serial.println("Start driver 2 set up...");
  driver_2.begin();                 // Initiate pins and registeries
  driver_2.setCurrent(400, 0.11, 0.5);      // Set stepper current to 400mA
  driver_2.stealthChop(1);          // Enable extremely quiet stepping
  driver_2.microsteps(ms);
  Serial.println("DRV_STATUS_2=0b");
  Serial.println(driver_2.DRV_STATUS(), BIN);
  Serial.println("Set-up driver 2 complete...");
}

void set_step_period() {
  float RPM_1= RPM_1_init*DR;
  float RPM_2= RPM_2_init*DR;
  step_period_1 = (long) round(1000000 / (RPM_1*steps_per_rev*ms/60));
//delay time for each square wave / microseconds
```

```
  step_period_2 = (long) round(1000000 / (RPM_2*steps_per_rev*ms/60));
//delay time for each square wave / microseconds
  Serial.println(step_period_1);
 }

//Code to receive new DR from serial
void recvWithEndMarker() {
    static byte ndx = 0;
    char endMarker = '>';
    char rc;

    if (Serial.available() > 0) {
        rc = Serial.read();

        if (rc != endMarker) {
            receivedChars[ndx] = rc;
            ndx++;
            if (ndx >= numChars) {
                ndx = numChars - 1;
            }
        }
        else {
            receivedChars[ndx] = '\0'; // terminate the string
            ndx = 0;
            newData = true;
        }
    }
}

void updateDR() {
    if (newData == true) {
        dataNumber = 0;
        dataNumber = atof(receivedChars);
        Serial.print("New draw ratio ... ");
        Serial.println(dataNumber);
        newData = false;
        DR = dataNumber;
        set_step_period();
    }
}
```

A5 ImageJ macro for determining fibre diameter

```
var input = getDirectory("Choose a directory");

list = getFileList(input);
for (i = 0; i < list.length; i++) {
open(input + list[i]);
name=list[i];
meta = split(name,"_.x");
scale=meta[1];
if (scale==4){
      run("Set Scale...", "distance=1 known=1.465 unit=um");
} else if (scale==10){
      run("Set Scale...", "distance=1 known=0.586 unit=um");
} else {
      waitForUser("ERROR: Scale not identified");
}
run("32-bit");
setAutoThreshold("Default");
waitForUser("check threshold");
//run("Threshold...");
setOption("BlackBackground", false);
run("Convert to Mask");
run("Local Thickness (masked, calibrated, silent)");
waitForUser("Create line selection down the middle.");
profile=getProfile();
Array.getStatistics(profile, min, max, mean, std);
print(name+": "+mean);
run("Close All");
}
```

A6 Calculating the INT orientational distribution function

The equatorial signals on X-ray scattering (XRS) patterns arise due to the form factor of the cylindrical INTs and present on the diffraction pattern at a position perpendicular to the projection of the INT axis. This is analogous to the equatorial signal observed in XRS patterns of liquid crystals and enables the use of the same formalisms to transform from a given orientational distribution function (ODF) to a calculated azimuthal scan of scattered intensity.

The ODF, $f(\beta)$, describes the orientational distribution of INTs as the frequency distribution of the angle β between the fibre axis and a constituent nanotube. A relationship between the ODF and the azimuthal scan of equatorial intensity, $I(\phi)$, was first derived by Kratky[247] and further developed to

$$I_{calc}(\phi) = \int_{\phi}^{\frac{\pi}{2}} \frac{f(\beta)}{\sqrt{\cos^2\phi - \cos^2\beta}} sin\beta \, d\beta \qquad (30)$$

where $I_{calc}(\phi)$ indicates that this pattern has been calculated from an ODF. A summary of the development of this equation can be found in reference [248]. Angles are defined as in Figure A7.

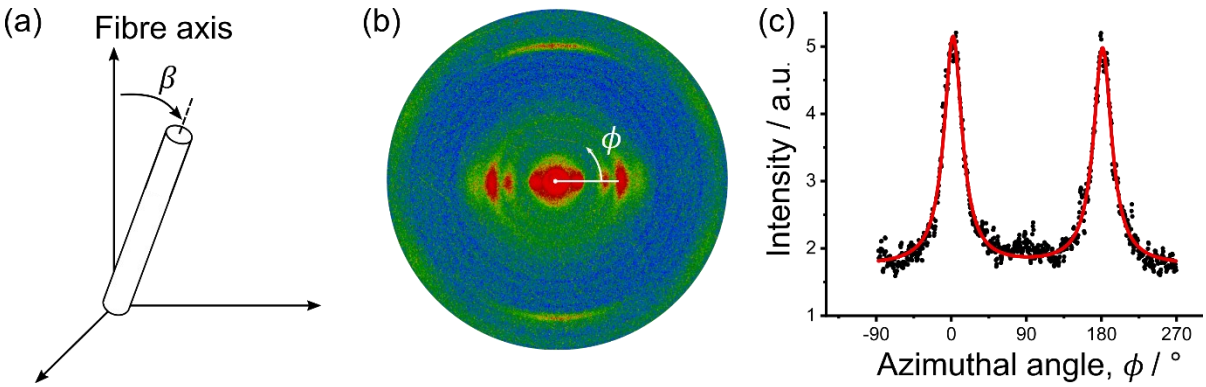


Figure A7. (a) Definition of angle β as the angle between a nanotube and the (vertical) fibre axis, (b) false colour image of typical XRS pattern for INT fibres with the indicated azimuthal angle ϕ, (c) azimuthal scan of scattered intensity along the arc of Q = 2.6 nm^{-1} with fitted Lorentzian peaks of HWHM 13.1°.

At this point it is useful to note that the azimuthal scan of scattered intensity obtained from experiments is fitted well by Lorentzian peaks (Figure A7c) which can be written as,

$$I_{exp}(\phi) = \frac{1}{\phi^2 + w_r^2} \tag{31}$$

where $I_{exp}(\phi)$ indicates that this function is fitted to experimental values and w_r is the fitted (reciprocal space) half-width-at-half-maximum (HWHM) of the Lorentzian peak.

Our aim is now to identify an ODF, $f(\beta)$, which is transformed by equation (30) to our experimentally identified Lorentzian peak $I_{exp}(\phi)$. It has previously[193] been empirically found that a direct space ODF of a Lorentzian to the power 1.5 such as

$$f(\beta) = \left[\frac{1}{\left(2^{\frac{2}{3}} - 1\right)\beta^2 + w_d^2}\right]^{\frac{3}{2}} \tag{32}$$

where w_d is the (direct space) HWHM of this ODF, is transformed by equation (30) to the function $I_{calc}(\phi)$ which closely matches the Lorentzian $I_{exp}(\phi)$ with $w_r = 1.29\, w_d$. A demonstration of this fit is shown in Figure A8 for three different experimental HWHMs, w_r, of 15, 20 and 25°.

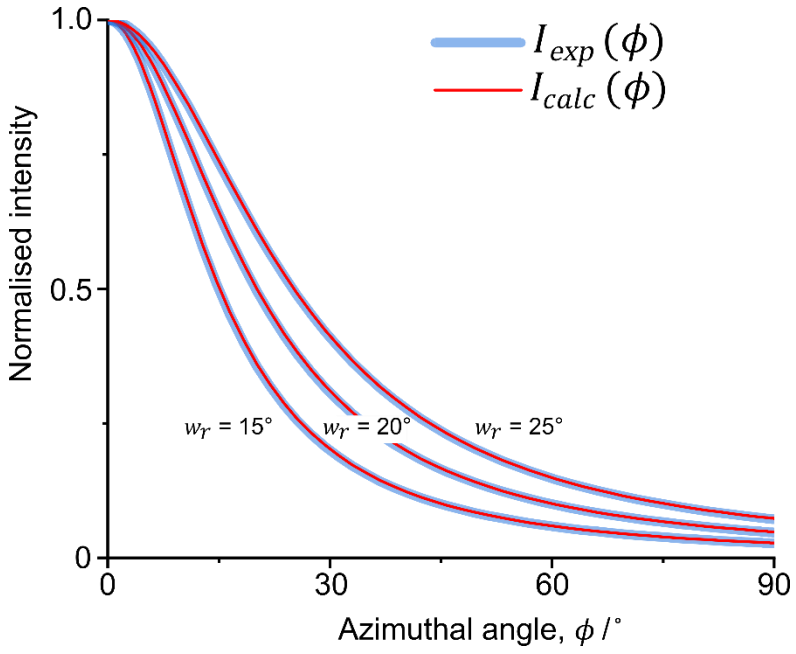


Figure A8. Normalised azimuthal scans of scattered intensity for (blue, $I_{exp}(\phi)$) example Lorentzian fits to experimental data with HWHM w_r and (red, $I_{calc}(\phi)$) scattering patterns calculated from direct space ODFs of the form in equation (32) with HWHM $w_d = \frac{w_r}{1.29}$. The calculated scans were determined by numerical integration of equation (30) in Mathematica.[249]

A key implication of this transformation is that the true degree of INT alignment, given by $f(\beta)$, is considerably greater than that implied by naïve usage of the HWHM from the reciprocal space diffraction pattern (Figure A9).

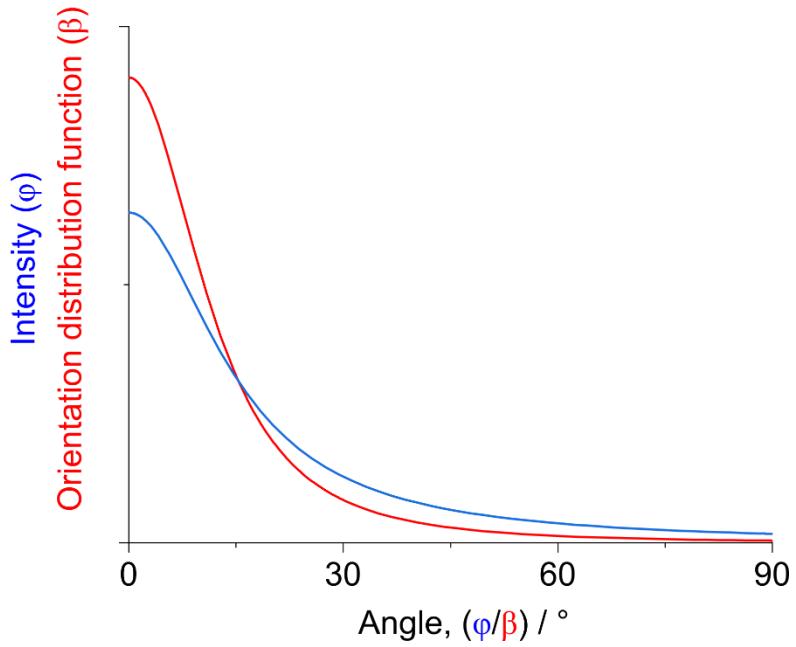


Figure A9. Comparison of azimuthal scans of intensity on XRS patterns with the corresponding deduced orientation distribution function of INTs relative to the fibre axis.

Calculations of the order parameters should be conducted using the direct space ODF as

$$S = \left\langle \frac{3}{2}\cos^2\beta - \frac{1}{2} \right\rangle = \frac{\int_0^{\frac{\pi}{2}} (\frac{3}{2}\cos^2\beta - \frac{1}{2})\, f(\beta)\sin(\beta)\ \mathrm{d}\beta}{\int_0^{\frac{\pi}{2}} f(\beta)\sin(\beta)\ \mathrm{d}\beta} \tag{33}$$

where the denominator is used here to normalise the ODF.

References

[1] M. Sauer, M. Kühnel, 'The global CF and CC market' in *Composites Market Report 2018*, AVK Federation of Reinforced Plastics, 2018.

[2] D. Sunter, I. I. I. W. Morrow, J. Cresko, H. Liddell, 'The manufacturing energy intensity of carbon fiber reinforced polymer composites and its effect on life cycle energy use for vehicle door lightweighting', *20th International Conference on Composite Materials (ICCM20)*, 2015.

[3] M. F. Ashby, 'Chapter 15 - Material profiles' in *Materials and the Environment (Second Edition)*, Butterworth-Heinemann, Boston, 2013, 459.

[4] R. S. Ruoff, D. Qian, W. K. Liu, 'Mechanical properties of carbon nanotubes: theoretical predictions and experimental measurements', *Comptes Rendus Physique*, 2003, 4, 993.

[5] L. Qian, Y. Xie, M. Zou, J. Zhang, 'Building a bridge for carbon nanotubes from nanoscale structure to macroscopic application', *Journal of the American Chemical Society*, 2021, 143, 18805.

[6] M. Pasquali, C. Mesters, 'Opinion: we can use carbon to decarbonize—and get hydrogen for free', *Proceedings of the National Academy of Sciences*, 2021, 118, e2112089118.

[7] J. Lee, D. M. Lee, Y. Jung, J. Park, H. S. Lee, Y. K. Kim, C. R. Park, H. S. Jeong, S. M. Kim, 'Direct spinning and densification method for high-performance carbon nanotube fibers', *Nat Commun*, 2019, 10, 2962.

[8] A. J. Clancy, J. Melbourne, M. S. P. P. Shaffer, 'A one-step route to solubilised, purified or functionalised single-walled carbon nanotubes', *Journal of Materials Chemistry A*, 2015, 3, 16708.

[9] A. J. Clancy, M. K. Bayazit, S. A. Hodge, N. T. Skipper, C. A. Howard, M. S. P. Shaffer, 'Charged carbon nanomaterials: Redox chemistries of fullerenes, carbon nanotubes, and graphenes', *Chemical Reviews*, 2018, 118, 7363.

[10] C. Jiang, A. Saha, C. C. Young, D. P. Hashim, C. E. Ramirez, P. M. Ajayan, M. Pasquali, A. A. Martí, 'Macroscopic nanotube fibers spun from single-walled carbon nanotube polyelectrolytes', *ACS Nano*, 2014, 8, 9107.

[11] E. Paineau, 'Imogolite nanotubes: A flexible nanoplatform with multipurpose applications', *Applied Sciences*, 2018, 8, 1921.

[12] T. W. Clyne, D. Hull, *An introduction to composite materials*, Cambridge University Press, Cambridge, 2019.

[13] A. R. Bunsell, J. Renard, *Fundamentals of fibre reinforced composite materials*, Institute of Physics, Bristol, 2005.

[14] ANSYS, Inc., *Ansys Granta EduPack software*, Cambridge, UK, 2022

[15] Toray T300 Datasheet

[16] Hexcel HexTow IM7 Datasheet

[17] Toray T1000G Datasheet

[18] Toray M55J Datasheet

[19] F. R. Jones, '6 - Glass fibres' in *High-Performance Fibres*, (Ed: J. W. S. Hearle), Woodhead Publishing, 2001, 191.

[20] D. W. Dwight, S. Begum, '1.10 Glass fiber reinforcements' in *Comprehensive Composite Materials II*, (Eds: P. W. R. Beaumont, C. H. Zweben), Elsevier, Oxford, 2018, 243.

[21] D. Hartman, M. E. Greenwood, D. M. Miller, 'High strength glass fibers', Owens Corning Inc, Technical Paper Ref. 1-PL-19025-A

[22] J. L. Thomason, 'Glass fibre sizing: A review', *Composites Part A: Applied Science and Manufacturing*, 2019, 127, 105619.

[23] E. Frank, L. M. Steudle, D. Ingildeev, J. M. Spörl, M. R. Buchmeiser, 'Carbon fibers: precursor systems, processing, structure, and properties', *Angewandte Chemie - International Edition*, 2014, 53, 5262.

[24] D. D. L. Chung, *Carbon fiber composites*, Butterworth-Heinemann, 1994.

[25] M. M. Iovleva, V. N. Smirnova, G. A. Budnitskii, 'The solubility of polyacrylonitrile', *Fibre Chemistry*, 2001, 33, 262.

[26] J. P. Bell, J. H. Dumbleton, 'Changes in the structure of wet-spun acrylic fibers during processing', *Textile Research Journal*, 1971, 41, 196.

[27] J. P. Craig, J. P. Knudsen, V. F. Holland, 'Characterization of acrylic fiber structure', *Textile Research Journal*, 1962, 32, 435

[28] J. P. Knudsen, 'The influence of coagulation variables on the structure and physical properties of an acrylic fiber', *Textile Research Journal*, 1963, 33, 13.

[29] M. Takahashi, M. Watanabe, 'Studies on acrylic fiber (VIII) Effects of the temperature of coagulation bath on the wet spinning of dimethyl formamide-glycerine system', *Sen'i Gakkaishi*, 1960, 16, 7.

[30] E. A. Morris, M. C. Weisenberger, G. W. Rice, 'Properties of PAN fibers solution spun into a chilled coagulation bath at high solvent compositions', *Fibers*, 2015, 3, 560.

[31] J.-S. Tsai, W.-C. Su, 'Control of cross-section shape for polyacrylonitrile fibre during wet-spinning', *Journal of Materials Science Letters*, 1991, 10, 1253.

[32] J. Chen, H. Ge, H. Liu, G. Li, C. Wang, 'The coagulation process of nascent fibers in PAN wet-spinning', *Journal of Wuhan University of Technology-Mater. Sci. Ed.*, 2010, 25, 200.

[33] M. S. Dresselhaus, G. Dresselhaus, K. Sugihara, I. L. Spain, H. A. Goldberg, *Graphite fibers and filaments*, Springer, Berlin, 1988.

[34] A. K. Gupta, D. K. Paliwal, P. Bajaj, 'Acrylic precursors for carbon fibers', *Journal of Macromolecular Science, Part C*, 1991, 31, 1.

[35] E. Fitzer, W. Frohs, M. Heine, 'Optimization of stabilization and carbonization treatment of PAN fibres and structural characterization of the resulting carbon fibres', *Carbon*, 1986, 24, 387.

[36] F. Liu, H. Wang, L. Xue, L. Fan, Z. Zhu, 'Effect of microstructure on the mechanical properties of PAN-based carbon fibers during high-temperature graphitization', *Journal of Materials Science*, 2008, 43, 4316.

[37] S. C. Bennett, D. J. Johnson, W. Johnson, 'Strength-structure relationships in PAN-based carbon fibres', *Journal of Materials Science*, 1983, 18, 3337.

[38] J. G. Lavin, '5 - Carbon fibres' in *High-Performance Fibres*, (Ed: J. W. S. Hearle), Woodhead Publishing, 2001, 156.

[39] S. M. Aldosari, M. Khan, S. Rahatekar, 'Manufacturing carbon fibres from pitch and polyethylene blend precursors: a review', *Journal of Materials Research and Technology*, 2020, 9, 7786.

[40] D. D. Edie, M. G. Dunham, 'Melt spinning pitch-based carbon fibers', *Carbon*, 1989, 27, 647.

[41] T. H. Lim, S. Y. Yeo, 'Investigation of the degradation of pitch-based carbon fibers properties upon insufficient or excess thermal treatment', *Scientific Reports*, 2017, 7, 4733.

[42] D. D. Edie, C. C. Fain, K. E. Robinson, A. M. Harper, D. K. Rogers, 'Ribbon-shape carbon fibers for thermal management', *Carbon*, 1993, 31, 941.

[43] X. Lin, Z. Sheng, J. He, X. He, C. Wang, X. Gu, Y. Wang, 'Preparation of isotropic spinnable pitch with high-spinnability by co-carbonization of coal tar pitch and bio-asphalt', *Fuel*, 2021, 295, 120627.

[44] Z. Qing-Fang, S. Jing-Li, J. Yong, L. Lang, Q. Shu-An, 'The effect of composition and process variables on the spinnability of mesophase pitch', *Carbon*, 1992, 30, 739.

[45] Z. Jiang, T. Ouyang, X. Yao, Y. Fei, 'The effect of the spinning conditions on the structure of mesophase pitch-based carbon fibers by Taguchi method', *Carbon Letters*, 2016, 19, 89.

[46] R. Naslain, 'Carbon fibers from PAN and pitch' in *Advanced Inorganic Fibers: Process - Structure - Properties - Applications*, (Eds: F. T. Wallenberger, R. Naslain, J. B. Macchesney, H. D. Ackler, F. T. Wallenberger), Springer US, Boston, MA, 2000, 233.

[47] U.S. Department of Energy, 'Bandwidth study on energy use and potential energy saving opportunities in U.S. carbon fiber reinforced polymer manufacturing', 2017, DOE/EE-1662

[48] A. M. Donald, A. H. Windle, S. Hanna, *Liquid crystalline polymers*, Cambridge University Press, Cambridge, 2005.

[49] X.-D. Hu, S. E. Jenkins, B. G. Min, M. B. Polk, S. Kumar, 'Rigid-rod polymers: synthesis, processing, simulation, structure, and properties', *Macromolecular Materials and Engineering*, 2003, 288, 823.

[50] G. C. Berry, P. M. Cotts, S.-G. Chu, 'Thermodynamic and rheological properties of rodlike polymers', *British Polymer Journal*, 1981, 13, 47.

[51] S. Rebouillat, '2 - Aramids' in *High-Performance Fibres*, (Ed: J. W. S. Hearle), Woodhead Publishing, 2001, 23.

[52] S. J. Picken, S. van der Zwaag, M. G. Northolt, 'Molecular and macroscopic orientational order in aramid solutions: a model to explain the influence of some spinning parameters on the modulus of aramid yarns', *Polymer*, 1992, 33, 2998.

[53] S. J. Picken, D. J. Sikkema, H. Boerstoel, T. J. Dingemans, S. van der Zwaag, 'Liquid crystal main-chain polymers for high-performance fibre applications', *Liquid Crystals*, 2011, 38, 1591.

[54] M. Afshari, D. J. Sikkema, K. Lee, M. Bogle, 'High performance fibers based on rigid and flexible polymers', *Polymer Reviews*, 2008, 48, 230.

[55] S. Bourbigot, X. Flambard, 'Heat resistance and flammability of high performance fibres: a review', *Fire and Materials*, 2002, 26, 155.

[56] M. Lammers, E. A. Klop, M. G. Northolt, D. J. Sikkema, 'Mechanical properties and structural transitions in the new rigid-rod polymer fibre PIPD (`M5') during the manufacturing process', *Polymer*, 1998, 39, 5999.

[57] P. Smith, P. J. Lemstra, 'Process for making polymer filaments which have a high tensile strength and a high modulus', 1979, US patent number 4,344,908

[58] R. Schaller, K. Feldman, P. Smith, T. A. Tervoort, 'High-performance polyethylene fibers “al dente”: improved gel-spinning of ultrahigh molecular weight polyethylene using vegetable oils', *Macromolecules*, 2015, 48, 8877.

[59] A. J. Pennings, J. M. A. A. van der Mark, A. M. Kiel, 'Hydrodynamically induced crystallization of polymers from solution', *Kolloid-Zeitschrift und Zeitschrift für Polymere*, 1970, 237, 336.

[60] Z. Wang, M. An, H. Xu, Y. Lv, F. Tian, Q. Gu, 'Structural evolution from shish-kebab to fibrillar crystals during hot-stretching process of gel spinning ultra-high molecular weight polyethylene fibers obtained from low concentration solution', *Polymer*, 2017, 120, 244.

[61] DSM Dyneema fact sheet

[62] R. Saito, M. Fujita, G. Dresselhaus, M. S. Dresselhaus, 'Electronic structure of chiral graphene tubules', *Applied Physics Letters*, 1992, 60, 2204.

[63] H. Kataura, Y. Kumazawaa, Y. Maniwa, I. Umezu, S. Suzuki, Y. Ohtsuka, Y. Achiba, 'Optical properties of single-wall carbon nanotubes', *Synthetic Metals*, 1999, 103, 2555.

[64] V. T. Truong, P. J. McMahon, C. L. Olsson-Jacques, A. R. Wilson, G. I. Mathys, 'Multi-walled carbon nanotubes of 200 nm diameter and carbon micro-balloons', presented at *2010 International Conference on Nanoscience and Nanotechnology*, 22-26 Feb., 2010.

[65] C.-H. Kiang, M. Endo, P. M. Ajayan, G. Dresselhaus, M. S. Dresselhaus, 'Size effects in carbon nanotubes', *Physical Review Letters*, 1998, 81, 1869.

[66] M. Terrones, 'Science and technology of the twenty-first century: Synthesis, properties, and applications of carbon nanotubes', *Annual Review of Materials Research*, 2003, 33, 419.

[67] D. Wunderlich, F. Hauke, A. Hirsch, 'Preferred functionalization of metallic and small-diameter single walled carbon nanotubesvia reductive alkylation', *Journal of Materials Chemistry*, 2008, 18, 1493.

[68] T. Saito, 'Chapter 2 - Multidimensional aspects of single-wall carbon nanotube synthesis' in *Carbon Nanotubes and Graphene (Second Edition)*, (Eds: K. Tanaka, S. Iijima), Elsevier, Oxford, 2014, 7.

[69] J. Prasek, J. Drbohlavova, J. Chomoucka, J. Hubalek, O. Jasek, V. Adam, R. Kizek, 'Methods for carbon nanotubes synthesis—review', *Journal of Materials Chemistry*, 2011, 21, 15872.

[70] M. Kumar, Y. Ando, 'Chemical vapor deposition of carbon nanotubes: a review on growth mechanism and mass production', *Journal of Nanoscience and Nanotechnology*, 2010, 10, 3739.

[71] F. Yang, X. Wang, D. Zhang, J. Yang, D. Luo, Z. Xu, J. Wei, J.-Q. Wang, Z. Xu, F. Peng, X. Li, R. Li, Y. Li, M. Li, X. Bai, F. Ding, Y. Li, 'Chirality-specific growth of single-walled carbon nanotubes on solid alloy catalysts', *Nature*, 2014, 510, 522.

[72] R. Rao, C. L. Pint, A. E. Islam, R. S. Weatherup, S. Hofmann, E. R. Meshot, F. Wu, C. Zhou, N. Dee, P. B. Amama, J. Carpena-Nuñez, W. Shi, D. L. Plata, E. S. Penev, B. I. Yakobson, P. B. Balbuena, C. Bichara, D. N. Futaba, S. Noda, H. Shin, K. S. Kim, B. Simard, F. Mirri, M. Pasquali, F. Fornasiero, E. I. Kauppinen, M. Arnold, B. A. Cola, P. Nikolaev, S. Arepalli, H.-M. Cheng, D. N. Zakharov, E. A. Stach, J. Zhang, F. Wei, M. Terrones, D. B. Geohegan, B. Maruyama, S. Maruyama, Y. Li, W. W. Adams, A. J. Hart, 'Carbon nanotubes and related nanomaterials: critical advances and challenges for synthesis toward mainstream commercial applications', *ACS Nano*, 2018, 12, 11756.

[73] H. Zhu, K. Suenaga, J. Wei, K. Wang, D. Wu, 'A strategy to control the chirality of single-walled carbon nanotubes', *Journal of Crystal Growth*, 2008, 310, 5473.

[74] Y. Li, X. Zhang, J. Luo, W. Huang, J. Cheng, Z. Luo, T. Li, F. Liu, G. Xu, X. Ke, L. Li, H. J. Geise, 'Purification of CVD synthesized single-wall carbon nanotubes by different acid oxidation treatments', *Nanotechnology*, 2004, 15, 1645.

[75] T. Sun, T. Zeng, C. Xia, S. Li, H. Wu, 'Purification and separation of single-walled carbon nanotubes (SWCNTs)', *Journal of Nanoscience and Nanotechnology*, 2012, 12, 2955.

[76] X. H. Chen, C. S. Chen, Q. Chen, F. Q. Cheng, G. Zhang, Z. Z. Chen, 'Non-destructive purification of multi-walled carbon nanotubes produced by catalyzed CVD', *Materials Letters*, 2002, 57, 734.

[77] P. D. G. Cradwick, V. C. Farmer, J. D. Russell, C. R. Masson, K. Wada, N. Yoshinaga, 'Imogolite, a hydrated aluminium silicate of tubular structure', *Nature Physical Science*, 1972, 240, 187.

[78] M. P. Lourenço, L. Guimarães, M. C. da Silva, C. de Oliveira, T. Heine, H. A. Duarte, 'Nanotubes with well-defined structure: single- and double-walled imogolites', *The Journal of Physical Chemistry C*, 2014, 118, 5945.

[79] S. Konduri, S. Mukherjee, S. Nair, 'Controlling nanotube dimensions: correlation between composition, diameter, and internal energy of single-walled mixed oxide nanotubes', *ACS Nano*, 2007, 1, 393.

[80] E. Paineau, S. Rouziere, G. Monet, C. C. Diogo, I. Morfin, P. Launois, 'Role of initial precursors on the liquid-crystalline phase behavior of synthetic aluminogermanate imogolite nanotubes', *Journal of Colloid and Interface Science*, 2020, 580, 275.

[81] S.-i. Wada, K. Wada, 'Effects of substitution of germanium for silicon in imogolite', *Clays and Clay Minerals*, 1982, 30, 123.

[82] P. Maillet, C. Levard, E. Larquet, C. Mariet, O. Spalla, N. Menguy, A. Masion, E. Doelsch, J. Rose, A. Thill, 'Evidence of double-walled Al−Ge imogolite-like nanotubes. A cryo-TEM and SAXS investigation', *Journal of the American Chemical Society*, 2010, 132, 1208.

[83] A. Thill, B. Guiose, M. Bacia-Verloop, V. Geertsen, L. Belloni, 'How the diameter and structure of $(OH)_3Al_2O_3Si_xGe_{1-x}OH$ imogolite nanotubes are controlled by an adhesion versus curvature competition', *The Journal of Physical Chemistry C*, 2012, 116, 26841.

[84] A. Thill, P. Maillet, B. Guiose, O. Spalla, L. Belloni, P. Chaurand, M. Auffan, L. Olivi, J. Rose, 'Physico-chemical control over the single- or double-wall structure of aluminogermanate imogolite-like nanotubes', *Journal of the American Chemical Society*, 2012, 134, 3780.

[85] M. S. Amara, E. Paineau, M. Bacia-Verloop, M. E. Krapf, P. Davidson, L. Belloni, C. Levard, J. Rose, P. Launois, A. Thill, 'Single-step formation of micron long $(OH)_3Al_2O_3Ge(OH)$ imogolite-like nanotubes', *ChemComm*, 2013, 49, 11284.

[86] N. P. Stepina, M. S. Galkov, M. R. Predtechenskiy, A. E. Bezrodny, V. V. Kirienko, A. V. Dvurechenskii, 'Preparation and transport properties of oriented buckypapers with single walled carbon nanotubes', *Modern Electronic Materials*, 2019, 5, 21.

[87] A. Mikhalchan, J. J. Vilatela, 'A perspective on high-performance CNT fibres for structural composites', *Carbon*, 2019, 150, 191.

[88] J. S. Bulmer, A. Kaniyoor, J. A. Elliott, 'A meta-analysis of conductive and strong carbon nanotube materials', *Advanced Materials*, 2021, e2008432.

[89] G. Gavrel, B. Jousselme, A. Filoramo, S. Campidelli, 'Supramolecular chemistry of carbon nanotubes' in *Making and Exploiting Fullerenes, Graphene, and Carbon Nanotubes*, (Eds: M. Marcaccio, F. Paolucci), Springer Berlin Heidelberg, Berlin, Heidelberg, 2014, 95.

[90] K. L. Lu, R. M. Lago, Y. K. Chen, M. L. H. Green, P. J. F. Harris, S. C. Tsang, 'Mechanical damage of carbon nanotubes by ultrasound', *Carbon*, 1996, 34, 814.

[91] S. Ramesh, L. M. Ericson, V. A. Davis, R. K. Saini, C. Kittrell, M. Pasquali, W. E. Billups, W. W. Adams, R. H. Hauge, R. E. Smalley, 'Dissolution of pristine single walled carbon nanotubes in superacids by direct protonation', *Journal of Physical Chemistry B*, 2004, 108, 8794.

[92] P. Wang, M. Kim, Z. Peng, C. F. Sun, J. Mok, A. Lieberman, Y. H. Wang, 'Superacid-surfactant exchange: enabling nondestructive dispersion of full-length carbon nanotubes in water', *ACS Nano*, 2017, 11, 9231.

[93] V. A. Davis, A. N. G. Parra-Vasquez, M. J. Green, P. K. Rai, N. Behabtu, V. Prieto, R. D. Booker, J. Schmidt, E. Kesselman, W. Zhou, H. Fan, W. W. Adams, R. H. Hauge, J. E. Fischer, Y. Cohen, Y. Talmon, R. E. Smalley, M. Pasquali, 'True solutions of single-walled carbon nanotubes for assembly into macroscopic materials', *Nature Nanotechnology*, 2009, 4, 830.

[94] O. Kleinerman, L. Liberman, N. Behabtu, M. Pasquali, Y. Cohen, Y. Talmon, 'Direct imaging of carbon nanotube liquid-crystalline phase development in true solutions', *Langmuir*, 2017, 33, 4011.

[95] N. Behabtu, M. J. Green, M. Pasquali, 'Carbon nanotube-based neat fibers', *Nano Today*, 2008, 3, 24.

[96] D. E. Tsentalovich, R. J. Headrick, F. Mirri, J. Hao, N. Behabtu, C. C. Young, M. Pasquali, 'Influence of carbon nanotube characteristics on macroscopic fiber properties', *ACS Applied Materials & Interfaces*, 2017, 9, 36189.

[97] S. A. Hodge, D. J. Buckley, H. C. Yau, N. T. Skipper, C. A. Howard, M. S. P. Shaffer, 'Chemical routes to discharging graphenides', *Nanoscale*, 2017, 9, 3150.

[98] C. Jiang, A. Saha, C. Xiang, C. C. Young, J. M. Tour, M. Pasquali, A. A. Martí, 'Increased solubility, liquid-crystalline phase, and selective functionalization of single-walled carbon nanotube polyelectrolyte dispersions', *ACS Nano*, 2013, 7, 4503.

[99] A. Pénicaud, P. Poulin, A. Derré, E. Anglaret, P. Petit, 'Spontaneous dissolution of a single-wall carbon nanotube salt', *Journal of the American Chemical Society*, 2005, 127, 8.

[100] M. Schirowski, G. Abellán, E. Nuin, J. Pampel, C. Dolle, V. Wedler, T. P. Fellinger, E. Spiecker, F. Hauke, A. Hirsch, 'Fundamental insights into the reductive covalent cross-linking of single-walled carbon nanotubes', *Journal of the American Chemical Society*, 2018, 140, 3352.

[101] M. De Marco, F. Markoulidis, R. Menzel, S. M. Bawaked, M. Mokhtar, S. A. Al-Thabaiti, S. N. Basahel, M. S. P. Shaffer, 'Cross-linked single-walled carbon nanotube aerogel electrodes via reductive coupling chemistry', *Journal of Materials Chemistry A*, 2016, 4, 5385.

[102] M. J. Green, A. N. G. Parra-Vasquez, N. Behabtu, M. Pasquali, 'Modeling the phase behavior of polydisperse rigid rods with attractive interactions with applications to single-walled carbon nanotubes in superacids', *The Journal of Chemical Physics*, 2009, 131, 084901.

[103] F. Mirri, R. Ashkar, V. Jamali, L. Liberman, R. A. Pinnick, P. van der Schoot, Y. Talmon, P. D. Butler, M. Pasquali, 'Quantification of carbon nanotube liquid crystal morphology via neutron scattering', *Macromolecules*, 2018, 51, 6892.

[104] L. M. Ericson, H. Fan, H. Peng, V. A. Davis, W. Zhou, J. Sulpizio, Y. Wang, R. Booker, J. Vavro, C. Guthy, A. N. G. Parra-Vasquez, M. J. Kim, S. Ramesh, R. K. Saini, C. Kittrell, G. Lavin, H. Schmidt, W. W. Adams, W. E. Billups, M. Pasquali, W.-F. Hwang, R. H. Hague, J. E. Fischer, R. E. Smalley, 'Macroscopic, neat, single-walled carbon nanotube fibers', *Science*, 2004, 305, 1447.

[105] R. J. Headrick, D. E. Tsentalovich, J. Berdegué, E. A. Bengio, L. Liberman, O. Kleinerman, M. S. Lucas, Y. Talmon, M. Pasquali, 'Structure-property relations in carbon nanotube fibers by downscaling solution processing', *Advanced Materials*, 2018, 30, 1704482.

[106] L. W. Taylor, O. S. Dewey, R. J. Headrick, N. Komatsu, N. M. Peraca, G. Wehmeyer, J. Kono, M. Pasquali, 'Improved properties, increased production, and the path to broad adoption of carbon nanotube fibers', *Carbon*, 2021, 171, 689.

[107] N. Behabtu, 'Dissolution, processing and fluid structure of graphene and carbon nanotube in superacids: the route toward high performance multifunctional materials', 2012, PhD Thesis, Rice University

[108] N. Behabtu, C. C. Young, D. E. Tsentalovich, O. Kleinerman, X. Wang, A. W. K. Ma, E. A. Bengio, R. F. ter Waarbeek, J. J. de Jong, R. E. Hoogerwerf, S. B. Fairchild, J. B. Ferguson, B. Maruyama, J. Kono, Y. Talmon, Y. Cohen, M. J. Otto, M. Pasquali, 'Strong, light, multifunctional fibers of carbon nanotubes with ultrahigh conductivity', *Science*, 2013, 339, 182.

[109] A. Ghemes, Y. Minami, J. Muramatsu, M. Okada, H. Mimura, Y. Inoue, 'Fabrication and mechanical properties of carbon nanotube yarns spun from ultra-long multi-walled carbon nanotube arrays', *Carbon*, 2012, 50, 4579.

[110] X. Yu, X. Zhang, J. Zou, Z. Lan, C. Jiang, J. Zhao, D. Zhang, M. Miao, Q. Li, 'Solvent-tunable microstructures of aligned carbon nanotube films', *Advanced Materials Interfaces*, 2016, 3, 1600352.

[111] A. Windle, 'Chapter 7 - Understanding the direct spinning of CNT fibers in terms of the thermodynamic and kinetic landscape: a personal view' in *Nanotube Superfiber Materials (Second Edition)*, (Eds: M. J. Schulz, V. Shanov, Z. Yin, M. Cahay), William Andrew Publishing, 2019, 149.

[112] L. Weller, F. R. Smail, J. A. Elliott, A. H. Windle, A. M. Boies, S. Hochgreb, 'Mapping the parameter space for direct-spun carbon nanotube aerogels', *Carbon*, 2019, 146, 789.

[113] T. S. Gspann, F. R. Smail, A. H. Windle, 'Spinning of carbon nanotube fibres using the floating catalyst high temperature route: purity issues and the critical role of sulphur', *Faraday Discussions*, 2014, 173, 47.

[114] R. M. Sundaram, A. H. Windle, 'One-step purification of direct-spun CNT fibers by post-production sonication', *Materials & Design*, 2017, 126, 85.

[115] B. Alemán, V. Reguero, B. Mas, J. J. Vilatela, 'Strong carbon nanotube fibers by drawing inspiration from polymer fiber spinning', *ACS Nano*, 2015, 9, 7392.

[116] J. C. Stallard, W. Tan, F. R. Smail, T. S. Gspann, A. M. Boies, N. A. Fleck, 'The mechanical and electrical properties of direct-spun carbon nanotube mats', *Extreme Mechanics Letters*, 2018, 21, 65.

[117] T. S. Gspann, S. M. Juckes, J. F. Niven, M. B. Johnson, J. A. Elliott, M. A. White, A. H. Windle, 'High thermal conductivities of carbon nanotube films and micro-fibres and their dependence on morphology', *Carbon*, 2017, 114, 160.

[118] J. N. Wang, X. G. Luo, T. Wu, Y. Chen, 'High-strength carbon nanotube fibre-like ribbon with high ductility and high electrical conductivity', *Nature Communications*, 2014, 5, 3848.

[119] W. Xu, Y. Chen, H. Zhan, J. N. Wang, 'High-strength carbon nanotube film from improving alignment and densification', *Nano Letters*, 2016, 16, 946.

[120] G. Liu, Y. Zhao, K. Deng, Z. Liu, W. Chu, J. Chen, Y. Yang, K. Zheng, H. Huang, W. Ma, L. Song, H. Yang, C. Gu, G. Rao, C. Wang, S. Xie, L. Sun, 'Highly dense and perfectly aligned single-walled carbon nanotubes fabricated by diamond wire drawing dies', *Nano Letters*, 2008, 8, 1071.

[121] J. Alvarenga, P. R. Jarosz, C. M. Schauerman, B. T. Moses, B. J. Landi, C. D. Cress, R. P. Raffaelle, 'High conductivity carbon nanotube wires from radial densification and ionic doping', *Applied Physics Letters*, 2010, 97, 182106.

[122] Y. Shang, Y. Li, X. He, S. Du, L. Zhang, E. Shi, S. Wu, Z. Li, P. Li, J. Wei, K. Wang, H. Zhu, D. Wu, A. Cao, 'Highly twisted double-helix carbon nanotube yarns', *ACS Nano*, 2013, 7, 1446.

[123] S. Zhang, L. Zhu, M. L. Minus, H. G. Chae, S. Jagannathan, C.-P. Wong, J. Kowalik, L. B. Roberson, S. Kumar, 'Solid-state spun fibers and yarns from 1-mm long carbon nanotube forests synthesized by water-assisted chemical vapor deposition', *Journal of Materials Science*, 2008, 43, 4356.

[124] Y. Shang, Y. Wang, S. Li, C. Hua, M. Zou, A. Cao, 'High-strength carbon nanotube fibers by twist-induced self-strengthening', *Carbon*, 2017, 119, 47.

[125] J. S. Bulmer, J. E. Mizen, T. S. Gspann, A. Kaniyoor, J. B. Ryley, P. J. Kiley, M. R. Sparkes, B. O'Neill, J. A. Elliott, 'Extreme stretching of high G:D ratio carbon nanotube fibers using super-acid', *Carbon*, 2019, 153, 725.

[126] H. Zhan, Y. W. Chen, Q. Q. Shi, Y. Zhang, R. W. Mo, J. N. Wang, 'Highly aligned and densified carbon nanotube films with superior thermal conductivity and mechanical strength', *Carbon*, 2022, 186, 205.

[127] H. Cho, H. Lee, E. Oh, S.-H. Lee, J. Park, H. J. Park, S.-B. Yoon, C.-H. Lee, G.-H. Kwak, W. J. Lee, J. Kim, J. E. Kim, K.-H. Lee, 'Hierarchical structure of carbon nanotube fibers, and the change of structure during densification by wet stretching', *Carbon*, 2018, 136, 409.

[128] T. Zhou, Y. Niu, Z. Li, H. Li, Z. Yong, K. Wu, Y. Zhang, Q. Li, 'The synergetic relationship between the length and orientation of carbon nanotubes in direct spinning of high-strength carbon nanotube fibers', *Materials & Design*, 2021, 203, 109557.

[129] N. Kateris, P. Kloza, R. Qiao, J. A. Elliott, A. M. Boies, 'From collisions to bundles: an adaptive coarse-grained model for the aggregation of high-aspect-ratio carbon nanotubes', *The Journal of Physical Chemistry C*, 2020, 124, 8359.

[130] M. Woo, R. T. Nishida, M. A. Schriefl, M. E. J. Stettler, A. M. Boies, 'Open-source modelling of aerosol dynamics and computational fluid dynamics: nodal method for nucleation, coagulation, and surface growth', *Computer Physics Communications*, 2021, 261, 107765.

[131] X. Zhang, Y. Deng, B. Graves, M. De Volder, A. Boies, 'Precise catalyst production for carbon nanotube synthesis with targeted structure enrichment', *Catalysts*, 2020, 10.

[132] F. Smail, A. Boies, A. Windle, 'Direct spinning of CNT fibres: past, present and future scale up', *Carbon*, 2019, 152, 218.

[133] J. J. Vilatela, J. A. Elliott, A. H. Windle, 'A Model for the strength of yarn-like carbon nanotube fibers', *ACS Nano*, 2011, 5, 1921.

[134] N. Gupta, J. M. Alred, E. S. Penev, B. I. Yakobson, 'Universal strength scaling in carbon nanotube bundles with frictional load transfer', *ACS Nano*, 2021, 15, 1342.

[135] D. Qian, W. K. Liu, R. S. Ruoff, 'Load transfer mechanism in carbon nanotube ropes', *Composites Science and Technology*, 2003, 63, 1561.

[136] J. A. Elliott, J. K. W. Sandler, A. H. Windle, R. J. Young, M. S. P. Shaffer, 'Collapse of single-wall carbon nanotubes is diameter dependent', *Physical Review Letters*, 2004, 92, 095501.

[137] N. M. Pugno, 'The design of self-collapsed super-strong nanotube bundles', *Journal of the Mechanics and Physics of Solids*, 2010, 58, 1397.

[138] H. Xu, G. Drozdov, J. G. Park, B. D. Jensen, K. E. Wise, Z. Liang, G. M. Odegard, E. J. Siochi, T. Dumitrică, 'Computationally guided design of large-diameter carbon nanotube bundles for high-strength materials', *ACS Applied Nano Materials*, 2021, 4, 11115.

[139] L. Zhang, X. Wang, W. Xu, Y. Zhang, Q. Li, P. D. Bradford, Y. Zhu, 'Strong and conductive dry carbon nanotube films by microcombing', *Small*, 2015, 11, 3830.

[140] D.-M. Lee, J. Park, J. Lee, S.-H. Lee, S.-H. Kim, S. M. Kim, H. S. Jeong, 'Improving mechanical and physical properties of ultra-thick carbon nanotube fiber by fast swelling and stretching process', *Carbon*, 2021, 172, 733.

[141] Y. Zhao, J. Wei, R. Vajtai, P. M. Ajayan, E. V. Barrera, 'Iodine doped carbon nanotube cables exceeding specific electrical conductivity of metals', *Scientific Reports*, 2011, 1, 83.

[142] B. D. Jensen, J.-W. Kim, G. Sauti, K. E. Wise, L. Dong, H. N. G. Wadley, J. G. Park, R. Liang, E. J. Siochi, 'Toward ultralight high-strength structural materials via collapsed carbon nanotube bonding', *Carbon*, 2020, 156, 538.

[143] W. Ma, L. Song, R. Yang, T. Zhang, Y. Zhao, L. Sun, Y. Ren, D. Liu, L. Liu, J. Shen, Z. Zhang, Y. Xiang, W. Zhou, S. Xie, 'Directly synthesized strong, highly conducting, transparent single-walled carbon nanotube films', *Nano Letters*, 2007, 7, 2307.

[144] X.-H. Zhong, Y.-L. Li, Y.-K. Liu, X.-H. Qiao, Y. Feng, J. Liang, J. Jin, L. Zhu, F. Hou, J.-Y. Li, 'Continuous multilayered carbon nanotube yarns', *Advanced Materials*, 2010, 22, 692.

[145] Y. Bai, R. Zhang, X. Ye, Z. Zhu, H. Xie, B. Shen, D. Cai, B. Liu, C. Zhang, Z. Jia, S. Zhang, X. Li, F. Wei, 'Carbon nanotube bundles with tensile strength over 80 GPa', *Nature Nanotechnology*, 2018, 13, 589.

[146] T. S. Gspann, N. Montinaro, A. Pantano, J. A. Elliott, A. H. Windle, 'Mechanical properties of carbon nanotube fibres: St Venant's principle at the limit and the role of imperfections', *Carbon*, 2015, 93, 1021.

[147] A. Rao, S. Tawfick, M. Bedewy, A. J. Hart, 'Morphology-dependent load transfer governs the strength and failure mechanism of carbon nanotube yarns', *Extreme Mechanics Letters*, 2016, 9, 55.

[148] J. C. Phillips, D. J. Hardy, J. D. C. Maia, J. E. Stone, J. V. Ribeiro, R. C. Bernardi, R. Buch, G. Fiorin, J. Henin, W. Jiang, R. McGreevy, M. C. R. Melo, B. K. Radak, R. D. Skeel, A. Singharoy, Y. Wang, B. Roux, A. Aksimentiev, Z. Luthey-Schulten, L. V. Kale, K. Schulten, C. Chipot, E. Tajkhorshid, 'Scalable molecular dynamics on CPU and GPU architectures with NAMD', *Journal of Chemical Physics*, 2020, 153, 044130.

[149] W. Humphrey, A. Dalke, K. Schulten, 'VMD: Visual molecular dynamics', *Journal of Molecular Graphics*, 1996, 14, 33.

[150] H. M. Berman, T. Battistuz, T. N. Bhat, W. F. Bluhm, P. E. Bourne, K. Burkhardt, Z. Feng, G. L. Gilliland, L. Iype, S. Jain, P. Fagan, J. Marvin, D. Padilla, V. Ravichandran, B. Schneider, N. Thanki, H. Weissig, J. D. Westbrook, C. Zardecki, 'The Protein Data Bank', *Acta Crystallographica Section D*, 2002, 58, 899.

[151] C. Ghayor, B. Gjoksi, J. Dong, B. Siegenthaler, A. Caflisch, F. E. Weber, 'N,N Dimethylacetamide a drug excipient that acts as bromodomain ligand for osteoporosis treatment', *Sci Rep*, 2017, 7, 42108.

[152] L. Martinez, R. Andrade, E. G. Birgin, J. M. Martinez, 'PACKMOL: a package for building initial configurations for molecular dynamics simulations', *Journal of Computational Chemistry*, 2009, 30, 2157.

[153] X. Zhang, L. Song, L. Cai, X. Tian, Q. Zhang, X. Qi, W. Zhou, N. Zhang, F. Yang, Q. Fan, Y. Wang, H. Liu, X. Bai, W. Zhou, S. Xie, 'Optical visualization and polarized light absorption of the single-wall carbon nanotube to verify intrinsic thermal applications', *Light: Science & Applications*, 2015, 4, e318.

[154] R. Prakash, S. Washburn, R. Superfine, R. E. Cheney, M. R. Falvo, 'Visualization of individual carbon nanotubes with fluorescence microscopy using conventional fluorophores', *Applied Physics Letters*, 2003, 83, 1219.

[155] M. A. Novak, S. Surwade, J. Prokop, K. Bolotin, J. Hone, L. Brus, C. Nuckolls, H. Liu, 'Visualizing individual carbon nanotubes with optical microscopy', *Journal of the American Chemical Society*, 2014, 136, 8536.

[156] S. L. Anderson, F. Benson, 'Fibre ellipticity and its effect on diameter measurement', *Journal of the Textile Institute Proceedings*, 1953, 44, 98.

[157] BSI Standards Limited, 'Carbon fibre - determination of filament diameter and cross-sectional area', 11567:2018

[158] K. Sears, C. Skourtis, K. Atkinson, N. Finn, W. Humphries, 'Focused ion beam milling of carbon nanotube yarns to study the relationship between structure and strength', *Carbon*, 2010, 48, 4450.

[159] D. B. Murphy, M. W. Davidson, *Fundamentals of light microscopy and electronic imaging*, Wiley-Blackwell, 2012.

[160] J. G. Delly, *Essentials of polarized light microscopy and ancillary techniques*, McCrone Group, 2019.

[161] B. Kozinsky, N. Marzari, 'Static dielectric properties of carbon nanotubes from first principles', *Physical Review Letters*, 2006, 96, 166801.

[162] E. K. Hobbie, 'Optical anisotropy of nanotube suspensions', *Journal of Chemical Physics*, 2004, 121, 1029.

[163] B. E. Sørensen, 'A revised Michel-Lévy interference colour chart based on first-principles calculations', *European Journal of Mineralogy*, 2012, 25, 5.

[164] R. P. Dougherty, K.-H. Kunzelmann, 'Computing local thickness of 3D structures with ImageJ', presented at *Microscopy & Microanalysis 2007 Meeting*, Ft. Lauderdale, FL, 2007.

[165] J. Goldstein, *Scanning electron microscopy and x-ray microanalysis*, Springer Science+Business Media, LLC, New York, NY, 2018.

[166] D. C. Joy, J. B. Pawley, 'High-resolution scanning electron microscopy', *Ultramicroscopy*, 1992, 47, 80.

[167] R. Heu, S. Shahbazmohamadi, J. Yorston, P. Capeder, 'Target material selection for sputter coating of SEM samples', *Microscopy Today*, 2019, 27, 32.

[168] T. Hayashi, H. Muramatsu, Y. A. Kim, H. Kajitani, S. Imai, H. Kawakami, M. Kobayashi, T. Matoba, M. Endo, M. S. Dresselhaus, 'TEM image simulation study of small carbon nanotubes and carbon nanowire', *Carbon*, 2006, 44, 1130.

[169] E. A. Bengio, D. E. Tsentalovich, N. Behabtu, O. Kleinerman, E. Kesselman, J. Schmidt, Y. Talmon, M. Pasquali, 'Statistical length measurement method by direct imaging of carbon nanotubes', *ACS Appl Mater Interfaces*, 2014, 6, 6139.

[170] J. E. Daniels, D. Pontoni, R. P. Hoo, V. Honkimaki, 'Simultaneous small- and wide-angle scattering at high X-ray energies', *Journal of Synchrotron Radiation*, 2010, 17, 473.

[171] A. Guinier, *X-ray diffraction: in crystals, imperfect crystals, and amorphous bodies*, W. H. Freeman, 1963.

[172] B. D. Cullity, S. R. Stock, *Elements of X-ray diffraction*, Pearson, Harlow, Essex, 2014.

[173] M. S. Amara, 'Nanotubes d'imogolite et propriétés de l'eau confinée : organisation, structure et dynamique', 2014, PhD Thesis, Université Paris Sud - Paris XI

[174] G. Monet, 'Nanotubes géo-inspirés : structure atomique, transformation en température et dynamiques corrélées nanotube-eau moléculaire', 2019, PhD Thesis, Université Paris Saclay - Paris XI

[175] N. Stribeck, 'On the determination of fiber tilt angles in fiber diffraction', *Acta Crystallogr A*, 2009, 65, 46.

[176] N. Stribeck, U. Nöchel, 'Direct mapping of fiber diffraction patterns into reciprocal space', *Journal of Applied Crystallography*, 2009, 42, 295.

[177] E. Paineau, M. E. Krapf, M. S. Amara, N. V. Matskova, I. Dozov, S. Rouziere, A. Thill, P. Launois, P. Davidson, 'A liquid-crystalline hexagonal columnar phase in highly-dilute suspensions of imogolite nanotubes', *Nature Communications*, 2016, 7, 10271.

[178] J. C. Fernández-Toribio, B. Alemán, Á. Ridruejo, J. J. Vilatela, 'Tensile properties of carbon nanotube fibres described by the fibrillar crystallite model', *Carbon*, 2018, 133, 44.

[179] M. S. Dresselhaus, G. Dresselhaus, R. Saito, A. Jorio, 'Raman spectroscopy of carbon nanotubes', *Physics Reports*, 2005, 409, 47.

[180] F. Hof, S. Bosch, J. M. Englert, F. Hauke, A. Hirsch, 'Statistical Raman spectroscopy: a method for the characterization of covalently functionalized single-walled carbon nanotubes', *Angewandte Chemie International Edition*, 2012, 51, 11727.

[181] L. G. Cançado, A. Jorio, M. A. Pimenta, 'Measuring the absolute Raman cross section of nanographites as a function of laser energy and crystallite size', *Physical Review B*, 2007, 76.

[182] A. Jorio, R. Saito, J. H. Hafner, C. M. Lieber, M. Hunter, T. McClure, G. Dresselhaus, M. S. Dresselhaus, 'Structural (n,m) determination of isolated single-wall carbon nanotubes by resonant raman scattering', *Physical Review Letters*, 2001, 86, 1118.

[183] R. Graupner, 'Raman spectroscopy of covalently functionalized single-wall carbon nanotubes', *Journal of Raman Spectroscopy*, 2007, 38, 673.

[184] L. G. Cançado, A. Jorio, E. H. M. Ferreira, F. Stavale, C. A. Achete, R. B. Capaz, M. V. O. Moutinho, A. Lombardo, T. S. Kulmala, A. C. Ferrari, 'Quantifying defects in graphene via Raman spectroscopy at different excitation energies', *Nano Letters*, 2011, 11, 3190.

[185] N. I. Rohaizat, K. Alharbi, C. Pinna, H. Ghadbeigi, D. N. Hanlon, I. A. Azid, 'Using a correction factor to remove machine compliance in a tensile test on DP1000 steel validated with 2D digital image correlation technique', presented at *Progress in Engineering Technology III*, Cham, 2021.

[186] J. T. Ash, W. M. Cross, J. J. Kellar, L. Kjerengtroen, 'Accurate determination of system compliance and young's modulus for single fibers', *Journal of ASTM International*, 2010, 8, 1.

[187] V. A. Davis, L. M. Ericson, A. N. G. Parra-Vasquez, H. Fan, Y. Wang, V. Prieto, J. A. Longoria, S. Ramesh, R. K. Saini, C. Kittrell, W. E. Billups, W. W. Adams, R. H. Hauge, R. E. Smalley, M. Pasquali, 'Phase behavior and rheology of SWNTs in superacids', *Macromolecules*, 2004, 37, 154.

[188] C. D. Han, *Rheology in polymer processing*, Academic Press, Cambridge, Mass., 1976.

[189] K. Walters, *Rheometry*, Chapman & Hall, London, 1975.

[190] L. S. K. Pang, J. D. Saxby, S. P. Chatfield, 'Thermogravimetric analysis of carbon nanotubes and nanoparticles', *Journal of Physical Chemistry*, 1993, 97, 6941.

[191] E. Mansfield, A. Kar, S. A. Hooker, 'Applications of TGA in quality control of SWCNTs', *Anal Bioanal Chem*, 2010, 396, 1071.

[192] J. F. Moore, E. Paineau, P. Launois, M. S. P. Shaffer, 'Continuous binder-free fibers of pure imogolite nanotubes', *ACS Appl Mater Interfaces*, 2021, 13, 17940.

[193] W. J. Lee, E. Paineau, D. B. Anthony, Y. Gao, H. S. Leese, S. Rouziere, P. Launois, M. S. P. Shaffer, 'Inorganic nanotube mesophases enable strong self-healing fibers', *ACS Nano*, 2020, 14, 5570.

[194] P. Du, P. Yuan, A. Thill, F. Annabi-Bergaya, D. Liu, S. Wang, 'Insights into the formation mechanism of imogolite from a full-range observation of its sol-gel growth', *Applied Clay Science*, 2017, 150, 115.

[195] G. I. Yucelen, D.-Y. Kang, I. Schmidt-Krey, H. W. Beckham, S. Nair, 'A generalized kinetic model for the formation and growth of single-walled metal oxide nanotubes', *Chemical Engineering Science*, 2013, 90, 200.

[196] P. Maillet, C. Levard, O. Spalla, A. Masion, J. Rose, A. Thill, 'Growth kinetic of single and double-walled aluminogermanate imogolite-like nanotubes: an experimental and modeling approach', *Physical Chemistry Chemical Physics*, 2011, 13, 2682.

[197] J. P. Gustafsson, 'The surface chemistry of imogolite', *Clays and Clay Minerals*, 2001, 49, 73.

[198] E. Paineau, G. Monet, V. Peyre, C. Goldmann, S. Rouziere, P. Launois, 'Colloidal stability of imogolite nanotube dispersions: a phase diagram study', *Langmuir*, 2019, 35, 12451.

[199] H. Khoshnevis, T. Q. Tran, S. M. Mint, A. Zadhoush, H. M. Duong, M. Youssefi, 'Effect of alignment and packing density on the stress relaxation process of carbon nanotube fibers spun from floating catalyst chemical vapor deposition method', *Colloids and Surfaces A: Physicochemical and Engineering Aspects*, 2018, 558, 570.

[200] C. Clemons, 'Nanocellulose in spun continuous fibers: a review and future outlook', *Journal of Renewable Materials*, 2016, 4, 327.

[201] H. L. Cupples, 'The surface tensions of calcium chloride solutions at 25° measured by their maximum bubble pressures', *Journal of the American Chemical Society*, 1945, 67, 987.

[202] H. N. Yoon, 'Strength of fibers from wholly aromatic polyesters', *Colloid and Polymer Science*, 1990, 268, 230.

[203] A. P. Philipse, 'The random contact equation and its implications for (colloidal) rods in packings, suspensions, and anisotropic powders', *Langmuir*, 1996, 12, 1127.

[204] A. Wouterse, S. Luding, A. P. Philipse, 'On contact numbers in random rod packings', *Granular Matter*, 2009, 11, 169.

[205] S. Toll, 'Note: On the tube model for fiber suspensions', *Journal of Rheology*, 1993, 37, 123.

[206] N. Weiner, Y. Bhosale, M. Gazzola, H. King, 'Mechanics of randomly packed filaments—The “bird nest” as meta-material', *Journal of Applied Physics*, 2020, 127, 050902.

[207] Y. Guo, C. Wassgren, B. Hancock, W. Ketterhagen, J. Curtis, 'Granular shear flows of flat disks and elongated rods without and with friction', *Physics of Fluids*, 2013, 25, 063304.

[208] S. S. Rahatekar, M. S. P. Shaffer, J. A. Elliott, 'Modelling percolation in fibre and sphere mixtures: routes to more efficient network formation', *Composites Science and Technology*, 2010, 70, 356.

[209] W. M. Deen, *Introduction to chemical engineering fluid mechanics*, Cambridge University Press, Cambridge, 2016.

[210] H. C. Kim, 'Melt elongational flow rheometry in converging channels', 1993, PhD Thesis, Louisiana State University

[211] H. C. Berg, 'Chapter 1. Diffusion: microscopic theory random walks in biology', Princeton University Press, 2018, 5.

[212] M. Doi, 'Rotational relaxation time of rigid rod-like macromolecule in concentrated solution', *Journal de Physique*, 1975, 36, 607.

[213] K. Y. Lee, D. J. Mooney, 'Alginate: properties and biomedical applications', *Progress in Polymer Science*, 2012, 37, 106.

[214] S. W. Swanton, 'Modelling colloid transport in groundwater; the prediction of colloid stability and retention behaviour', *Advances in Colloid and Interface Science*, 1995, 54, 129.

[215] L. Heller-Kallai, 'Thermally modified clay minerals' in *Handbook of Clay Science*, Vol. 1, 2006, 289.

[216] S. Rouzière, M. S. Amara, E. Paineau, P. Launois, 'Deformations and thermal modifications of imogolite' in *Nanosized Tubular Clay Minerals - Halloysite and Imogolite*, 2016, 254.

[217] G. Monet, S. Rouzière, D. Vantelon, C. Coelho Diogo, D. Maurin, J.-L. Bantignies, P. Launois, E. Paineau, 'Mechanisms of structural reordering during thermal transformation of aluminogermanate imogolite nanotubes', *The Journal of Physical Chemistry C*, 2021, 125, 12414.

[218] K. J. D. MacKenzie, M. E. Bowden, I. W. M. Brown, R. H. Meinhold, 'Structure and thermal transformations of imogolite studied by 29Si and 27Al high-resolution solid-state nuclear magnetic resonance', *Clays and Clay Minerals*, 1989, 37, 317.

[219] C. Zanzottera, A. Vicente, M. Armandi, C. Fernandez, E. Garrone, B. Bonelli, 'Thermal collapse of single-walled alumino-silicate nanotubes: transformation mechanisms and morphology of the resulting lamellar phases', *The Journal of Physical Chemistry C*, 2012, 116, 23577.

[220] L. M. Johnson, T. J. Pinnavaia, 'Silylation of a tubular aluminosilicate polymer (imogolite) by reaction with hydrolyzed (γ-aminopropyl)triethoxysilane', *Langmuir*, 1990, 6, 307.

[221] C. Zanzottera, A. Vicente, E. Celasco, C. Fernandez, E. Garrone, B. Bonelli, 'Physico-chemical properties of imogolite nanotubes functionalized on both external and internal surfaces', *The Journal of Physical Chemistry C*, 2012, 116, 7499.

[222] M. Sun, Y. Chen, J. Zhu, T. Sun, Z. Shui, G. Ling, H. Zhong, 'Effect of modified polyvinyl alcohol fibers on the mechanical behavior of engineered cementitious composites', *Materials*, 2018, 12, 37.

[223] L. A. Girifalco, M. Hodak, R. S. Lee, 'Carbon nanotubes, buckyballs, ropes, and a universal graphitic potential', *Physical Review B - Condensed Matter and Materials Physics*, 2000, 62, 13104.

[224] C. H. Sun, L. C. Yin, F. Li, G. Q. Lu, H. M. Cheng, 'Van der Waals interactions between two parallel infinitely long single-walled nanotubes', *Chemical Physics Letters*, 2005, 403, 343.

[225] I. M. Smallwood, *Handbook of Organic Solvent Properties*, Arnold, London, UK, 1996.

[226] D. Voiry, C. Drummond, A. Pénicaud, 'Portrait of carbon nanotube salts as soluble polyelectrolytes', *Soft Matter*, 2011, 7, 7998.

[227] G. S. Manning, 'Limiting laws and counterion condensation in polyelectrolyte solutions I. Colligative properties', *The Journal of Chemical Physics*, 1969, 51, 924.

[228] K. Vanommeslaeghe, E. Hatcher, C. Acharya, S. Kundu, S. Zhong, J. Shim, E. Darian, O. Guvench, P. Lopes, I. Vorobyov, A. D. Mackerell, Jr., 'CHARMM general force field: A force field for drug-like molecules compatible with the CHARMM all-atom additive biological force fields', *Journal of Computational Chemistry*, 2010, 31, 671.

[229] S. Arepalli, P. Nikolaev, O. Gorelik, V. G. Hadjiev, W. Holmes, B. Files, L. Yowell, 'Protocol for the characterization of single-wall carbon nanotube material quality', *Carbon*, 2004, 42, 1783.

[230] D. E. Tsentalovich, A. W. K. Ma, J. A. Lee, N. Behabtu, E. A. Bengio, A. Choi, J. Hao, Y. Luo, R. J. Headrick, M. J. Green, Y. Talmon, M. Pasquali, 'Relationship of extensional viscosity and liquid crystalline transition to length distribution in carbon nanotube solutions', *Macromolecules*, 2016, 49, 681.

[231] N. Phansalkar, S. More, A. Sabale, M. Joshi, 'Adaptive local thresholding for detection of nuclei in diversity stained cytology images', presented at *2011 International Conference on Communications and Signal Processing*, 10-12 Feb. 2011, 2011.

[232] J. Schindelin, I. Arganda-Carreras, E. Frise, V. Kaynig, M. Longair, T. Pietzsch, S. Preibisch, C. Rueden, S. Saalfeld, B. Schmid, J. Y. Tinevez, D. J. White, V. Hartenstein, K. Eliceiri, P. Tomancak, A. Cardona, 'Fiji: an open-source platform for biological-image analysis', *Nat Methods*, 2012, 9, 676.

[233] D. J. Buckley, S. A. Hodge, M. D. Marco, S. Hu, D. B. Anthony, P. L. Cullen, K. Mckeigue, N. T. Skipper, M. S. P. Shaffer, C. A. Howard, 'Trajectory of the selective dissolution of charged single-walled carbon nanotubes', *Journal of Physical Chemistry C*, 2017, 121, 21703.

[234] N. Fakhri, D. A. Tsyboulski, L. Cognet, R. B. Weisman, M. Pasquali, 'Diameter-dependent bending dynamics of single-walled carbon nanotubes in liquids', *Proceedings of the National Academy of Sciences*, 2009, 106, 14219.

[235] B. I. Yakobson, L. S. Couchman, 'Persistence length and nanomechanics of random bundles of nanotubes', *Journal of Nanoparticle Research*, 2006, 8, 105.

[236] M. Sano, A. Kamino, J. Okamura, S. Shinkai, 'Ring closure of carbon nanotubes', *Science*, 2001, 293, 1299.

[237] B. Scrosati, C. A. Vincent, 'Alkali metal, alkaline earth metal and ammonium halides, amide solvents', *Solubility Data Series, Internation Union of Pure and Applied Chemistry*, 1980.

[238] B. Gebhardt, Z. Syrgiannis, C. Backes, R. Graupner, F. Hauke, A. Hirsch, 'Carbon nanotube sidewall functionalization with carbonyl compounds--modified Birch conditions vs the organometallic reduction approach', *Journal of the American Chemical Society*, 2011, 133, 7985.

[239] S. Chen, W. Shen, G. Wu, D. Chen, M. Jiang, 'A new approach to the functionalization of single-walled carbon nanotubes with both alkyl and carboxyl groups', *Chemical Physics Letters*, 2005, 402, 312.

[240] F. Cataldo, 'Synthesis of ketonic resins from self-polymerization of acetone, 2. Action of bases on acetone and the synthesis of halogenated and diels-alder adducts', *Die Angewandte Makromolekulare Chemie*, 1996, 236, 21.

[241] Z. Tadmor, C. G. Gogos, '14 Stretch shaping' in *Principles of Polymer Processing*, John Wiley & Sons, 2006.

[242] C. B. Weinberger, G. F. Cruz-saenz, G. J. Donnelly, 'Onset of draw resonance during isothermal melt spinning: A comparison between measurements and predictions', *AIChE Journal*, 1976, 22, 441.

[243] H. D. Jeong, S. G. Kim, G. M. Choi, M. Park, B.-C. Ku, H. S. Lee, 'Theoretical and experimental investigation of the wet-spinning process for mechanically strong carbon nanotube fibers', *Chemical Engineering Journal*, 2021, 412, 128650.

[244] K. Koziol, J. Vilatela, A. Moisala, M. Motta, P. Cunniff, M. Sennett, A. Windle, 'High-performance carbon nanotube fiber', *Science*, 2007, 318, 1892.

[245] OriginLab, *Origin Help 14.2.3*, https://www.originlab.com/doc/en/Origin-Help/GridMethod-RandomSpaced#Thin_Plate_Spline_.28TPS.29

[246] G. Donato, S. J. Belongie, 'Approximation methods for thin plate spline mappings and principal warps', 2002.

[247] O. Kratky, 'Zum deformationsmechanismus der faserstoffe, I', *Kolloid-Zeitschrift*, 1933, 64, 213.

[248] D. M. Agra-Kooijman, M. R. Fisch, S. Kumar, 'The integrals determining orientational order in liquid crystals by X-ray diffraction revisited', *Liquid Crystals*, 2018, 45, 680.

[249] Wolfram Research, Inc., *Mathematica*, Champaign, Illinois, USA, 2021